Automatic Landing of a Rotary-Wing UAV in Rough Seas

Author:
Yang, Xilin

Publication Date:
2011

DOI:
https://doi.org/10.26190/unsworks/15086

Automatic Landing of a Rotary-Wing UAV in Rough Seas

Xilin Yang

A thesis submitted in fulfillment
of the requirements of the degree of
Doctor of Philosophy

School of Engineering and Information Technology
University College
University of New South Wales
Australian Defence Force Academy

May 2011

Declaration

I hereby declare that this submission is my own work and, to the best of my knowledge, it contains no material previously published or written by another person, nor material which to a substantial extent has been accepted for the award of any other degree or diploma at UNSW or any other educational institution, except where due acknowledgement is made in the thesis. Any contribution made to the research by others, with whom I have worked at UNSW or elsewhere, is explicitly acknowledged in the thesis.

I also declare that the intellectual content of this thesis is the product of my own work, except to the extent that assistance from others in the project's design and conception, or in style, presentation and linguistic expression is acknowledged.

Xilin Yang
UNSW@ADFA

Abstract

Rotary-wing unmanned aerial vehicles (RUAVs) have created extensive interest in the past few decades due to their unique maneuverability and because of their suitability in a variety of flight missions ranging from traffic inspection to surveillance and reconnaissance. The ability of a RUAV to operate from a ship in the presence of adverse winds and deck motion could greatly extend its applications in both military and civilian roles. This requires the design of a flight control system to achieve safe and reliable automatic landings. Although ground-based landings in various scenarios have been investigated and some satisfactory flight test results are obtained, automatic shipboard recovery is still a dangerous and challenging task. Also, the highly coupled and inherently unstable flight dynamics of the helicopter exacerbate the difficulty in designing a flight control system which would enable the RUAV to attenuate the gust effect.

This thesis makes both theoretical and technical contributions to the shipboard recovery problem of the RUAV operating in rough seas. The first main contribution involves a novel automatic landing scheme which reduces time, cost and experimental resources in the design and testing of the RUAV/ship landing system. The novelty of the proposed landing system enables the RUAV to track slow-varying mean deck height instead of instantaneous deck motion to reduce vertical oscillations. This is achieved by estimating the mean deck height through extracting dominant modes from the estimated deck displacement using the recursive Prony Analysis procedure. The second main contribution is the design of a flight control system with gust-attenuation and rapid position tracking capabilities. A feedback-feedforward controller has been devised for height stabilization in a windy environment based on the construction of an effective gust estimator. Flight tests have been conducted to verify its performance, and they demonstrate improved gust-attenuation capability in the RUAV. The proposed feedback-feedforward controller can dynamically and synchronously compensate for the gust effect. In addition, a nonlinear $\mathcal{H}_\infty$ controller has been designed for horizontal position tracking which shows rapid position tracking performance and gust-attenuation capability when gusts occur.

This thesis also contains a description of technical contributions necessary for a real-time evaluation of the landing system. A high-fidelity simulation framework has been developed with the goal of minimizing the number of iterations required for theoretical analysis, simulation verification and flight validation. The real-time performance of the landing system is assessed in simulations using the C-code, which can be easily transferred to the autopilot for flight tests. All the subsystems are parameterized and can be extended to different RUAV platforms. The integration of helicopter flight dynamics, flapping dynamics, ship motion, gust effect, the flight control system and servo dynamics justifies the reliability of the simulation results. Also, practical constraints are imposed on the simulation to check the robustness of the flight control system. The feasibility of the landing procedure is confirmed for the Vario helicopter using real-time ship motion data.

Acknowledgements

First and foremost, I would like to thank Dr. Matt Garratt and Dr. Hemanshu Pota for their encouragement and support during my PhD studies at UNSW@ADFA. They have been a constant source of inspiration both in my academic life and beyond. In particular, I am extremely grateful to Dr. Matt Garratt for giving me the idea for this work. Without his guidance, support, encouragement and patience, this work would not be possible. I would also thank him for spending so many hours with me on the flight tests. He has been a constant source of inspiration for this research. I am also indebted to Dr. Hemanshu Pota for his valuable suggestions in research problems. His persistent encouragement has always been an impetus for my research. Many thanks also go to his family.

I would also like to thank Dr. Valeri Ugrinovski for his valuable suggestions and thoroughness in discussing research questions.

I wish to thank my colleague Mr. Hendra for being an inspiring friend with whom I have enjoyed interesting theoretical conversations. I also benefited from the discussions with Mr. S Z Sayed Hassen, Mr. Obaid Ur Rehman and Mr. Hua Ouyang. I also appreciate the help given by Xiaochen Wei when I was experiencing hard times. Also, thanks go to the Australian Defence Science and Technology Organization for providing the ship motion data to test my algorithms.

Finally, I would like to thank my family. My aunt and uncle, Xiaoxia Zhang and Jingzhu Yang, have always been an invaluable source of encouragement throughout my education along with my cousins, Lijuan Yang and Hao Yang. I would also like to thank my parents for their love and support. I owe my sincerest gratitude to my grandparents, Kemin Yang and Suqing Li, who are sorely missed but whose memory will continue to inspire me to expand my horizons further.

Last but not least, one last word of my gratitude goes to Hercy He, for her encouragement and for her smile.

Dedicated to my grandparents, parents, my aunt and uncle, and my cousins, Lijuan Yang and Hao Yang

Publications

The following papers follow from the material presented in the thesis:

Journal Papers

1. Xilin Yang, Matt Garratt and Hemanshu Pota (2011) "Monotonous Trend Estimation of Deck Displacement for Automatic Landing of Rotorcraft UAVs", *Journal of Intelligent and Robotic Systems*, to appear in January 2011.

Conference Papers

1. Xilin Yang, Hemanshu Pota, Matthew Garratt and Valery Ugrinovski (2008) "Ship Motion Prediction for Maritime Flight Operations", *Proceedings of the 17th IFAC World Congress*, 6-11 July, Seoul, Korea.
2. Xilin Yang, Hemanshu Pota, Matthew Garratt and Valery Ugrinovski (2008) "Heave Motion Prediction for Maritime Operations of UAVs", *Proceedings of the American Society for Naval Engineers Launch and Recovery Conference*, 19-21 May, Annapolis, USA.
3. Xilin Yang, Hemanshu Pota, Matthew Garratt and Valery Ugrinovski (2008) "Prediction of Vertical Motions for Landing Operations of UAVs", *proceedings of the 47th IEEE Conference on Decision and Control*, 9-11 December, Cancun, Mexico.
4. Xilin Yang, Hemanshu Pota and Matt Garratt (2009) "Design of a Gust-attenuation Controller for Landing Operations of Unmanned Autonomous Helicopters", *18th IEEE International Conference on Control Applications*, 8-10 July, Saint Petersburg, Russia.
5. Xilin Yang, Matt Garratt and Hemanshu Pota (2010) "Estimation of Monotonous Trend of Deck Displacement Dynamics for Landing Operations of Rotorcraft UAVs", *3rd International Symposium on Unmanned Aerial Vehicles*, 21-23 June, Dubai, United Arab Emirates.
6. Xilin Yang, Matt Garratt and Hemanshu Pota (2010) "An Autonomous Recovery System for a Rotorcraft UAV Operating in rough Seas", *AIAA Guidance, Navigation and Control Conference*, 2-5 August, Toronto, Canada.

Contents

List of Tables

List of Figures

List of Symbols

Symbols

a_0	rotor coning angle
a_1	longitudinal flapping
$a_1, \ldots, a_{n_p}$	coefficients of Prony model
a_l	lift curve slope
$a_{(m,1)}, \cdots, a_{(m,m)}$	model coefficients of the predictor
b_1	lateral flapping
$b_{(n,0)}, \cdots, b_{(n,n-1)}$	model coefficients of the predictor
c_{af}	filtered signal
c_{bf}	noisy signal
c_{mr}	main rotor blade chord
d_i	exogenous disturbance
d_r	relative distance
$e(t)$	white noise
e_b	rotor blade hinge offset
e_θ	RUAV pitch error
e_φ	RUAV roll error
e_ψ	RUAV yaw error
$f^{[2+]}(x)$	high-order expansion of system model
g	gravitational acceleration
$h^{[2+]}(x)$	high-order expansion of measurement model
i_s	main rotor shaft angle
k_d	derivative gain
k_i	integral gain
k_{md}	derivative gain for main rotor
k_{mp}	proportional gain for main rotor
k_p	proportional gain
k_{td}	derivative gain for tail rotor
k_{tp}	proportional gain for tail rotor
k_β	center-spring rotor stiffness

m, n	model orders of the predictor
m^*, n^*	optimal orders of the predictor
n_p	Prony model order
p	helicopter roll rate
q	helicopter pitch rate
$q_0, \cdots, q_3$	quaternion parameters
r	helicopter yaw rate
s_l	slope
u	longitudinal body-axis velocity
v	lateral body-axis velocity
v_{xh}, v_{yh}, v_{zh}	velocity components of the RUAV in navigation frame about x, y and z axes
v_{xs}, v_{ys}, v_{zs}	ship velocity components in navigation frame about x, y and z axes
w	vertical body-axis velocity
x	control plant state vector
x_b, y_b, z_b	RUAV position components in body frame about x, y and z axes
x_h, y_h, z_h	RUAV position components in navigation frame about x, y and z axes
x_r, y_r, z_r	relative position components in navigation frame about x, y and z axes
x_s, y_s, z_s	ship position components in navigation frame about x, y and z axes
$y(t)$	measurement of deck displacement
$\hat{y}(t)$	predicted deck displacement
$\hat{y}_{ins}$	system trend
z_b^d	desired vertical distance
$\hat{z}_b$	estimated height of the RUAV
$\bar{z}_d$	mean deck height
z_i	zero of the characteristic equation
z_{ins_deck}	estimated deck displacement
z_m	penalty variable
z_p	peak value of vertical distance
z_∞	stable value of vertical distance
A_1, A_2, A_3	Taylor expansions of system model

A_b	main rotor blade area
A_d	rotor disk area
A_{lat}	lateral cyclic
A_m	amplitude of vibration
B_1	disturbance input matrix
B_2	control input matrix
B_{lon}	longitudinal cyclic
C_1	first-order expansion of measurement matrix
C_b^n	direction cosine matrix
C_{d_0}	profile drag coefficient
C_L^{fn}	vertical fin lift coefficient
C_{lat}	effective steady-state lateral gain
C_{lon}	effective steady-state longitudinal gain
$C_{P_{cli}}$	climb power coefficient
$C_{P_{ind}}$	induced power coefficient
$C_{P_{par}}$	parasite power coefficient
$C_{P_{pro}}$	profile power coefficient
C_T	thrust coefficient
D_i	complex residue
D_{mx}, D_{my}, D_{mz}	geometry parameters of main rotor with respect to CG about x, y and z axes
D_{tx}, D_{ty}, D_{tz}	geometry parameters of tail rotor with respect to CG about x, y and z axes
D_u	forming filter for longitudinal gusts
D_v	forming filter for lateral gusts
D_w	forming filter for vertical gusts
H_a	height above the ground
Im_i	imaginary part of zero of the characteristic equation
I_{xx}, I_{yy}, I_{zz}	moments of inertia of the RUAV about x, y and z axes
I_{xz}	cross product of inertia of the RUAV about x and z axes
I_β	flapping moment of inertia
K	Kalman gain
K_{Fd}	derivative gain
K_{Fp}	proportional gain
L	prediction step

L_{deck}	horizontal moment arm between the landing deck and CG of the ship
L_{fn}, M_{fn}, N_{fn}	external aerodynamic moments on the vertical fin about x, y and z axes
$L_{fus}, M_{fus}, N_{fus}$	external aerodynamic moments on the fuselage about x, y and z axes
L_h, M_h, N_h	external aerodynamic moments on the RUAV about x, y and z axes
L_{mr}, M_{mr}, N_{mr}	external aerodynamic moments on the main rotor about x, y and z axes
L_{tp}, M_{tp}, N_{tp}	external aerodynamic moments on the tail plane about x, y and z axes
L_{tr}, M_{tr}, N_{tr}	external aerodynamic moments on the tail rotor about x, y and z axes
L_u, L_v, L_w	turbulent scales for longitudinal, lateral and vertical gusts
M	updating matrix
M_a	mass of the RUAV
M_i, N_i	mapping matrix
N	width of data window
N_b	number of blades
NP	number of points for testing the predictor
NT	number of points for training the predictor
O_b	CG in body frame
P	error covariance matrix
$\bar{P}$	solution to the Riccati equation
P_{cli}	climb power
P_{ind}	induced power
P_{mr}	main rotor power
P_{par}	parasite power
P_{pro}	profile power
$Q_{(\cdot)}$	covariance matrix of system noise
$R_{(\cdot)}$	covariance matrix of measurement noise
R_b	main rotor radius
Re_i	real part of zero of the characteristic equation
R_h	nonsingular constant matrix

$S^X_{fus}, S^Y_{fus}, S^Z_{fus}$	equivalent flat plate areas of the fuselage about x, y and z axes
S_i	weighting matrix of the $\mathcal{H}_\infty$ controller
T_{mr}	main rotor thrust
T_s	sampling time
T_{tr}	tail rotor thrust
U_c	control input vector
U_r	relative speed of RUAV to the frozen air stream
V_{cl}	climbing velocity
V_i	induced velocity
$\hat{V}_{i0}$	estimated induced velocity when no gusts come
$\hat{V}_i$	estimated induced velocity
$\hat{V}_{ig}$	estimated induced velocity when gusts come
V_{ih}	induced velocity at hover condition
V_n	airflow component perpendicular to TPP
V_t	airflow component tangential to TPP
V_∞	magnitude of free-stream velocity
$V_{\psi s}$	ship yaw rate
V_t^2	horizontal gusts
$\hat{V}_t^2$	estimated horizontal gusts
W	number of dominant poles
X_{fn}, Y_{fn}, Z_{fn}	forces acting on the vertical fin about x, y and z axes
$X_{fus}, Y_{fus}, Z_{fus}$	forces acting on the fuselage about x, y and z axes
X_h, Y_h, Z_h	forces acting on the RUAV about x, y and z axes
X_{mr}, Y_{mr}, Z_{mr}	forces acting on the main rotor about x, y and z axes
X_{tp}, Y_{tp}, Z_{tp}	forces acting on the tail plane about x, y and z axes
X_{tr}, Y_{tr}, Z_{tr}	forces acting on the tail rotor about x, y and z axes
Z_{deck}	landing deck displacement
Z_{CG}	heave motion at the CG of the ship
α	angle of attack
α_r	azimuth angle
β	steady blade flapping angle
β_r	elevation angle
γ_f	lock number
γ_r	prediction capacity factor

δ_{col}	collective pitch servo command
δ_{lat}	lateral servo command
δ_{lon}	longitudinal servo command
δ_{ped}	yaw servo command
δ_{tol}	error tolerance
$\epsilon_{(\cdot)}$	measurement noise
$\varepsilon_{(\cdot)}$	system noise
η	estimation capacity factor
θ	RUAV pitch angle
θ_a	applied blade pitch
$\dot{\theta}_{col}$	rate limit in servo dynamics of collective pitch
θ_p	coefficient vector
θ_r	coefficient vector
θ_s	ship pitch angle
λ	forgetting factor
λ_i	inflow coefficient
λ_i	continuous-time pole of Prony model
λ_β	flapping frequency ratio
μ_b	advanced ratio
$\mu(t)$	vector of lagged measurements
ρ	air density
$\rho_h(x_b, y_b, z_b)$	mass density of the RUAV
σ^2	summed squared error
σ_b	main rotor solidity ratio
σ_{ov}	overshoot
$\sigma_u, \sigma_v, \sigma_w$	turbulent intensity factor for longitudinal, lateral and vertical gusts
ς	maximum relative estimation error
τ_f	main rotor flapping time constant
τ_m	main rotor time constant
τ_s	time constant for servo dynamics
ϕ	RUAV roll angle
φ_p	measurement vector
φ_r	measurement vector
φ_s	ship roll angle

ψ	RUAV yaw angle
ψ_b	azimuth angle
ψ_s	ship yaw angle
ω	exogenous disturbance vector
ω_m	frequency of vibration
$\Delta\theta$	collective pitch offset
Ω_{mr}	main rotor angular velocity
Ψ	maximum prediction error
$\Phi_{k\|k-1}$	state transition matrix
Φ_r	mean squared prediction error
Π	Vandermonde matrix

Abbreviations and Acronyms

AIC	Akaike Information Criterion
AR	Auto-Regressive
BIC	Bayes Information Criterion
CFD	Computational Fluid Dynamics
CG	Center of Gravity
CIC	feedback Control system Information Criterion
DOF	Degree of Freedom
EKF	Extended Kalman Filter
FFRLS	Forgetting Factor Recursive Least Square
FPE	Final Prediction Error
FPGA	Field Programmable Gate Array
GPS	Global Positioning System
HOTO	Hand Over Take Over
IMU	Inertial Measurement Unit
INS	Inertial Navigation Sensor
LMI	Linear Matrix Inequality
LPM	Linear Prediction Model
LQG	Linear Quadratic Gaussian
LQR	Linear Quadratic Regulator
LRF	Laser Range Finder
LS	Least Square
MAF	Moving Average Filter
MB	Megabyte
MIMO	Multiple-Input and Multiple-Output
OLS	Over-determined Least Square
PA	Prony Analysis
PD	Proportional Derivative
PID	Proportional-Integral-Derivative
PLS	Predictive Least Square
PWM	Pulse Width Modulation
RLS	Recursive Least Square
RSLS	Rotary-wing Unmanned Aerial Vehicle/Ship Landing System
RUAV	Rotary-wing Unmanned Aerial Vehicle

SISO	Single-Input and Single-Output
SNR	Signal-to-Noise Ratio
SSE	Summed Squared Error
TPP	Tip Path Plane
TS	Tracking Sensor
UAV	Unmanned Aerial Vehicle
VTOL	Vertical Take-Off and Landing
3D	Three-Dimensional

Chapter 1

Introduction

1.1 Motivation

1.1.1 Unmanned Aerial Vehicle

An increasing demand exists for the deployment of unmanned aerial vehicles (UAVs) in recent years. This has been inspired by the success of several projects, e.g., the *Global Hawk* [3], the *Predator* [4] and the *MQ-8B Firescout* [5]. The reason why UAVs become popular is their usefulness in a variety of applications such as surveillance, reconnaissance, target acquisition and battle damage assessment [6–8]. Compared with manned aircraft, UAVs can greatly reduce potential risks by eliminating the need for a pilot. Operational costs are also decreased as expenses and time-consuming professional training for operators and maintenance personnel can be greatly reduced. It has been revealed from an Australian National Audit Office report [9] that operational costs of piloted helicopters operated by the Royal Australian Navy are normally over 20,000 Australian dollars per hour. In contrast, operational costs of the Yamaha R-Max unmanned helicopter used in our project are only one twentieth of these of manned helicopters, and still remains a relatively small level in consideration of extra costs of fixtures for the ship deck, operator training and sensor system installation.

UAVs can be divided into two categories: fixed-wing and rotary-wing. Fixed-wing UAVs have been subject to extensive investigation in the literature [10–15], and several fixed-wing UAVs have already seen extensive service such as the Global Hawk and the Predator [3, 4]. The rotary-wing unmanned aerial vehicles (RUAVs) have attracted increasing interest over the past few decades due to their suitability for a variety of flight missions ranging from traffic inspection, fire detection and agricultural survey to surveillance and reconnaissance, coastal scientific investigation and battlefield loss assessment [16–21]. Operational flexibilities, including vertical take-off and landing (VTOL) capacity, hovering at a desired height, longitudinal and lateral manoeuvre, make the RUAV an ideal platform for such applications.

RUAVs also have the potential to enable a range of new maritime applications if automatic recovery operations from ships in rough seas are to be achieved reliably [22]. These potential applications include search and rescue, ocean water sampling, fish spotting, cargo transport, maritime weather observation, anti-submarine warfare, border protection and communications relay [23–25].

1.1.2 Problem Statement and Complexity

The research work contained in this thesis was conducted in support of a research project which is aimed at achieving an automatic landing of a RUAV from a ship at sea. Successful landing on an oscillating ship deck will extend the use of the RUAV in a variety of maritime operations [22]. This project is devoted to developing a feasible procedure for achieving this goal.

An automatic landing operation is referred to as a full-envelope landing mission in the absence of a pilot inside the RUAV. It is characterized by completing approach and landing procedures automatically based on cooperation between onboard equipment and a base station. Implementing an autonomous flight is difficult as the open-loop flight dynamics of helicopters are often unstable and highly coupled, and vary widely across the flight envelope [26]. Also, compared with manned helicopters, the RUAV is more vulnerable because less payload is available to incorporate fail-safe equipment in bad weather [27]. Furthermore, for manned helicopters, when they approach the vicinity of a ship deck in a turbulent environment, experienced pilots, based on observation of the ambient environment, inspect, evaluate and trigger the appropriate moment to start the landing process to implement the desired trajectory. They continuously adjust attitudes and height to attain anticipative controllability to prevent unexpected accidents. In contrast, for the RUAV, considerable efforts are required to complete the same landing process intelligently and automatically [28]. This unavoidably complicates onboard configurations.

The realization of an automatic landing arouses a number of theoretical and technical complexities [28, 29]. During the landing mission, the RUAV needs to fulfill a series of tasks which would be completed by an experienced pilot in a manned helicopter [30]. Firstly, the RUAV should have a complete and accurate knowledge of its position, velocity and attitude information in a turbulent environment. One of the key problems, however, is to enable the RUAV to locate the instantaneous positions of the landing deck accurately. Furthermore, the RUAV is expected to capture the mean deck height for the purpose of designing an applicable descent trajectory.

The design process of a successful landing system for a RUAV is composed of the following activities:

- To plan a smooth landing trajectory, the RUAV should be able to predict the deck motion with sufficient prediction horizon. Accurate and rapid prediction of deck displacement can help to decide the best time to start descent;
- The design of an effective integrated navigation system which comprises supplementary sensors. The primary goal is to take advantage of auxiliary attributes of multiple sensors to enhance estimation performance with a better accuracy than a single sensor operating in an isolated fashion;
- A smooth landing requires an accurate estimation of mean height of the deck. By doing this, the RUAV can avoid following instantaneous deck positions, which lead to fluctuations of the RUAV height;
- The RUAV experiences great thrust fluctuations when approaching the vicinity of the landing deck in a gusty environment [31]. This requires development of a gust-attenuation controller to stabilize the height of the RUAV before the landing operation is triggered;
- Strong gusts occur when the RUAV approaches the landing deck which make it challenging to maintain the desired horizontal position. To improve the tracking performance of the desired horizontal position, a controller with the ability to achieve gust-attenuation and rapid response is preferred;
- The RUAV is subject to rigorous limitations on flight envelopes in adverse weather [32]. This situation leads to more complexities in operational capacities, which should be taken into account when designing the landing trajectory.

1.1.3 Research Objective

The primary objective of this thesis is to design a generic automatic landing strategy for the RUAV operating in rough sea conditions, and to develop a high-fidelity parameterized simulation model with the goal of methodology verification and eventual flight validation. This contributes to understanding the characteristics of ship/RUAV dynamic interactions, and the resultant limitations on flight envelopes during landing operations. Practical constraints will also be taken into account to evaluate the

Figure 1.1. The UNSW@ADFA Eagle helicopter

Figure 1.2. The UNSW@ADFA Vario helicopter

performance of the landing scheme. A consideration of these factors helps to minimize the time, cost and physical resources necessary in designing a reliable landing system for RUAVs.

1.2 Main Contributions

My main contributions in this thesis are summarized as follows:

1. Based on the bisection method, a convenient procedure is developed to calculate the main rotor thrust and the induced velocity in a gusty environment. This procedure explicitly considers the gust effect, and results in the accurate estimation of the main rotor thrust and the induced velocity. Its feasibility into the RUAV/ship landing system (RSLS) has been confirmed in simulations using the C code.
2. An effective deck displacement predictor is presented. The construction of this predictor involves determination of model orders using the proposed order-selection principle, and identification of model coefficients by the forgetting factor recursive least square (FFRLS) method. Performance of the resultant predictor has been evaluated in simulations, and the predictor shows satisfactory results with promising prediction horizon when applied for deck displacement prediction.
3. An integrated navigation system is designed based on the extended Kalman filtering technique. By fusing measurements from onboard multiple sensors, the extended Kalman filter (EKF) can efficiently smooth out noisy positions and velocities of the RUAV. The landing deck positions can also be accurately estimated due to the relative motion information provided by the tracking sensor. Performance of the EKF has been validated in simulations using real-time deck motion data.
4. A recursive Prony Analysis (PA) procedure is presented to estimate the mean deck height to assist in an automatic landing. This procedure makes use of the FFRLS method to achieve online curve-fitting with model order selected in consideration of model complexity and computational burden. The mean deck height is obtained after dominant modes are extracted. Performance of the recursive PA is demonstrated using real-time deck motion data.
5. An effective gust estimator is designed based on available measurements, which leads to the construction of a feedback-feedforward controller. This controller can synchronously compensate for the gust effect and be applied to the height control of the RUAV operating in a gusty environment. The gust-attenuation capability of the proposed controller has been evaluated by considering practical requirements in simulations using the C code. Flight tests have been completed for the Eagle helicopter (Fig. 1.1) to verify the performance of the proposed control strategy.

6. A nonlinear $\mathcal{H}_\infty$ controller is developed to achieve gust-attenuation and improve horizontal position tracking capability of the RUAV. The control problem is formulated as finding a state feedback controller which improves the disturbance attenuation capability of the RUAV. Compliance with practical constraints is then checked using parameters of the Vario helicopter, and it is shown that the $\mathcal{H}_\infty$ controller delivers promising dynamic performance when gusts occur. Comparison with proportional-integral-derivative (PID) controllers is also conducted to evaluate the gust attenuation capability of the $\mathcal{H}_\infty$ controller.
7. A novel automatic landing scheme for maritime operations of the RUAV is outlined. By synthesizing the related subsystems, a generic closed-loop simulation framework is established to investigate flying qualities of the RUAV during landing operations in rough seas. This high-fidelity simulation model was implemented using the C code. Based on the estimation of the mean deck height, the feedback-feedforward controller and the $\mathcal{H}_\infty$ controller are combined to control helicopter positions in a gusty environment. A high-fidelity simulation model (Fig. 1.3), taking into account practical constraints, is developed to evaluate the RSLS. Based on parameters of the Vario helicopter shown in Fig. 1.2, it is demonstrated that the RUAV is able to achieve a successful landing by following the proposed procedure. The proposed landing scheme has been justified by using parameters of two helicopter platforms in our lab, and can be modified to accommodate other helicopter platforms with different configurations.

1.3 Organization of the Dissertation

The remainder of this thesis is organized as follows:

Chapter 2: This chapter presents the literature review on existing landing strategies and helicopter control approaches.

Chapter 3: This chapter reviews flight dynamics of a helicopter. The main rotor thrust calculation procedure is designed and implemented. External forces and moments acting on model-scale helicopters are analyzed. Avionics of the helicopter platforms, the *Eagle* and the *Vario*, are described. A closed-loop simulation model used to conduct automatic landing research is also introduced, which integrates

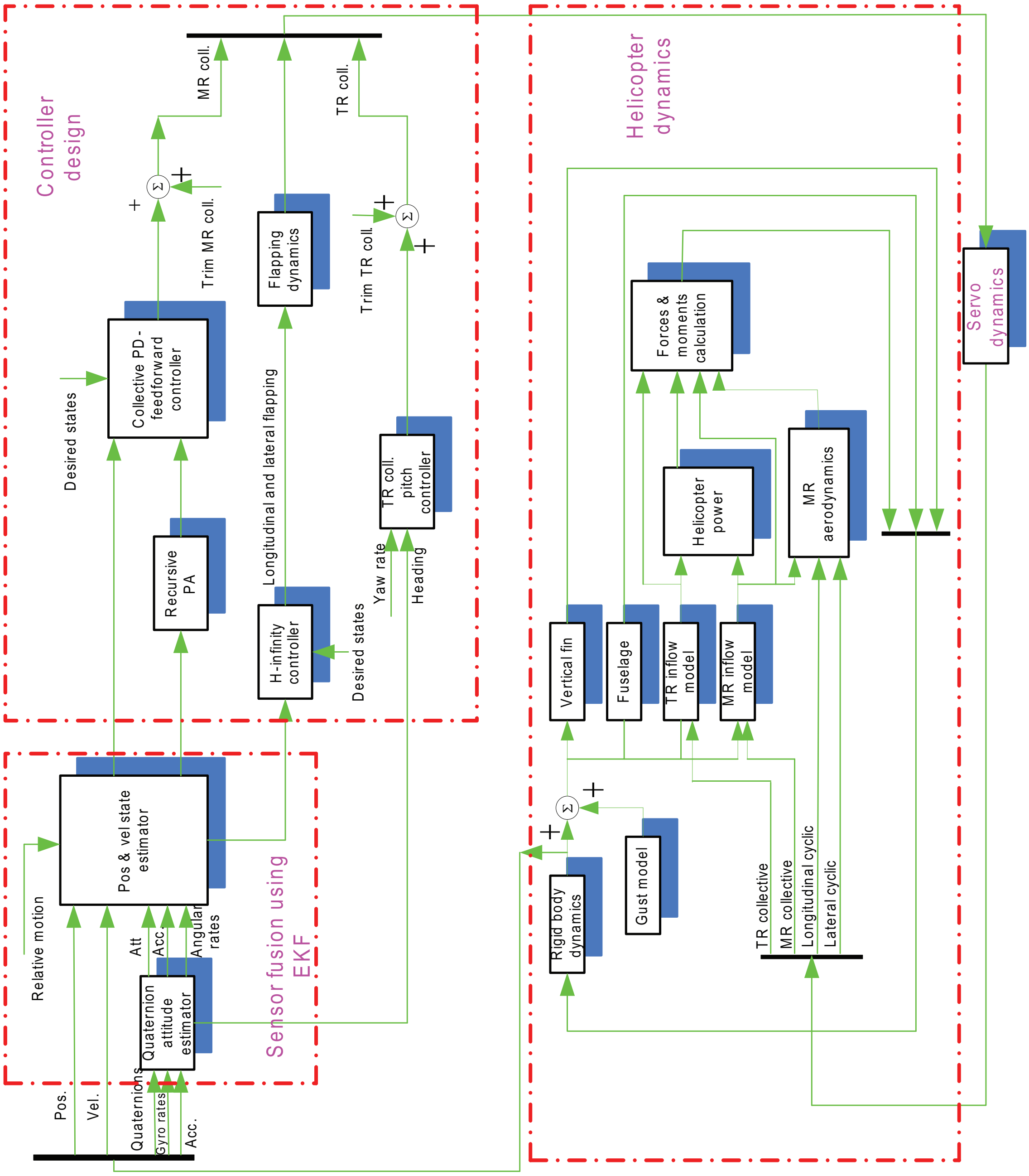

Figure 1.3. Top view of the RSLS

helicopter flight dynamics, state estimator, relative motion, control algorithms and servo dynamics.

Chapter 4: This chapter proposes a predictor for displacement motion of the landing deck. Identification of model orders is firstly addressed. Then the structure of the proposed predictor is explained. Simulation results are also given.

Chapter 5: This chapter shows how to develop an integrated navigation algorithm based on the EKF technique. The structure of the EKF which integrates the inertial navigation sensor, the global positioning system and the visual tracking sensor is discussed. The detailed update and measurement models are derived in terms of quaternion parameters. Implementation of the integrated navigation algorithm is also given.

Chapter 6: In this chapter, a recursive PA procedure is presented to estimate the mean deck height to assist in an automatic landing. The conventional PA is firstly reviewed, and its numerical limitations are summarized. Structure of the proposed recursive PA is described. This chapter also includes a description of the dominant mode selection criterion. Procedure of estimating the mean deck height is also shown using real-time deck motion data.

Chapter 7: This chapter shows how a feedback-feedforward controller is designed for the height control of the RUAV operating in a gusty environment. Heave motion dynamics under wind gusts are firstly analyzed. Then development of a gust estimator in consideration of sensor errors is described. A feedback-feedforward controller is derived based on the gust estimator. This chapter also consists of simulation and flight test results of the proposed controller.

Chapter 8: This chapter introduces a nonlinear $\mathcal{H}_\infty$ controller to achieve gust-attenuation capability for the RUAV. A nonlinear dynamic model is firstly derived. Then procedure of the $\mathcal{H}_\infty$ design approach is described in detail. Comparative studies of this controller is also conducted in consideration of practical constraints.

Chapter 9: This chapter presents a systematic procedure for an automatic landing of the RUAV in rough seas. It begins with a description of the proposed landing strategy. Then architecture of the flight control system is introduced. A high-fidelity simulation model, taking into account practical constraints, is developed to evaluate the RSLS. Simulation results using real-time ship motion data are also given.

Chapter 10: This chapter summarizes the main contributions and provides some suggestions for future work.

Chapter 2

Literature Review

2.1 Introduction

This chapter reviews the existing literature on automatic landing systems, RUAV control and the modeling of wind gusts. Several landing strategies for automatic recovery of fixed-wing UAVs are firstly described, followed by a description of possible landing strategies for RUAVs. Helicopter control approaches are also reviewed.

2.2 Automatic Landing Strategies for the RUAV

Landing of a helicopter on a ship deck is acknowledged to be one of the most challenging and dangerous of all helicopter flight operations [33, 34]. This results from both the confined deck space and the random oscillating ship motion. Also, the descent trajectory of the RUAV deviates greatly from the desired trajectory when strong gusts occur. These challenges greatly exacerbate the difficulty in designing a safe and reliable landing system. Currently, there are several available landing methods particularly suitable for a narrow group of fixed-wing UAVs. These methods include parachute landing, net capture and deep stall landing.

Parachute landing is a possible solution which captures the induced air and generates the drag to control vertical motion [35]. A safe landing can be achieved when the descent speed is relatively slow at the moment of touchdown. This landing strategy has been applied to *Starbird* (Northrop Grumman), *SkyEye* (BAE), *Dakota* (Daedalus) and other fixed-wing UAVs. However, it is very difficult to arrange the proper moment to trigger the deployment of a parachute to land the UAV on the desired spot. Also, the parachute recovery system is easily subject to wind gusts, which lead to the difficulty in predicting the precise point of touchdown [35].

Another method, net capture, is a simple shipboard recovery solution [36]. In this strategy, the stretched net hangs above the stern of the ship and captures the UAV when it flies into the net. This landing method has been tested on the *RQ-2 Pioneer* UAV. The major drawback is that the rotor blades could be broken down. Similarly, the deep stall landing strategy, which often employs an elastic net as an impact force and moment attenuator, has the same disadvantage. Thus, the existing landing strategies suitable for fixed-wing UAVs cannot be applied to automatic landing of RUAVs.

To achieve a reliable automatic landing, it is necessary that the flight control and guidance systems have the ability to evaluate the operational environment and determine the proper descent strategy. Flight control system design is thus one of the crucial issues and has been investigated in several papers. Design of a flight control system for shipboard landings of helicopters was discussed by Gevaert and Schulze [37]. They proposed a method which was based on the accurate prediction of ship heave and roll motion. The helicopter was controlled to touch down on the deck at the moment of zero ship roll motion. However, ignoring pitch motion is unsuitable for general landing operations since the pitch motion at the stern of the ship could generate destructive impact forces.

A hierarchical two-scale landing strategy using a tether was proposed by Oh *et al.* [38] for an automatic landing of the RUAV on a rocking ship. Detection of the deck motion was performed using an instrumented tether with angle sensors. The horizontal position of the RUAV was treated as fast dynamics and attitudes were grouped as slow dynamics together with the height. The proposed tracking controller was designed based on the assumption that the commanded position for fast dynamics have been achieved due to the rapid response of fast dynamics. One possible weakness of this landing method is the disturbance-attenuation capability when gusts occur since the gust effect is not considered. Thus, the accurate position tracking performance is not guaranteed. Also, it is impractical to apply this landing approach as it is very difficult for the RUAV to hook up the cable to the desired position on an oscillating deck in rough seas to enable the landing operation.

Gliding descent and landing when the helicopter is exposed to the autorotation was addressed by Lee *et al.* [39]. They formulated the landing issue as a nonlinear optimal control problem and added path inequality constraints. The optimal solutions led to a control technique similar to those used by helicopter pilots in actual autorotation landings. Although this strategy has been tested in simulations for a simplified helicopter model, many practical constraints have not been considered (e.g., wind shear, turbulence and calculation of achievable landing sites). Similarly, automatic landing was treated as a suboptimal control problem in [40], and the controller was designed by solving the state dependent Riccati equation. This method, however, suffers from difficulties in the real-time implementation due to the solvability of the Riccati equation. An automatic landing controller that can tolerate actuator stuck faults was designed by Liao *et al.* [41]. The proposed controller used the $\mathcal{H}_2$ control technique and solved a group of linear matrix inequalities (LMIs). Thus, solving the LMIs online becomes a major limitation in real-time applications.

The landing problems of RUAVs were also investigated using vision-based techniques in various situations [29, 42–47]. Available experimental tests have mainly concentrated on autonomous landings on horizontal or quasi-horizontal surfaces [48]. Garcia-Pardo *et al.* [29] proposed and experimentally tested a visual detection algorithm to make a safe landing decision. A vision-based algorithm was presented to enable an autonomous helicopter to land on a moving target with planar motion constraints [49]. An optimal trajectory controller was derived for landing the RUAV on a moving target with a cubic spline landing trajectory based on a simplified kinematic model of the helicopter [50]. In [34], an automatic flight control strategy was developed which made use of optical flow. The objective was to make the landing system behave in a natural way, similar to that achieved by an actual pilot. The attitudes and horizontal positions were controlled using classical design techniques. The natural inspired flight control and flight envelope protection systems were implemented only in vertical motion. This landing system was evaluated in simulations in good weather conditions without involvement of ship motion, and further research needs to be conducted to verify its feasibility into real-time applications.

It can be concluded that most of the literature on automatic landing of RUAVs focuses on the ground-based landing, and there are very limited papers dealing with maritime automatic landing. Also, real-time ship motion is not considered in the existing landing strategies when designing the flight control system. This weakness limits the usefulness of such landing strategies for real applications.

2.3 Helicopter Control

2.3.1 PID Control

Simple PID controllers have been designed in various scenarios on small helicopters [51, 52]. Three independent single-input and single-output (SISO) systems were established for attitude control of a model helicopter by Park *et al.* [53]. The proportional-derivative (PD) controllers were applied and their performance were verified in flight experiments. Dzul *et al.* [54] focused on the design and implementation of a controller for a two degree-of-freedom (DOF) system. This system was composed of a small-scale helicopter which was mounted on a vertical platform. A proper controller was derived using the classical pole-placement technique for the yaw dynamics and an adaptive pole-placement method was designed for the altitude dynamics. Mettler *et al.* [55] reported that the stabilizer bar which is fitted on small helicopters to increase the main rotor stability, was a major performance limitation for PD controllers. They introduced a second-order notch filter which allowed higher gains and provided sufficient gain and phase margin. The control system was subsequently optimized using a specialized control design framework with a frequency response envelope specification, which allows the attitude control performance to be accurately specified while ensuring that the lightly damped rotor/stabilizer/fuselage mode is adequately compensated.

2.3.2 Robust Control

The objective of the $\mathcal{H}_\infty$ control theory is to minimize the maximal energy characterized by the closed-loop transfer function over all frequencies from exogenous inputs to the error signal. The transfer function, referred to as the lower linear fractional transformation, is represented by $F_l(P_h, K_h)$. Given a generalized plant P_h, the $\mathcal{H}_\infty$ controller design problem is equivalent to finding a stabilizing controller K_h such that the performance specifications are satisfied in the presence of the uncertainties. On many occasions, the controller design problem is reduced to conducting the suboptimal $\mathcal{H}_\infty$ synthesis with the objective to obtain a stabilizing controller K_h such that the maximum norm

$$\|F_l(P_h, K_h)\|_\infty < \gamma_h \tag{2.1}$$

where $\frac{1}{\gamma_h}$ is the minimum norm of the perturbation that destabilizes the closed-loop system. For helicopter control, $\mathcal{H}_\infty$ design approaches have been extensively investigated. In [56], a linear state-space model for the hover flight was set up with identified parameters validated by flight tests, and the $\mathcal{H}_\infty$ controller was designed for stabilization of helicopter attitudes. It was experimentally shown that the $\mathcal{H}_\infty$ controller resulted in faster attitude response than the linear quadratic Gaussian (LQG) controller due to introducing more damping effect. The authors concluded that this advantage stemmed from the fact that the $\mathcal{H}_\infty$ design technique explicitly took into account the descriptions for model errors. Civita *et al.* [57] succeeded in implementing an $\mathcal{H}_\infty$ loop-shaping controller on a Yamaha R-50 helicopter. They reported that the tracking performance was improved greatly using this design approach. Yang *et al.* [58] designed 6-DOF $\mathcal{H}_\infty$ controllers for the helicopter hover control. The design procedure was decoupled and controllers were divided into two groups with one for translational motion and the other for rotational motion. They also extended the design methodology in the presence of parameter uncertainties [59], and discussed how to minimize the tracking errors between the $\mathcal{H}_\infty$ flight control commands and the actually achievable control forces and moments using the control surface inverse algorithm [60]. Kureemun *et al.* [61] conducted a controller synthesis using a decoupled control scheme with the goal of minimizing the coupling among different channels. This was achieved by the $\mathcal{H}_\infty$ robust stabilization combined with the classical loop shaping. It was claimed in this paper that the $\mathcal{H}_\infty$ controller performed better than the baseline controller. In [62], system identification experiments were carried out for a large-scale unmanned helicopter, followed by the design of a position control system based on the $\mathcal{H}_\infty$ control theory. Experiments verified that the proposed design approach could be used for practical applications. In [63], an $\mathcal{H}_\infty$ flight control system was designed to improve helicopter stability, manoeuvrability and agility. The linear $\mathcal{H}_\infty$ design approach was applied to a linearized model of the helicopter dynamics, and its performance was evaluated in simulations when constraints on actuators were taken into account. However, there were no experimental results in this paper to verify the practicality of the proposed controller.

There is also some literature on helicopter control using the $\mathcal{H}_2$ and $\mu-$synthesis methods [64, 65]. Performance of the $\mathcal{H}_2$ and $\mathcal{H}_\infty$ controllers when applied to helicopter control were assessed by Weilenmann *et al.* [64]. They concluded that the static $\mathcal{H}_2$ design method with available guaranteed robustness allowed for a rapid initial estimate of the possible bandwidth. Significant performance improvement can be obtained using the $\mathcal{H}_\infty$ design approach, which is only attainable when the actual constraints and disturbances of the plant are well-known. Similarly, given specific performance requirements, Rozak and Ray [65] constructed robust controllers based on the $\mathcal{H}_\infty$ and $\mu-$synthesis theories to determine which configuration provided the best overall handling quality performance. For the control objectives stated there, it was found out that the rate command controller using the $\mu-$synthesis produced the best overall performance. It was suggested by Shim *et al.* [66] that the $\mu-$synthesis control theory is advantageous for the uncertain and strongly coupled helicopter dynamics as it can [66]:

- quantify the uncertainty and unmodeled dynamics present in the plants;
- model the noise characteristics of the sensor system;
- specify performance objectives in a quantitative manner.

Kadmiry *et al.* [67] designed a fuzzy gain scheduled dynamic output feedback $\mathcal{H}_\infty$ controller to track the desired values in altitude and attitude angles of an unmanned helicopter when performing aggressive manoeuvres by constructing the linear bounds of nonlinearities.

2.3.3 LQR/LQG

Linear quadratic regulator (LQR) and LQG theories have also been applied to helicopter control. Cunha *et al.* [68, 69] addressed a nonlinear gain scheduled control framework based on a group of linear controllers using the LQR synthesis technique, and verified it in simulations. Abbeel *et al.* [70] proposed a reinforcement learning algorithm to find the controller that was optimized for the resulting model and reward function. The suggested differential dynamic programming was an extension to the LQR, and solved the general Markov decision process by iterating the following two steps [70]:

1. Compute a linear approximation to the model dynamics and a quadratic approximation to the reward function around the trajectory obtained when using the current policy;
2. Compute the optimal policy for the LQR problem obtained in Step 1 and set the current policy equal to the optimal policy.

The controller has been successfully tested for a group of challenging manoeuvres with an acrobatic helicopter. In [71], a simplified helicopter model was employed to design an enhanced LQR controller by means of an unscented Kalman filter for the helicopter hover condition. It was shown by the authors in simulations that the proposed LQR could achieve adaptive performance without the need to adjust controller parameters. A LQG controller with set point tracking capacity was designed and implemented on a state-space model for a small radio-controlled helicopter by Morris *et al.* [72]. The flight test results showed that the yaw motion using the LQG was not satisfied due to poor modeling of yaw dynamics. The disadvantage of the LQG was reported to be the large degree of uncertainty present in the system that could not be modeled explicitly.

2.3.4 Adaptive Control

Adaptive control is a technique which alters control parameters to adapt to variations in dynamics of a system. It can be used for helicopter control when the environment the RUAV experiences changes. Hovakimyan *et al.* [73] constructed an error state observer for the design of adaptive control laws which accommodate both parametric uncertainty and unmodeled dynamics. This method was applied to design a high-bandwidth attitude command system for an autonomous helicopter. In [74, 75], researchers used the adaptive technique to cancel dynamic model errors when designing the control scheme. The pseudo-control hedging was employed to prevent the unwanted adaptation to actuator limits in the inner loop. An adaptive pole-placement technique for altitude control of a radio-controlled helicopter was proposed by Dzul *et al.* [54]. Experimental results showed that the adaptive controller improved the performance of the pole-placement algorithm and could be used for landing and taking-off of small helicopters.

2.3.5 Backstepping Control

The backstepping technique proposed by Kokotovic and others [76] is well-known in the literature. It is useful for a special class of nonlinear systems which are built from subsystems radiating out from an irreducible subsystem that can be stabilized using proper methods. This procedure begins with a known-stable system and continues to design new controllers that progressively stabilize each outer subsystem. It terminates when the final external control is reached. Backstepping control has been applied to helicopter control in a number of papers. Cheviron *et al.* [77] proposed a control law which was based on the backstepping approach and took into account the disturbance estimation. The control gains in the backstepping procedure were set using the $\mathcal{H}_2$ optimization conception. A controller design framework was devised based on the backstepping technique for the dynamic model of an autonomous helicopter in [78]. The Lyapunov function was used to analyze the closed-loop performance of the full system and prior bounds on initial error and trajectory parameters were provided which guaranteed the acceptable tracking performance of the system. Frazzoli *et al.* [79] proposed a backstepping based nonlinear controller. This approach began with determining the desired main rotor thrust and attitudes based on velocity and position commands, and then oriented the rotor to the desired directions. It was proven to provide proficient tracking performance for a wide class of trajectories. Avoidance of singularities due to the attitude representation was also considered in a paper from this research group [80].

2.3.6 Fuzzy Control

Helicopter control using fuzzy approaches has received increasing interest in recent years. The advantage of fuzzy control is that the fuzzy logic has physical interpretation and human operator experience can be used in the design of controllers. Fuzzy control is achieved by referring to control engineers' knowledge and can be considered as the application of expert systems. In [81], fuzzy PD-like and PID-like controllers were used for attitude and height control of small-scale helicopters in non-aggressive flight conditions. Sanchez *et al.* [82] proposed a hybrid control scheme by combining fuzzy, PID and linear regulation control. In the flight control system, the altitude/attitude control was achieved by a MIMO linear regulator and two SISO PID controllers, and two fuzzy controllers were adopted to stabilize the lateral/longitudinal motion. Altitude/attitude control using a fuzzy gain-scheduler was investigated by Kadmiry and Driankovin [83] for an unmanned helicopter able to perform aggressive manoeuvres. In this approach, helicopter model was linearized by bounding the nonlinearities in the states by linear functions to form a fuzzy model, which led to design of an output feedback controller. A robust stabilizing controller was designed to achieve good speed response for a 3-DOF helicopter [84]. This controller compensated for the discrepancies between the real dynamic model and the simplified dynamic model. Also, input constraints were represented in terms of LMIs. Therefore, the control strategy involved simultaneously solving a group of LMIs, and real-time implementation would require high-performance flight computers. Other fuzzy logic controllers were also designed and tested in [85–92]. In this thesis, we aim to develop a recovery system applicable to general landing operations, and this research is not restricted to specific ship/RUAV combinations. Thus, prior knowledge on the landing environment may not be available, and therefore the fuzzy logic controller which is derived based on existing experience is not preferred.

2.3.7 Other Control Methods

Helicopter control can also be achieved using other approaches apart from these methods mentioned above. Wan *et al.* [93] presented an approach using model predictive control which consisted of a neural network feedback controller and a state-dependent Riccati equation controller. The tracking performance of the control structure was examined on a 6-DOF helicopter model. A nonlinear predictive control algorithm was suggested for a 2-DOF helicopter by Dutka *et al.* [94]. They dealt with the nonlinearity by converting the state-dependent state-space representation into the linear time-varying representation, and used the generalized predictive control method which minimized the cost function using a static optimization technique. Marconi *et al.* [95] designed a vertical landing scheme for a fixed-wing UAV using an internal-model based approach. By constructing the model in vertical plane, a robust controller was proposed to offset the effect of major parameter uncertainties. Isidori *et al.* [96] presented a robust controller to synchronize the vertical motion of the helicopter with that of an oscillating deck. Performance of the proposed controller was tested in simulations without using the real ship motion data. Vilchis *et al.* [97] developed a nonlinear 3-DOF model for the Vario helicopter and a nonlinear control strategy was proposed based on this model. Numerical simulations and experimental applications were presented to show the performance and robustness of the proposed controller. Castro *et al.* [98] obtained a linear equivalent form of a 6-DOF nonlinear helicopter model in hover flight using the static state feedback technique. However, the linearization is valid only when the helicopter is near the hover condition. The output tracking control of a helicopter was investigated by Koo and Sastry in [99]. It was pointed out that the output variables should be chosen properly to avoid unstable zero dynamics. By neglecting the coupling between moments and forces, the authors showed that the approximated system with dynamic decoupling was full state linearizable by choosing positions and heading as outputs.

2.4 Modeling of Wind Gusts

The gusts imposed on the RUAV mainly come from the ship airwakes, which are governed by a variety of factors such as the geometry of the ship superstructure, the intensity and relative direction of the natural wind and free-stream turbulence, and interactions of the sea motion and weather conditions with ship dynamics [31, 100]. Typically, the interactions of atmospheric winds with the ship superstructure lead to substantive flow separations and the formation of violent vortices over the landing deck. Consequently, severe spatial gradients in wind speed and directions prevail over the landing deck, which increase the levels of turbulence in the airwakes to three times the magnitude of that in the natural wind over the sea [101]. Ship airwake modeling using proper approaches has been subject to extensive investigation in a considerable number of papers, and significant efforts, including theoretical analysis and experimental research, have been made to deal with different practical problems for various combinations of ships and helicopters [102–105]. In general, ship airwakes can be modeled using computational fluid dynamics (CFD) data or deterministic gust models. The CFD approach is suitable for both steady-state and unsteady-state (time-accurate) ship airwake scenarios for the specified ship/helicopter combinations [102, 104, 106]. However, practical implementation difficulties need to be considered, as the CFD method requires dealing with large quantities of data, making it impossible for real-time computation using current technologies [103]. In our case, since the detailed ship deck configuration is unknown and we aim to develop a generic landing procedure, the gust model is approached by passing white noise through shaping filters with scalable wind speed and turbulence intensity.

2.5 Summary

In this chapter, automatic landing strategies for fixed-wing UAVs are reviewed. Also, several landing approaches for RUAVs are described, and their feasibility into real applications are discussed. This chapter also gives a description of the existing helicopter control methods.

Chapter 3

Helicopter Simulation and Experimental Platforms

3.1 Introduction

This chapter reviews flight dynamics of a helicopter and introduces the experimental platforms used for flight validation. The model-scale helicopters, the *Eagle* and the *Vario*, are employed as platforms to evaluate the proposed landing strategy. Their avionics are briefly described. Also, the structure for modeling the RSLS by synthesizing helicopter flight dynamics, flapping dynamics, ship motion, gust effect, the flight control system and servo dynamics in MATLAB/SIMULINK is given.

3.2 Coordinate Frames

To investigate flight dynamics of a helicopter, it is required to set up a proper coordinate frame in which dynamic motion of the helicopter can be formulated conveniently. Therefore, the following coordinate frames are defined:

- The body frame is fixed orthogonally to the origin O_b which is located at the center of gravity (CG) with axis set aligned with the roll, pitch and yaw axes of the helicopter, as illustrated in Fig. 3.1;
- The navigation frame, also referred to as the north-east-down coordinate frame, defines its origin O_n at the location of the navigation system where a proper navigation solution is found out. Its orthogonal axes align with the directions pointing north, east, and the local vertical (down) [107, 108].

Numerous mathematical notations can be given after definitions of coordinate frames, and will be used later. Symbols x_h, y_h and z_h stand for helicopter positions in the navigation frame. Velocity components u, v and w are defined along with the body axes x_b, y_b and z_b. The attitudes of the helicopter are described by roll ϕ, pitch θ and yaw ψ. Angular rates are denoted by p, q and r with anti-clockwise rotations about the body axes defining the positive directions.

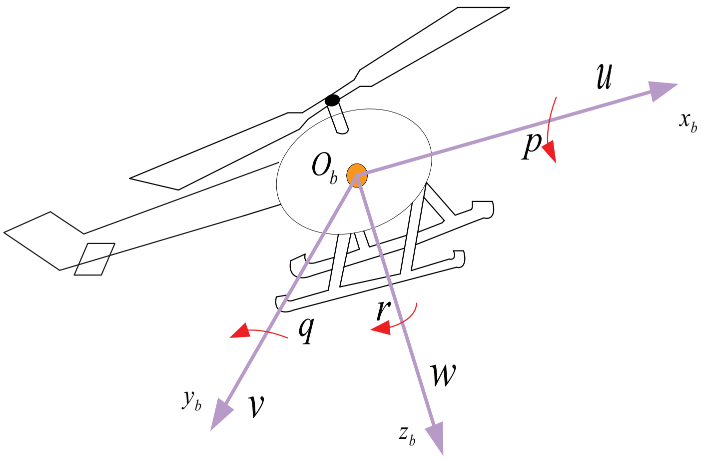

Figure 3.1. Helicopter body frame

3.3 Rigid-body Equations of a Helicopter

The force equations of the helicopter are [1]

$$\dot{u} = \quad rv - qw + \frac{X_h}{M_a} - g\sin\theta \tag{3.1}$$

$$\dot{v} = -ru + pw + \frac{Y_h}{M_a} + g\cos\theta\sin\phi \tag{3.2}$$

$$\dot{w} = -pv + qu + \frac{Z_h}{M_a} + g\cos\theta\cos\phi \tag{3.3}$$

and the moment equations are

$$I_{xx}\dot{p} = (I_{yy} - I_{zz})qr + I_{xz}(\dot{r} + pq) + L_h \tag{3.4}$$

$$I_{yy}\dot{q} = (I_{zz} - I_{xx})rp + I_{xz}(r^2 - p^2) + M_h \tag{3.5}$$

$$I_{zz}\dot{r} = (I_{xx} - I_{yy})pq + I_{xz}(\dot{p} - qr) + N_h \tag{3.6}$$

The attitude equations are described by

$$\dot{\phi} = p + (q\sin\phi + r\cos\phi)\tan\theta \tag{3.7}$$

$$\dot{\theta} = q\cos\phi - r\sin\phi \tag{3.8}$$

$$\dot{\psi} = \frac{q\sin\phi + r\cos\phi}{\cos\theta} \tag{3.9}$$

where M_a is mass of the helicopter, and g the gravitational acceleration. Given the mass density $\rho_h(x_b, y_b, z_b)$ of the helicopter, moments of inertia are computed as follows in the body frame [109]

$$I_{xx} = \int\int\int (y_b^2 + z_b^2)\rho_h(x_b, y_b, z_b)dx_b dy_b dz_b \tag{3.10}$$

$$I_{yy} = \int\int\int (x_b^2 + z_b^2)\rho_h(x_b, y_b, z_b)dx_b dy_b dz_b \tag{3.11}$$

$$I_{zz} = \int\int\int (x_b^2 + y_b^2)\rho_h(x_b, y_b, z_b)dx_b dy_b dz_b \tag{3.12}$$

$$I_{xz} = -\int\int\int x_b z_b \rho_h(x_b, y_b, z_b)dx_b dy_b dz_b \tag{3.13}$$

If the mass distribution of the body is symmetric with respect to the body frame, then the cross product of inertia $I_{xz} = 0$.

The forces (X_h, Y_h, Z_h) and moments (L_h, M_h, N_h) result from external aerodynamic and propulsive contributions, and can be decomposed into several elements in terms of five subsystems on the helicopter

$$X_h = X_{mr} + X_{tr} + X_{fus} + X_{tp} + X_{fn} \tag{3.14}$$

$$Y_h = Y_{mr} + Y_{tr} + Y_{fus} + Y_{tp} + Y_{fn} \tag{3.15}$$

$$Z_h = Z_{mr} + Z_{tr} + Z_{fus} + Z_{tp} + Z_{fn} \tag{3.16}$$

$$L_h = L_{mr} + L_{tr} + L_{fus} + L_{tp} + L_{fn} \tag{3.17}$$

$$M_h = M_{mr} + M_{tr} + M_{fus} + M_{tp} + M_{fn} \tag{3.18}$$

$$N_h = N_{mr} + N_{tr} + N_{fus} + N_{tp} + N_{fn} \tag{3.19}$$

Here, the subscript mr denotes the main rotor, tr for the tail rotor, fus for the fuselage, tp for the tail plane, and fn for the vertical fin. Essentially, the main rotor and the tail rotor provide the main means of propulsion, lift and control for small RUAVs, and the aerodynamics of the main rotor and the tail rotor are dominant when conducting trim and stability analysis.

3.4 Helicopter Aerodynamics

There are some distinct aerodynamic differences between a helicopter and a fixed-wing aircraft. A helicopter is characterized by the unique flexibilities of hovering,

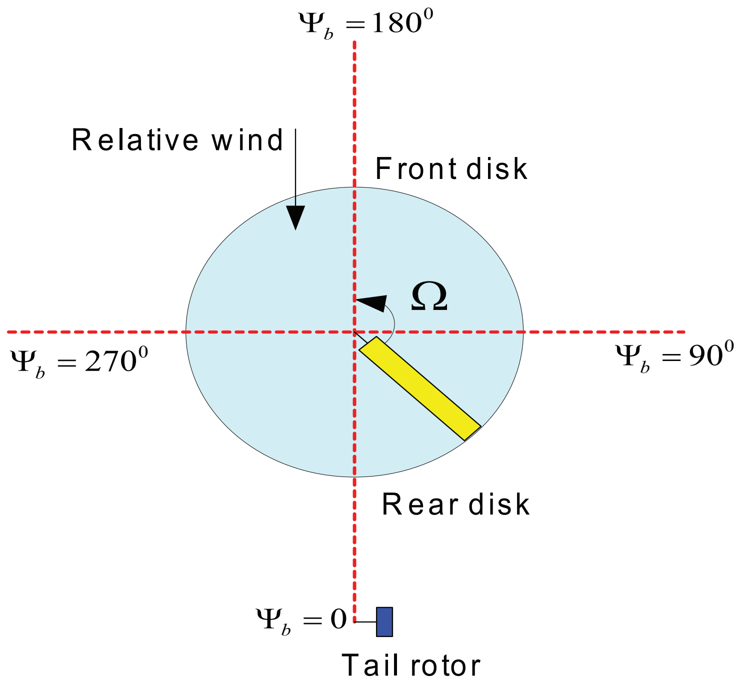

Figure 3.2. Blade azimuth angle of main rotor

flying backwards and sidewards, which give it the ability to achieve tasks that a fixed-wing aircraft cannot. Without separate mechanism generating forces to provide lift and forward propulsion, the helicopter is equipped with main rotors which interact with a swash plate to produce required forces and moments. Also, employment of the rotor blade flapping motion results in an indirect means of controlling the direction of the main rotor thrust and the rotor hub moments. Moreover, the helicopter is a highly underactuated system with only four control inputs–three inputs acting on the main rotor and one on the tail rotor. The 6-DOF helicopter flight dynamics are controlled by these four control inputs. The helicopter responds to a single-axis control input with multi-axis behaviors. This adds to the difficulty of designing controllers to achieve desired flight qualities.

There are four basic control channels on a helicopter: main rotor collective pitch (θ_{col}), longitudinal cyclic (B_{lon}), lateral cyclic (A_{lat}) and tail rotor collective pitch (θ_{ped}). Strictly speaking, there is another control channel referred to as throttle. This channel is usually controlled automatically by an onboard governor to regulate the main rotor speed, thus not subject to the pilot control. Therefore, the throttle channel is ignored throughout the thesis, and the constant main rotor speed is

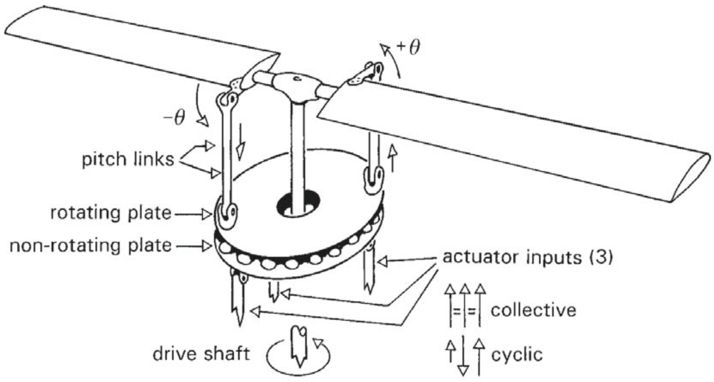

Figure 3.3. Mechanism of the swash plate ([1])

assumed. For the RUAV platforms used in this thesis, the main rotor speed is 1600 revolutions per minute for the Eagle helicopter, and 850 for the Vario helicopter.

Main Rotor Collective Pitch

The main rotor collective pitch is the primary source of direct lift generation. It controls rotor blades simultaneously, or collectively, as the name indicates. The main rotor blows the airflow downwards relative to the helicopter for a positive collective pitch, and the airflow is driven upward for a negative collective pitch [70]. As the collective pitch is raised, there is a simultaneous and equal increase in the pitch angle of all rotor blades. Consequently, the angle of attack on each blade is increased which leads to the increased thrust. Conversely, a decreased collective pitch gives rise to a decrease in the main rotor thrust. The thrust generated is perpendicular to the tip path plane (TPP), and essentially controls the altitude of the helicopter. The TPP is the plane connecting the rotor blade tips as they rotate. While hovering, the thrust vector of a helicopter is oriented mostly upwards, perpendicular to the TPP. In general flight conditions, the applied blade pitch θ_a takes the following form in consideration of the rotor flapping motion

$$\theta_a = \theta_{col} + A_{lat} \cos\ \psi_b + B_{lon} \sin \psi_b \tag{3.20}$$

Here, the azimuth angle ψ_b is positive in the direction of anti-clockwise blade rotation with zero reference located at the rear of the rotor disk, as is shown in Fig. 3.2. To avoid confusion in the context, symbols $\delta_i,\ i = col, lon, lat, ped$ represent the corresponding servo commands in terms of Pulse Width Modulation (PWM) signals.

PWM is a well-developed technique for controlling analog circuits using digital outputs from a processor. The servo position as an angle is set by the pulse width which is determined by the duty cycle. For the Eagle helicopter, the PWM sequence repeats every 20 milliseconds (ms) with the minimum duty cycle of 1 ms and the maximum of 2 ms.

Cyclic Pitch

Cyclic pitch accounts for pitching moment, rolling moment and horizontal movement of the helicopter. It causes the main rotor blades to flap in a once-per-revolution sinusoidal manner such that the main rotor TPP is tilted, which in turn affects the direction of thrust. Cyclic pitch tilts the main rotor disk to generate horizontal components of forces and pitching and rolling moments. These forces and moments control both the attitudes of the helicopter and the lateral and longitudinal motion. The cyclic pitch is applied through a swash plate comprising rotating and non-rotating plates which are connected by bearings as is shown in Fig. 3.3. The non-rotating plate is linked to the actuator inputs which receive control commands, and the rotating plate is attached to the main rotor blades through pitch links. The pitch angle of the blades varies cyclically due to the periodical tilting of the rotating plate.

Tail Rotor Collective Pitch

The tail rotor thrust is regulated by the positions of the anti-torque pedals. Tail rotor control is mainly aimed at balancing the combined effects of the main rotor torque reaction, airframe aerodynamic yawing and inertial moments during manoeuvres [110]. Basically, the tail rotor thrust contributes to the heading control during the hovering flight.

3.4.1 Momentum Theory

The fundamental theory to understand the dynamic relationship between the main rotor and air inflow is commonly known as momentum theory [1]. It assumes that airflow above and below the rotor disk is inviscid and incompressible. The actuator disk is assumed to impart an energy change on the airflow. It is shown that the velocity changes at various locations in the stream tube [1]. Applying the conservation laws of mass, momentum and energy allows the acquirement of the dynamic relationship between the main rotor thrust T_{mr} and the induced velocity V_i

$$T_{mr} = 2\rho A_d (V_{cl} + V_i) V_i \tag{3.21}$$

where ρ is the air density, A_d the rotor disk area, and V_{cl} the climbing velocity.

Hover is a typical flight condition for the helicopter research, and the induced velocity during the hover flight V_{ih} is

$$V_{ih} = \sqrt{\frac{T_{mr}}{2\rho A_d}} \tag{3.22}$$

3.4.2 Blade Element Theory

The momentum theory postulates that the rotor is uniformly loaded with an infinite number of blades. However, it does not give insight into the interactions between the airflow and individual rotor blades. Neither does it show us a mathematical description of the quantitative relationship between the main rotor thrust and the collective pitch.

Blade element theory mainly investigates the effect of airflow on the rotating blades using aerofoil theory. Basically, the rotor blade is divided into a series of blade sections with each one experiencing elementary lift and drag forces. The resultant element of thrust can be integrated to derive the main rotor thrust. Different expressions for the thrust can be developed depending on the assumptions made for specific operational conditions, e.g., the expression for thrust in forward level flight can be obtained based on assumptions of uniform induced velocity across the disk, constant solidity along the span and zero blade twist. It stands as a working formula for general helicopter flight [110]. The solution to the main rotor thrust employed in this thesis takes the form of

$$T_{mr} = \frac{\rho a_l N_b A_b (\Omega_{mr} R_b)^2}{2} \left[\frac{\theta_{col}}{3} \left(1 + \frac{3V_t^2}{2\Omega_{mr}^2 R_b^2} \right) - \frac{V_n + V_i}{2\Omega_{mr} R_b} \right] \tag{3.23}$$

where a_l and Ω_{mr} are lift curve slope and angular velocity of the main rotor. N_b denotes the number of blades, V_n and V_t are airflow components perpendicular and tangential to the TPP. The main rotor blade area is $A_b = R_b c_{mr}$ with rotor radius and blade chord described by R_b and c_{mr}.

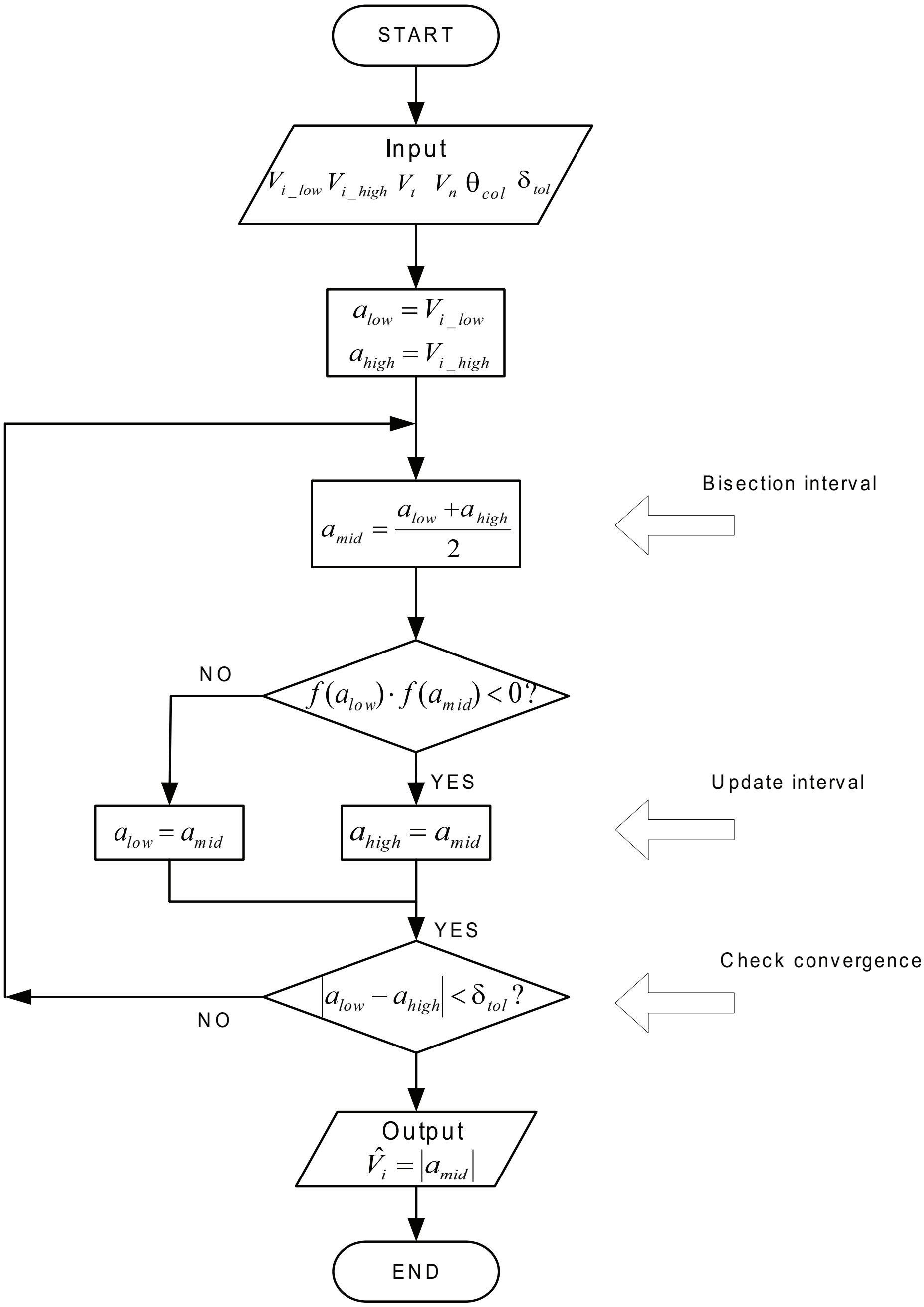

Figure 3.4. Flow chart for induced velocity calculation using the bisection algorithm

3.4.3 Rotor Thrust Calculation

To simulate thrust variations in Eq. (3.23), it is necessary to know the relationship between the induced velocity V_i and the thrust T_{mr}. This relationship is described by the Glauert's formula [110–112]

$$V_i^2 = \sqrt{\left(\frac{\hat{V}^2}{2}\right)^2 + \left(\frac{T_{mr}}{2\rho A_d}\right)^2} - \frac{\hat{V}^2}{2} \tag{3.24}$$

where

$$\hat{V} = \sqrt{V_t^2 + (V_n + V_i)^2} \tag{3.25}$$

and $A_d = \pi R_b^2$ is rotor disk area.

It is seen that equations (3.23)–(3.25) are coupled nonlinear equations which must be solved numerically to find the main rotor thrust. Several possible solutions are listed and discussed by Garratt [111]. It is mentioned that most of these techniques suffer from either divergence issues or being sensitive to the guess of initial values. In this thesis, the bisection search method is utilized and implemented by myself as a C-file S-function block to obtain the thrust T_{mr} and the induced velocity V_i. Given a physically meaningful guess of the induced velocity, the unique induced velocity V_i can be found which is used to calculate the rotor thrust T_{mr}.

The bisection search method requires that the equation should be expressed in terms of only one unknown variable. By substituting Eq. (3.23) and Eq. (3.25) into Eq. (3.24), we eliminate T_{mr} and end up with an equation involving the single unknown V_i. We then need to solve the resulting equation $f(Vi) = 0$ where $f(Vi)$ is given by Eq. (3.26) below:

$$f(V_i) = \sqrt{\frac{[V_t^2 + (V_n + V_i)^2]^2}{4} + \left\{\frac{B_t[\frac{\theta_{col}}{3}(1 + \frac{3V_t^2}{2\Omega_{mr}R_b^2}) - \frac{V_n+V_i}{2\Omega_{mr}R_b}]}{2\rho A_d}\right\}^2} - \frac{V_t^2 - (V_n + V_i)^2}{2} - V_i^2 \tag{3.26}$$

where $B_t = 0.5\rho a_l N_b A_b (\Omega_{mr} R_b)^2$. After the induced velocity V_i is calculated using the bisection method, the thrust T_{mr} can be obtained using Eq. (3.23).

The flow chart for induced velocity calculation is depicted in Fig. 3.4. The bisection algorithm begins with a proper choice of the searching interval $[a_{low}, a_{high}]$ which guarantees that a reasonable solution $\hat{V}_i$ is enclosed. Then the bisection point is calculated $a_{mid} = \frac{a_{low}+a_{high}}{2}$. If $f(a_{low})$ is of opposite sign to $f(a_{mid})$, then the solution must lie within the smaller interval $[a_{low}, a_{mid}]$, and the upper bound a_{high} is reset to a_{mid}. In contrast, the possibility that $f(a_{low})$ is the same sign as $f(a_{mid})$ indicates that the lower bound a_{low} should be replaced with a_{mid}. Therefore, the algorithm iteratively bisects the intervals, generating a sequence of subintervals which guarantee to converge to a proper solution. The bisection algorithm keeps going until the length of the subinterval is within the predefined error tolerance δ_{tol}. Typically, it takes 28 iterations to converge within an error tolerance of $1e-7$ m/s. The main rotor thrust can be obtained using Eq. (3.23) after the V_i is calculated.

3.4.4 Rotor Flapping Motion

Rotor flapping motion is the consequence of dynamic interactions among aerodynamic lift, centrifugal force and the blade inertia [110]. For a steady-state flight condition, the periodic flapping motion is expressed as an infinite Fourier series

$$\beta = a_0 + a_1 \cos\psi_b + b_1 \sin\psi_b + a_2 \cos 2\psi_b + b_2 \sin 2\psi_b + \cdots \tag{3.27}$$

It has been shown that values of higher harmonic terms (e.g., $\cos 2\psi_b$ and $\sin 2\psi_b$) are usually one tenth of these of lower harmonic terms (e.g., $\cos\psi_b$ and $\sin\psi_b$) [113,114]. Therefore, for general flight cases, it is reasonable to neglect the higher harmonics, and the steady blade flapping angle β is described as

$$\beta = a_0 + a_1 \cos\psi_b + b_1 \sin\psi_b \tag{3.28}$$

where a_0 is rotor coning angle. Symbols a_1 and b_1 are longitudinal flapping and lateral flapping, respectively. It is seen that the flapping angles a_1 and b_1 describe the tilting of the main rotor TPP in the longitudinal and lateral directions, as is shown in Fig. 3.5.

It is possible to formulate the flapping dynamics as two coupled first-order dynamic equations in consideration of the cross-coupling effect [115]. The cross-coupling effect means each of the two update equations for the flapping motion has a relationship with both longitudinal flapping and lateral flapping. The flapping dynamics can also be converted to simplified forms by neglecting the cross-coupling effect without loss of generality [116]. Hence, the following equations are used to

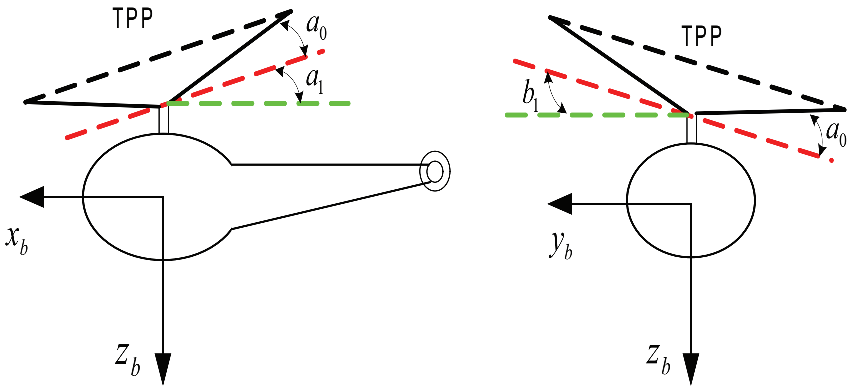

Figure 3.5. Physical interpretation of flapping angles

model the flapping dynamics [111]

$$\dot{a}_1 = -q - \frac{1}{\tau_f}\Big(a_1 + \frac{da_1}{dB_{lon}}B_{lon}\Big) \tag{3.29}$$

$$\dot{b}_1 = -p - \frac{1}{\tau_f}\Big(b_1 + \frac{db_1}{dA_{lat}}A_{lat}\Big) \tag{3.30}$$

where time constant τ_f is

$$\tau_f = \frac{16\Big(1 - \frac{e_b}{R_b}\Big)}{\gamma_f \Omega_{mr}\Big(1 - \frac{e_b}{R_b}\Big)^4\Big(1 + \frac{e_b}{3R_b}\Big)} \tag{3.31}$$

with the rotor blade hinge offset denoted by e_b. Symbol γ_f is the lock number.

3.4.5 Control Force and Moment Calculation

To derive control forces and moments acting on the helicopter, it is necessary to define the geometry configuration. Figure 3.6 shows the geometry parameters of the main rotor and the tail rotor with respect to the CG in the body frame. Here, horizontal, sideways and vertical displacement are denoted by D_{mx}, D_{my} and D_{mz} for the main rotor, and D_{tx}, D_{ty} and D_{tz} for the tail rotor. Geometry parameters for the two helicopter platforms (Eagle and Vario) used in this thesis are given in Table 3.1.

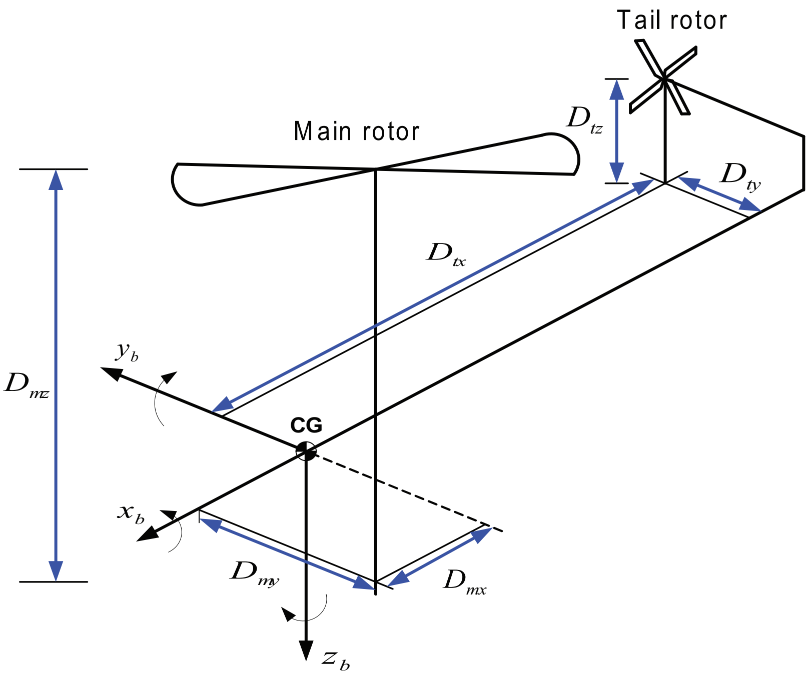

Figure 3.6. Geometry configuration of the main rotor and the tail rotor

Table 3.1. Configuration parameters of Eagle and Vario helicopters

	D_{mx}(m)	D_{my}(m)	D_{mz}(m)	D_{tx}(m)	D_{ty}(m)	D_{tz}(m)
Eagle	0	0	-0.2840	-0.9150	0	-0.1040
Vario	0.036	-0.0029	-0.3321	-1.4440	-0.0029	1.1379

Main Rotor Forces and Moments

The forces and moments acting on the main rotor are shown in Fig 3.7. It is seen that existence of the flapping angles decomposes the thrust into horizontal components, making it possible for the helicopter to move forwards, backwards and sidewards. The signs of forces and moments should be consistent with the definition of the body frame. Therefore, for the main rotor, employing the small angle approximation leads

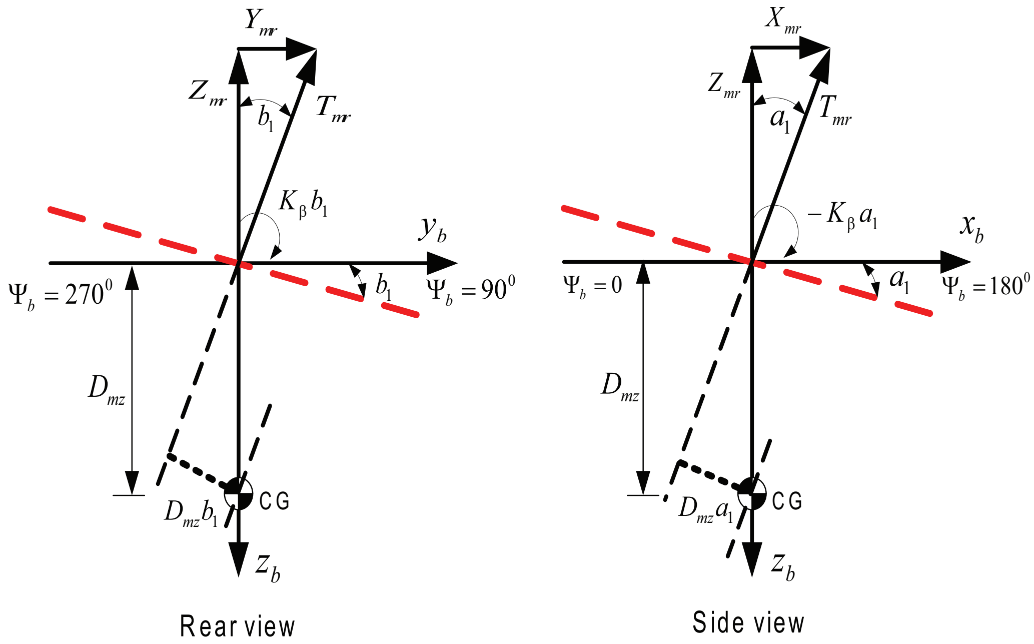

Figure 3.7. Control forces and moments acting on the main rotor

to

$$X_{mr} = T_{mr}a_1 \tag{3.32}$$

$$Y_{mr} = T_{mr}b_1 \tag{3.33}$$

$$Z_{mr} = -T_{mr} \tag{3.34}$$

$$L_{mr} = (k_\beta + T_{mr}D_{mz})b_1 \tag{3.35}$$

$$M_{mr} = (-k_\beta - T_{mr}D_{mz})a_1 \tag{3.36}$$

$$N_{mr} = \frac{P_{mr}}{\Omega_{mr}} + T_{mr}D_{mx}b_1 \tag{3.37}$$

The center-spring rotor stiffness k_β is measured through a force deflection test for the Eagle helicopter, and takes the value of 270 Nm/rad. An equivalent spring stiffness is calculated for the Vario helicopter based on its hinge offset using the method proposed by Cooke *et al.* [117] and takes the value of 1165.7 Nm/rad.

The main rotor power P_{mr} required in the general flight consists of several sources: the induced power P_{ind} constitutes the majority of total power of the main rotor in the hover flight, and primarily contributes to the power requirement during the forward flight. It creates the induced velocity, and generates the thrust to overcome the force of gravity by imparting momentum to a mass of air; the profile power P_{pro} is required to overcome the viscous drag forces on the rotor blades; the parasite power P_{par} is the portion of power which overcomes the drag of the fuselage in straight and level flight. It increases greatly when the helicopter operates in an higher airspeed regime [114]; P_{cli} is the climb power required to increase the gravitational potential energy of the helicopter. The total power equation can be written in a non-dimensional form

$$C_{Ptot} = C_{P_{ind}} + C_{P_{pro}} + C_{P_{par}} + C_{P_{cli}} \tag{3.38}$$

in which the induced power coefficient $C_{P_{ind}}$ is [118, 119]

$$C_{P_{ind}} = k_{ind} C_T \lambda_i \tag{3.39}$$

with the thrust coefficient C_T given by $C_T = \dfrac{T_{mr}}{\rho A_d (\Omega_{mr} R_b)^2}$. The typical value for k_{ind} is 1.2.

The profile power coefficient $C_{P_{pro}}$ is written as [111, 118]

$$C_{P_{pro}} = \frac{\sigma_b C_{d_0}}{8}(1 + \kappa_b \mu_b^2) \tag{3.40}$$

with the rotor solidity σ_b and the advanced ratio μ_b given by

$$\sigma_b = \frac{N_b c_{mr}}{\pi R_b} \tag{3.41}$$

$$\mu_b = \frac{V_\infty \cos\alpha}{\Omega_{mr} R_b} \tag{3.42}$$

Here, V_∞ is the magnitude of free-stream velocity, and α angle of attack. The value of κ_b is approximately 4.7, and profile drag coefficient C_{d_0} is 0.012 according to [118].

The parasite power coefficient $C_{P_{par}}$ is calculated by [111, 116]

$$C_{P_{par}} = |X_{fus} u| + |Y_{fus} v| + |Z_{fus}(w - V_i)| \tag{3.43}$$

The fuselage forces $(X_{fus}, Y_{fus}, Z_{fus})$ will be calculated later.

The climb power coefficient $C_{P_{cli}}$ is given by [111, 118]

$$C_{P_{cli}} = \frac{M_a g \dot{H}_a}{\rho A_d (\Omega_{mr} R_b)^3} \tag{3.44}$$

where H_a is the height above the ground.

Tail Rotor Forces and Moments

The tail rotor thrust T_{tr} is generated in the same way as the main rotor thrust. However, flapping motion is not considered for the tail rotor. The forces and moments acting on the tail rotor are written as

$$X_{tr} = 0 \tag{3.45}$$
$$Y_{tr} = T_{tr} \tag{3.46}$$
$$Z_{tr} = 0 \tag{3.47}$$
$$L_{tr} = T_{tr} D_{tz} \tag{3.48}$$
$$M_{tr} = 0 \tag{3.49}$$
$$N_{tr} = T_{tr} D_{tx} \tag{3.50}$$

Fuselage Forces and Moments

The generalized forms for fuselage forces and moments are given in [1], in which typical force and moment coefficients are derived from the table look-up functions in terms of incidence and sideslip angles. In this work, the following simplified expressions are adopted [111]

$$X_{fuse} = \frac{1}{2} \rho S^X_{fus} u^2 \tag{3.51}$$
$$Y_{fuse} = \frac{1}{2} \rho S^Y_{fus} v^2 \tag{3.52}$$
$$Z_{fuse} = \frac{1}{2} \rho S^Z_{fus} (w - V_i)^2 \tag{3.53}$$
$$L_{fus} = 0 \tag{3.54}$$
$$M_{fus} = 0 \tag{3.55}$$
$$N_{fus} = 0 \tag{3.56}$$
$$\tag{3.57}$$

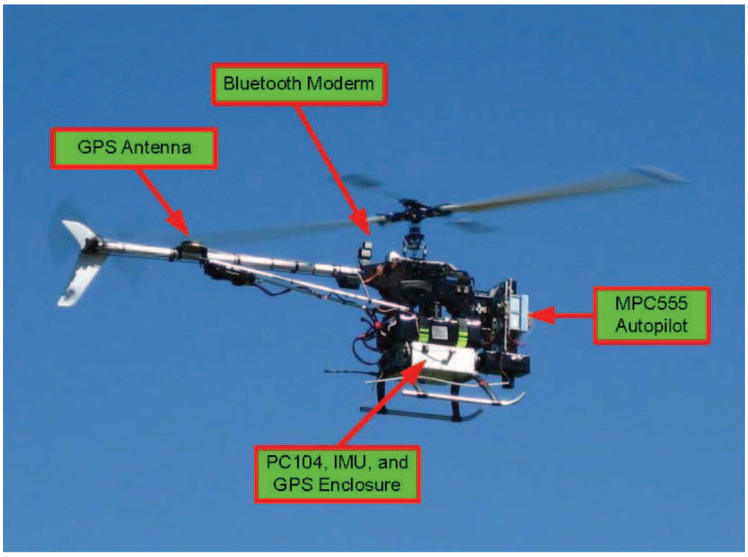

Figure 3.8. The UNSW@ADFA Eagle helicopter in flight

where S_{fus}^X, S_{fus}^Y, and S_{fus}^Z are equivalent flat plate areas of the fuselage in respective directions.

Vertical Fin Forces and Moments

The function of the vertical fin on the Eagle is to stabilize the helicopter in the forward flight. The lift is provided when the fin is exposed to an angle of attack. The equations for forces and moments acting on the vertical fin are [111]

$$X_{fn} = 0 \tag{3.58}$$

$$Y_{fn} = \frac{1}{2}\rho(u^2 + v^2)C_L^{fn} \tag{3.59}$$

$$Z_{fn} = 0 \tag{3.60}$$

$$L_{fn} = 0 \tag{3.61}$$

$$M_{fn} = 0 \tag{3.62}$$

$$N_{fn} = Y_{fn}D_{fn} \tag{3.63}$$

Here, parameter D_{fn} is the distance between the central line of the vertical fin and CG of the helicopter, and C_L^{fn} lift coefficient for the vertical fin.

3.5 Platform Description

The research work completed in this thesis is concerned with two helicopter platforms: the *Eagle* and the *Vario*. Both of them are characterized by the conventional helicopter layout comprising a single main rotor and a single tail rotor for the yawing moment compensation. The main difference between the Eagle and the Vario is the installment of a flybar on the Eagle for the purpose of augmenting the stability of its main rotor. This is achieved by providing pitch and roll rates as feedback to the cyclic pitch of the rotor blades. In addition, the presence of the flybar slows down the time constant, increasing the response time and facilitating control actions by a human pilot. Cunha *et al.* [120] investigated the mechanics of the flybar dynamics, and gave a mathematical description.

3.5.1 Eagle Helicopter

The Eagle helicopter constructed from a 60-size Hirobo helicopter kit serves as the main experimental platform for flight validation of the research work. All the algorithms are tested on the Eagle as a precursor to larger platforms (e.g., the Vario and the RMAX helicopters) to reduce operational risks. Control algorithms successfully tested on the Eagle can be updated to adapt to large platforms. The geometry and aerodynamic parameters of the Eagle helicopter are shown in Appendix A.

The Eagle helicopter is shown in Fig. 3.8 with onboard equipment. It is driven by the electric power provided by a brushless DC motor, reducing excessive vibration effect and avoiding fuel spills. The control inputs $(\theta_{col}, A_{lat}, B_{lon}, \theta_{ped})$ are encoded into PWM signals for implementation purposes. The servo actuators update control commands at a frequency of 50 Hz and implement the desired control actions through activating the swash plate assembly.

The successful flight of the Eagle depends on effective interactions among ground control station, avionic system and communication, as is shown in Fig. 3.9.

Ground Control Station

The primary task of the ground control station is to calculate the required control commands and send them up to the helicopter through the radio link. In this way, parameter settings can be easily modified without reprogramming on the helicopter. The ground control station comprises a standard personal computer for processing sensor information, a graphic user interface allowing for updating control parameters

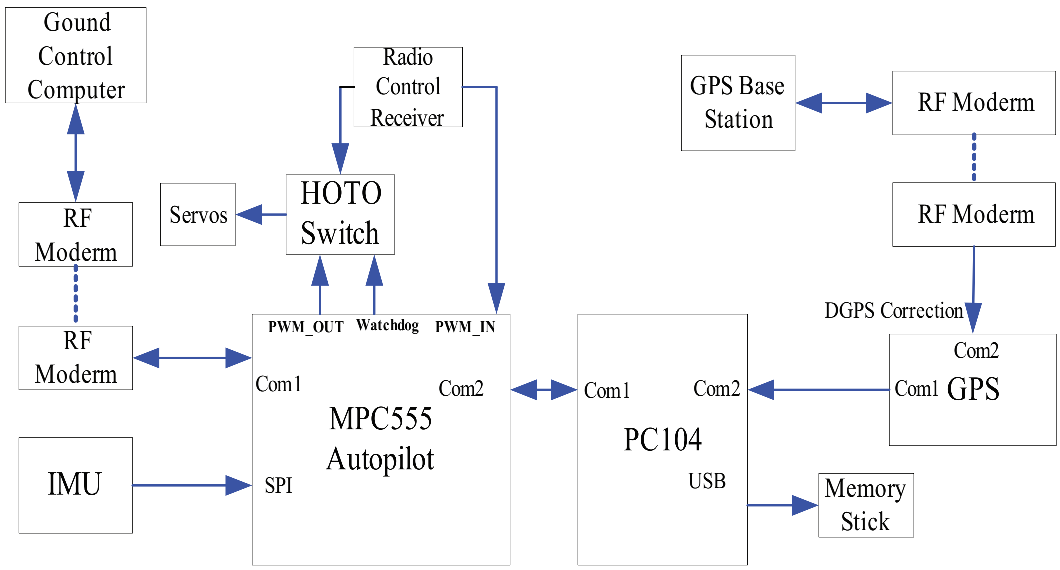

Figure 3.9. Eagle avionic architecture

in real-time and providing a graphic display of navigation and state information, and a bluetooth modem for wireless communication.

Avionics

The avionics consists of the flight computer and multiple sensors. The autopilot system is a combination of MPC555 based autopilot and PC104 based flight computer, as is seen in Fig. 3.9. The Motorola MPC555 micro-computer is able to embed basic attitude and position control systems. The PC104 flight computer increases the computational capabilities to deal with high-end processing such image processing and sophisticated state estimation algorithms.

For experimental convenience and safety, a hand over take over (HOTO) switch scheme has been developed to allow the control of helicopter to be switched between the manual mode and the automatic mode. In the manual mode, a human pilot flies the helicopter with a hand held radio control transmitter. While in the automatic mode, the helicopter is controlled by the autopilot.

The sensors employed onboard include inertial measurement unit (IMU) and global positioning system (GPS). The IMU utilizes three Analog Devices ADXL105 accelerometers, three Honeywell HMC1021S magnetometers and three Murata ENV-05D rate gyroscopes. The Eagle helicopter also carries a NovAtel OEM4-2GL differential GPS, providing position accuracy of 2 cm at an update rate of 20 Hz.

Figure 3.10. The UNSW@ADFA Vario helicopter in flight

Communication

Communication includes data uploading, synchronization and exchange among ground control station, the flight computer and multiple sensors. A RS-232 communication link allows the data to be transferred between the PC104 and the MPC autopilot. Also, several bluetooth modems are mounted onboard for data transmission. More technical details can be found in [111].

3.5.2 Vario Helicopter

The XL-C Vario helicopter is designed with the capability of transporting a payload of up to 15 kg with its own weight of around 17 kg. It features the reliable Vario main rotor head, long lasting centrifugal clutch and clutch bell system, and stainless steel torque tube drive. It also provides generous space margins for external payloads. In addition, the low vibration of the 3-blade main rotor makes it feasible to be fitted with the visual tracking sensor for landing purposes. The angular speed of the main rotor can be either set ahead of flight by entering the appropriate values, or switched in flight from the transmitter.

The avionics on the UNSW@ADFA Vario helicopter is similar to those on the Eagle (see Fig. 3.9). Close-up of the PC104 and MPC555 flight computer are shown in Fig. 3.11. The Vario is more responsive due to the absence of the flybar, which also

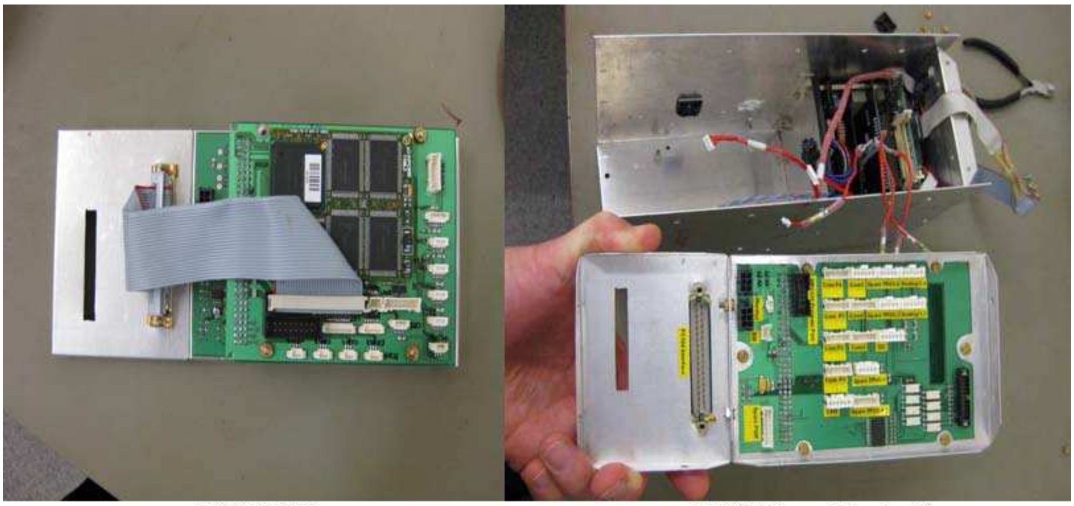

MPC555 PC104 and interface

Figure 3.11. PC104 and MPC555 on the Vario helicopter

facilitates the controller design process. The geometry and aerodynamic parameters of the Vario helicopter are shown in Appendix A.

In this thesis, the gust-attenuation controller is tested on the Eagle helicopter platform. The configuration parameters of the Vario helicopter are used when designing the automatic landing system.

3.5.3 Sensors

Laser Range Finder

In our project, a laser range finder (LRF) is devised with a spinning mirror installed in the front, as is shown in Fig. 3.12. Owing to the tilting of the mirror shaft and offset of the mirror face, the laser is able to scan the ship deck in a conical pattern. When the laser tracks an oval of points on the deck, an array of three-dimensional (3D) coordinates is constructed to define the intersection of the laser scan pattern and the ship deck. The range accuracy of each scanning point on the deck is less than 2 cm. This leads to very small errors in the estimation of deck positions.

The configuration of the deck attitude sensor assembly is shown in Fig. 3.12. The mirror is located on the shaft of a small DC motor, which is mounted at 45° to the beam of the LRF. The speed of the motor is controlled by the input voltage using the multi-position switch technique. An optical encoder is fitted on the shaft of the motor, generating a quadrature pulse sequence with the precision of 4,096 pulses per revolution.

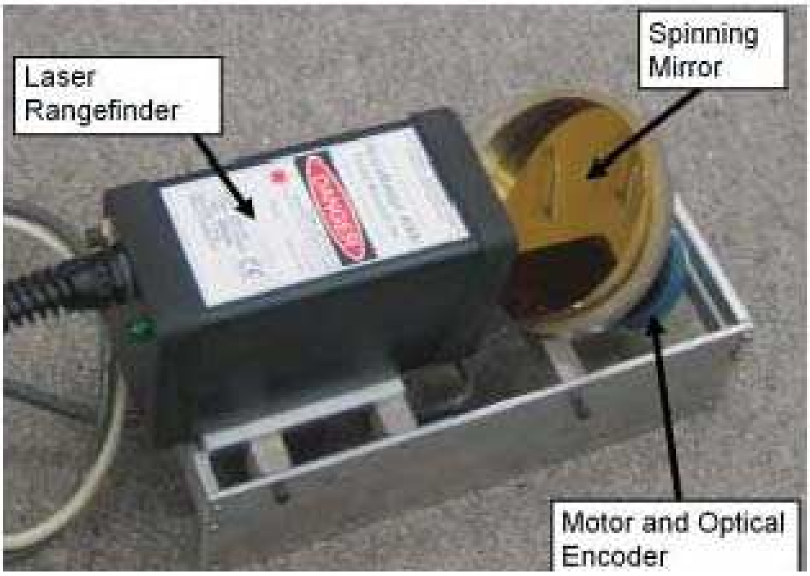

Figure 3.12. Deck attitude sensor assembly

The deck measurement algorithm begins with storing the 3D points into a buffer in the processing unit memory. Then a subroutine receiving the buffer of 3D points is employed to construct a plane which fits the stored data best. The 3D plane is described by

$$K_1x + K_2y + K_3z = 1 \tag{3.64}$$

The least square method is used to find the coefficients K_1, K_2 and K_3 based on minimizing the sum of squared error residuals. Once these coefficients are found, the instantaneous height of the helicopter and the deck attitudes can be calculated [121].

Tracking Sensor

The combination of IMU/GPS is able to give satisfactory estimation of helicopter positions. However, ship positions are unknown. To provide the missing information, a visual tracking sensor has been developed which can give the relative motion information between a RUAV and a ship deck.

In previous work, Garratt *et al.* [122] developed a system of three visual landmarks on the ground to control a small RUAV in hover. The tracking system suffers from the problem of losing track when it is used for tracking landmarks on an oscillating ship deck. This results from the possibility that the sea spray could obscure parts of a visual pattern or parts of the pattern disappear from the field of view frequently due to the combined motion of the RUAV and the ship.

To improve the estimation accuracy, two colored *beacons* are employed which center around the field of view with known configuration information [2], as is shown in Fig. 3.13. The use of color enables the sun to be eliminated as a target and allows the left and right beacons to be discriminated. The combination of a digital camera and a target detection algorithm can provide reliable relative motion information between a RUAV and a ship deck. The relative motion information can be obtained by tracking the motion of the center of the two beacons. Range, azimuth and elevation are functions of the frame coordinates of the captured images (center of the beacons) within the field of view. The relative range can be derived using the beacon horizontal separation information and vertical and horizontal positions of the heading pointer within the frame.

The structure of the tracking sensor hardware is depicted in Fig. 3.14. The beacon tracking system is lightweight, self-contained, and consumes low power. The employment of a mega-pixel CMOS image sensor makes it possible to combine all of the necessary image processing and coordinate determination within a single *Xilinx Spartan* IIE Field Programmable Gate Array (FPGA). The FPGA interfaces to the flight control system using the RS232 serial communications, and provides extra diagnostics to an external monitor. The test results of the tracking system show that robust color segmentation and accurate target coordinate generation are achieved with the minimal use of FPGA resources. Additionally, the data generated from the tracking algorithm can be used to obtain an accurate estimate of the relative range up to 30 m [2].

3.6 Gust Model

Previous investigation [123, 124] on aircraft dynamic response to atmosphere disturbance reveals the validity of considering wind effect as a stationary random process, and gust disturbance can be modeled by passing white noise through a forming filter. There are two mainstream turbulence models to design the forming filter: the *Von Karman* and the *Dryden*. The *Von Karman* model typically characterizes atmosphere turbulence at higher altitudes and speeds [125]. Thus, in our application

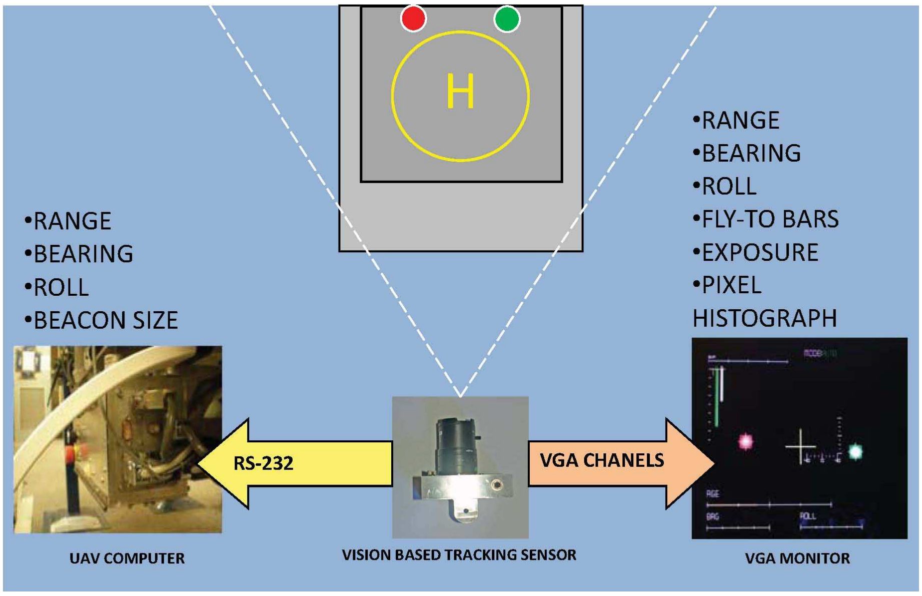

Figure 3.13. Vision based tracking sensor [2]

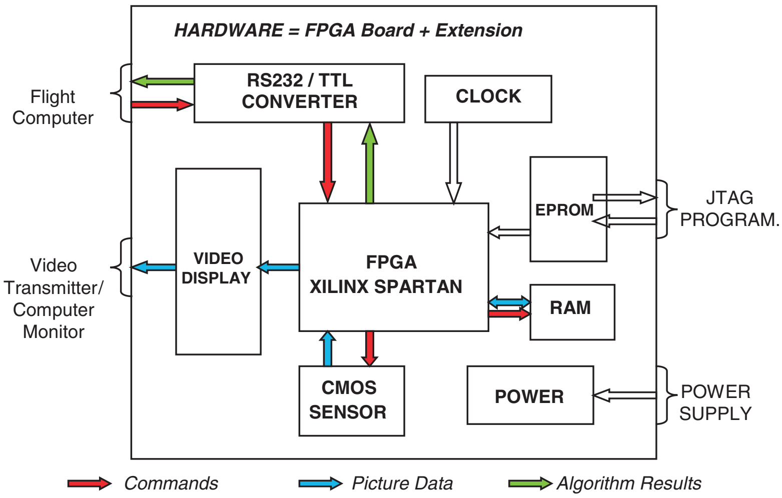

Figure 3.14. Structure of the tracking sensor hardware

where the RUAV is close to the sea level, the *Dryden* turbulence model is adopted. The corresponding forming filters, including $D_u(s)$ for longitudinal direction, $D_v(s)$ for lateral direction and D_w for vertical direction, take the following transfer function forms [126]

$$D_u(s) = \sigma_u \frac{1}{1 + \frac{L_u}{U_r} s} \sqrt{\frac{2L_u}{\pi U_r}} \tag{3.65}$$

$$D_v(s) = \sigma_v \frac{1 + \frac{\sqrt{3}L_v}{U_r} s}{(1 + \frac{L_v}{U_r} s)^2} \sqrt{\frac{L_v}{\pi U_r}} \tag{3.66}$$

$$D_w(s) = \sigma_w \frac{1 + \frac{\sqrt{3}L_w}{U_r} s}{(1 + \frac{L_w}{U_r} s)^2} \sqrt{\frac{L_w}{\pi U_r}} \tag{3.67}$$

where U_r denotes relative speed of helicopter to the frozen air stream. The scale of turbulence, L_u, L_v and L_w, are assigned constant values of $L_u = L_v = 722.5$ m, $L_w =$ 3 m in our scenario. Parameters σ_u, σ_v and σ_ω representing turbulence intensity factors are calculated by

$$\sigma_u = \sigma_v = \frac{\sigma_\omega}{(0.177 + 0.000823H_a)^{0.4}} \tag{3.68}$$

$$\sigma_\omega = 0.1W_{20} \tag{3.69}$$

Here, parameter W_{20} denotes wind speed at 6 m above the ground, and can be approximated by U_r.

3.7 Modeling of RUAV/Ship Landing System

Normally, numerous flight tests are required to evaluate safe flight envelopes of the RUAV under a variety of sea conditions [127]. Unavoidably, enormous experimental resources and time would be spent on flight tests to cover the possible flight conditions in reality. Also, such flight tests would be infeasible under some extreme weather conditions (e.g., storm, fog). Developing a high-fidelity simulation model for the RSLS would contribute to reducing the number of experiments and assessing flying qualities of the RUAV in rough seas.

The primary objective of modeling the RSLS is to specify the applicable landing trajectories in consideration of RUAV maximum operational limitations in a variety

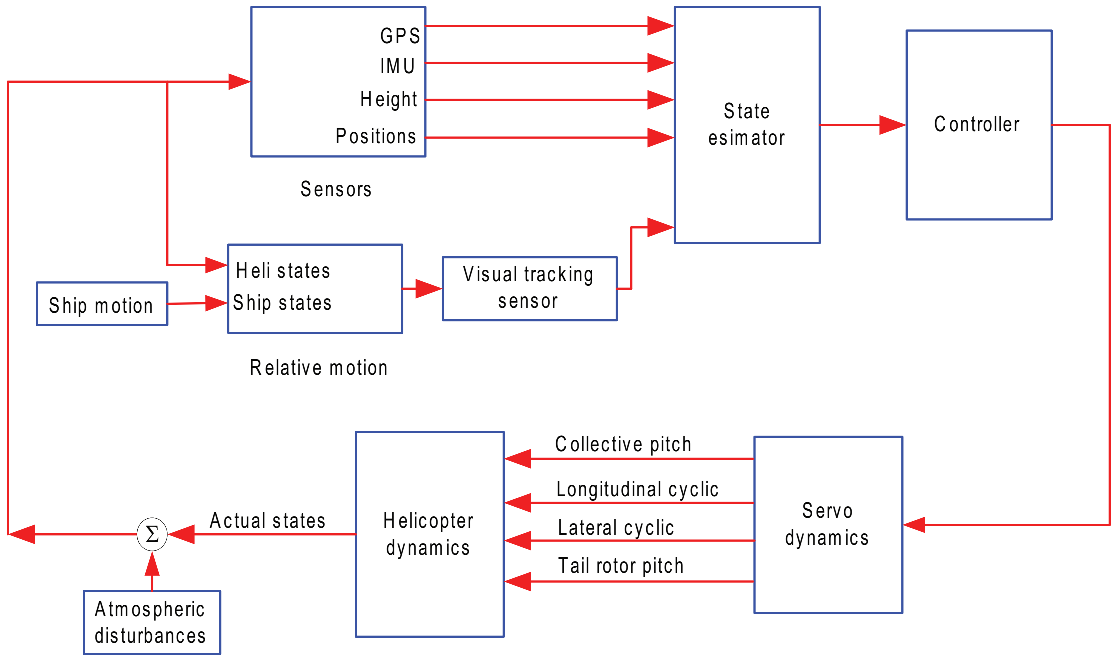

Figure 3.15. Top level of RSLS simulation model

of sea conditions. A portion of the emphasis should also be placed on maintaining adequate dynamic performance and in particular, on stability of the RUAV in the presence of variations in plant dynamics and atmospheric disturbances. Modeling of the RSLS is supposed to reflect the potential issues which possibly happen during the real-time landing operations, and contributes to finding solutions ahead of flight tests.

Development of a high-fidelity RSLS is a challenging task. Theoretically, the helicopter is a highly nonlinear and unstable dynamic system, making it difficult to build accurate mathematical descriptions for various flight conditions. Also, the random deck movement exacerbates the complications of arranging safe landing trajectories to avoid unexpected accidents. Technically, the RSLS should be modeled in a systematic and generic way, i.e., all the simulation blocks are parameterized and can be modified conveniently to adapt to specific helicopter/ship combinations. It is also desired to build the subsystems in the RSLS as separate flexible modules which can be easily extended or reduced for future research.

The structure of the simulation model for the RSLS used in this thesis is shown in Fig. 3.15. The simulation scheme attempts to provide a systematic framework taking into account helicopter dynamics, atmospheric disturbances, ship motion dynamics, and relative motion dynamics. It is built in consistent with both theoretical fundamentals and technical constraints. The simulation model has been modified to accommodate several RUAV models in our team as an effective and reliable platform for theoretical evaluation before flight tests.

3.8 Summary

This chapter introduces flight dynamics of the RUAV, including force and moment calculations for the main subsystems of the helicopter. RUAV platforms used in this thesis are also described, followed by a presentation of the modeling of the RSLS.

Chapter 4

Displacement Motion Prediction of a Landing Deck

This chapter proposes a practical procedure for prediction of vertical displacement of a landing deck. This procedure aims to predict the best time to start descending such that the impact force is minimized at the touchdown moment. A time series model which captures characteristics of the dynamic relationship between an observer and a landing deck is constructed. Model orders are determined by a principle based on the Bayes Information Criterion (BIC) and coefficients are identified using the FFRLS method. In addition, a predictor is developed with satisfactory prediction horizon. Simulation results demonstrate that the proposed prediction approach exhibits satisfactory prediction performance and modest computational requirements, making it suitable for integration into ship-helicopter approach and landing guidance systems.

4.1 Introduction

There are two mainstream approaches to predicting dynamic motion of deck displacement. The first one is to develop a proper dynamic model able to capture main system features, such as uncertain stochastic processes (e.g., wind gusts, sea waves), characteristics of unknown ship motion behavior, and unmodeled dynamics. In such models, available prediction methods depend greatly on the fidelity of the model. A complete modeling of deck displacement motion requires an accurate knowledge of ship motion configuration parameters and local sea states. In practical scenarios, it would be time-consuming and infeasible to build an accurate model since many parameters (wave frequency, incoming wave angle, ship configuration, etc.) are not available. Alternatively, system dynamics can be treated as a black box, and approached by an approximate model which captures system dynamics implicitly. In this way, measured data can be input into the model, which outputs the prediction results. We propose a time series methodology that aims to build a model to capture deck displacement without building or solving intrinsic ship dynamic equations, and only based on previous measurements of deck displacement.

Ship motion dynamics have been studied in numerous papers in the past decades. Seakeeping theory investigates ship motion in waves based on the assumption that the dynamic motion of ships is subject to oscillations around the equilibrium motion [128, 129]. Linear seakeeping theory assumes the sea wave elevation to be a Gaussian stochastic process with zero mean. However, the fact that characteristics of real wave dynamics are not Gaussian constrains application of this method to preliminary stages of ship motion control [129]. Ship motion prediction using state-space approaches has been the subject of extensive investigations in a considerable number of papers, and significant efforts have been made to deal with different practical problems. Triantafyllou *et al.* [130] addressed the Kalman filtering technique for prediction of six motions of vessels using a precise state-space model, which requires tremendous computational efforts in that the transfer functions between ship dynamics and sea elevation are irrational nonminimum-phase functions. Also, how to develop a proper state-space model for prediction still remains a difficult problem. Lainiotis *et al.* [131] focused on deriving a state-space model based on a knowledge of ship motion dynamics, but this suffers from the dependency on available information. Ra *et al.* [132] regarded the ship motion as a particular sinusoidal form, and obtained a recursive robust least square frequency estimator by assuming that the ship motion frequency changed slowly. An initial prediction algorithm using minor component analysis developed by Zhao *et al.* [133] requires substantial computation efforts for updating identifying coefficients, which compromises its practicality in real-time prediction.

Time series theory is another possible solution to accomplishing prediction of deck displacement motion. Building a time series model involves determination of model orders and corresponding coefficients. Recently, Jie *et al.* [134] suggested an auto-regressive (AR) fitting model, in which model orders were verified using the Akaike Information Criterion (AIC). However, this method lacks long-term prediction capability and also suffers from the inconsistency feature of AIC, i.e., probability of estimation error does not go to zero as observations tend to infinity [135]. Dong *et al.* [136] presented an autoregressive moving average model to predict generalized heave displacement of a ship-borne helicopter platform, in which system parameters were estimated using a damped recursive least square algorithm. This method is only valid for short-time prediction. Long-term prediction capacity is required for landing operations as it can provide enough time margin to arrange safe descent and touchdown trajectories. In addition, the magnitude of heave displacement investigated in the paper was small (typically 6cm from bottom to top).

For automatic landing of the RUAV, accurate and rapid prediction of deck displacement can help to decide the best time to start descent, so that the RUAV can land on the deck when relative velocity between the RUAV and the deck is small. The proposed deck displacement predictor has implementation advantages. It computes rapidly on the flight computer when used for long-term prediction. Furthermore, the algorithm does not require much random access memory to execute, which would reduce the burden on the flight computer.

4.2 Determination of the Optimal Model Order and Coefficients

In our case, we approach the characteristics of deck motion using a time series model. The proposed model relates a stochastic process $y(t)$ contaminated by white noise $e(t)$ to a known set of delayed measurements $u(t)$. Here, the dynamic relationship between current and previous vertical displacement can be described by

$$y(t) = A(q^{-1})y(t) + B(q^{-1})u(t) + e(t) \tag{4.1}$$

$$A(q^{-1}) := \sum_{i=1}^{m} a_{(m,i)}q^{-i}, m \in N \tag{4.2}$$

$$B(q^{-1}) := \sum_{j=0}^{n-1} b_{(n,j)}q^{-j}, n \in N, n < m \tag{4.3}$$

$$u(t) = q^{-L}y(t), L > m, L \in N \tag{4.4}$$

where $y(t)$ refers to the vertical displacement, symbol q^{-1} is the backward shift operator (i.e., $q^{-1}y(t) = y(t-1)$), parameters $a_{(m,i)}, i = 1, \ldots, m$ and $b_{(n,j)}, j = 0, \ldots, n-1$ denote system coefficients to be determined, m is the order of $A(q^{-1})$, and n indicates the order of $B(q^{-1})$. This structure is chosen such that it is convenient to construct the L-step predictor given by $\frac{\hat{B}(q^{-1})}{1-\hat{A}(q^{-1})}$ after estimates of polynomials $\hat{A}(q^{-1})$ and $\hat{B}(q^{-1})$ are obtained. The suggested prediction procedure consists of two parts: determination of model parameters (model orders and corresponding coefficients), and prediction of deck displacement dynamics.

Without loss of generality, it is justifiable to assume that model order pairs lie within the following bounds

$$m \in V_1 = \{m | 1 \leq m \leq m_{max},\ m \in N\} \tag{4.5}$$

$$n \in V_2 = \{n | 1 \leq n \leq n_{max},\ n \in N\} \tag{4.6}$$

where m_{max} and n_{max} are upper bounds on the order m and the order n. For the purpose of determining the optimal order pairs (m^*, n^*), reasonable bounds on (m_{max}, n_{max}) should be assigned in consideration of some important aspects. It is apparent that small upper bounds on model orders will lead to a simplistic model unable to represent displacement dynamics accurately. Hence, upper bounds on model orders should be large enough to guarantee an acceptable accuracy. Meanwhile, the selection of upper bounds has a great influence on complexity of the model, i.e., excessively large upper bounds would increase the model complexity and aggravate computational burden. Therefore, an appropriate model without loss of prediction accuracy is preferable. Since the number of available data samples provided by sensors is in the order of thousands, in consideration of achieving a good trade-off between the factors mentioned above, a feasible selection scheme is to select (m_{max}, n_{max}) such that

$$m_{max} = O(\sqrt{T}) \quad n_{max} = O(\sqrt{T}/2) \tag{4.7}$$

Here, symbol T denotes the number of measured data. The suggested principle (4.7) constrains the searching scope for the optimal model order selection by avoiding either a too simplistic model or excessive computational burden. The parameter T is chosen to be thousands in our case, and can have different values in different circumstances.

By introducing the vector of lagged measured data

$$\varphi_r^T(t) = [y(t-1), \ldots, y(t-m), u(t), \ldots, u(t-n+1)] \tag{4.8}$$

and the following notation

$$\theta_r^T(m, n, t) = [a_{(m,1)}(t), \ldots, a_{(m,m)}(t), b_{(n,0)}(t), \ldots, b_{(n,n-1)}(t)] \tag{4.9}$$

we can write Eq. (4.1)-Eq. (4.4) in a compact form

$$y(t) = \theta_r^T(m,n,t)\varphi_r(t) + e(t) \tag{4.10}$$

Vector $\theta_r^T(m,n,t)$ consists of system coefficients to be determined.

The least square (LS) method can be employed to specify system parameters. The LS method aims to estimate system coefficients in such a way that the sum of the squared error between measured values and estimated values reaches a minimum, i.e., minimizing the loss function [137]

$$J(\theta_r) = \sum_{j=1}^{t}[y(j) - \theta_r^T(m,n,j)\varphi_r(j)]^2 \tag{4.11}$$

leads to the estimates for system coefficients. Apparently, all measured data are treated equally in the loss function, and the LS scheme can be considered as averaging the measured data to produce the optimal estimates [138]. However, in our application, when more and more measured data are collected and calculated, the variation of system dynamics would be submerged when old data and new data are weighted equally. Therefore, the estimation error would increase greatly, and the estimation process is possibly subject to collapse when a substantial number of measured data are collected and processed.

It has been pointed out in [138] that for a system with parameters varying continuously and slowly, the concept of forgetting should be introduced to gradually discard the old data. Therefore, the FFRLS is suitable for slow-varying process. In light of this, the new loss function can be defined as [137, 138]

$$J(\theta_r) = \sum_{j=1}^{t}\lambda^{t-j}[y(j) - \theta_r^T(m,n,j)\varphi_r(j)]^2 \tag{4.12}$$

Here, forgetting factor is denoted by parameter λ. The principle to choose λ is to select λ in such a way that loss function $J(\theta_r)$ essentially contains those measurements which are mostly relevant for current properties of the dynamic system. In particular, for a system that varies gradually, forgetting factor can be set to be a constant value ranging between 0.98 and 0.995 [137].

Therefore, model coefficients vector can be estimated using the FFRLS method, and can be expressed as [139]

$$\theta_r(m,n,t) = [\sum_{j=1}^{t} \lambda^{t-j} \varphi_r(m,n,j)\varphi_r^T(m,n,j)]^{-1}[\sum_{j=1}^{t} \lambda^{t-j} \varphi_r(m,n,j)y(j)] \tag{4.13}$$

which can be implemented recursively by

$$\theta_r(m,n,t+1) = \theta_r(m,n,t) + M(m,n,t+1)[y(t+1) - \varphi_r^T(t+1)\theta_r(m,n,t)] \tag{4.14}$$

$$M(m,n,t+1) = P(m,n,t)\varphi_r(t+1)[\lambda + \varphi_r^T(t+1)P(m,n,t)\varphi_r(t+1)]^{-1} \tag{4.15}$$

$$P(m,n,t+1) = [P(m,n,t) - M(m,n,t+1)\varphi_r^T(t+1)P(m,n,t)]/\lambda \tag{4.16}$$

$$\theta_r(m,n,0) = 0 \quad P(m,n,0) = \alpha I \tag{4.17}$$

Here, matrix $P(m,n,t+1)$ is referred to as error covariance matrix, matrix $M(m,n,t+1)$ denotes the updating matrix, and α is a large positive number.

Define the prediction error as

$$\xi(m,n,t+1) = y(t+1) - \varphi_r^T(m,n,t+1)\theta_r(m,n,t) \tag{4.18}$$

The maximum likelihood estimate of the error covariance until time T is given by

$$\sigma^2 = \frac{1}{T-m-n} \sum_{t=m+n+1}^{T} \xi^2(m,n,t) \tag{4.19}$$

Several available methods to specify model orders are AIC [140], BIC [141], predictive least squares criterion (PLS) [142], and feedback control system information criterion (CIC) [143]

$$AIC(m,n,T) = \log \sigma^2(m,n,T) + \frac{2(m+n)}{T} \tag{4.20}$$

$$BIC(m,n,T) = \log \sigma^2(m,n,T) + \frac{(m+n)\log T}{T} \tag{4.21}$$

$$PLS(m,n,T) = \sigma^2(m,n,T) \tag{4.22}$$

$$CIC(m,n,T) = \sum_{t=m+n+1}^{T} \xi^2(m,n,t) + (m+n)(\log T)^2 \tag{4.23}$$

For our model, AIC is not proper since the consistency feature of AIC cannot be guaranteed [135]. Meanwhile, PLS exclusively considers error accumulation, neglecting fitting model complexity. For CIC, the second term $(m+n)(\log T)^2$ dominates when the error is small and in such cases the method fails to determine the optimal model orders. Such phenomena arise when model coefficients are determined very accurately by the FFRLS at the initial computation stage, thus preventing CIC from finding optimal model orders. Additionally, CIC also needs sufficient information regarding initial model orders, which is impractical.

The concept of consistency is fundamental when identifying the true model of a system. Here, consistency means that the probability of selecting the true model from a set of candidates tends to unity as the number of measurements increases if the true model is one of the candidate models under consideration [144, 145]. AIC is not consistent as it always has a probability of selecting models with large orders [144, 145]. The advantage of BIC criterion is that it aims to identify the models with the highest probabilities of being the true model for observations [144]. It follows from the consistency of BIC that the unique model orders can be obtained when BIC value reaches a minimum. Our model requires the joint determination of m and n. For every given order $n \leq n_{max}$, BIC value changes convexly. Thus, the minimum BIC value corresponds to the optimal order m for a given order n, which results in the difficulty of selecting the desired model orders in the global sense. In our case, selection of the optimal pairs (m^*, n^*) should include a trade-off among prediction ability, accumulated prediction error, and model complexity.

In the displacement estimation problem, our main concern is the prediction capability. Meanwhile, the accumulated prediction error and model complexity should also be considered.

The following three important aspects should be analyzed:

- How can order pairs $(m,n),\ m \in V_1,\ n \in V_2$ be determined to maximize the prediction horizon?
- How to reduce the model complexity to reduce the computational burden?
- How can the prediction error accumulated be contained within an acceptable range?

Regarding the first question, a trade-off should be achieved between the seemingly incompatible aspects. When recursive prediction models are considered, prediction capability should come first. Our main purpose is to increase prediction horizon, as large as possible, with acceptable prediction error. The proposed selection principle begins with computing the candidate order series

$$m_i^* = \arg\{\min(BIC(j,i,T))\}, j = 1,\ldots,m_{max} \text{ for every } i = 1,\ldots,n_{max} \quad (4.24)$$

Here, for every order n changing within its bound, the BIC guarantees that multiple local optimal orders $m_i^*, i = 1,\ldots,n_{max}$ are acquired (local optimal orders are obtained when BIC values reach the minimum). Then the largest order m^* in the candidate order series is chosen to maximize the prediction horizon,

$$m^* = \max\{m_i^*\}, \quad i = 1,\ldots,n_{max} \quad (4.25)$$

For the m^*, there usually exist several orders $n_1, n_2, \ldots, n_r, n_r \leq n_{max}$. To reduce the model complexity, the proposed order selection principle selects optimal order n^* such that

$$n^* = \min\{n_k\}, \quad k = 1,2,\ldots,r \quad (4.26)$$

Eq. (4.26) seeks to reduce the model complexity in consideration of long-term prediction requirement, i.e., the model with the smallest model orders while achieving satisfactory prediction ability is obtained.

4.3 Deck Displacement Prediction Algorithm

After the optimal order pairs (m^*, n^*) and corresponding coefficients of the model are calculated using the FFRLS, we now focus on the prediction of deck displacement dynamics.

Let $\hat{A}(q^{-1})$ and $\hat{B}(q^{-1})$ be estimates of $A(q^{-1})$ and $B(q^{-1})$ determined in previous section. Rewrite our model as follows

$$[1 - \hat{A}(q^{-1})]y(t) = \hat{B}(q^{-1})u(t) + C(q^{-1})e(t) \quad (4.27)$$

Where $C(q^{-1})$ is polynomial in the backward shift operator q^{-1},

$$C(q^{-1}) = \sum_{i=0}^{m^*} c_i q^{-i}, c_0 = 1 \quad (4.28)$$

In our case, it can be seen from Eq. (4.1) that $C(q^{-1}) = 1$.

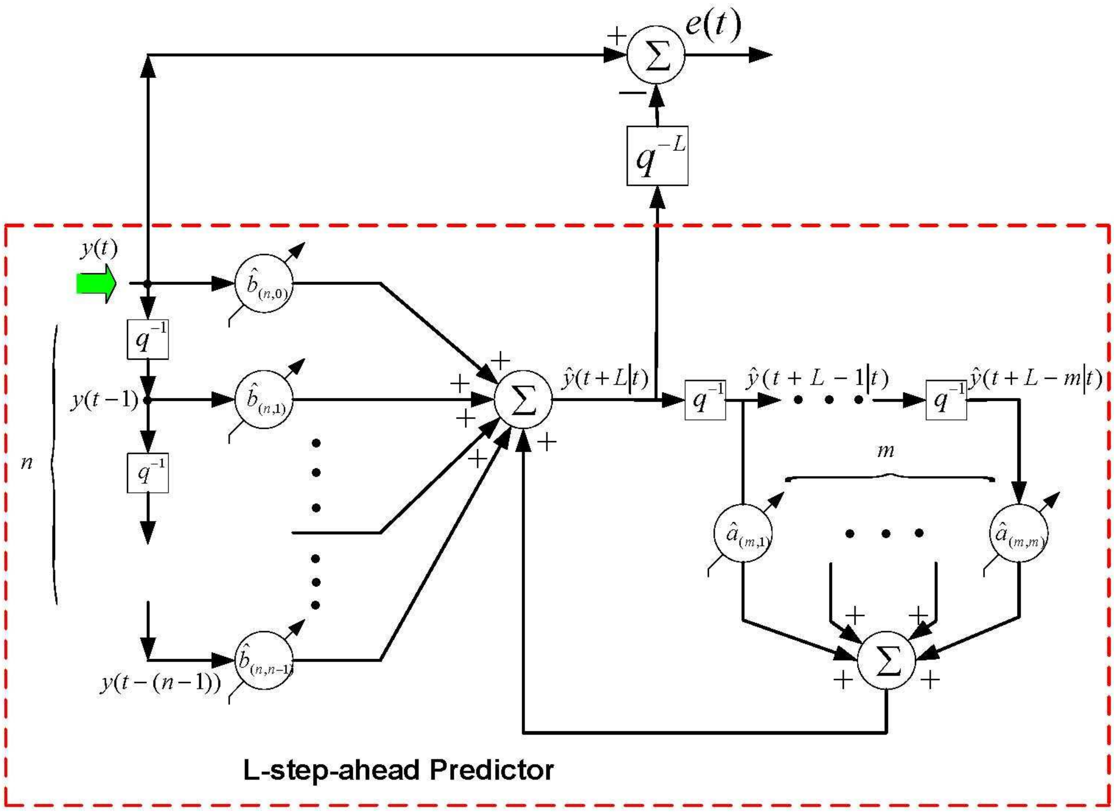

Figure 4.1. Explanations to the proposed predictor

Based on Eq. (4.27)-(4.28), we propose the following predictor

$$\hat{y}(t+L|t) = \hat{a}_{(m,1)}\hat{y}(t+L-1|t) + \cdots$$

$$+\hat{a}_{(m,m)}\hat{y}(t+L-m|t) + \hat{b}_{(n,0)}y(t) + \hat{b}_{(n,1)}y(t-1) + \cdots + \hat{b}_{(n,n-1)}y(t-(n-1)) \quad (4.29)$$

Here, $\hat{y}(t+L|t)$ is the predicted value based on the measurements until time t.

The structure of the proposed predictor is shown in Fig. 4.1. In the considered application, the prediction procedure involves the determination of $\hat{A}(q^{-1})$ and $\hat{B}(q^{-1})$, which are obtained using the identification procedure described in Section 4.2. Afterwards, $\hat{A}(q^{-1})$ and $\hat{B}(q^{-1})$ are employed to obtain the predictor $\hat{y}(t+L|t)$. The identification is carried out by collecting enough data until time t, and the model is identified using FFRLS algorithm. The obtained coefficients of the polynomials $\hat{A}(q^{-1})$ and $\hat{B}(q^{-1})$ are used in Eq. (4.29) to predict the displacement of the deck motion L-step ahead once the new measurements come. The predictor keeps employing the unchanged coefficients for $L * T_s$ (T_s is sampling period) seconds,

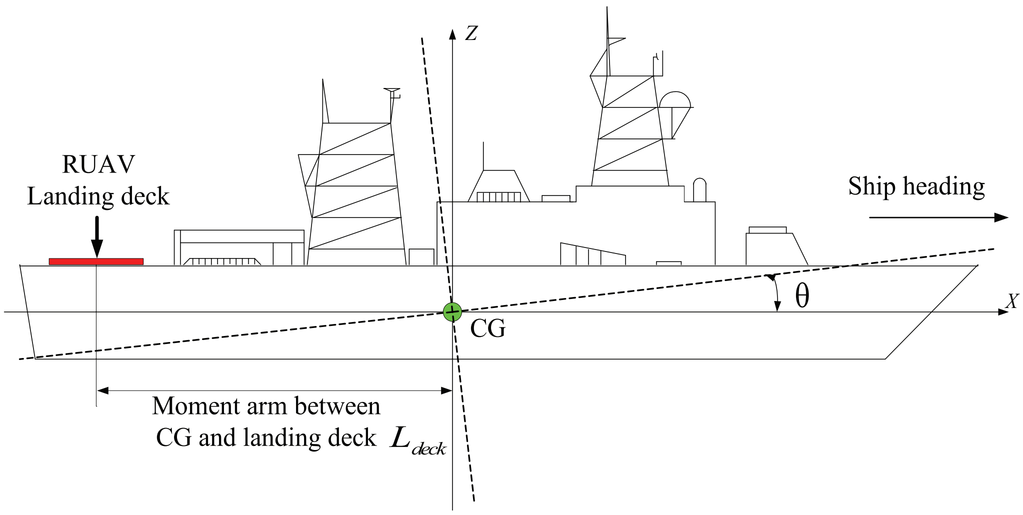

Figure 4.2. Displacement description of the landing deck

then starts specifying coefficients again using the recursive identification procedure after collecting enough measurements. Therefore, identification and prediction processes repeat every $L * T_s$ seconds to deal with the varying characteristics of deck displacement motion.

In our project, limited memory allocations on the flight computer make it proper to adopt the proposed predictor. Here, we are aiming at a feasible long-term predictor which can be rapidly implemented with acceptable prediction errors. Also, the predictor is expected to take limited memory allocations. Due to these constraints, our predictor is not optimal and we sacrifice the optimality for fast realization. The proposed procedure has implementation advantage, and can ease the computational burden greatly. Also, numerous random memories can be saved.

4.4 Simulation Results

The performance of the proposed predictor is evaluated in this section. The deck displacement data were generated from the FREDYN 8.0 software package for an 8,500-ton LPA class amphibious platform. This software simulates the dynamic behavior of a ship subjected to waves and winds, and has been validated against model tests with frigates and containerships. In the considered application, the forward speed of the ship is 20 knots, and the relative wave heading angle (angle between incoming waves and ship moving direction) is zero. The deck displacement data were sampled at every 0.25 swith a typical deck height of 4.5 m (from bottom to

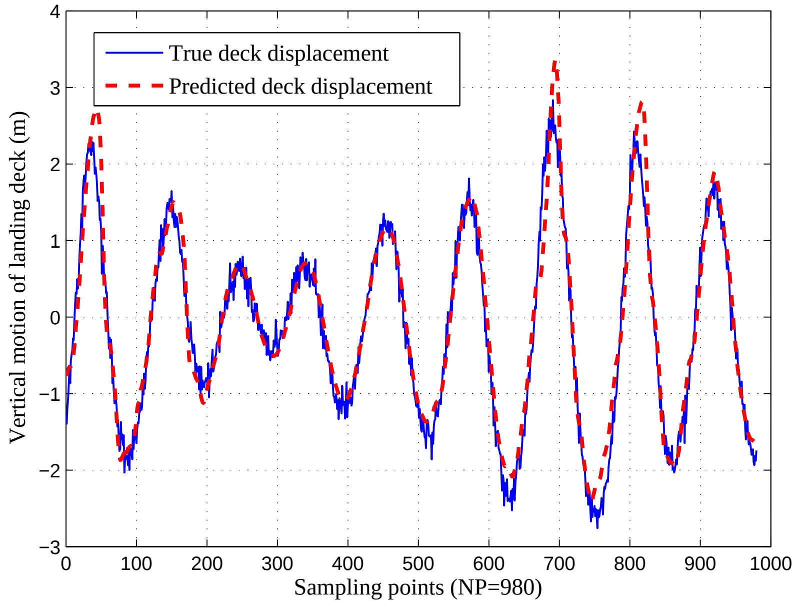

Figure 4.3. Prediction of deck displacement of the landing deck (20-step-ahead)

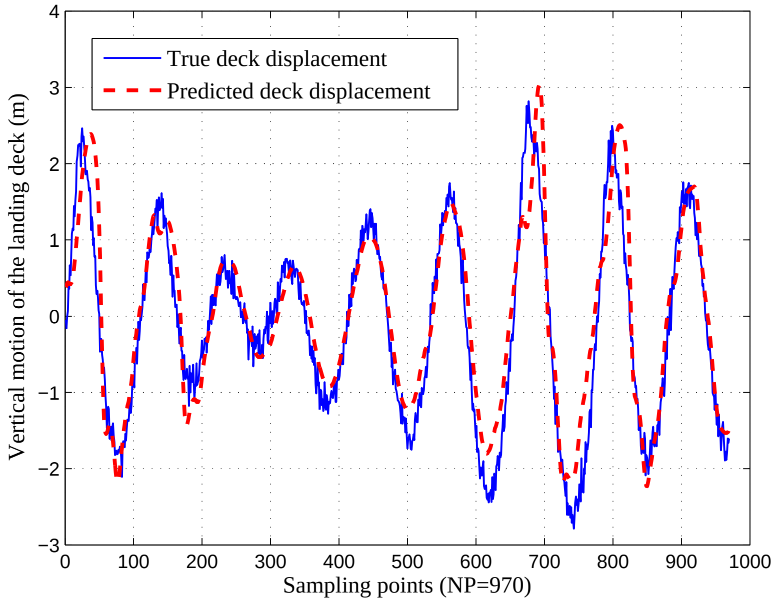

Figure 4.4. Prediction of deck displacement of the landing deck (30-step-ahead)

top the landing deck). As data obtained from the FREYDYN 8.0 software package only indicate ship motion at the CG, vertical deck displacement should be computed in consideration of the ship size. Owing to the fact that pitch motion of the ship θ_s varies within a small range, the small angle approximation is valid. Therefore, as depicted in Fig. 4.2, deck displacement can be described by

$$Z_{deck} = Z_{CG} + L_{deck}\theta_s \tag{4.30}$$

where Z_{CG} denotes heave motion at the CG. Since in our project, the moment arm between CG and the landing deck L_{deck} takes a value of 67.7 m, it can be noted that small ship pitch motion results in significant deck displacement at the landing deck.

The deck displacement data were divided into two segments: the first group of NT points were used for training and another of NP points as test data. We chose NT and NP large enough in the sense that NT points could capture deck displacement features and NP could be utilized for testing. Hence, we chose NT =200, 500, 1000, 1500 for training, and NP = NT-L points with simulated measurement error to check the prediction results. Numerous simulations were carried out. The predicted and the true deck displacement data versus time with NP =980 are plotted in Fig. 4.3 (20-step-ahead), and with NP =970 in Fig. 4.4 (30-step-ahead). Here, the optimal order pairs are (15, 4). The solid lines correspond to the true motion data, and the dashed lines to the predicted values. It is seen that the prediction results produced by the proposed algorithm match well with the true deck displacement data. Since the sampling period is 0.25 s and one period of the deck displacement can be covered by 100 points, the period of the deck displacement is 25 s. The prediction horizon is 20% of the period of the displacement motion in Fig. 4.3 (20-step-ahead), and 30% in Fig. 4.4 (30-step-ahead). As is shown in Table 4.1, the proposed predictor can predict a half period of the displacement motion satisfactorily. It can be noticed that the time it takes the deck from the peak point to the lowest point remains unchanged. This would help us to predict the quiescent period of deck displacement.

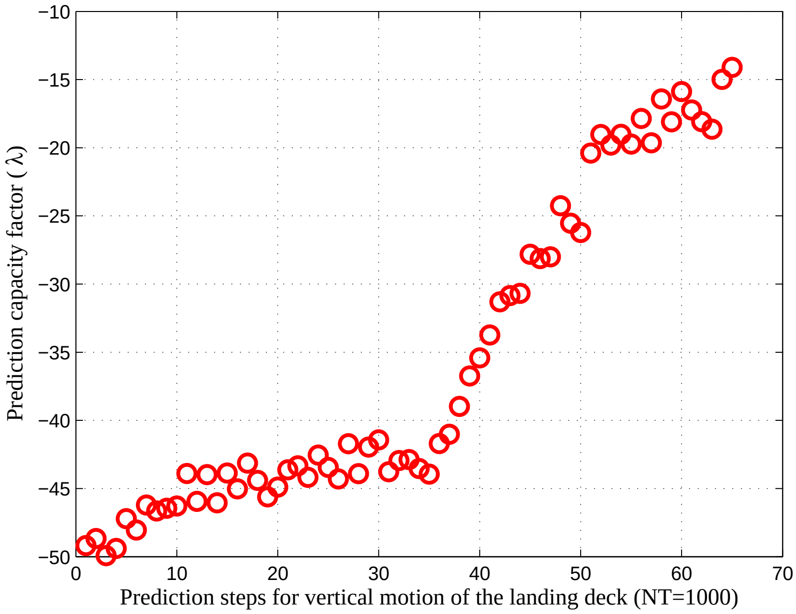

Figure 4.5. Accumulated prediction errors for different prediction steps

4.5 Comparative Studies

4.5.1 Evaluation of the Proposed Predictor

We compare the performance of our predictor with other order-predefined predictors which take the general form of

$$\frac{Y(z)}{U(z)} = \frac{b_0 + b_1 z^{-1} + \cdots + b_n z^{-n}}{1 + a_1 z^{-1} + \cdots + a_m z^{-m}} \tag{4.31}$$

Here, orders m and n are fixed for order-predefined predictors. The pairs (m, n) are set to be $(2, 2)$ for second order predictor [146], and $(18, 10)$ for high order predictor. This section aims to check the effectiveness of the proposed order selection criterion.

4.5.2 Performance Comparisons among Different Predictors

A zero-mean Gaussian random noise is added to deck displacement data in order to represent measurement errors. The peak amplitude percentage rate of the white noise to the measured data is 10%. The prediction capacity factor γ_r is employed

Table 4.1. Performance comparison for different predictors

Prediction method	N_p	System orders (m, n)	25-step Φ_r	25-step Ψ	50-step Φ_r	50-step Ψ
The proposed method	200	$(10, 3)$	2.7105e-3	1.0099	1.7398e-1	1.0249
	500	$(11, 3)$	1.9368e-3	2.3996	3.6791e-2	2.4223
	1000	$(15, 4)$	3.6671e-4	1.5039	1.9428e-2	1.6381
	1500	$(17, 4)$	1.8226e-5	1.2790	3.5567e-4	1.7158
Predictor with second order	200	$(2, 2)$	2.4151e-2	1.0215	2.6113e-1	1.2690
	500	$(2, 2)$	3.7592e-3	2.4378	5.2758e-2	2.4084
	1000	$(2, 2)$	7.2117e-3	1.5174	9.3661e-2	1.7478
	1500	$(2, 2)$	9.3255e-4	1.3917	9.6986e-3	1.8077
Predictor with high order	200	$(18, 10)$	3.1039e-3	1.0315	2.1981e-1	1.2714
	500	$(18, 10)$	2.4931e-3	2.7980	4.1541e-2	2.5214
	1000	$(18, 10)$	1.6317e-3	1.5901	7.4590e-2	1.8607
	1500	$(18, 10)$	8.4460e-5	1.6022	2.9186e-3	2.0190

to measure the overall prediction performance, which takes the form of

$$\gamma_r = 20 \log_{10} \frac{\sqrt{\Phi_r}}{y_{max}} \tag{4.32}$$

where the mean squared prediction error Φ_r is expressed as

$$\Phi_r = \frac{1}{N} \sum_{i=T+1}^{T+N_p} [y(i) - \hat{y}(i)]^2 \tag{4.33}$$

For a given trajectory, the maximum prediction error is evaluated by

$$\Psi = \max_i |y(i) - \hat{y}(i)| \tag{4.34}$$

where $y(i)$ and $\hat{y}(i)$ are the true and the predicted data. The index Ψ is a useful measure from a practical viewpoint, as it is important to know if there are some points where our predictor fails and gives extremely large discrepancies, which could lead to wrong control commands and cause fatal crash of the RUAV. As is shown in Fig. 4.5, the prediction capacity factor γ_r remains less than -20dB until 50 steps, i.e., the prediction error within 10% of true data can be obtained up to 50-step-ahead (12.5 seconds). This is assumed to be acceptable in the considered application where period of dynamics of deck displacement is 25 s.

Table 4.1 summarizes the experimental results on mean square errors Φ_r and maximum errors Ψ_r of different predictors, each taking four groups of NP points and predicting 25 and 50 steps ahead. For 25-step-ahead prediction, the proposed algorithm gives consistently good performance even when NP is much larger, whereas the order-predefined predictors produce larger Φ_r and Ψ_r. It is seen that our predictor produces large maximum prediction errors Ψ_r at some points, which indicate it sacrifices Ψ_r to compensate for overall performance. The proposed prediction method can effectively find the time moment when the deck reaches the maximum height. Thus, it can be used to arrange the landing trajectory to achieve safe touch down operations.

4.6 Summary

In this chapter, a black-box approach from the viewpoint of time series theory is proposed to predict displacement of an 8,500-ton LPA class amphibious platform. The resultant model is obtained with model orders determined by a new principle and coefficients identified using the FFRLS. With a view to the limited processing and memory capacity of the flight computer, our predictor sacrifices the optimality for fast implementation. Comparative studies show advantages of the proposed predictor over second-order and high-order predictors, which make it suitable for the long-term accurate prediction of deck displacement dynamics for ship-helicopter flight operations.

Chapter 5

Advanced Sensor Fusion for Integrated Navigation

This chapter presents an applicable framework to synthesize multi-sensor navigation information for localization of a RUAV and estimation of ship positions when the RUAV approaches the landing deck. The estimation performance of the visual tracking sensor can also be improved through integrated navigation. Three different sensors (inertial navigation sensor, GPS and visual tracking sensor) are utilized complementarily to perform the navigation tasks for the purpose of an automatic landing. An EKF is developed to fuse data from the distinct navigation sensors to provide reliable navigation information.

5.1 Introduction

A successful automatic landing of the RUAV requires the accurate navigation capability to plan a smooth trajectory and to land in the correct location of the deck. Also, the limited landing deck space indicates there is not much room for errors. The combination of various navigation sensors provides a feasible means of achieving a high accuracy whilst reducing the cost. It can take advantage of auxiliary attributes of multiple sensors for estimation with a better accuracy. The current integrated navigation system carried aboard our RUAV comprises three measurement sensors: inertial navigation sensor (INS), GPS and visual tracking sensor (TS).

The GPS/INS synergy strategy is an efficient integration able to operate in a wide range of scenarios and provides low-cost high-accuracy estimation performance, and has been discussed extensively in a number of articles [107, 147–149]. Dittrich *et al.* [147] considered design and development of a practical avionics system which can provide reliable navigation information for the flight computer of an autonomous helicopter. The navigation system was constructed using the extended Kalman filtering technique by fusing measurements from GPS, IMU, sonar and radar altimeters. In Ref. [148], a linearized integrated GPS/INS model was utilized and an extended Kalman filter was developed with its performance evaluated for a typical aerospace application. The sensitivity analysis was also conducted to determine the optimal filter parameters. Jan *et al.* [149] developed an integrated navigation system to provide attitude information with sufficient accuracy for a four rotor helicopter. Specifically, the navigation system aimed to ensure the optimal usage of the GPS measurements, achieving robust performance in case of GPS data loss by switching between two operating modes. Each mode included design of a Kalman filter to estimate attitude errors and gyroscope biases and correct them. A family of nonlinear Kalman filers called sigma-point Kalman filter was presented for integrated navigation in Ref. [150]. It was reported that the proposed Kalman filter can capture the posterior mean and covariance more accurately, and its implementation was often substantially easier than the EKF. The example given in this paper showed an approximate 30% error reduction in attitudes and positions can be achieved compared with the EKF when the proposed method was applied to a rotorcraft platform. Zhang *et al.* presented a navigation system for an autonomous vehicle by integrating measurements from IMU, GPS and digital compass. To overcome low precision of separate sensors, system estimation was implemented by using the unscented Kalman filter which had a higher calculation accuracy compared with the EKF. The unscented Kalman filter is a derivative-free variant of Kalman filter and can capture the posterior mean and covariance accurately to the third-order (Taylor series expansion) for nonlinear systems [150]. Implementation of the unscented Kalman filter requires a set of weighted sigma points to be chosen such that certain properties of these points match those of the prior distributions [151]. Also, additional weight parameters should be selected according to the type of sigma-point approach used [150]. Therefore, implementation of the unscented Kalman filter requires careful choice of weight parameters, and it is time-consuming to obtain these parameters by implementing the nonlinear unscented transformation online for a flight computer performing multiple tasks during flight operations. In our case, we are targeting a feasible filtering approach which can be implemented easily at the cost of limited flight computer memory and provide sufficient estimation accuracy. Also, due to the fact that introduction of high order (second order and higher orders) system dynamics does not generally lead to an improvement in system performance [111], we use the EKF in this chapter to perform the sensor fusion task.

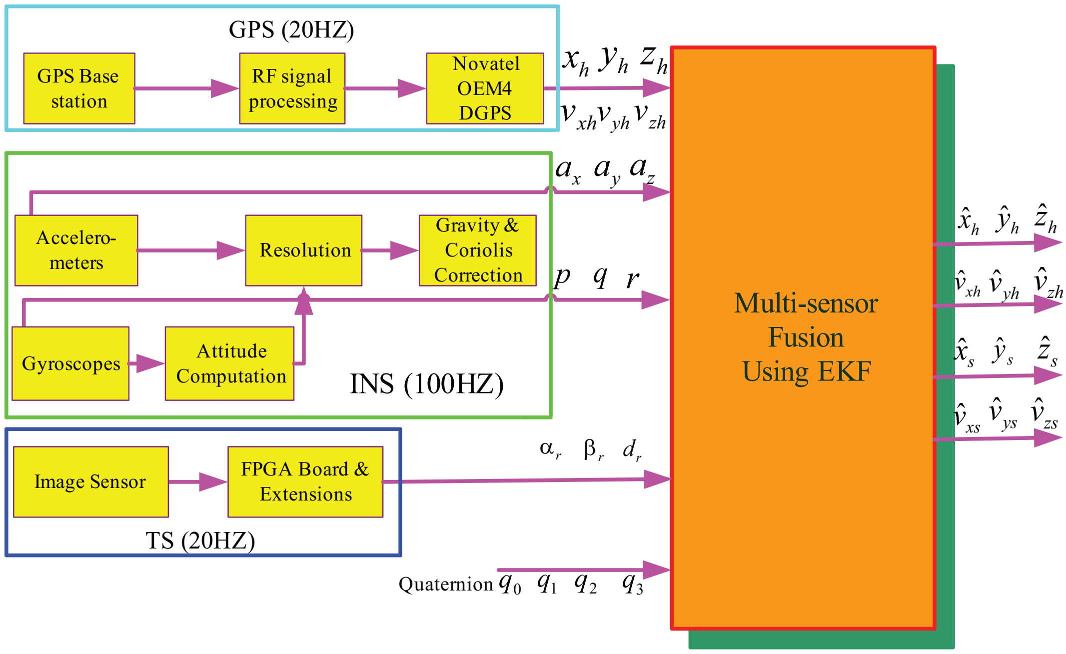

Figure 5.1. Architecture of the EKF for multi-sensor fusion

In the considered application, positions and velocities of the RUAV can be estimated accurately through combination of GPS and INS. For an automatic landing, of particular interest are ship positions which cannot be measured by the RUAV. However, they can be estimated if the relative position information between the ship and the RUAV is obtained. Therefore, an auxiliary TS is developed in our lab, and fitted aboard the RUAV [146], yielding reliably relative positions. Therefore, the collaboration of INS, GPS and TS makes it feasible to provide navigation information with satisfactory precision by developing an effective sensor fusion algorithm to filter noisy measurements and estimate ship motion dynamics. Moreover, the effective estimation of ship positions facilitates extraction of the mean height of the landing deck, relieving the RUAV of maneuvering its height to track the instantaneous deck dynamics which would cause substantive consumption of power.

5.2 Sensor Fusion Algorithm using the EKF

The structure of the integrated navigation scheme is shown in Fig. 5.1. Due to the fact that the GPS-based receiver is susceptible to jamming in a dynamic environment and velocity measurements from the GPS are also noisy owing to variations in signal strength, the effects of changing multi-path and user lock instability [107],

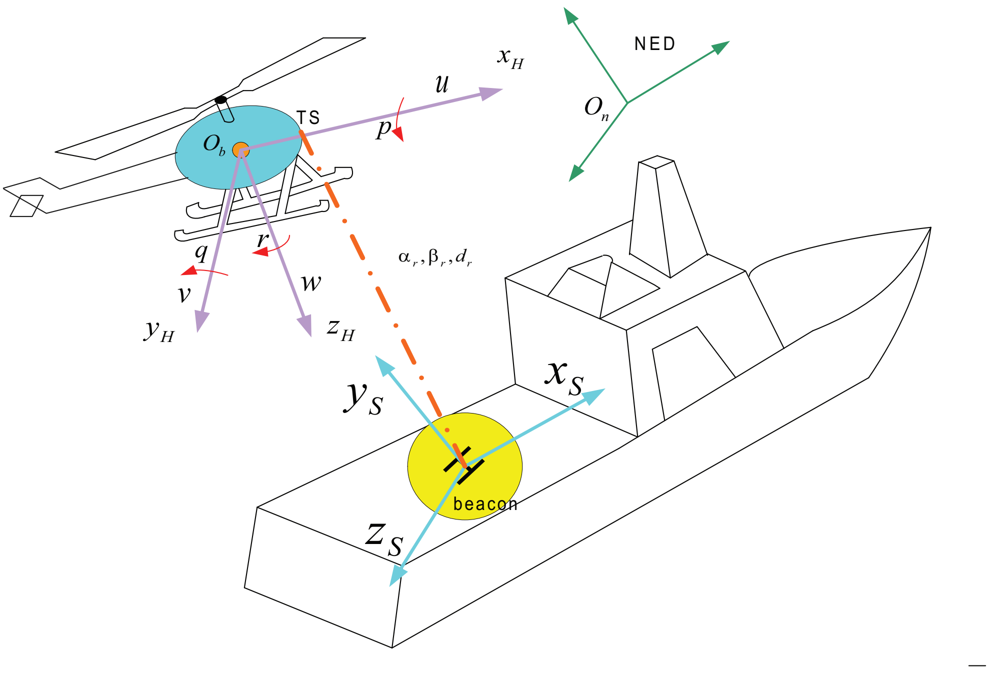

Figure 5.2. A RUAV approaches a moving ship deck

it is necessary to incorporate the INS into the navigation system to yield benefits over operating the GPS alone. Normally, measurements from different sensors require calibrations before the sensor fusion is performed. The GPS onboard employs Novatel OEM4-G2L GPS cards which perform differential corrections, thus providing positions and velocities with high precision (1-2 cm circular error probability). Therefore, there is no need to design calibration method for the GPS. In the IMUs used in these sort of projects (e.g. Crossbow NAV-440, NovAtel SPAN), corrections for offsets and other errors are already compensated for using GPS/INS sensor fusion inside these commercially available systems. Hence further error compensation is not warranted for the attitude and rate states. The major source of errors is in the position and velocity estimates and we address these issues in our sensor fusion paradigm. Also, standard deviations of noise levels in measurements of azimuth and elevation angles from the visual tracking sensor are 0.18^o, which is accurate enough to be used for sensor fusion. The integrated navigation system aims to smooth out noise in position and velocity measurements of the RUAV. Also, it serves to estimate deck displacement by fusing the following groups of measurements (Fig. 5.2): helicopter position (x_h, y_h, z_h) and velocity (v_{xh}, v_{yh}, v_{zh}) from the GPS, relative motion information (α_r, β_r, d_r) described in the spherical coordinates from the TS, and helicopter accelerations (a_x, a_y, a_z) and angular rates (p, q, r) from the INS. Here, helicopter velocity (u, v, w) in the body frame is related to velocity (v_{xh}, v_{yh}, v_{zh}) in the navigation frame by the direction cosine matrix C_b^n

$$[v_{xh}, v_{yh}, v_{zh}]^T = \ C_b^n \ [u, v, w]^T \tag{5.1}$$

with C_b^n expressed in quaternion parameters [107]

$$C_b^n = \begin{bmatrix} c_{11} & c_{12} & c_{13} \\ c_{21} & c_{22} & c_{23} \\ c_{31} & c_{32} & c_{33} \end{bmatrix}$$

$$= \begin{bmatrix} q_0^2 + q_1^2 - q_2^2 - q_3^2 & 2(q_1 q_2 - q_0 q_3) & 2(q_1 q_3 + q_0 q_2) \\ 2(q_1 q_2 + q_0 q_3) & q_0^2 - q_1^2 + q_2^2 - q_3^2 & 2(q_2 q_3 - q_0 q_1) \\ 2(q_1 q_3 - q_0 q_2) & 2(q_2 q_3 + q_0 q_1) & q_0^2 - q_1^2 - q_2^2 + q_3^2 \end{bmatrix}$$

where quaternion elements are denoted by $\boldsymbol{q} = [q_0, q_1, q_2, q_3]^T$. The quaternion attitude expression is a four-element representation based on the viewpoint that a transformation from one frame to another can be interpreted as a single rotation about a vector defined with respect to the reference frame [107]. The singular problems encountered when attitudes are expressed in Euler forms can be avoided via adoption of the quaternion form.

The discrete-time system updating model of EKF takes the form of

$$X_k = f(X_{k-1}, k-1) + \varepsilon_k \tag{5.2}$$

where state vector X corresponds to 17 state variables

$$X = [x_h, y_h, z_h, u, v, w, x_s, y_s, z_s, v_{xs}, v_{ys}, v_{zs}, x_r, y_r, z_r, \psi_s, V_{\psi s}]^T \tag{5.3}$$

and system noise ε is

$$\varepsilon = [\varepsilon_1, \cdots, \varepsilon_{17}]^T \tag{5.4}$$

Here, positions of the RUAV (x_h, y_h, z_h), ship positions (x_s, y_s, z_s) and velocities (v_{xs}, v_{ys}, v_{zs}), and relative positions (x_r, y_r, z_r) are in navigation coordinate frame. Ship yaw and yaw rate are denoted by ψ_s and $V_{\psi s}$. The RUAV can receive ship heading (yaw) information sent by the ship.

Equation (5.3) can be expressed in an explicit form

$$(x_h)_k = (x_h)_{k-1} + T_s[(c_{11})_{k-1}u_{k-1} + (c_{12})_{k-1}v_{k-1} + (c_{13})_{k-1}w_{k-1}] + (\varepsilon_1)_k \tag{5.5}$$
$$(y_h)_k = (y_h)_{k-1} + T_s[(c_{21})_{k-1}u_{k-1} + (c_{22})_{k-1}v_{k-1} + (c_{23})_{k-1}w_{k-1}] + (\varepsilon_2)_k \tag{5.6}$$
$$(z_h)_k = (z_h)_{k-1} + T_s[(c_{31})_{k-1}u_{k-1} + (c_{32})_{k-1}v_{k-1} + (c_{33})_{k-1}w_{k-1}] + (\varepsilon_3)_k \tag{5.7}$$
$$u_k = u_{k-1} + T_s[r_{k-1}v_{k-1} - q_{k-1}w_{k-1} + (a_x)_{k-1}] + (\varepsilon_4)_k \tag{5.8}$$
$$v_k = v_{k-1} + T_s[-r_{k-1}u_{k-1} + p_{k-1}w_{k-1} + (a_y)_{k-1}] + (\varepsilon_5)_k \tag{5.9}$$
$$w_k = w_{k-1} + T_s[q_{k-1}u_{k-1} - p_{k-1}v_{k-1} + (a_z)_{k-1}] + (\varepsilon_6)_k \tag{5.10}$$
$$(x_s)_k = (x_s)_{k-1} + T_s(v_{xs})_{k-1} + (\varepsilon_7)_k \tag{5.11}$$
$$(y_s)_k = (y_s)_{k-1} + T_s(v_{ys})_{k-1} + (\varepsilon_8)_k \tag{5.12}$$
$$(z_s)_k = (z_s)_{k-1} + T_s(v_{zs})_{k-1} + (\varepsilon_9)_k \tag{5.13}$$
$$(v_{xs})_k = (v_{xs})_{k-1} + (\varepsilon_{10})_k \tag{5.14}$$
$$(v_{ys})_k = (v_{ys})_{k-1} + (\varepsilon_{11})_k \tag{5.15}$$
$$(v_{zs})_k = (v_{zs})_{k-1} + (\varepsilon_{12})_k \tag{5.16}$$
$$(x_r)_k = (x_r)_{k-1} + (\varepsilon_{13})_k \tag{5.17}$$
$$(y_r)_k = (y_r)_{k-1} + (\varepsilon_{14})_k \tag{5.18}$$
$$(z_r)_k = (z_r)_{k-1} + (\varepsilon_{15})_k \tag{5.19}$$
$$(\psi_s)_k = (\psi_s)_{k-1} + T_s(V_{\psi s})_{k-1} + (\varepsilon_{16})_k \tag{5.20}$$
$$(V_{\psi s})_k = (V_{\psi s})_{k-1} + (\varepsilon_{17})_k \tag{5.21}$$

Equations (5.5)-(5.21) propagate states variables from time instant $k-1$ to k. The sampling time is denoted by T_s. System noise $\varepsilon_{(\cdot)}$ is mutually independent with Gaussian distributions, and covariance matrix of system noise $Q_{(\cdot)}$ satisfies

$$E\{\varepsilon^i_{(\cdot)}[\varepsilon^j_{(\cdot)}]^T\} = \delta(i-j)Q_{(\cdot)} \tag{5.22}$$

where δ is Kronec function taking the form of

$$\delta(i-j) = \begin{cases} 1 & \text{if } i = j \\ 0 & \text{if } i \neq j \end{cases}$$

Equations (5.5)-(5.7) describe relationship of velocities between body frame and navigation frame. Local velocity propagations are revealed in Eq. (5.8)-(5.10) with knowledge of accelerations (a_x, a_y, a_z). In the considered application, it is not possible to build up an accurate ship motion model. However, it is reasonable to assume ship motion remains approximately constant in speed and heading during the landing phase, as is shown in Eq. (5.11)-(5.16). Of particular significance is the relative vertical motion which greatly affects magnitude of the impact forces during touchdown.

Equations (5.5)-(5.7) can be written in explicit forms

$$\begin{aligned}(x_h)_k = (x_h)_{k-1} + T_s[&\frac{4 + (p_{k-1}^2 - q_{k-1}^2 - r_{k-1}^2)T_s^2}{4}u_{k-1} \\ &+ \frac{p_{k-1}q_{k-1}T_s^2 - 2r_{k-1}T_s}{2}v_{k-1} + \frac{p_{k-1}r_{k-1}T_s^2 + 2q_{k-1}T_s}{2}w_{k-1}] + (\varepsilon_1)_k \quad (5.23)\end{aligned}$$

$$\begin{aligned}(y_h)_k = (y_h)_{k-1} + T_s[&\frac{p_{k-1}q_{k-1}T_s^2 + 2r_{k-1}T_s}{2}u_{k-1} \\ &+ \frac{4 + (q_{k-1}^2 - p_{k-1}^2 - r_{k-1}^2)T_s^2}{4}v_{k-1} + \frac{q_{k-1}r_{k-1}T_s^2 - 2p_{k-1}T_s}{2}w_{k-1}] + (\varepsilon_2)_k \quad (5.24)\end{aligned}$$

$$\begin{aligned}(z_h)_k = (z_h)_{k-1} + T_s[&\frac{p_{k-1}r_{k-1}T_s^2 - 2q_{k-1}T_s}{2}u_{k-1} + \frac{q_{k-1}r_{k-1}T_s^2 + 2p_{k-1}T_s}{2}v_{k-1} \\ &+ \frac{4 + (r_{k-1}^2 - p_{k-1}^2 - q_{k-1}^2)T_s^2}{4}w_{k-1}] + (\varepsilon_3)_k \quad (5.25)\end{aligned}$$

Therefore, the state transition matrix $\Phi_{k|k-1}$ can be derived by differentiating Eq. (5.23)-(5.25) and Eq. (5.8)-(5.21) with respect to each state. Here, the angular rates at time instant k are described by p_k, q_k, r_k. In our case, the body rate information obtained from the INS has been filtered and can be used for sensor fusion. Angular rates (p_k, q_k, r_k) do not remain constant and keep updating when measurements from the INS change.

The measurement model can be described by

$$Z_k = h(X_k, k) + \epsilon_k \quad (5.26)$$

where 10 measurements are

$$Z = [x_h, y_h, z_h, v_{xh}, v_{yh}, v_{zh}, \alpha_r, \beta_r, d_r, \psi_s]^T \quad (5.27)$$

and measurement noise ϵ is

$$\epsilon = [\epsilon_1, \ldots, \epsilon_{10}]^T \quad (5.28)$$

The detailed measurement equations are

$$(x_h)_k = (x_h)_k + (\epsilon_1)_k \tag{5.29}$$

$$(y_h)_k = (y_h)_k + (\epsilon_2)_k \tag{5.30}$$

$$(z_h)_k = (z_h)_k + (\epsilon_3)_k \tag{5.31}$$

$$u_k = u_k + (\epsilon_4)_k \tag{5.32}$$

$$v_k = v_k + (\epsilon_5)_k \tag{5.33}$$

$$w_k = w_k + (\epsilon_6)_k \tag{5.34}$$

$$(\alpha_r)_k = \arctan\left\{\frac{(y_r)_k}{(x_r)_k}\right\} + (\epsilon_7)_k \tag{5.35}$$

$$(\beta_r)_k = \arccos\left\{\frac{(z_r)_k}{\sqrt{[(x_r)_k]^2 + [(y_r)_k]^2 + [(z_r)_k]^2}}\right\} + (\epsilon_8)_k \tag{5.36}$$

$$(d_r)_k = \sqrt{[(x_r)_k]^2 + [(y_r)_k]^2 + [(z_r)_k]^2} + (\epsilon_9)_k \tag{5.37}$$

$$(\psi_s)_k = (\psi_s)_k + (\epsilon_{10})_k \tag{5.38}$$

Measurement noise $\epsilon_{(\cdot)}$ is mutually independent with Gaussian distributions, and covariance matrix of measurement noise $R_{(\cdot)}$ satisfies

$$E\{\epsilon^i_{(\cdot)}[\epsilon^j_{(\cdot)}]^T\} = \delta(i-j)R_{(\cdot)} \tag{5.39}$$

Given the system model and measurement model, an EKF can be developed to fulfill the sensor fusion task by taking the following procedure [108, 152]:

Computing the prior state estimate:

$$\hat{X}_{k|k-1} = f(\hat{X}_{k-1|k-1}, k-1) \tag{5.40}$$

Computing the predicted measurement:

$$\hat{Z}_k = h(\hat{X}_{k|k-1}, k) \tag{5.41}$$

Linearize system updating equations:

$$\Phi_{k|k-1} \approx \frac{\partial f(X, k-1)}{\partial X}|_{X=\hat{X}_{k-1|k-1}} \tag{5.42}$$

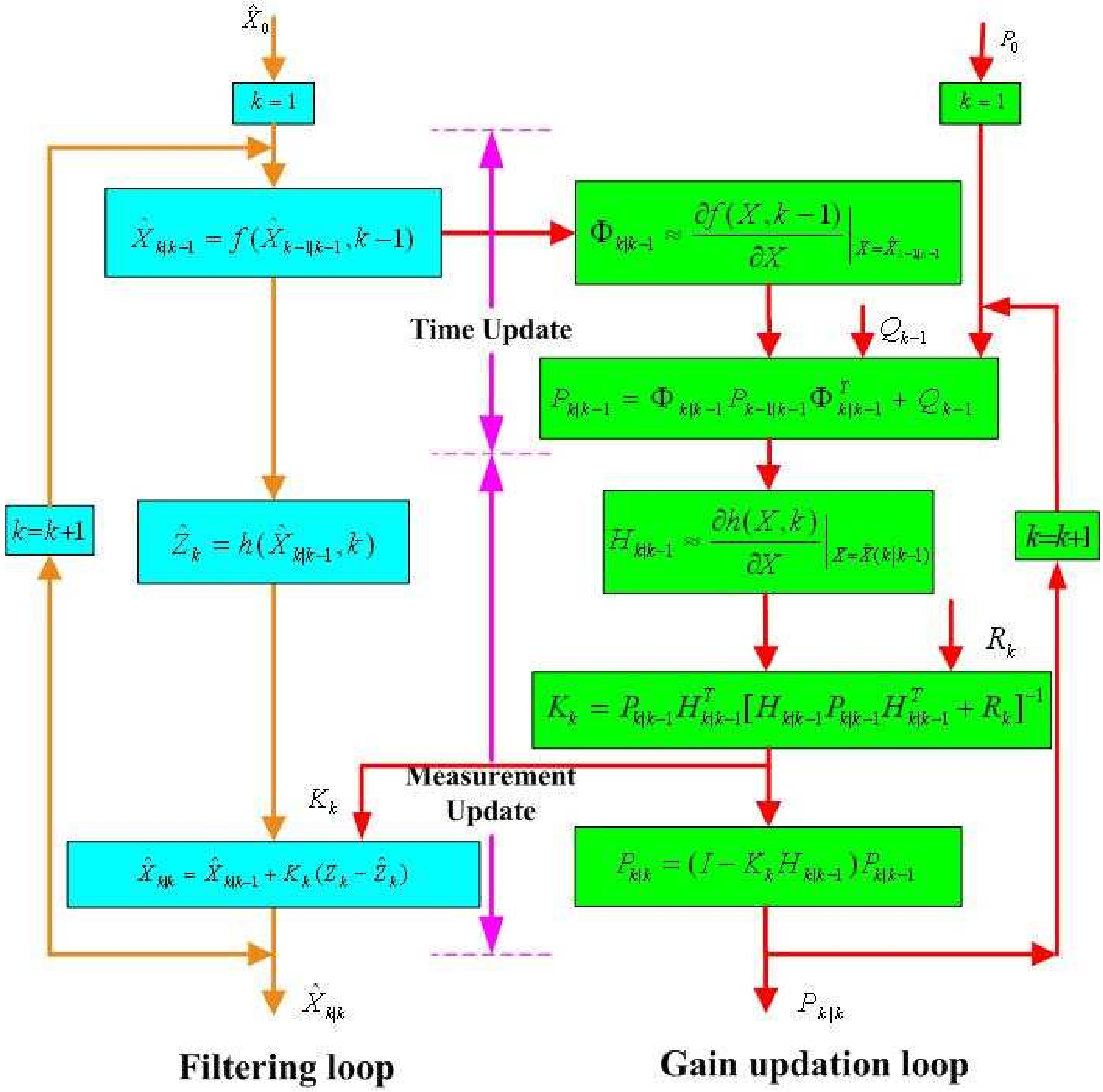

Figure 5.3. Flow chart for implementation of the EKF

Conditioning the predicted estimate on the measurement and linearize measurement equation:

$$\hat{X}_{k|k} = \hat{X}_{k|k-1} + K_k(Z_k - \hat{Z}_k) \tag{5.43}$$

$$H_{k|k-1} \approx \frac{\partial h(X,k)}{\partial X}|_{X=\hat{X}_{k|k-1}} \tag{5.44}$$

Computing the prior covariance matrix:

$$P_{k|k-1} = \Phi_{k|k-1}P_{k-1|k-1}\Phi^T_{k|k-1} + Q_{k-1} \tag{5.45}$$

Computing the Kalman gain:

$$K_k = P_{k|k-1}H^T_{k|k-1}[H_{k|k-1}P_{k|k-1}H^T_{k|k-1} + R_k]^{-1} \tag{5.46}$$

Computing the posteriori covariance matrix:

$$P_{k|k} = [I - K_kH_{k|k-1}]P_{k|k-1} \tag{5.47}$$

The flow chart for EKF implementation is shown in Fig. 5.3. The EKF algorithm is implemented as a C-file S-function block for integration into the ship/helicopter landing system.

5.3 Simulation Results

In this section, the EKF algorithm is tested using real-time deck displacement data for the Vario helicopter model. In the simulation, the RUAV is supposed to follow the middle line of the ship, approach the deck in the constant speed of 3 m/s, and hover at a height of 10 m. For the NovAtel GPS receiver on our helicopter, the distance accuracy is 2 cm in the longitudinal-lateral plane and 4 cm in the elevation. Thus, white noise with standard deviations of 2 cm, 2 cm and 4 cm were added to real positions of the RUAV to test the performance of the EKF. Also, azimuth angle α_r and elevation angle β_r were contaminated by white noise with standard deviations of 0.18°. This agrees with the noise levels in our visual tracking sensor.

Performance of the EKF when applied to estimate positions of the RUAV is shown in Fig. 5.4. For the sake of observation convenience, estimation results for the first 10 s are plotted. It is noticed that noise effects in positions are attenuated

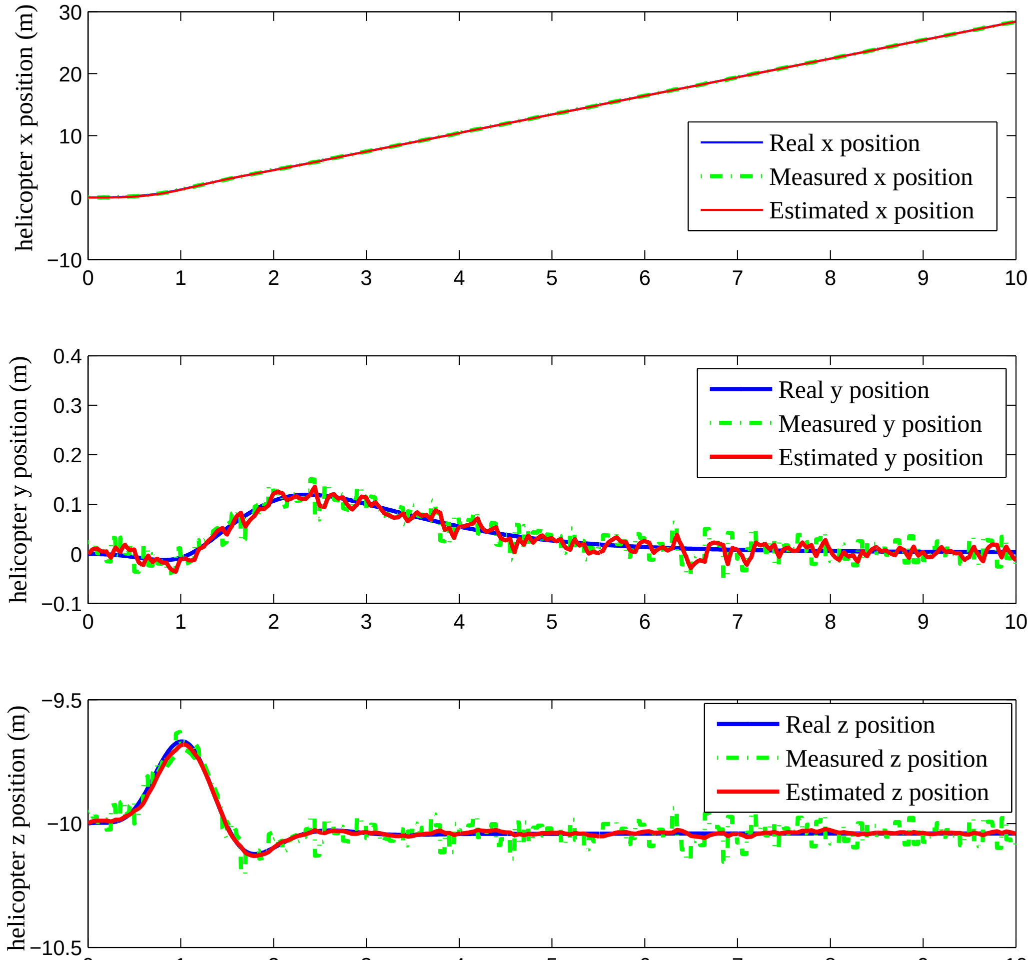

Figure 5.4. Estimation of RUAV positions using the EKF

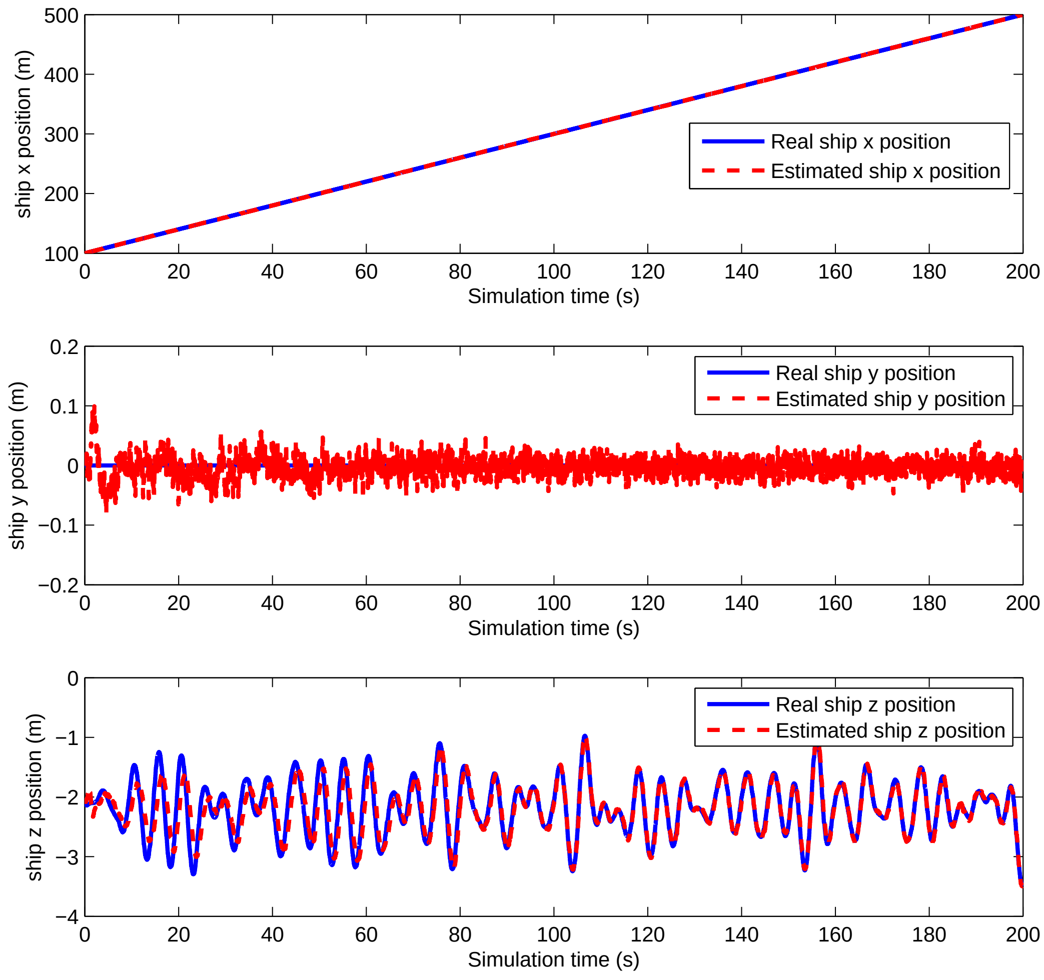

Figure 5.5. Estimation of ship positions using the EKF

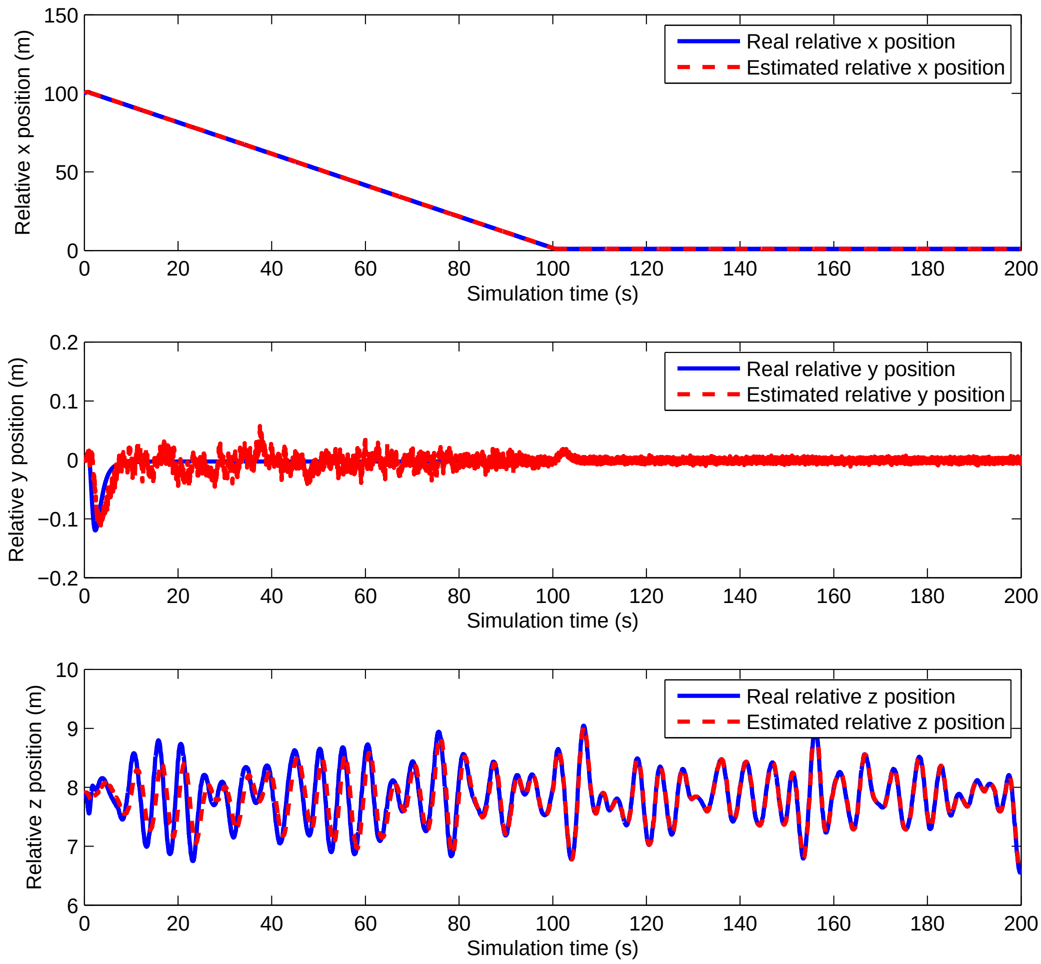

Figure 5.6. Estimation of relative positions

Table 5.1. Standard deviations of the estimated states

States	Unit	Std. Dev.
x_h	m	0.15
y_h	m	0.01
z_h	m	0.02
x_s	m	0.15
y_s	m	0.01
z_s	m	0.20
x_r	m	0.04
y_r	m	0.01
z_r	m	0.19

efficiently. Also, the unknown ship positions are estimated accurately, as is shown in Fig. 5.5. Estimations of relative positions between the ship and the RUAV are given in Fig. 5.6. It takes around 80 s for the EKF to capture the system dynamics accurately. In particular, deck displacement is estimated smoothly, which greatly contributes to extracting instantaneous mean deck position for landing operations. The standard deviations of the estimated states are shown in Table 5.1. It is seen that the EKF can smooth out the noisy measurements and estimate ship positions effectively.

5.4 Summary

In this chapter, an EKF is designed and implemented for the purpose of integrated navigation. Noisy measurements from GPS and INS are filtered, and performance of the TS has been improved when the RUAV approaches the ship deck from far away. Also, the unknown ship motion dynamics are effectively estimated, which can be used to extract the trend of deck motion for ship/helicopter landing systems.

Chapter 6

Trend Estimation of Deck Displacement

This chapter presents a practical procedure for estimating monotonous tendency of deck displacement to assist in an automatic landing of a RUAV. The proposed procedure begins with the modified PA, which involves developing an appropriate model with parameters identified using the FFRLS method. The model order is specified based on minimizing the summed squared estimation errors. Also, dominant modes are extracted to obtain an accurate estimation of the mean deck height. Simulation results demonstrate that the proposed recursive procedure exhibits satisfactory performance when applied to real-time deck displacement measurements.

6.1 Introduction

A fundamental requirement for a successful landing operation necessitates an accurate estimation of the dynamic trend of deck displacement so that a smooth landing trajectory can be arranged which enables the RUAV to track the mean deck height as opposed to the instantaneous deck displacement. This will enable the RUAV to approach the deck, and land with a smooth trajectory. Here, the mean deck height cannot be extracted using a moving average filter since it only averages the measurements, and is unable to identify the slow-varying modes from system dynamics. Also, the moving average filter would delay the mean calculation unacceptably because the period of the ship motion is so long.

A variety of real-time dynamic systems experience oscillations which comprise distinct sinusoidal components resulting from unknown nonlinearities, uncertainty of system dynamics, and random external disturbances. Normally, nonlinear dynamic systems can be approached around a set of equilibrium points using proper linear models. Developing the form of such models depends on the specific applications under consideration. There are two mainstream approaches: the first one is to linearize the nonlinear model by expanding the nonlinear terms around the equilibrium points of interest. These equilibrium points are chosen to represent the typical working conditions the system experiences, and ignoring high-order terms would not harm system dynamics. Alternatively, curve-fitting techniques are an option to optimally fit a linear combination of terms to the measurements [153]. Since it takes tremendous effort to build an accurate system model of deck motion due to the irrational non-minimum phase transfer functions between ship motion and sea elevation [130], it is preferred to use a curve-fitting technique to analyze deck motion for real-time applications.

PA is a branch of parametric curve-fitting techniques, which employs a group of exponential terms to approximate the impulse response of a dynamic system [154]. The resultant parameters can be related to magnitude, frequency and phase giving physical interpretation of an oscillating system. Application of PA in power systems has been subject to extensive investigation and significant efforts, including theoretical analysis and experimental research, have been made to deal with various scenarios. Hauer *et al.* [154, 155] presented results for modal analysis and model construction of power systems based on field measured data. The identification of modal content from oscillating power systems in different scenarios has also been reported in [156–159]. Trudnowski *et al.* [160] extended the PA to allow for analyzing multiple input signals. Recently, PA was implemented to monitor power system transient harmonics, and the dominant harmonics identified were used as the harmonic reference for harmonic selective active filters in [161]. A small number of papers have addressed the use of PA in oscillating systems other than power systems. A recursive approach to PA estimation was employed to analyze the response of a beam to transient excitations by Davies [162]. PA was also used for radar target identification [163, 164] and signal processing [165, 166].

Extracting trend of oscillating systems in various scenarios has been discussed for different applications. This has been achieved using linear models [167], weighted exponential models [168] and polynomial models [169]. These methods essentially aim to find the best model coefficients to match the measurements by minimizing the mean square errors, and the model coefficients identified normally do not have clear physical interpretation. Zhou *et al.* [170] proposed an iterative nonlinear trend identification algorithm, in which the trend was taken as the mean values of upper and lower envelopes following a five-step iteration procedure. Signal trend identification has also been investigated using artificial neural network models [171, 172]. Moreover, fuzzy-logic-based methodologies for online trend estimation were proposed for practical use [173, 174].

In this chapter, a modified recursive PA model is built with model order specified based on minimizing the summed squared estimation errors and model coefficients identified using the FFRLS procedure. The use of the FFRLS aims to highlight the measurements mostly relevant for the training process. Also, a suitable box selection principle is proposed to choose the dominant modes in the oscillating system. Simulation results demonstrate that the proposed methodology exhibits satisfactory performance when applied to analyze real-time deck motion data.

6.2 Prony Analysis

Given a sampled sequence of discrete-time system observations, numerous curve-fitting methodologies (such as linear, nonlinear, quadratic and high-order polynomials, etc.) are available and expressions of models to be chosen depend on dynamic variations revealed in the systems and tractability of the estimation problems corresponding to the dynamic models [175, 176]. The real deck motion is oscillating, which motivates us to employ a weighted sum of sinusoidal functions to approach deck dynamics. The emerging PA has been widely used to analyze oscillating power systems with the advancement of modern computational capacity [161, 177, 178].

PA was initially developed by Gaspard Riche Baron de Prony in 1795 to explain the expansion of various gases. It provides an effective way of extracting valuable information from a group of uniformly sampled data [179]. It adopts a series of damped complex exponentials to approximate system dynamics, which represent system information in terms of amplitude, frequency, phase and damping components.

A continuous-time sequence $y(t)$ can be approximated by a weighted linear combination of exponential terms

$$\hat{y}(t) = \sum_{i=1}^{n_p} D_i e^{\lambda_i t} \tag{6.1}$$

where each complex residue D_i corresponds to its complex pole λ_i, $i = 1, ..., n_p$, and the model order is denoted by n_p. The proper identification of model parameters D_i, λ_i and n_p enables the model to match the known measurements satisfactorily. Essentially, our objective is to determine these parameters such that $\hat{y}(t)$ is the optimal approximation to the measurements $y(t)$ in the least square sense.

Practically, continuous-time data are sampled at a constant sampling period T_s. If data are sampled at $t = \tilde{k}T_s, \tilde{k} = 0, ..., N-1$, then the discrete-time form for Eq. (6.1) is

$$\hat{y}(\tilde{k}T_s) = \sum_{i=1}^{n_p} D_i z_i^{\tilde{k}} \tag{6.2}$$

$$z_i = e^{\lambda_i T_s}, \ \tilde{k} = 0, ..., N-1 \tag{6.3}$$

where the complex number z_i is termed the discrete-time system pole, and N is the number of measurements. For simplicity, let $k = \tilde{k}T_s$, then $\hat{y}(\tilde{k}T_s)$ can be replaced with $\hat{y}(k)$.

System measurement $y(k)$ can be used to construct the linear prediction model (LPM) [161]

$$y(k) = a_1 y(k-1) + \cdots + a_{n_p} y(k-n_p) \tag{6.4}$$

The traditional PA consists of three fundamental steps. The first step is to determine coefficients $a_i, \ i = 1, ..., n_p$. This is paramount as the accurate estimation of residues and poles depends on the precision of these coefficients.

A matrix representation of sequential samples is constructed by expanding the LPM at various time instants, and coefficients a_i are acquired by inverting the matrix T in Eq. (6.5)

$$F = TA \tag{6.5}$$

$$F = [y(n_p), y(n_p+1), ..., y(N-1)]^T \tag{6.6}$$

$$T = \begin{bmatrix} y(n_p-1) & y(n_p-2) & \cdots & y(0) \\ y(n_p) & y(n_p-1) & \cdots & y(1) \\ \vdots & \vdots & \vdots & \vdots \\ y(N-2) & y(N-3) & \cdots & y(N-n_p-1) \end{bmatrix} \tag{6.7}$$

$$A = [a_1, a_2, ..., a_{n_p}]^T \tag{6.8}$$

In the second step, the corresponding characteristic equation can be derived from coefficients a_i. From these coefficients damping factor and frequency can be acquired after zeros z_i are attained according to Eq. (6.9) through factorizing the following polynomial

$$z^{n_p} - a_1 z^{n_p-1} - \cdots - a_{n_p-1} z - a_{n_p} = \prod_{i=1}^{n_p} (z - z_i) \tag{6.9}$$

Each continuous-time pole λ_i can be accessed from the corresponding discrete-time pole z_i. The zeros z_i appear only in the form of real numbers or complex conjugate pairs due to a_i are real in Eq. (6.9). Therefore, if z_i is completely real, then [180]

$$\lambda_i = \frac{\ln z_i}{T_s} \tag{6.10}$$

Otherwise, if z_i is a complex conjugate pair,

$$\begin{aligned} \lambda_i &= Re_i \pm jIm_i \\ Re_i &= \frac{\ln |z_i|}{T_s} \\ Im_i &= \frac{1}{T_s} \tan^{-1}\{\frac{z_{Ii}}{z_{Ri}}\} \end{aligned} \tag{6.11}$$

where $z_i = z_{Ri} \pm j \cdot z_{Ii}$.

In the last step, the residues are obtained through solving the following linear algebra equation

$$Y = \Pi D \tag{6.12}$$

$$Y = [y(0), y(1), ..., y(N-1)]^T \tag{6.13}$$

$$\Pi = \begin{bmatrix} 1 & 1 & \cdots & 1 \\ z_1^1 & z_2^1 & \cdots & z_{n_p}^1 \\ \vdots & \vdots & \vdots & \vdots \\ z_1^{N-1} & z_2^{N-1} & \cdots & z_{n_p}^{N-1} \end{bmatrix} \tag{6.14}$$

$$D = [D_1, D_2, ..., D_{n_p}]^T \tag{6.15}$$

Here, the Vandermonde matrix Π is constructed based on the zeros z_i of characteristic equation (6.9), and appears as a square matrix in the traditional PA. Normally, if zeros z_i of Eq. (6.9) appear in conjugate pairs, the corresponding D_i in Eq. (6.15) will also appear in conjugate forms.

Remark 1 The fundamental limitation of the PA lies in inverting the large matrices T in Eq. (6.7) and Π in Eq. (6.14) when a large number of measurements are available. For slow-varying systems, the estimation involves dealing with a large number of instantaneous measurements, which greatly exacerbate the difficulties in real-time implementation of the PA.

Remark 2 The LS exclusively deals with the measurements for a separate sliding window, and starts estimation without consideration of information in the previous data window. Therefore, estimation of instantaneous mean is subject to great changes when successive data windows are processed.

Remark 3 The manipulation of matrix inversion may suffer from singularity issues. Ill-conditioned matrices may occur when inverting the T and Π, which would cause the PA to fail. Therefore, there is a need to modify the PA to deal with the general oscillating systems.

6.3 The Modified Prony Analysis

6.3.1 The Proposed Recursive Prony Analysis

To remedy the weakness of PA, the following factors are significant:

1. How to obtain accurate and reliable model parameters when new measurements are collected?
2. How to carry forward system information for successive data windows to achieve an accurate estimation?
3. How to reduce computational burden to accomplish a rapid online estimation of the mean deck height to reduce hover period of the RUAV?

A possible solution to the first question is to employ the FFRLS as it can gradually discard the effect of old measurements and highlight the contribution of the most recent measurements.

To implement the FFRLS, the vector of lagged measured data

$$\varphi_p(t) = [y(t-1), ..., y(t-n_p)]^T \tag{6.16}$$

and coefficient vector

$$\hat{\theta}_p(t) = [\hat{a}_1(t), ..., \hat{a}_{n_p}(t)]^T \tag{6.17}$$

up to time instant t are introduced. Coefficients $\hat{a}_1(t), ..., \hat{a}_{n_p}(t)$ are updated recursively to approach the real values $a_1, ..., a_{n_p}$. The LPM can be written in a more compact form

$$y(t) = \varphi_p^T(t)\hat{\theta}_p(t) \tag{6.18}$$

where $\hat{\theta}_p(t)$ contains the coefficients to be determined. The loss function for FFRLS is defined as [139, 181]

$$J(\hat{\theta}_p) = \sum_{j=1}^{t} \lambda^{t-j}[y(j) - \varphi_p^T(j)\hat{\theta}_p(j-1)]^2 \tag{6.19}$$

Here, forgetting factor is denoted by parameter λ.

The FFRLS can be implemented recursively by [138, 139]

$$\hat{\theta}_p(t+1) = \hat{\theta}_p(t) + K_p(t+1)[y(t+1) - \varphi_p^T(t+1)\hat{\theta}_p(t)] \tag{6.20}$$

$$K_p(t+1) = P_p(t)\varphi_p(t+1)[\lambda + \varphi_p^T(t+1)P_p(t)\varphi_p(t+1)]^{-1} \tag{6.21}$$

$$P_p(t+1) = [P_p(t) - K_p(t+1)\varphi_p^T(t+1)P_p(t)]/\lambda \tag{6.22}$$

$$\hat{\theta}_p(0) = 0 \quad P_p(0) = \Gamma I \tag{6.23}$$

Here, matrix $P_p(t+1)$ is referred to as error covariance matrix, matrix $K_p(t+1)$ denotes the updating matrix, and Γ is a large positive number.

Remark 4 As there are $2n$ parameters in Eq. (6.1), the number of measurements N should satisfy $N \geq 2n$. To quantify suitable length of the data window N, we employ the signal-to-noise ratio (SNR) [154]

$$SNR = -20\log_{10}\frac{\|\hat{y} - y\|}{\|y\|} = -20\log_{10}\frac{\sqrt{\sum_{k=1}^{N} e^2(k)/N}}{\sqrt{\sum_{k=1}^{N} y^2(k)/N}} \tag{6.24}$$

where $\|\cdot\|$ is root-mean-square norm, and $e(\cdot)$ the estimation error. SNR is used to evaluate the match accuracy between the measured and estimated data. The number of samples is considered to be sufficient if SNR is larger than the predefined limit of above 20 dB.

Regarding the second question, the error covariance $P_p(t)$ and model coefficients $\hat{\theta}_p(t)$ are initialized once for the first data window, then the FFRLS carries them forward as the sliding window moves to the next one. This implies the model coefficient vector $\hat{\theta}_p(t)$ is slow-varying, and its components for adjacent data windows are closely related. Therefore, error covariance matrix $P_p(t)$ and estimation vector $\hat{\theta}_p(t)$ carry forward system information to improve estimation performance.

The third step of PA can be followed according to Eq. (6.12)-(6.15) once zeros of characteristic equation are found. Similarly, the number of measurements is more than that of the coefficients to be estimated, and recursive least square (RLS) can be used to estimate the magnitude D_i. However, the vector of lagged measured data $\varphi_p(t)$ in Eq. (6.16) should be replaced with

$$\mu(t) = [z_1^{t-1}, ..., z_{n_p}^{t-1}]^T \tag{6.25}$$

which corresponds to row components in Eq. (6.14). It should be noticed that the vector $\mu(t)$ at different time instants t varies significantly. Therefore, carrying forward the error covariance matrix and the estimation vector is not proper in this step, as the vector $\mu(t)$ is not always slow-varying. Indeed, simulation results show that the estimation performance decreases if the error covariance matrix and the estimation vector are carried forward owing to the fact that there are actually large discrepancies between the error covariance and the model coefficients at different time instants.

6.3.2 Determination of Model Order

Regarding the third question in Section 6.3.1, computational burden is significantly affected by the choice of model order n_p. Some available information criteria are AIC [140] and its variant final prediction error (FPE) [153], BIC [141], i.e.,

$$AIC(n_p) = \log \sigma^2 + \frac{2n_p}{N} \tag{6.26}$$

$$BIC(n_p) = \log \sigma^2 + \frac{n_p \log N}{N} \tag{6.27}$$

$$FPE(n_p) = \frac{N + n_p + 1}{N - n_p - 1}\sigma^2 \tag{6.28}$$

where summed squared error (SSE)

$$\sigma^2 = \sum_{k=0}^{N-1} [y(k) - \hat{y}(k)]^2 \tag{6.29}$$

AIC and BIC aim to make a trade-off between estimation errors accumulated and model complexity, and the optimal order is determined when they appear in a convex trend and reach the minimum. However, in our case, AIC and BIC consistently decrease when model order becomes large, and the estimation performance does not deteriorate. Underlying this fact is that the extra exponential terms are actually trying to fit the noise effect [153]. Therefore, a Prony model with order much larger than the true order is still an option for estimation purposes. However, extremely large model order consumes huge memory allocations of the flight computer. For example, 247MB is required when model order is 50, and 947MB when model order is 100. Therefore, it is necessary to make a balance between model match precision and available computational capacity of the flight computer.

The choice of proper model order is subjective according to various scenarios [153]. Practically, the model order should be selected such that a trade-off can be achieved between estimation accuracy and computational burden. In our case, FPE is a feasible option to choose the model order. Since sliding widow length N is much larger than model order n_p in our case, the proper model order can be found out only by checking the SSE

$$SSE = \sum_{k=0}^{N-1} [y(k) - \sum_{i=1}^{n_p} D_i e^{\lambda_i k}]^2 \tag{6.30}$$

The estimation performance using the SSE is close to the best available approaches which are based on maximum likelihood or on the use of eigenvector or singular value decompositions [182].

The order selection procedure consists of three steps:

1. Set the predicted model order R_N which is larger than the maximum number of model order which is expected;

2. Determine the model order n_l out of predicted order R_N such that there is a significant drop in SSE when the LPM is constructed by n_l exponential terms. This gives a lower bound of acceptable model order;

3. Calculate the computational burden when order is larger than n_l. The proper model order is chosen when a balance between the match accuracy and the computational burden is achieved.

Remark 5 In practice, if the predefined curve-fitting match accuracy is satisfied, the Prony model with small order is preferred to reduce the computational burden. In situations where computational burden is a minor factor, the proper model order can be found out when there is a significant drop in SSE.

6.3.3 Dominant Mode Selection Criterion

The proposed dominant mode selection criterion begins with defining a suitable threshold. The coefficients D_i with respect to the poles within the threshold are taken as dominant residues. The threshold is chosen according to the following criterion, as illustrated in Fig. 6.1

1. Choose the pole with its negative real part closest to the imaginary axis, which corresponds to the smallest horizontal distance d;
2. The threshold L_p is 5 times of the horizontal distance d;
3. The width of the box threshold W_p depends on the magnitude of rounding errors, which takes a very small value ($O(e^{-8})$).

Remark 6 Poles with horizontal distance less than L_p are considered to be dominant. The closest distance d can be found out following the proposed PA. Here, the threshold L_p is chosen from the viewpoint of reducing the order of a high-order dynamic system [183]. In practice, poles are considered to determine system response when their negative real parts are within 5 times of the smallest real part. In our case, trend of the ship deck motion can be captured by combining the slow-varying modes. Poles with the real parts far away from the imaginary axis indicate the corresponding system responses decay quickly and cannot be used to extract the trend. When determining the dominant poles, the PA sometimes identifies them with the complex parts very close to real axis and not appearing in conjugate forms. This results from the rounding errors of the computer calculation. These poles should be included as dominant poles. For the deck motion, it is shown in simulations that $W_p = 1e^{-8}$ is a proper threshold.

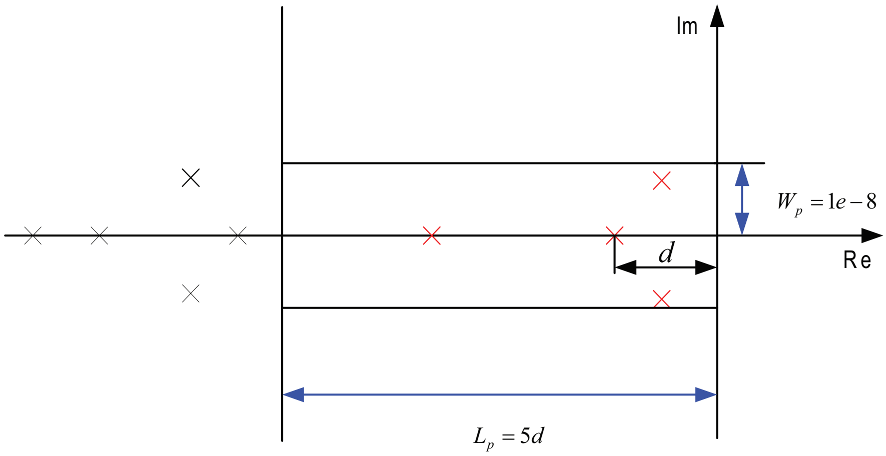

Figure 6.1. Threshold to choose dominant poles

The system trend $\bar{y}_{ins}$ can be expressed as

$$\bar{y}_{ins} = \sum_{i=1}^{W} B_{Di} e^{\lambda_{Di}(N-1)T_s} \tag{6.31}$$

where λ_{Di} is dominant pole, and B_{Di} is the corresponding residue. The number of dominant poles is denoted by W.

The flow chart for online estimation of the mean height of deck displacement is depicted in Fig. 6.2. The proposed approach firstly collects enough samples. Then, model order and parameters are specified using the FFRLS, and poles of the characteristic equation are computed. Afterwards, the corresponding residues are calculated using the RLS. The instantaneous mean is obtained after selecting the dominant poles and residues.

6.4 Simulation Results and Analysis

6.4.1 Model Mode Identification for Systems with Known Modes

In this section, performance of the proposed procedure is investigated for the purpose of applications. We aim to check the performance of the proposed PA when noise and vibration effect exist in the measured data. Thus, we firstly employ the measurements with known model modes so that a comparison can be made. A $5th$-order damping system is constructed with known model modes: $\lambda_i = -1.5, \ -3 \pm$

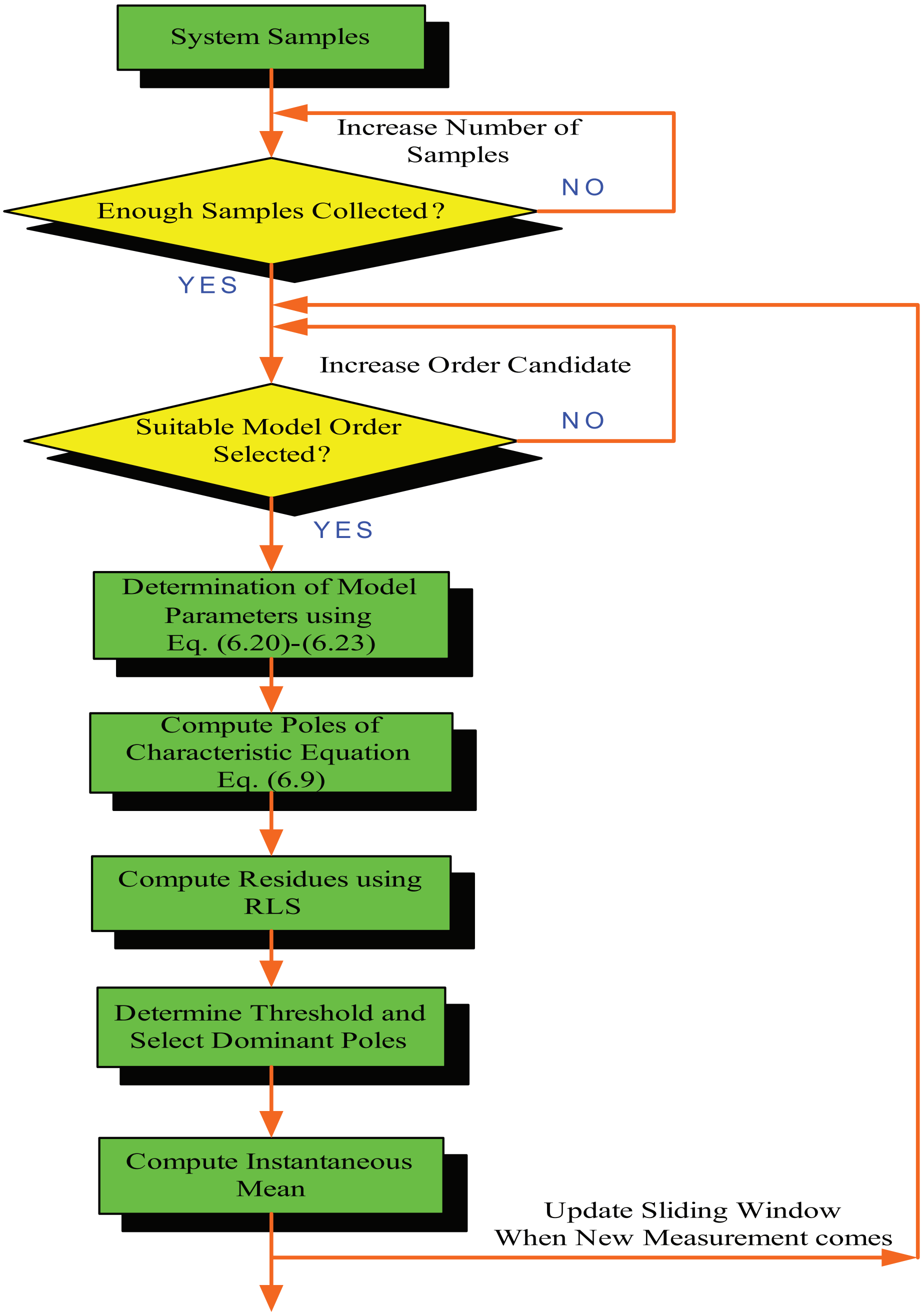

Figure 6.2. Flow chart for extracting instantaneous mean

$j4$, $-3.5 \pm j4.5$. The data generated by the known dynamic system are employed to evaluate how well the proposed procedure is able to extract model modes.

The proposed estimation procedure is carried out for the noise-free data generated by the known model. Sliding windows are constructed for FFRLS implementations. The proper model order is sought to be identified by minimizing the SSE. As is shown in Fig. 6.3, SSE takes the value of $2.7472e^{-4}$ when model order $n = 4$, and $5.4805e^{-14}$ when $n = 5$. SSE is found to be around $O(e^{-16})$ when a larger order is selected, and there is no significant decrease in SSE when model order increases. Therefore, model order $n = 5$ can be effectively identified by evaluating the SSE.

To verify the efficiency of estimating model poles using the proposed procedure, 30 groups of data are generated with 10 samples in each group. Figures 6.4-6.6 show the distributions of poles for different model modes, in which the estimated poles are very close to the real ones. The average of the estimated poles is accurate, and corresponding standard deviations are remarkably small. It is seen that the suggested PA is capable of estimating system poles with a high accuracy for noise-free data.

Measurement noise is an inevitable factor significantly affecting estimation performance of PA in the real applications. It should be remembered that PA is inherently vulnerable to measurement noise [153]. The sensitivity analysis of PA indicates that estimation performance would degrade even if the true model is assigned when low-level measurement noise is present [153]. Here, we evaluate the tolerable noise level of the proposed PA. It is illustrated in Table 6.1 that the proposed PA is able to capture model modes for high SNR when white noise is present at a sampling rate of 10 Hz, and model modes are found out effectively when SNR is above 160 dB. Given white noise with slow sampling rate (5 Hz), our PA approach functions well even for lower SNR. It is seen from Table 6.2 that model modes can be determined with high accuracy when SNR is above 120 dB. This proves that the suggested PA works efficiently for measurements with small sampling frequency.

For maritime landing operations, sensor measurement noise on the RUAV takes sinusoidal forms primarily due to vibration effects. Sinusoidal noise with progressively increasing levels is added to check our algorithm. For the Vario helicopter, the main rotor speed is 14 Hz. Higher frequencies are attenuated by the vibration isolation scheme installed on the helicopter. Lower frequencies cannot be isolated mechanically. Thus, the frequency of the vibration effect is chosen to be 14 Hz to test the proposed algorithm in the considered application, and measurements are sampled every 0.2 s. It is seen from Table 6.3 that for SNR over 100 dB, our method

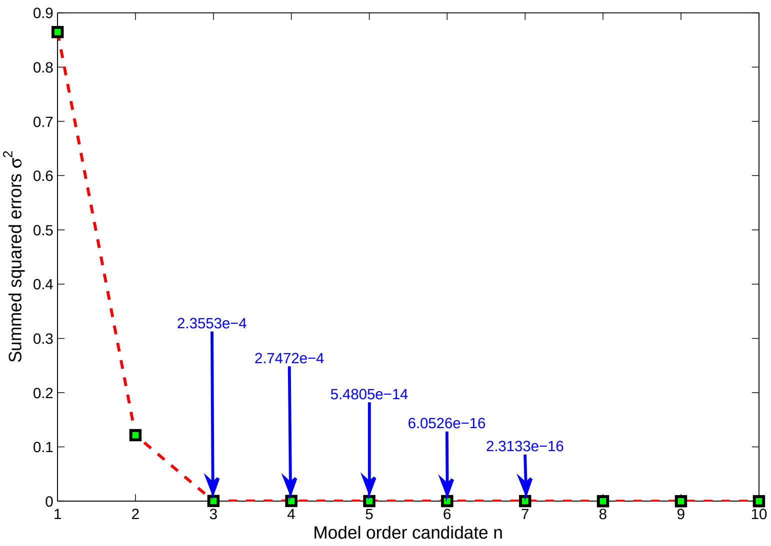

Figure 6.3. Summed squared errors versus model order candidates

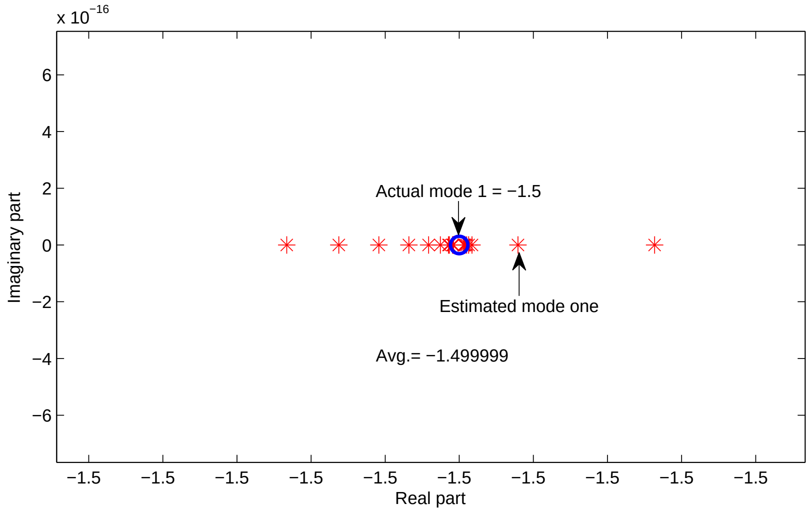

Figure 6.4. Estimation of the first mode

can give promising results consistently. However, identification results degrade for lower SNR. In our case, an EKF has been designed to give a smooth estimation of deck position. The EKF attenuates the sinusoidal noise effects greatly, and makes the proposed PA work well.

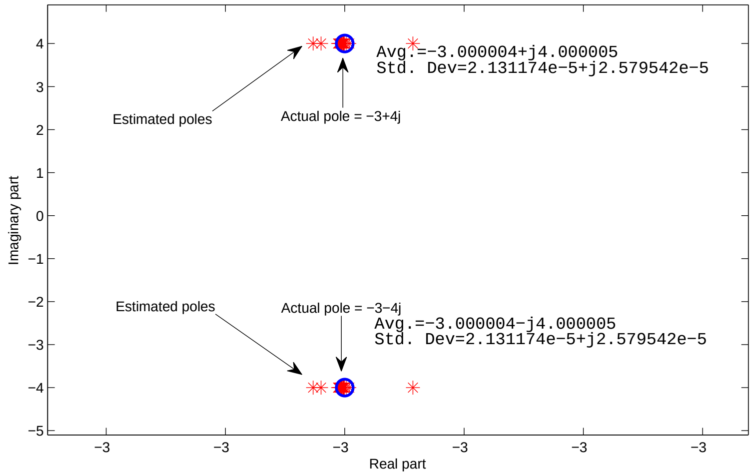

Figure 6.5. Estimation of the second mode

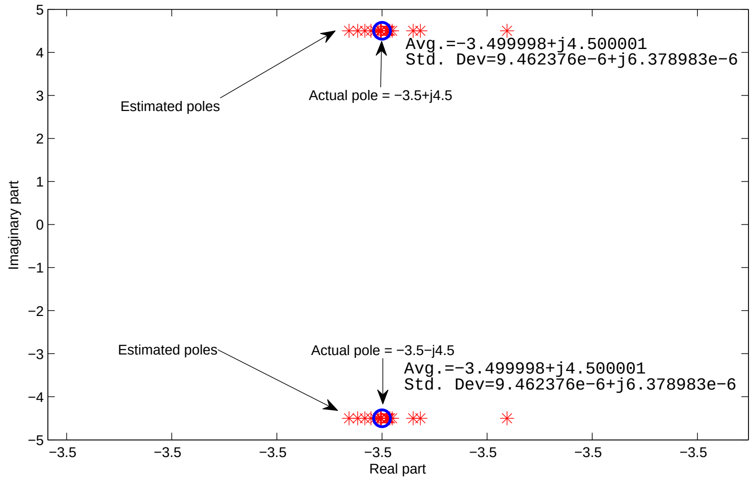

Figure 6.6. Estimation of the third mode

Table 6.1. Identification of model modes when sampling frequency of white noise is 10 Hz

SNR	-1.5	$-3 \pm j4$	$-3.5 \pm j4.5$
140	-1.3974	$-3.6680 \pm j5.8258$	$-3.5628 \pm j4.2057$
150	-1.4511	$-3.3375 \pm j4.8869$	$-3.4072 \pm j4.1710$
160	-1.4816	$-3.1517 \pm j4.1274$	$-3.4277 \pm j4.5588$
170	-1.4938	$-3.0444 \pm j4.0459$	$-3.4809 \pm j4.5143$
180	-1.4980	$-3.0137 \pm j4.0149$	$-3.4943 \pm j4.5042$

Table 6.2. Identification of model modes when sampling frequency of white noise is 5 Hz

SNR	-1.5	$-3 \pm j4$	$-3.5 \pm j4.5$
100	-1.4440	$-1.6110 \pm j4.1712$	$-3.5824 \pm j4.3023$
110	-1.4837	$-2.5649 \pm j4.1563$	$-3.5188 \pm j4.3680$
120	-1.4950	$-2.8750 \pm j4.0665$	$-3.4924 \pm j4.4446$
130	-1.4983	$-2.9607 \pm j4.0232$	$-3.4949 \pm j4.4808$
140	-1.4995	$-2.9885 \pm j4.0070$	$-3.4982 \pm j4.4943$

Table 6.3. Identification of model modes for sinusoidal vibration effect (14 Hz)

SNR	-1.5	$-3 \pm j4$	$-3.5 \pm j4.5$
80	-1.5504	$-2.9985 \pm j3.1858$	$-3.6361 \pm j4.4016$
90	-1.5116	$-3.0012 \pm j3.7705$	$-3.5732 \pm j4.4831$
100	-1.5036	$-2.9987 \pm j3.9230$	$-3.5281 \pm j4.4979$
110	-1.5011	$-2.9993 \pm j3.9748$	$-3.5096 \pm j4.4998$
120	-1.5004	$-2.9998 \pm j3.9914$	$-3.5033 \pm j4.5000$
130	-1.5001	$-2.9999 \pm j3.9975$	$-3.5010 \pm j4.5000$

6.4.2 Extracting Mean Height of Real Deck Displacement

The real data of deck displacement motion were collected by the onboard inertial measurement unit for ANZAC warship operating in a harsh sea environment. The ANZAC ship is able to embark a multi-role Sikorsky S-70B-2 Seahawk helicopter. Therefore, ship motion data collected from ANZAC are representative and provide insight into displacement motion of the landing deck. Pitch motion θ_s at the CG of the ship, collected every 0.1 s, is multiplied by the moment arm $L_{deck} = 67.7$ m to produce the local deck motion. Here, the deck displacement is expressed as

$$Z_{deck} = Z_{CG} + Rot_{3\times3}\begin{bmatrix} 0 \\ 0 \\ L_{deck} \end{bmatrix} \tag{6.32}$$

with rotation matrix

$$Rot_{3\times3} = \begin{bmatrix} c_{\theta_s}c_{\psi_s} & s_{\phi_s}s_{\theta_s}c_{\psi_s} - c_{\phi_s}s_{\psi_s} & s_{\phi_s}s_{\psi_s} + c_{\phi_s}s_{\theta_s}c_{\psi_s} \\ c_{\theta_s}s_{\psi_s} & s_{\phi_s}s_{\theta_s}s_{\psi_s} + c_{\phi_s}c_{\psi_s} & c_{\phi_s}s_{\theta_s}s_{\psi_s} - s_{\phi_s}c_{\psi_s} \\ -s_{\theta_s} & s_{\phi_s}c_{\theta_s} & c_{\phi_s}c_{\theta_s} \end{bmatrix} \tag{6.33}$$

where $c_{(\cdot)} = \cos(\cdot)$ and $s_{(\cdot)} = \sin(\cdot)$, Z_{CG} is heave at the CG. Here, pitch motion is denoted by θ_s, yaw motion ψ_s, and roll motion ϕ_s.

Table 6.4. CPU running time ($N = 600, CPU = 3.2$ GHz$, RAM = 2$ GB)

	Running Time (s)	Model Order	Running Time (s)	Model Order
Group One	114.3	7	261.4	25
	125.4	9	279.3	30
	131.9	11	305.4	35
	146.9	13	340.7	40
	211.3	15	397.1	45
	250.7	20	543.1	50
Group Two	89.3	7	215.5	25
	95.2	9	249.0	30
	155.6	11	286.7	35
	152.1	13	349.4	40
	188.9	15	404.2	45
	199.8	20	521.3	50

We firstly seek to collect adequate length of deck displacement data. The length of the data window is chosen based on the SNR in Eq. (6.24). Given the predefined SNR level SNR=35 dB, it is found that 600 measurements are required. The estimated deck trend for different window width is illustrated in Fig. 6.9 and 6.11. Due to the great curve-fitting errors, the estimated deck trend suffers from evident oscillations and deck trend is not well captured when $N = 300$. It is seen that the slow-varying trend are obtained when $N = 600$, and there is no significant performance improvement when N is chosen larger. Therefore, the window width is set $N = 600$. The model order is chosen based on the SSE shown in Fig. 6.7 and the computational burden depicted in Table 6.4. It is noticed that the SSE decreases slightly when $n > 13$. For $n > 13$, although there is a slight decrease in SSE, the running time increases greatly. For $n < 13$, the SSE becomes large. Therefore, the order $n = 13$ is selected to make a trade-off between match accuracy and computational burden.

Once the proper order is determined, we start estimating the poles and residues, then the dominant residues will be sought. The deck trends are given in Fig. 6.8 and Fig. 6.10 for two groups of real deck data (red dotted). Since measurement noise is always present, an EKF is designed to smooth out the deck motion measurements. This enables the proposed method to deal with measurements with large noise level, thus improving the robustness. It is seen that the estimated deck motion (green solid) is smoother than the noisy measurements (black solid) and makes it easier for the PA to handle. The estimated deck motion using the proposed PA is shown on the same graphs (blue dotted), it is seen that data produced by the Prony model match the measurements well. The standard deviations are 0.82 cm and 0.91 cm for Fig. 6.8 and Fig. 6.10. Practically, the UAV is supposed to hover 30 seconds-2 minutes before landing operation is triggered. Based on the proposed PA, the deck trend can be estimated about 1 minute, and sufficient time is given for trajectory planning and controller design.

6.5 Summary

In this chapter a recursive procedure is outlined for estimating the mean height of deck displacement. A modified version of PA is proposed with model order identified by minimizing squared estimation errors and model coefficients determined using the FFRLS. Also, the dominant modes are found out based on a box selection criterion. Simulation results justify the suitability of our procedure for analyzing real ship motion data.

The estimation efficiency of the proposed PA can be enhanced if smoother measurements are available. In real-time applications, noisy deck motion measurements can be filtered using the EKF before being processed by the proposed PA.

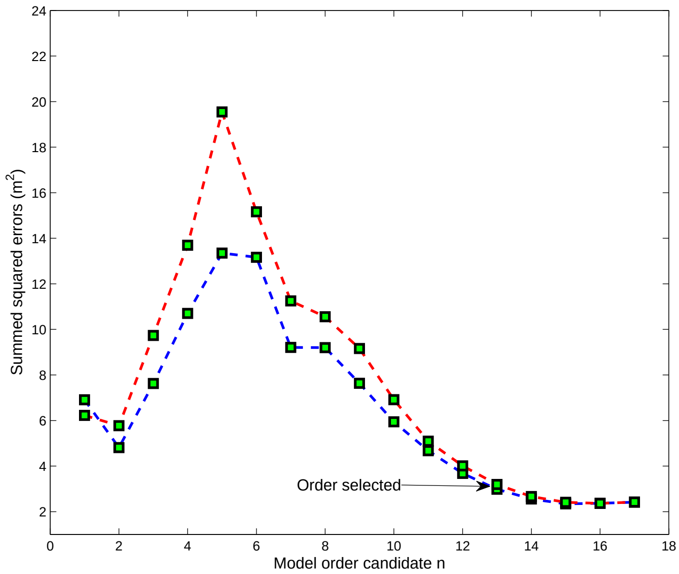

Figure 6.7. Summed squared errors for different model orders

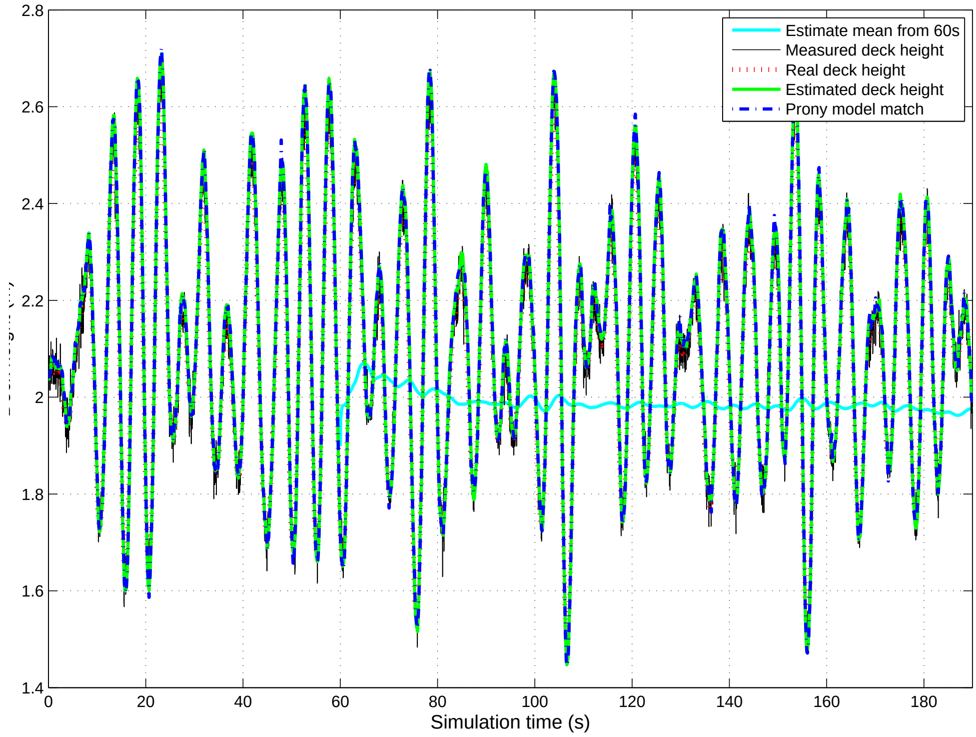

Figure 6.8. Extracting mean height of real deck displacement (group 1)

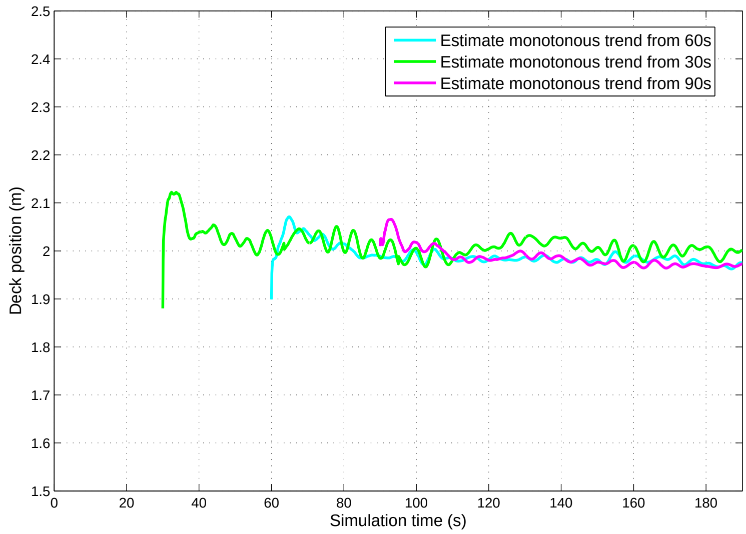

Figure 6.9. Comparison of estimation results using different data length (group 1)

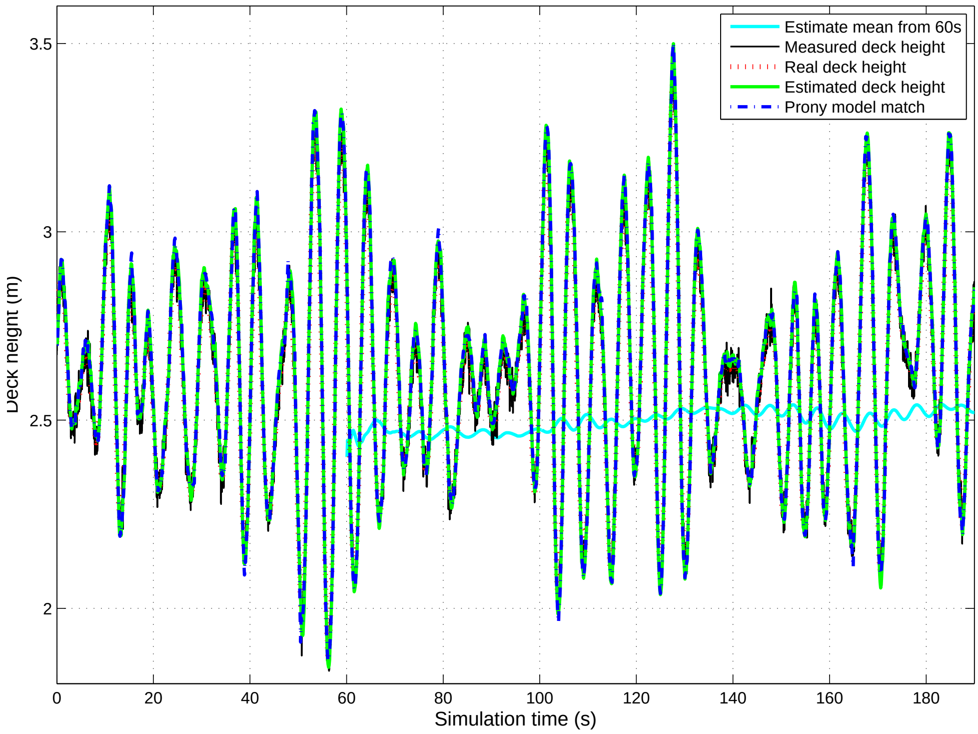

Figure 6.10. Extracting mean height of real deck displacement (group 2)

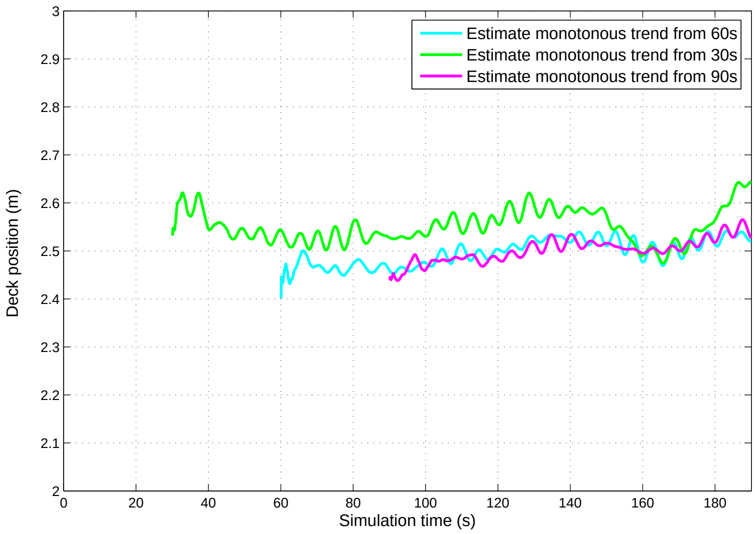

Figure 6.11. Comparison of estimation results using different data length (group 2)

Chapter 7

A Feedback-feedforward Controller for RUAVs Operating in a Gusty Environment

This chapter presents a practical scheme to control heave motion for hover and automatic landing of a RUAV in the presence of strong horizontal gusts. A heave motion model is constructed for the purpose of capturing dynamic variations of thrust due to horizontal gusts. Through construction of an effective gust estimator, a feedback-feedforward controller is developed which uses available measurements from onboard sensors. The proposed controller dynamically and synchronously compensates for aerodynamic variations of heave motion, enhancing disturbance-attenuation capability of the RUAV. Simulation results justify the reliability and efficiency of the suggested gust estimator. Flight tests conducted on our Eagle helicopter verify suitability of the proposed control strategy for small RUAVs operating in a gusty environment.

7.1 Introduction

There are notable variations of ship air-wake due to ship's superstructure and ambient surface conditions when a RUAV approaches the landing deck [184]. Thus, the RUAV operates in a partial ground effect condition where both the magnitude of the rotor flow and the inflow distribution over the rotor disk vary greatly [185]. This phenomenon results in a considerable change in the aerodynamic loading of the rotor system, which affects the RUAV control margins, autopilot workload and power margins [32]. Also, landing tasks may occur in an adverse environment where gusts come from any direction relative to the RUAV. On such occasions, it is impractical to ensure a successful landing through operation of ship movement. An alternative approach is to acquire the characteristics of turbulent gusts based on available measurements, and design an active controller to attenuate gust effects.

Therefore, investigation on wind gusts is influential. The main difficulty in estimating gusts results from the complex mechanism of vortex dynamics near the ship deck. Previous study [31] shows that the air-wake turbulence caused by high-speed wind greatly impairs controllability of the RUAV, and leads to exorbitant control efforts required to avoid accidents. In rough sea states where there are variations of horizontal gusts both in direction and in level, random wind gusts unavoidably lead to abrupt change in thrust level. Therefore, dynamic performance of the RUAV is deteriorated, and pure feedback driven controllers fail to stabilize the heave motion. This difficulty justifies the need for a controller with gust attenuation property.

At present, numerous papers have addressed the effect of gusts on fixed-wing aircraft. Based on a linearized model, Aouf *et al.* [123] designed the $\mathcal{H}_\infty$ controller to reduce effect of gusts on aircraft vertical motion using a Dryden gust model. Buffington *et al.* [186] presented a minimal-order robust controller to attenuate lateral gusts of an aircraft. A spatial sliding mode controller was proposed by Jackson *et al.* [187], in which wind disturbances with known bounds were explicitly considered in their UAV model. However, it may be challenging to set upper bounds on wind gusts in real scenarios due to the complex mechanism of turbulence. In contrast, investigation on helicopters in a turbulent environment has received less attention than their fixed-wing counterparts. Recently, Cheviron *et al.* [188] proposed a robust guidance and control scheme for an autonomous helicopter in the presence of wind gusts. A high-gain observer was used to reconstruct the unknown inputs, and time derivatives of the inputs were assumed to be uniformly bounded. This observer requires prior information on bounds of the unknown inputs. Also, construction of the uncertainties/disturbances requires solving the Lyapunov equation online, which makes it difficult to be implemented in real-time applications. Martini *et al.* [189] addressed control of a model-scale helicopter under wind gusts. The disturbances in their paper were vertical wind gusts with typical levels less than 1 m/s. In our case, we concentrate on horizontal gusts with a typical level of 10 m/s, since the main factor influencing thrust in hover comes from horizontal gusts, particularly close to the ground where the vertical gust component is near zero.

There are several limitations of the PD controller when applied for height control. The PD controller requires high control gains to respond to gust disturbance rapidly, and large gains would lead to system instability when operational conditions of the nonlinear system change. Also, the PD controller cannot provide synchronous compensation, and corrective action is performed after the height deviates from the desired setpoint. In contrast, a PD controller working in parallel with a feedforward controller can compensate for gust influence synchronously, whilst keeping PD gains within a reasonable range for feasible implementation. Therefore, by constructing a gust estimator based on available measurements, the amount of collective pitch required to compensate for gusts can be computed, and put into the feedforward loop to attenuate gust influence.

The present study begins with establishing a dynamic relationship between gusts and thrust. A gust estimator is constructed to estimate horizontal gust levels in the presence of sensor errors and measurement errors. A feedback-feedforward controller is presented to compensate for side effects from horizontal gusts. Simulation results demonstrate that our gust estimator can efficiently estimate gust levels, and the proposed controller is able to attenuate impact of the horizontal gusts and stabilize heave motion of the RUAV in a gusty environment. Experimental tests have confirmed the validity of this method.

7.2 Heave Motion Dynamics under Atmospheric Disturbances

Heave motion dynamics of the RUAV can be described by

$$\dot{w} = \frac{M_a g - T_{mr}}{M_a} \tag{7.1}$$

$$\dot{z}_b = w \tag{7.2}$$

Here, w is vertical velocity, z_b vertical distance, and M_a mass of the RUAV. The main rotor thrust T_{mr} is vulnerable to fluctuations when gusts V_t^2 occur. To design a proper controller reducing the detrimental effect, we begin with analysis of horizontal wind gusts, and then investigate thrust variations due to the gusts.

The oncoming air stream velocity V_∞ consists of two components, V_t and V_n shown in Fig. 7.1, which are tangential and perpendicular to the TPP,

$$V_\infty^2 = V_t^2 + V_n^2 \tag{7.3}$$

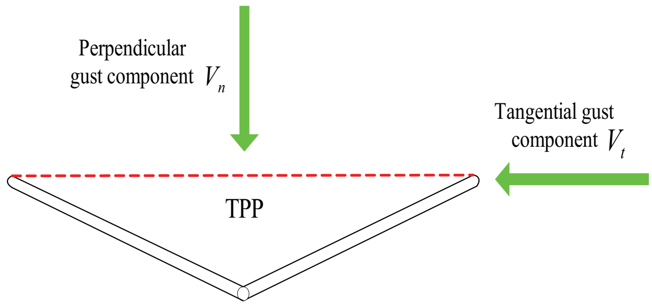

Figure 7.1. Decomposition of horizontal gusts acting on the main rotor

The relationships between air stream velocity components and velocity components of the RUAV are described by [111]

$$V_t^2 = u^2 + v^2 \tag{7.4}$$

$$V_n = (a_1 + i_s)u - b_1 v - w \tag{7.5}$$

where the main rotor shaft angle is denoted by i_s.

Since flapping angles rarely exceed 10 degrees during normal flight [111, 114], compared with the perpendicular component V_n, it is seen from Eq. (7.4)-(7.5) that the tangential component V_t is dominant in a gusty environment, and referred to as gusts in the following context. The perpendicular component V_n can be approximated by vertical velocity w with opposite sign due to the small quantities of (a_1+i_s) and b_1 ($a_1, b_1 < 5^0, i_s < 10^0$) [111, 114].

The main rotor thrust (T_{mr}) in a conventional helicopter is generally controlled using the *collective pitch* control with symbol θ_{col}. The collective pitch controls the mean angle of attack of the rotor blades and hence the lift that is generated. The change in collective pitch is done through a series of mechanical linkages, and the amount of movement in the collective lever determines the amount of the blade pitch change.

The thrust equation (3.23) in Chapter 3 can be rearranged into

$$V_i = 2\Omega_{mr} R_b [\frac{\theta_{col}}{3}(1 + \frac{3V_t^2}{2\Omega_{mr}^2 R_b^2}) - \frac{T_{mr}}{B_t}] - V_n \tag{7.6}$$

where $B_t = 0.5\rho a_l N_b A_b (\Omega_{mr} R_b)^2$.

Another formula is needed to solve for the unknowns V_i and T_{mr}. We use Glauert's formula [110–112]

$$V_i^2 = \sqrt{(\frac{\hat{V}^2}{2})^2 + (\frac{T_{mr}}{2\rho A_d})^2} - \frac{\hat{V}^2}{2} \tag{7.7}$$

where

$$\hat{V} = \sqrt{V_t^2 + (V_n + V_i)^2} \tag{7.8}$$

The resultant velocity $\hat{V}$ is employed. The formula is reported to be true for all loading distributions on occasions when high speed gusts are encountered [112]. Equations (7.6)-(7.8) are coupled nonlinear equations which must be solved numerically to find the estimated gusts.

7.3 Development of a Gust Estimator

7.3.1 Design of a Filter to Reduce Sensor Errors

Vibration Effects in Accelerometers

Vibration occurs due to dynamic forces resulting from differences in distribution of aerodynamic loads, fuselage fluctuation, and inertial forces caused by the blade flapping and lagging motion [112]. Mechanical isolation is a feasible solution to reducing the vibration. In our project, eight elastomeric isolators are installed to prevent the autopilot and inertial sensors from damaging vibration. However, physical isolation of accelerometers cannot eliminate vibration effects to an acceptable level for control purposes, and acceleration sensors are frequently subject to simultaneous noise yielded by vibration. Based on measurements on the Eagle, the periodic vibration experienced by the vertical accelerometer takes the form of $A_m \sin(\omega_m t)$ with the amplitude A_m of 2 m^2/s^2 and frequency ω_m of 20 Hz.

Zero Drift in Accelerometers

Zero drift is one of the intrinsic errors in accelerometers, and is a significant source of error in the lower precision micro-electro-mechanical-system sensors typically used in small unmanned helicopters. The zero drift is usually strongly influenced by thermal effects, and is likely to change greatly according to variations of temperature in diverse operational environments.

Measurement Error in Vertical Velocity

Measured vertical velocity contaminated by sensor errors also impairs performance of the gust estimator. The measurement error is considered as white noise with a normal distribution.

Due to undesired contamination from different errors mentioned above, these measurements cannot be directly utilized to develop the gust estimator. The moving average filters (MAFs) are employed to smooth out the measurements taking the form

$$c_{af}(i) = \frac{1}{N_0}\sum_{k=0}^{N_0-1} c_{bf}(i-k), \tag{7.9}$$

where c_{bf} can be noisy a_z, w, or θ_{col}, and c_{af} can be filtered acceleration $a_{z\text{-}f}$, velocity w_f, or collective pitch $\theta_{col\text{-}f}$. N_0 denotes the number of neighboring data points. The MAFs serve when enough data points N_0 are stored in computer memory.

7.3.2 Implementation of the Gust Estimator

The bisection search method requires that the equation should be expressed in terms of only one unknown variable. By substituting Eq. (7.6) and Eq. (7.8) into Eq. (7.7), we eliminate V_i and end up with an equation involving the single unknown V_t^2. We then need to solve the resulting equation $f(V_t^2) = 0$ where $f(V_t^2)$ is given by Eq. (7.10):

$$f(V_t^2) = \sqrt{\frac{[V_t^2 + (V_n + V_i)^2]^2}{4} + (\frac{M_a a_z}{2\rho A_d})^2} - \frac{V_t^2 + (V_n + V_i)^2}{2} - V_i^2 \tag{7.10}$$

the estimated gusts $\hat{V}_t^2$ can be obtained using the bisection algorithm depicted in Fig. 7.2. The bisection algorithm has been explained in Section 3.4.3.

The procedure for estimating the gust levels $\hat{V}_t^2$ and corresponding induced velocity $\hat{V}_i$ is shown in Fig. 7.3. Firstly, MAFs are adopted with proper window width to filter measured acceleration, velocity and collective pitch. Afterwards, through setting a suitable searching scope and an error tolerance, we can solve the dynamic equations of heave motion (7.1)-(7.2) to acquire estimated gusts $\hat{V}_t^2$ and induced velocity $\hat{V}_i$ using the bisection search method.

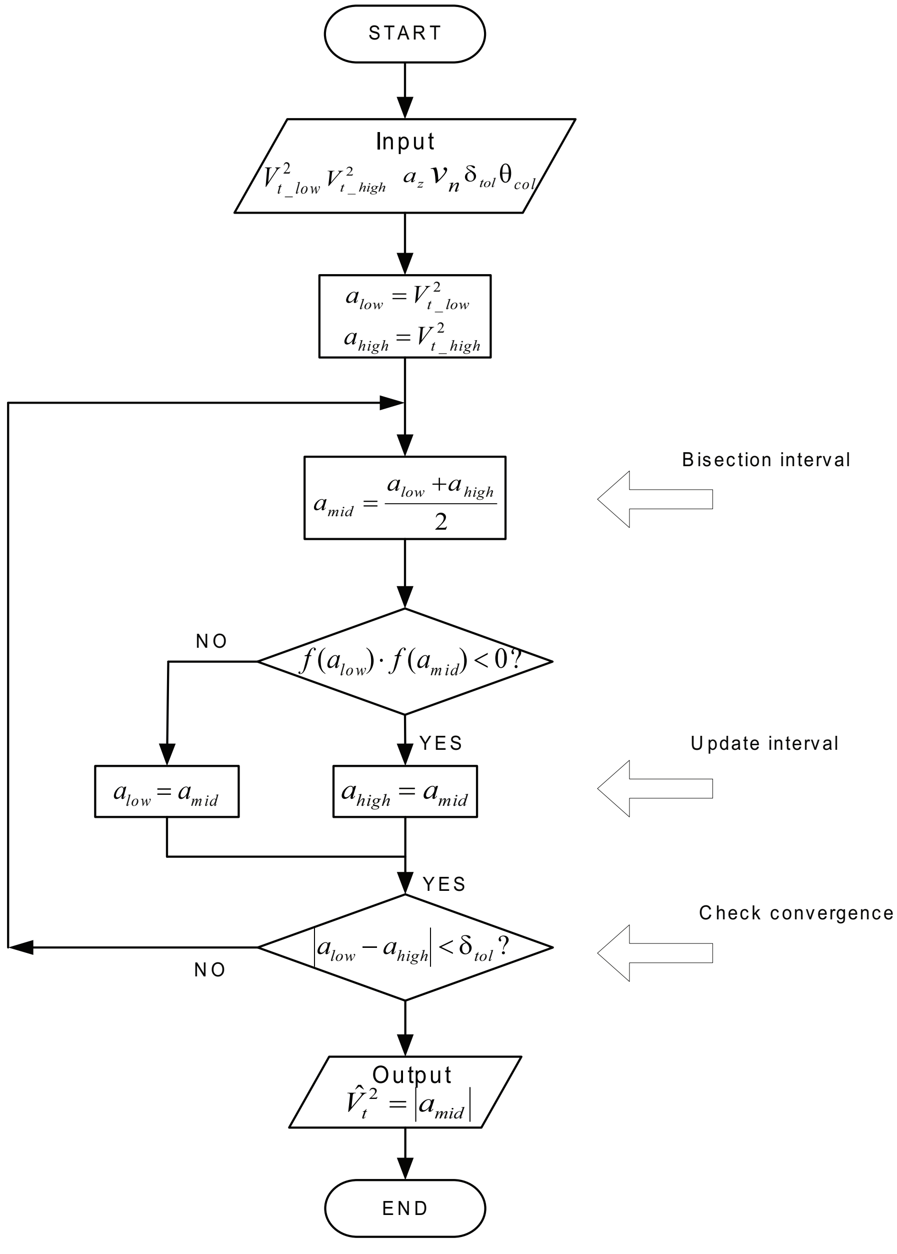

Figure 7.2. Flow chart to compute the estimated gusts

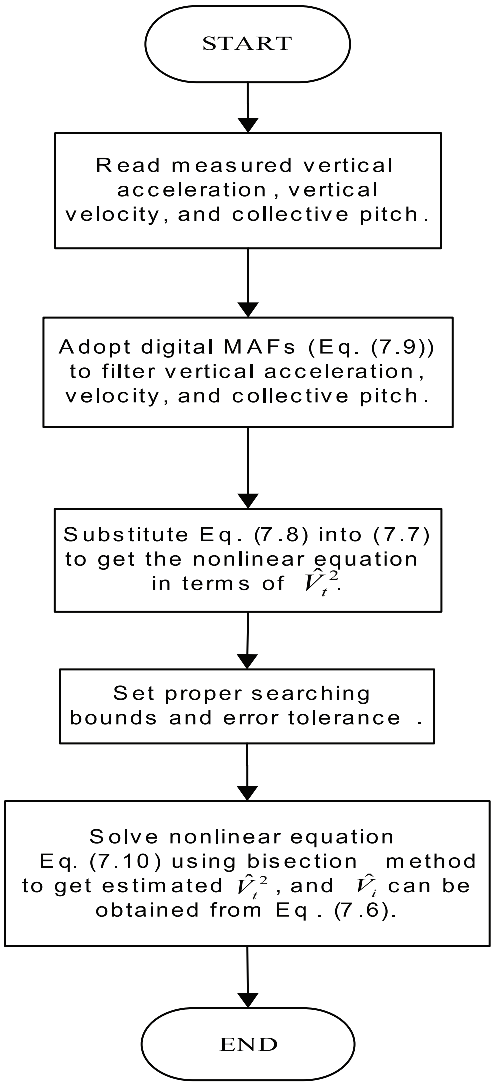

Figure 7.3. Flow chart for implementation of the gust estimator

7.4 A Gust-attenuation Controller for Heave Motion of a RUAV

The proposed feedback-feedforward controller consists of two parts. The first part is to design a PD controller with the intention of achieving satisfactory dynamic performance when no gusts occur; the second part, which is based on the estimation of the gusts $\hat{V}_t^2$ and induced velocity $\hat{V}_i$, aims to calculate the required collective pitch to compensate for dynamic variations when gusts occur.

The architecture of the disturbance-attenuation control strategy is illustrated in Fig. 7.4. Firstly, the RUAV heave dynamics are modeled by Equations (7.1)-(7.2). In the gust estimator block, feasible MAFs are constructed to extract true states from the noisy measurements of vertical velocity w, acceleration a_z, and collective pitch θ_{col}. Here, window widths of MAFs are 0.4s for measured w, a_z, and θ_{col}. Then, these filtered variables serve as inputs to the gust estimator, and estimated gusts $\hat{V}_t^2$ and induced velocity $\hat{V}_i$ are acquired by the estimation procedure shown in Fig. 7.3.

Our ultimate purpose is to calculate the required collective pitch $\Delta\theta$, and add it to the nominal collective pitch (collective pitch required when no gusts occur) to compensate for dynamic variations. The feedback-feedforward control law θ_c is in the form of

$$\theta_c = K_{Fp}(z_b^d - z) + K_{Fd}w + \Delta\theta \tag{7.11}$$

where z_b^d is the desired height, K_{Fp} and K_{Fd} are proportional and derivative gains.

The introduction of $\Delta\theta$ aims to indicate how much collective pitch deviates from the nominal value. The collective pitch offset $\Delta\theta$ is calculated through subtraction of $\theta|_{V_t^2=0}$ from $\theta|_{V_t^2=V_g}$, which is in the form of

$$\Delta\theta = \theta|_{V_t^2=V_g} - \theta|_{V_t^2=0} = \frac{3\left(\frac{T_{mr}}{B_t} + \frac{\hat{V}_{ig}+V_{ng}}{2\Omega_{mr}R_b}\right)}{1 + \frac{3\hat{V}_t^2}{2{\Omega_{mr}}^2 R_b^2}} - 3\left(\frac{T_{mr}}{B_t} + \frac{\hat{V}_{i0}+V_{n0}}{2\Omega_{mr}R_b}\right) \tag{7.12}$$

Here, symbol $\theta|_{V_t^2=V_g}$ represents the required collective pitch when gust levels are V_g, and the required collective pitch when no gusts occur is denoted by $\theta|_{V_t^2=0}$. Coefficients $\hat{V}_{ig}$ and V_{ng} denote the estimated induced velocity and vertical component of air stream (V_{ng} is approximated by w with the opposite sign) when $\hat{V}_t^2 = V_g$, and $\hat{V}_{i0}$ and V_{n0} when no gusts occur. As we are only concerned with the hover state,

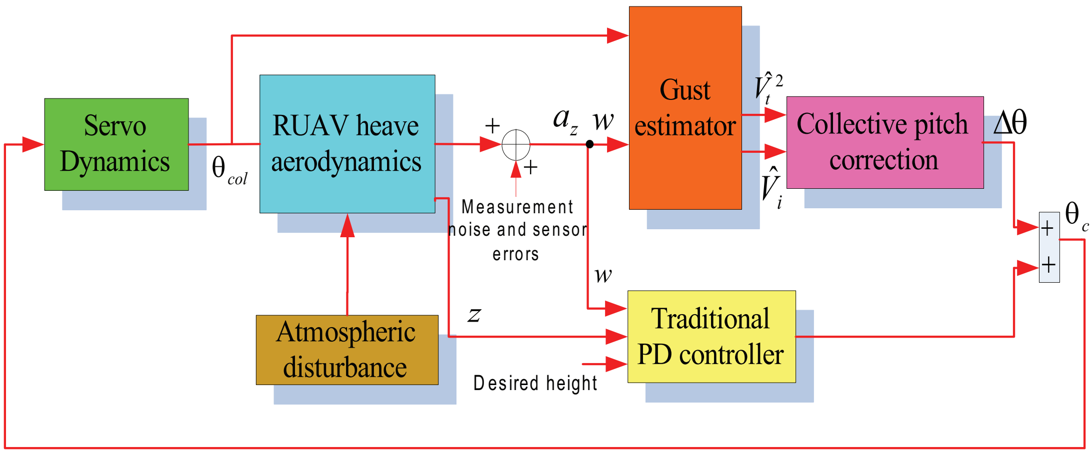

Figure 7.4. Architecture of the proposed feedback-feedforward control strategy

vertical components V_{ng} and V_{n0} in Eq. (7.12) can be set to 0, and thrust T_{mr} is replaced with weight $M_a g$ of the RUAV. Therefore, Equation (7.12) becomes

$$\Delta\theta = \theta|_{V_t^2=V_g} - \theta|_{V_t^2=0} = \frac{3\left(\frac{M_a g}{B_t} + \frac{\hat{V}_{ig}}{2\Omega_{mr} R_b}\right)}{1 + \frac{3\hat{V}_t^2}{2{\Omega_{mr}}^2 R_b^2}} - 3\left(\frac{M_a g}{B_t} + \frac{\hat{V}_{i0}}{2\Omega_{mr} R_b}\right) \tag{7.13}$$

It is seen that the required collective pitch $\Delta\theta$ to remove the steady-state error in the height can be obtained, provided the estimates of $\hat{V}_{ig}$ and $\hat{V}_t^2$ are available, which are outputs of the gust estimator. The resultant $\Delta\theta$ is combined with the PD controller to increase the gust-attenuation capacity of the RUAV.

The detailed block diagram of the proposed control structure is depicted in Fig. 7.5. When no gusts occur, the feedback control law enables the RUAV to hover at the desired height. Once gusts occur, the feedforward part $f^{-1}(\hat{V}_t^2, \hat{V}_i)$ computes the instantaneous amount of collective pitch $\Delta\theta$ given by Eq. (7.13). It is seen that $\Delta\theta$ is the required amount which should be added to control command to compensate for dynamic changes in collective pitch caused by gusts. Therefore, the heave motion can be stabilized once the feedforward part $f^{-1}(\hat{V}_t^2, \hat{V}_i)$ yields the instantaneous $\Delta\theta$.

7.5 Simulation Results

In this section, overall performance of the proposed controller, in combination with a comprehensive evaluation of the gust estimator, is tested using the heave

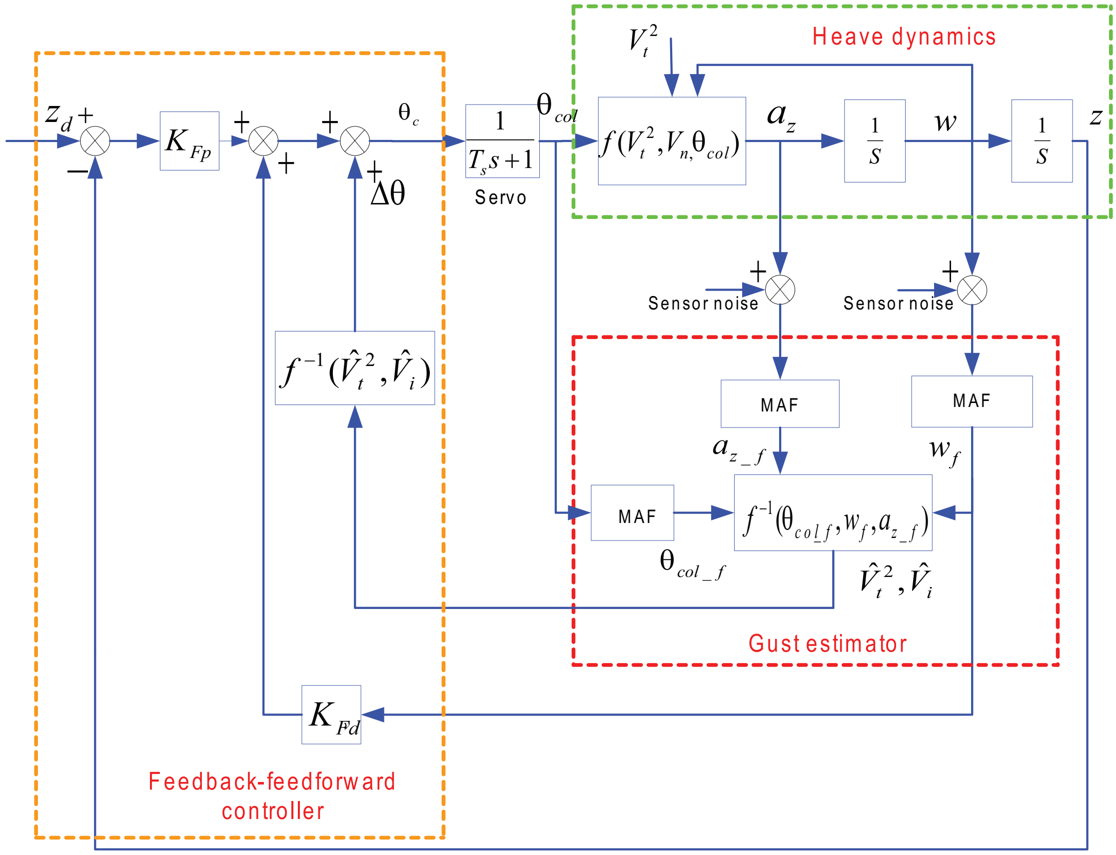

Figure 7.5. Block diagram of the proposed control strategy

motion model of our helicopter based on simulation parameters consistent with those employed in real applications. Operational limits in the collective pitch ($1^\circ < \theta_{col} < 10^\circ$) and the rate limit in servo dynamics ($|\dot{\theta}_{col}| < 20^\circ/\mathrm{s}$), are taken into account in the simulation model. The simulation structure is shown in Appendix B. The control commands are implemented using the PWM mechanism. There is an approximate linear relationship between collective pitch commands and PWM signals, which can be computed after proper calibrations. Also, to acquire a reliable performance evaluation of the proposed gust estimator, simulation seeds of turbulence model are set differently within an extensive scope to produce wind gusts with diversified maximum levels and different distributions.

To acquire a reliable performance evaluation of the gust estimator, horizontal gusts are constructed using Dryden turbulence model by passing white noise through shaping filters in longitudinal and lateral directions [126]. The Dryden gust model in Section 3.6 typically captures properties of atmospheric turbulence at low altitudes and flight speeds [125], and can be employed to generate representative gusts to test performance of the proposed controller. It should be clarified that no stochastic properties of the gusts are used to design the gust estimator, and the validity of the gust estimator is not restricted to specific gust conditions.

Numerous simulations have been carried out for possible oncoming gusts, and the performance of the gust estimator is illustrated in Fig. 7.6. All the simulations are implemented for 100 s with sampling time of 0.02 s. For the purpose of making the investigation more representative, helicopter velocity relative to the air stream is set to be 10 m/s. The survival possibility of the RUAV is threatened by strong unpredictable gusts, especially on occasions when gust variations resulting from turbulence change take place with a high speed, and last for a certain period of time. Also, the RUAV is vulnerable to frequent changing gusts. Consequently, our gust estimator is tested in such challenging environments. Two typical cases are tested in Fig. 7.6. Comparison results show that the estimated gusts are very close to the gusts generated by software (assumed to be real gusts), with maximum estimation errors of 4.5458 m/s and 2.4541 m/s, separately. Here, control gains K_{Fp} is 0.022, and K_{Fd} is 0.045.

Several quantitative specifications are employed to evaluate performance of estimated $\hat{V}_t^2$, which consist of maximum relative estimation error ς, and estimation capacity factor η. The index ς is used to check maximum relative estimation error, and η aims to evaluate overall estimation performance. The definition of these specifications are listed as follows

$$\varsigma = \frac{\max_i |V_t^2(i) - \hat{V}_t^2(i)|}{V_t^2(i)} \tag{7.14}$$

$$\eta = 20 \log_{10} \frac{\sqrt{\Phi}}{\max_i |V_t^2(i)|} \tag{7.15}$$

where mean squared error Φ_r is defined by

$$\Phi_r = \frac{1}{N} \sum_{i=1}^{N} [V_t^2(i) - \hat{V}_t^2(i)]^2 \tag{7.16}$$

As is shown in Fig. 7.7, maximum relative estimation error ς of $\hat{V}_t^2$ is consistently within 50% of V_t^2, which is satisfactorily accepted in our scenario. Also, the

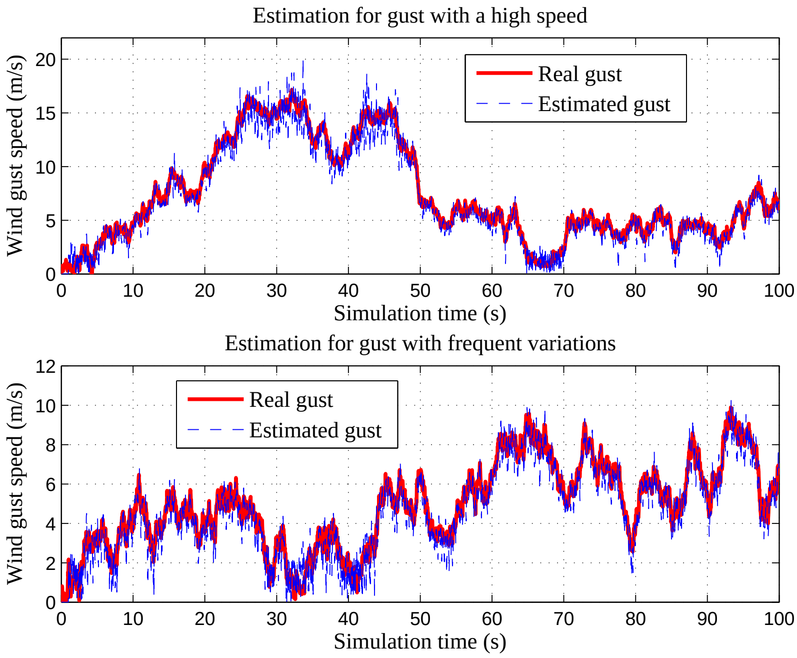

Figure 7.6. Estimation of gust variations

estimation capacity factor η of $\hat{V}_t^2$ remains less than -20 dB, which indicates that the mean estimation error within 10% of real gusts can always be obtained.

System performance using the proposed feedback-feedforward controller is also tested. The feedforward part is constructed through employment of the estimated gusts $\hat{V}_t^2$ and induced velocity $\hat{V}_i^2$. Comparisons on induced velocity are displayed in Fig. 7.8 for the two typical gusts mentioned before. Although there are some small deviations at the initial stage, our estimator can consistently give good estimation of induced velocity. As is depicted in Fig. 7.9, the resultant collective pitch command θ_{col} can effectively compensate for the gusts, and the RUAV can hover at the desired height stably (-2 m). Here, negative direction is above the ground. It can be seen that vertical velocity converges quickly to zero, and is not subject to fluctuations. It is evident in Fig. 7.9 that the proposed controller can efficiently compensate for heave motion once random gusts occur when compared with a PD controller. Therefore, our control strategy can effectively ensure stable dynamic response of the RUAV in a windy environment, so that the RUAV hovers safely at the desired altitude over the ship deck before landing on an assigned location.

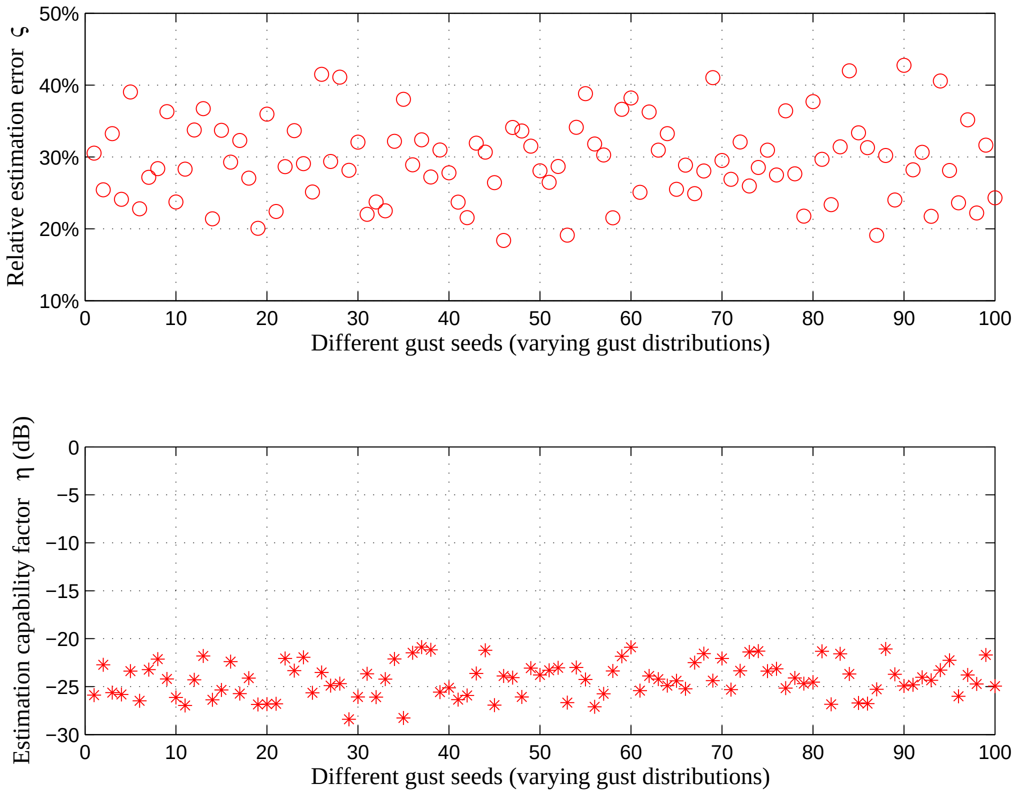

Figure 7.7. Performance evaluation of the proposed gust estimator

To evaluate transient response of heave motion using the proposed controller, 100 simulations are conducted. The overshoot

$$\sigma_{ov} = |\frac{z_p - z_\infty}{z_\infty}| \times 100\% \tag{7.17}$$

is employed, where z_p and z_∞ are peak and stable values of vertical distance. It is shown in Fig. 7.10 that the maximum overshoot is under 5%, which illustrates satisfactory transient response in a gusty environment. The mean square error Φ_r is $2.2875e-4$ m^2, which indicates the system experiences very small standard deviations.

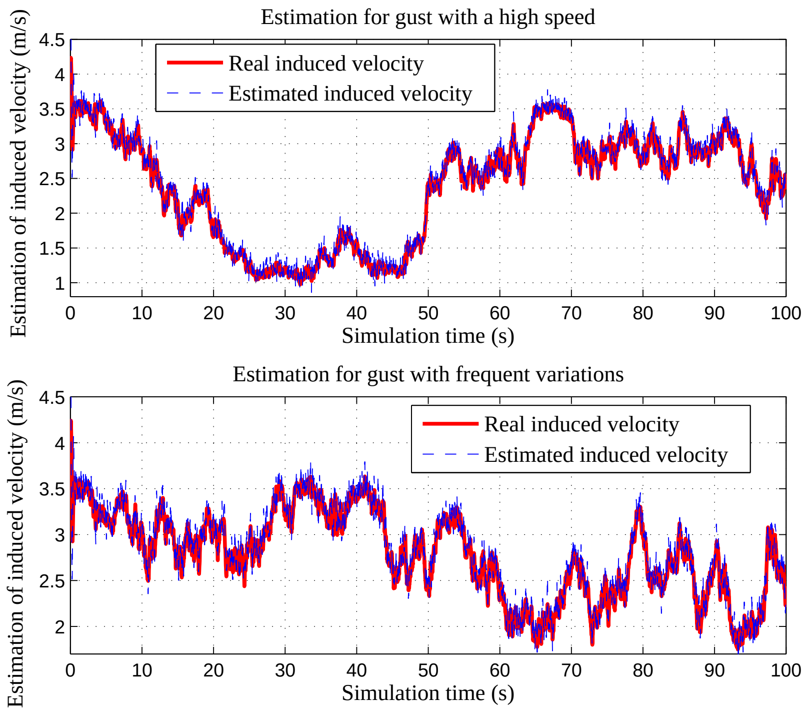

Figure 7.8. Estimation of induced velocity

7.6 Flight Test Results

A series of experiments have been conducted to evaluate the performance of the proposed gust estimator for further integration with the feedback-feedforward controller. The small size and available remote-control capability make the Eagle helicopter an ideal platform for the flight validation.

The initial field tests showed that the measurement noise in acceleration, velocity and collective pitch deteriorates the performance of the gust estimator. This necessitates design of MAFs with proper window width. The choice of the width of MAFs should guarantee effective removal of measurement noise, and reduce oscillations in the estimated thrust. Meanwhile, the inherent transport lag (0.08 s) should be considered to make measured signals entering into the gust estimator occur simultaneously. Therefore, the window width for the three average filters are increased to 20 points after a few flight trials.

The collective pitch servo receives the anticipated control commands, and drives

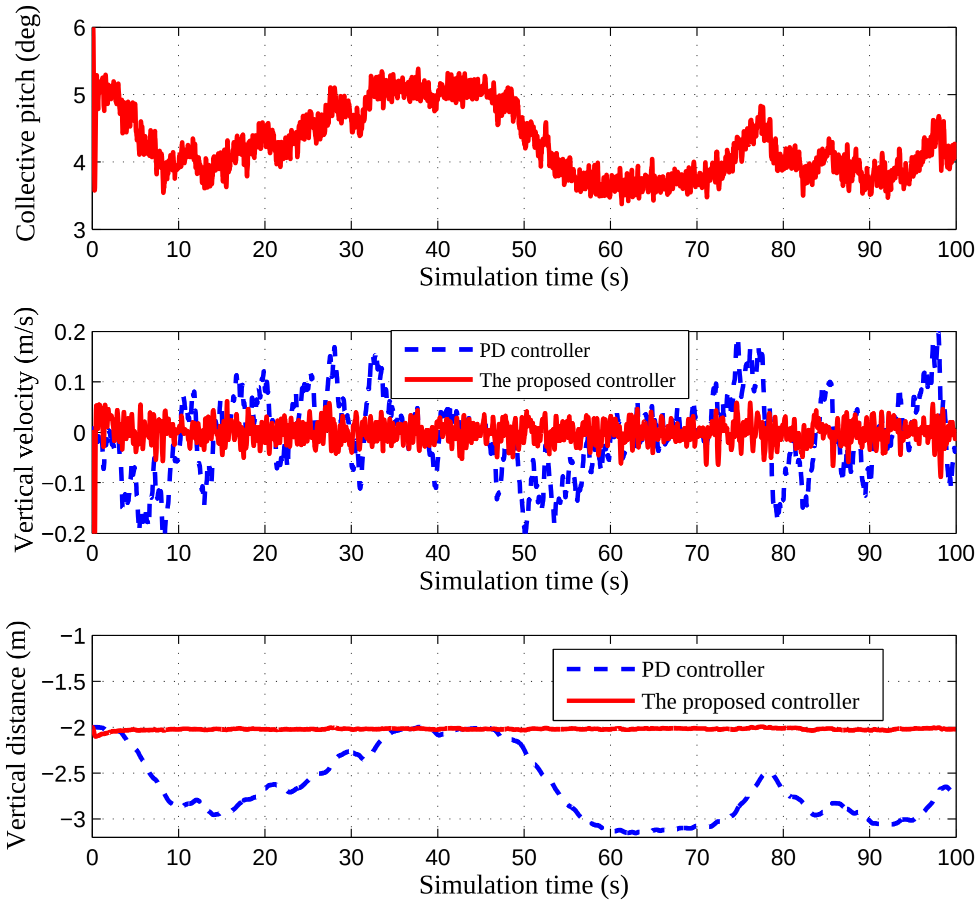

Figure 7.9. Control variable and dynamic response of the heave motion

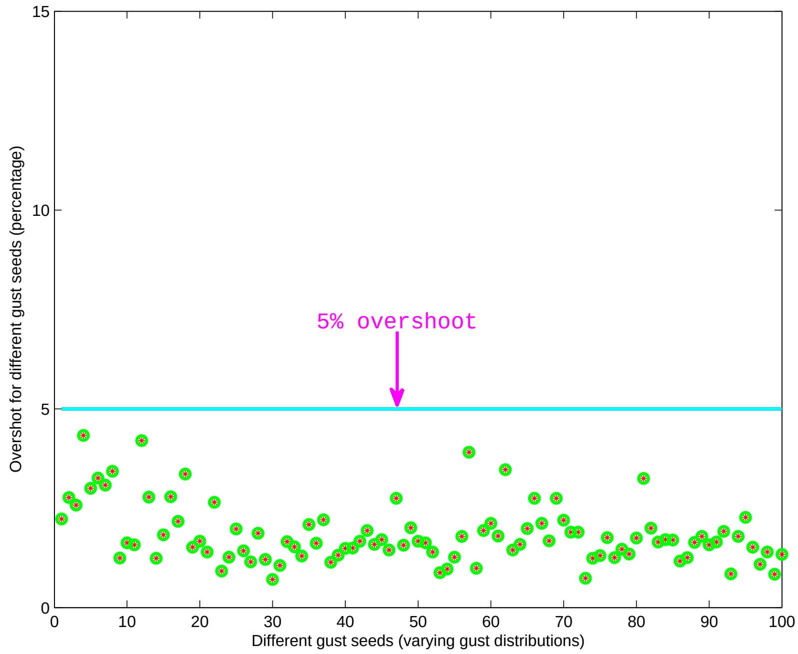

Figure 7.10. Overshoot for heave motion

the corresponding mechanical equipment (servo horns) to implement desired activities through linkages. Control signals generated by the MPC555 autopilot are sent to the digital collective pitch servo in the form of PWM signals at an update rate of 50 Hz. The PWM sequences repeat every 20 ms with the minimum duty cycle of 1 ms and the maximum of 2 ms.

The field test began with finding out the proper trim collective pitch under the particular flight conditions when flight tests were conducting, then the trim collective were kept unchanged for the remaining tests. Since the main purpose is to control collective pitch due to its vulnerability to wind gusts, it is reasonable to control tail rotor, aileron and elevator channels individually using the PD controllers. This would reduce experimental complexities when tuning control gains for a specific control channel. During flight tests, the Eagle helicopter was initially brought to a safe flight condition using the manual control mode, which is necessary for potentially hazardous experiments requiring successive attempts for satisfactory flight performance. Also, special attention was paid to the flight close to the ground as slight variations in collective pitch would lead to rapid changes in height. Therefore, handover to the automatic mode was forbidden to prevent unexpected transient response from resulting in dynamic oscillations which would cause crash of the helicopter. Handover to the automatic mode was activated after the helicopter reached to the desired height, and the autopilot micro-controller started sending control signals used for closed-loop flight tests. The automatic control mode was running for a few seconds to achieve smooth transition response before the feedforward controller was switched on. Once turned on, the feedforward part operated in parallel with the feedback controller to produce the desired amount of collective pitch.

The experimental results from the flight test conducted on a windy day with the gust speed of approximately 20 km/h are shown. The gust speed was known by checking the official web site of the Australian Bureau of Meteorology on that day [190]. The flight test results shown in Fig. 7.11 indicate that the helicopter experienced significant oscillations in height when only controlled by PD controller. The oscillations reduced greatly after the feedforward controller was initiated at 52.5 s, and the height remained around 1.6 m under wind gusts. After the feedfoward controller was turned on, there were transient response which last for about 16.4 s. The transition is revealed in vertical velocity shown in Fig. 7.12. Afterwards, the velocity tended to experience smaller changes. It is seen from Fig. 7.13 that the MAFs extracted the acceleration effectively from the noisy measurements. As is shown in Fig. 7.14, it took around 10 s for the gust estimator to effectively estimate the real gust levels owing to the transient response in collective pitch and ground effect during the take-off phase. The collective pitch commands are depicted in Fig. 7.15 (degree) and Fig. 7.16 (PWM). It is noticed that the rate of change of the collective pitch increased greatly after 52.5 s, which was introduced by the rapid change of collective pitch correction commands shown in Fig. 7.17. The corresponding PWM pitch correction commands are shown in Fig. 7.18.

7.7 Summary and Future Work

In this chapter we concentrate on building a feasible gust estimator for controlling heave motion dynamics of a RUAV. Based on construction of heave motion dynamics in a gusty environment and measurable signals from aboard equipment, an effective gust estimator is developed. In addition, a feedback-feedforward control architecture is presented to stabilize heave motion. Simulation results demonstrate that the proposed gust estimator exhibits satisfactory estimation performance. Flight tests

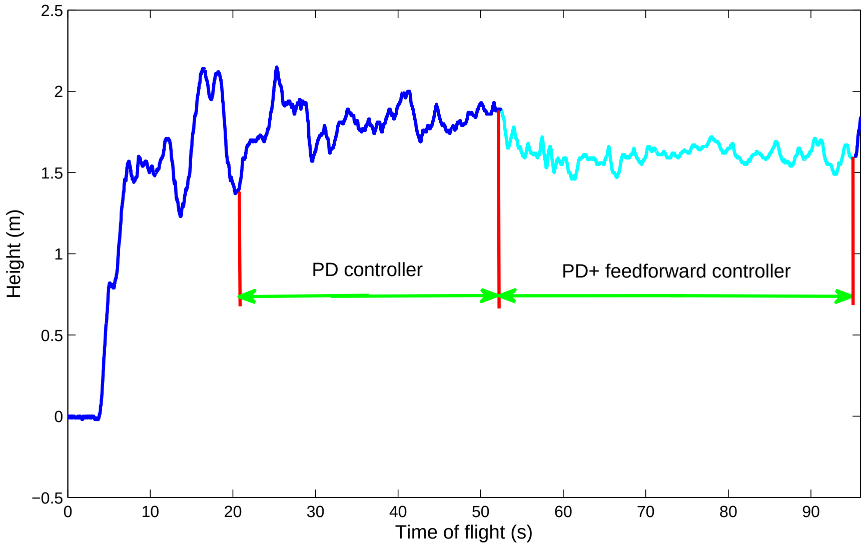

Figure 7.11. Height in the flight test

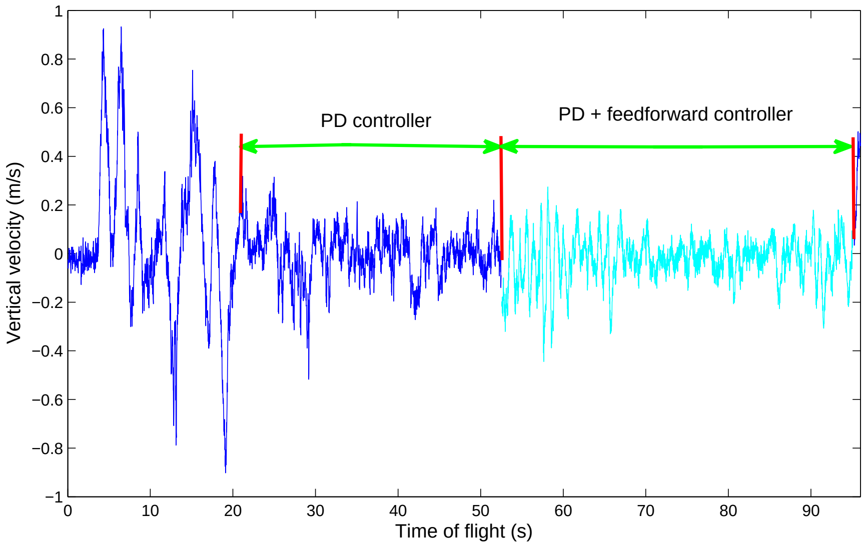

Figure 7.12. Vertical velocity in the flight test

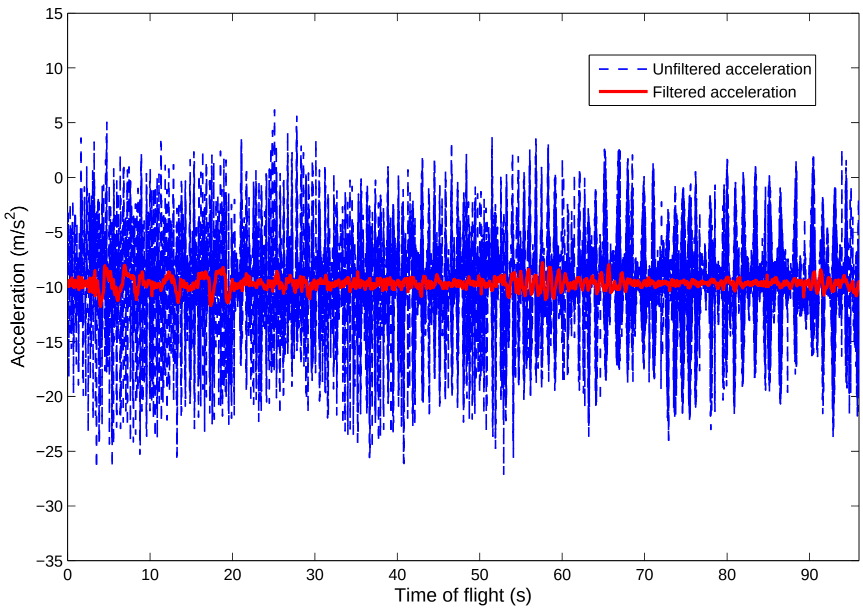

Figure 7.13. Filtered and unfiltered accelerations

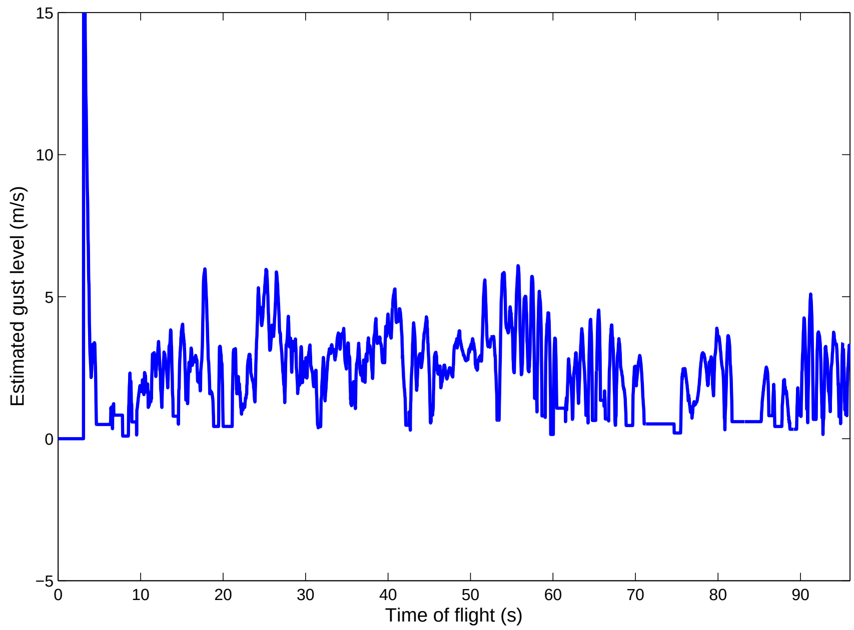

Figure 7.14. Estimated gusts in the flight test

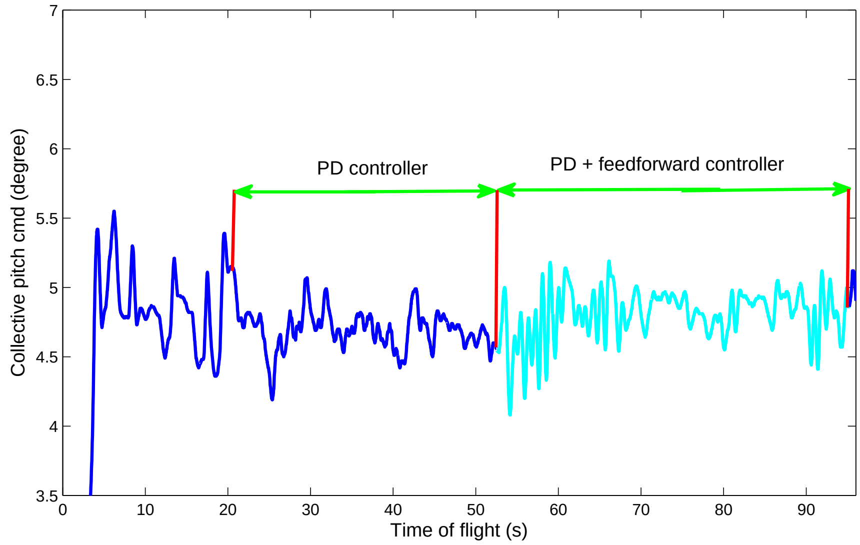

Figure 7.15. Collective pitch signals (degree)

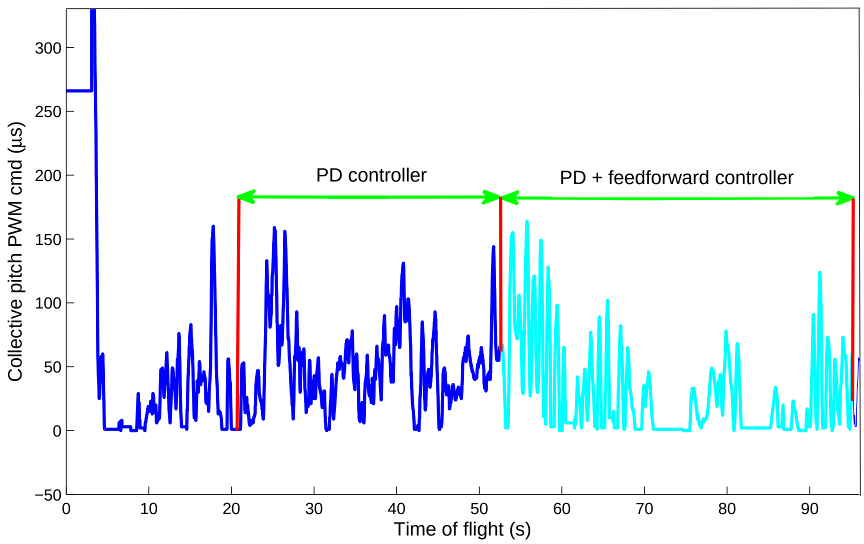

Figure 7.16. Collective pitch signals (PWM)

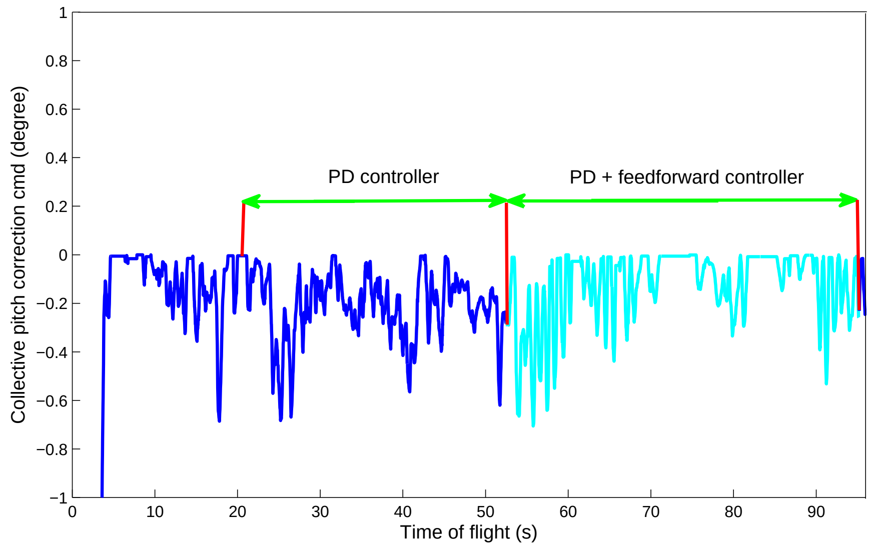

Figure 7.17. Collective pitch correction signals (degree)

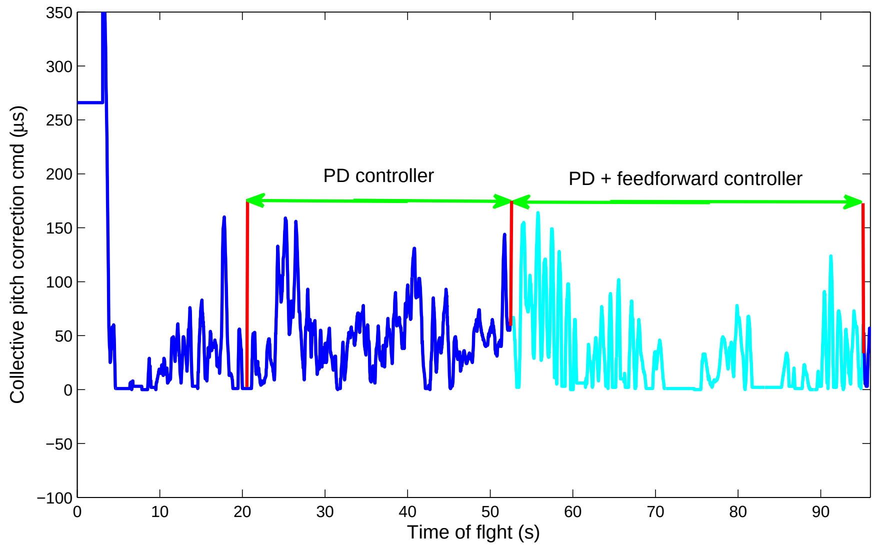

Figure 7.18. Collective pitch correction signals (PWM)

have justified the feasibility of the proposed control strategy when random gusts occur, which prove its suitability for use in ship-helicopter flight operations.

Chapter 8

Nonlinear Position Control using the $\mathcal{H}_\infty$ Theory

This chapter presents a disturbance attenuation controller for horizontal position stabilization for hover and automatic landings of a RUAV operating close to the landing deck in rough seas. Based on a helicopter model representing aerodynamics during the landing phase, a nonlinear state feedback $\mathcal{H}_\infty$ controller is designed to achieve rapid horizontal position tracking in a gusty environment. The resultant control variables are further treated in consideration of practical constraints (flapping dynamics, servo dynamics and time lag effect) for implementation purposes. The high-fidelity closed-loop simulation using parameters of the Vario helicopter verifies the performance of the proposed position controller. It not only increases the disturbance attenuation capability, but also enables rapid position response when gusts occur. Comparative studies show that the $\mathcal{H}_\infty$ controller exhibits performance improvement in tracking and disturbance-attenuation capabilities, and can be applied to ship/RUAV landing systems.

8.1 Introduction

In Chapter 7, a feedback-feedforward controller has been designed to achieve height control in a gusty environment, and its performance has been confirmed in flight tests. In this work, our objective is to design a controller with disturbance-attenuation property and rapid horizontal position tracking performance. This work begins with establishing a simplified model capturing dynamics of the RUAV during landing operations. Afterwards, a nonlinear $\mathcal{H}_\infty$ controller is developed to achieve gust attenuation and fast horizontal position control. Simulation results demonstrate that the proposed controller can effectively attenuate gust effect and achieve rapid and accurate position tracking when gusts occur.

8.2 Formation of the Nonlinear RUAV Dynamic Model

As we have shown in chapter 7 the vertical position z_b can be stabilized in a gusty environment by incorporating a PD controller with a feedforward compensator, and control of yaw motion can also be achieved by the existing PD controller. In this chapter, particular emphasis is placed on the more challenging task of rapid control of RUAV horizontal positions in the presence of strong wind gusts.

The design of a disturbance attenuation controller depends greatly on the choice of the typical working conditions expected and tractability of the control problem associated with the resultant control plants. During the final stages of landing, the typical working condition is basically the hover condition, and stabilization of the hover state is a prerequisite for an automatic landing. Therefore, the control plant is derived for the hover condition, where main rotor thrust T_{mr} and tail rotor thrust T_{tr} are constant. Thus, update equations for position and velocity introduced in Section 3.3 can be written as follows,

$$\dot{x}_b = u + d_1 \tag{8.1}$$

$$\dot{y}_b = v + d_2 \tag{8.2}$$

$$\dot{u} = r_c v - q w_c + \frac{X_h}{M_a} - g \sin\theta + d_3 \tag{8.3}$$

$$\dot{v} = -r_c u + p w_c + \frac{Y_h}{M_a} + g \cos\theta \sin(\phi + \phi_0) + d_4 \tag{8.4}$$

Here, adoption of existing controllers for vertical and yaw motion makes it possible not to consider $\dot{z}_b$ and $\dot{w}$, and the subscript c indicates that the yaw rate r and vertical velocity w are obtained from INS and GPS. Symbols d_i represents the exogenous disturbances. A constant offset ϕ_0 is added to system equations to establish the desired equilibrium point.

It is known from Section 3.3 that the moment equations for roll and pitch are

$$I_{xx}\dot{p} = (I_{yy} - I_{zz})qr + I_{xz}(\dot{r} + pq) + L_h \tag{8.5}$$

$$I_{yy}\dot{q} = (I_{zz} - I_{xx})rp + I_{xz}(r^2 - p^2) + M_h \tag{8.6}$$

In order to form convenient expressions for the purpose of controller design, the derivative term $\dot{r}$ on the right-hand side of Eq. (8.5) is removed through variable substitution. Hence, moment equations can be simplified and rearranged into the following forms in consideration of disturbance d_i

$$\dot{p} = k_1 pq + k_2 qr + k_3 L_h + k_4 N_h + d_5 \tag{8.7}$$
$$\dot{q} = k_5 pr + k_6(r^2 - p^2) + k_7 M_h + d_6 \tag{8.8}$$

where the parameters $k_{(\cdot)}$ are listed as follows

$$\begin{aligned} \xi &= I_{xx}I_{zz} - I_{xz}^2 & k_1 &= \frac{I_{xz}(I_{xx} - I_{yy} + I_{zz})}{\xi} \\ k_2 &= \frac{I_{zz}(I_{yy} - I_{zz}) - I_{xz}^2}{\xi} & k_3 &= \frac{I_{zz}}{\xi} \\ k_4 &= \frac{I_{xz}}{\xi} & k_5 &= \frac{I_{zz} - I_{xx}}{I_{yy}} \\ k_6 &= \frac{I_{xz}}{I_{yy}} & k_7 &= \frac{1}{I_{yy}} \end{aligned}$$

The roll and pitch update equations are described as

$$\dot{\phi} = p + (q\sin(\phi + \phi_0) + r_c\cos(\phi + \phi_0))\tan\theta + d_7 \tag{8.9}$$
$$\dot{\theta} = q\cos(\phi + \phi_0) - r_c\sin(\phi + \phi_0) + d_8 \tag{8.10}$$

As the attitudes are very small in our case ($\phi, \phi_0, \theta, \psi < 5^o$), using small angle approximation leads to

$$\begin{aligned} &\sin\theta \approx \theta \\ &\cos\theta \approx 1 \\ &\sin(\phi + \phi_0) \approx \phi + \phi_0 \\ &\cos(\phi + \phi_0) \approx 1 \\ &\tan\theta \approx \theta \end{aligned}$$

Hence, the attitude update equations are simplified to

$$\dot{\phi} = p + q(\phi + \phi_0)\theta + r_c\theta + d_7 \tag{8.11}$$
$$\dot{\theta} = q - r_c(\phi + \phi_0) + d_8 \tag{8.12}$$

For small helicopters, forces (X_h, Y_h, Z_h) and moments (L_h, M_h, N_h) acting on the RUAV are predominantly determined by the main rotor and tail rotor, which have been calculated in Section 3.4.5 taking the form of

$$L_h = k_\beta b_1 + T_{mr} D_{mz} b_1 + T_{tr} D_{tz} \tag{8.13}$$

$$M_h = (-k_\beta - T_{mr} D_{mz}) a_1 \tag{8.14}$$

$$N_h = \frac{P_{mr}}{\Omega_{mr}} + T_{mr} D_{mx} b_1 + T_{tr} D_{tx} \tag{8.15}$$

Therefore, the mathematical description of the nonlinear RUAV model under investigation is

$$\dot{x}_b = u + d_1 \tag{8.16}$$

$$\dot{y}_b = v + d_2 \tag{8.17}$$

$$\dot{u} = r_c v - q w_c + \frac{T_{mr}}{M_a} a_1 - g\theta + d_3 \tag{8.18}$$

$$\dot{v} = -r_c u + p w_c + \frac{T_{mr}}{M_a} b_1 + \frac{T_{tr}}{M_a} + g(\phi + \phi_0) + d_4 \tag{8.19}$$

$$\begin{aligned} \dot{p} = {} & k_1 pq + k_2 q r_c + (k_3 k_\beta + k_3 T_{mr} D_{mz} + k_4 T_{mr} D_{mx}) b_1 \\ & + k_3 T_{tr} D_{tz} + k_4 \frac{P_{mr}}{\Omega} + k_4 T_{tr} D_{tx} + d_5 \end{aligned} \tag{8.20}$$

$$\dot{q} = k_5 p r_c + k_6 (r_c^2 - p^2) + k_7 (-k_\beta - T_{mr} D_{mz}) a_1 + d_6 \tag{8.21}$$

$$\dot{\phi} = p + q(\phi + \phi_0)\theta + r_c \theta + d_7 \tag{8.22}$$

$$\dot{\theta} = q - r_c(\phi + \phi_0) + d_8 \tag{8.23}$$

The main rotor flapping dynamics are described by

$$\dot{a}_1 = -q - \frac{a_1}{\tau_m} + \frac{1}{\tau_m}\left(\frac{\partial a_1}{\partial u} u + C_{lon} B_{lon}\right) \tag{8.24}$$

$$\dot{b}_1 = -p - \frac{b_1}{\tau_m} + \frac{1}{\tau_m}\left(\frac{\partial b_1}{\partial v} v + C_{lat} A_{lat}\right) \tag{8.25}$$

where the main rotor time constant is

$$\tau_m = \frac{16}{\gamma_f \Omega_{mr}}$$

and the lock number γ_f is

$$\gamma_f = \frac{\rho c_{mr} a_l R_b^4}{I_\beta} \tag{8.26}$$

where I_β is the flapping moment of inertia. The lock number γ_f is a non-dimensional scaling coefficient, describing the ratio of aerodynamics to inertia forces acting on a rotor blade. Symbols C_{lon} and C_{lat} are effective steady-state longitudinal and lateral gains, B_{lon} and A_{lat} are longitudinal cyclic and lateral cyclic. The Dihedral effect is

$$\frac{\partial a_1}{\partial u} = -\frac{\partial b_1}{\partial v} = \frac{2}{\Omega_{mr} R_b}\left(\frac{8C_T}{a_l \sigma_b} + \sqrt{\frac{C_T}{2}}\right) \tag{8.27}$$

where σ_b is the solidity ratio, and C_T thrust coefficient.

Remark 7 For model-scale helicopters, control forces and moments are mainly generated by main rotor and tail rotor. Forces and moments from fuselage, empennage and vertical fin are neglected.

Remark 8 Control inputs in the controller design process are set to be longitudinal flapping and lateral flapping. They will be converted later into longitudinal cyclic and lateral cyclic for implementation.

The following vectors are defined for the purpose of controller design,

$$\begin{aligned} x &= [x_b, y_b, u, v, p, q, \phi, \theta]^T \\ \omega &= [d_1, d_2, d_3, d_4, d_5, d_6, d_7, d_8]^T \\ U_c &= [a_1, b_1]^T \end{aligned}$$

which lead to a compact form of system dynamics

$$\dot{x} = f(x) + g_1(x)\omega + g_2(x)U_c \tag{8.28}$$

$$z_m = h(x) + l(x)U_c \tag{8.29}$$

Here, $x \in \mathbf{R}^8$ is plant state, $\omega \in \mathbf{R}^8$ disturbance, and $U_c \in \mathbf{R}^2$ control input, and $z_m \in \mathbf{R}^{10}$ is a penalty variable. It is assumed that all functions involved are smooth and defined in a neighborhood U_e of the origin in $\mathbf{R}^8$ and $f(0) = 0,\ h(0) = 0$. The following assumptions are also made,

$$\begin{aligned} h^T(x)l(x) &= 0 \\ l^T(x)l(x) &= R_h \end{aligned} \tag{8.30}$$

where $R_h \in \mathbf{R}^{2\times 2}$ is a nonsingular constant matrix, and is chosen to be symmetric to facilitate controller design.

8.3 Design of the $\mathcal{H}_\infty$ Controller for Horizontal Position Control

The design approach is based on the theory proposed in [191,192] with modifications necessitated by RUAV aerodynamics. The control objective is to design a controller $U_c = L(x)$ to achieve satisfactory closed-loop system performance evaluated either in time domain (overshoot, steady-state error and settling time etc.) or in frequency domain (magnitude and phase margin). It is expected that the initial state departing in the vicinity of the equilibrium point converges to the equilibrium point when time goes to infinity. The disturbance attenuation capability can be described as [191]: Given a real number $0 < \gamma_h < 1$, it is said that the exogenous signals are locally attenuated by γ_h if there exists a neighborhood U_e of the point $x = 0$ such that for every $T > 0$ and for every piecewise continuous function $\omega : [0, T]$, the sate trajectory starting from $x_0 = 0$ remains in U_e for all $t \in [0, T]$, and the response $z_m : [0, T]$ satisfies

$$\int_0^T z_m^T(s) z_m(s) ds \leqslant \gamma_h^2 \int_0^T \omega^T(s)\omega(s) ds \tag{8.31}$$

The design approach begins with Taylor series expansion of the nonlinear functions in Eq. (8.28)-(8.29),

$$f(x) = \sum_{i=1}^{\infty} A_i x^{(i)} = A_1 x + f^{[2+]}(x) \tag{8.32}$$

$$h(x) = \sum_{i=1}^{\infty} C_i x^{(i)} = C_1 x + h^{[2+]}(x) \tag{8.33}$$

$$g_1(x) = B_1 + g_1^{[1+]}(x) \tag{8.34}$$

$$g_2(x) = B_2 + g_2^{[1+]}(x) \tag{8.35}$$

where $f^{[2+]}(x), h^{[2+]}(x), g_1^{[1+]}(x)$ and $g_2^{[1+]}(x)$ are high-order expansions.

For the RUAV model Eq.(8.16)-(8.23), $f(x)$ has a third-order expansion, and the three terms A_1, A_2 and A_3 are written as follows

$$A_1 = \begin{bmatrix} 0 & 0 & 1 & 0 & 0 & 0 & 0 & 0 \\ 0 & 0 & 0 & 1 & 0 & 0 & 0 & 0 \\ 0 & 0 & 0 & r_c & 0 & -w_c & 0 & -g \\ 0 & 0 & -r_c & 0 & w_c & 0 & g & 0 \\ 0 & 0 & 0 & 0 & k_1 q & k_1 p + k_2 r_c & 0 & 0 \\ 0 & 0 & 0 & 0 & k_5 r_c - 2k_6 p & 0 & 0 & 0 \\ 0 & 0 & 0 & 0 & 1 & (\phi+\phi_0)\theta & q\theta & q(\phi+\phi_0) \\ 0 & 0 & 0 & 0 & 0 & 1 & -r_c & 0 \end{bmatrix}_{8\times 8}$$

where $A_2 \in \mathbf{R}^{8\times 64}$ and $A_3 \in \mathbf{R}^{8\times 512}$ are large sparse matrices with a small number of non-zero values. The non-zero elements with their indices are listed below

$$\begin{array}{ll} A_2(5,38) = k_1 & A_2(5,45) = k_1 \\ A_2(6,37) = -2k_6 & A_2(7,47) = \theta \\ A_2(7,48) = \phi+\phi_0 & A_2(7,54) = \theta \\ A_2(7,56) = q & A_2(7,62) = \phi+\phi_0 \\ A_2(7,63) = q & \\ A_3(7,376) = 1 & A_3(7,383) = 1 \\ A_3(7,432) = 1 & A_3(7,446) = 1 \\ A_3(7,495) = 1 & A_3(7,502) = 1 \end{array}$$

and $A_i = 0$ for $i > 3$.

The functions $g_1(x)$ and $g_2(x)$ can be expanded to the first-order,

$$B_1 = B_1^0 = [B_{11}, \ldots, B_{18}] = I_8 \tag{8.36}$$

$$B_2 = B_2^0 = [B_{21}, B_{22}] \tag{8.37}$$

where

$$B_{21} = \begin{bmatrix} 0 \\ 0 \\ \frac{T_{mr}}{M_a} \\ 0 \\ 0 \\ k_7(-k_\beta - T_{mr}D_{mz}) \\ 0 \\ 0 \end{bmatrix} \quad B_{22} = \begin{bmatrix} 0 \\ 0 \\ 0 \\ \frac{T_{mr}}{M_a} \\ k_3k_\beta + k_3T_{mr}D_{mz} + k_4T_{mr}D_{mx} \\ 0 \\ 0 \\ 0 \end{bmatrix}$$

The constant matrices $h(x)$ and $l(x)$ are given by the expressions

$$h(x) = \left[\begin{array}{cccc} x_1 & & & \\ & \delta\cdot x_2 & & \\ & & \ddots & \\ & & & \delta\cdot x_8 \\ \hline 0 & \cdots & \cdots & 0 \\ 0 & \cdots & \cdots & 0 \end{array}\right]_{10\times 8} \qquad l(x) = \left[\begin{array}{c} O_{8\times 2} \\ \hline I_2 \end{array}\right]_{10\times 2} \tag{8.38}$$

where δ is a non-negative real number for making the controller design trade-off.

8.3.1 Linear Part of the $\mathcal{H}_\infty$ Controller

The linear part of the $\mathcal{H}_\infty$ controller can be obtained after solving the algebraic Riccati equation described by

$$H_{px}^T\bar{P} + \bar{P}H_{px} + \bar{P}H_{pp}\bar{P}x + H_{xx} = 0 \tag{8.39}$$

with the following definitions

$$\begin{aligned} H_{px} &= A_1 \\ H_{xx} &= C_1^T C_1 \\ H_{pp} &= \frac{B_1B_1^T}{\gamma_h^2} - B_2R_h^{-1}B_2^T \end{aligned} \tag{8.40}$$

The solution $\bar{P}$ is required to construct the controller.

Equation (8.39) can be rearranged into standard $\mathcal{H}_\infty$-like Riccati Equation form ($R_h = I_2$)

$$A_1^T \bar{P} + \bar{P} A_1 - \bar{P} \begin{bmatrix} B_1 & B_2 \end{bmatrix} \begin{bmatrix} -\gamma_h^2 I_{m_1} & O_{m_1 \times m_2} \\ O_{m_2 \times m_1} & I_{m_2} \end{bmatrix}^{-1} \begin{bmatrix} B_1^T \\ B_2^T \end{bmatrix} \bar{P} + C_1^T C_1 = 0 \tag{8.41}$$

where $m_1 = 8, m_2 = 2$ and γ_h is the attenuation factor.

Remark 9 The rank of the controllability matrix M_C

$$rank\ M_C = rank \begin{bmatrix} B_2 & A_1 B_2 & \cdots & A_1^7 B_2 \end{bmatrix} = 8 \tag{8.42}$$

This indicates the system is controllable (full-row rank). Also, for the observability matrix M_O,

$$rank\ M_O = rank \begin{bmatrix} C_1 & C_1 A_1 & \cdots & C_1 A_1^7 \end{bmatrix}^T = 8 \tag{8.43}$$

Thus, the system is observable, and the unique positive semi-definite matrix $\bar{P}$ exists [193].

8.3.2 Nonlinear Part of the $\mathcal{H}_\infty$ Controller

The nonlinear part of the controller involves iterative computation of several intermediate matrices. The resultant controller weighting matrices aims to deal with high-order dynamics of the helicopter.

Notations and Definitions

The following notations are introduced

$$x^{(0)} = 1 \quad x^{(1)} = x \tag{8.44}$$

$$x^{(i)} = \underbrace{x \otimes x \otimes \cdots \otimes x}_{i \text{ factor}},\ i = 2, 3, \cdots \tag{8.45}$$

where $\otimes$ is the Kronecker product. Similarly, it is also defined that

$$x^{[0]} = 1 \quad x^{[1]} = x, \tag{8.46}$$

$$x^{[k]} = [x_1^k, x_1^{k-1} x_2, \cdots, x_1^{k-1} x_n, x_1^{k-2} x_2^2, x_1^{k-2} x_2 x_3, \cdots, x_1^{k-2} x_2 x_n, \cdots, x_n^k]^T, k \geq 1 \tag{8.47}$$

Constant matrices M_k and N_k can be used to set up relationship between $x^{(k)}$ and $x^{[k]}$

$$x^{[k]} = M_k x^{(k)} \tag{8.48}$$

$$x^{(k)} = N_k x^{[k]} \tag{8.49}$$

where $M_k \in \mathbf{R}^{C(n_x,k)\times n_x^k}$ and $N_k \in \mathbf{R}^{n_x^k \times C(n_x,k)}$ satisfy

$$M_k N_k = I_{n_x}^{[k]} \tag{8.50}$$

Here, $I_{n_x}^{[k]}$ is an identity matrix of dimension

$$C(n_x, k) := C_{n_x+k-1}^k = \frac{\prod_{i=1}^k (n_x + k - i)}{k!} \tag{8.51}$$

In our case, the number of states $n_x = 8$.

We adopt the following operator $row(A)$ which maps n by m matrix $A = (a)_{ij}$ to a 1 by mn row vector

$$row(A) = [a_{11}, a_{12}, \cdots, a_{1m}, \cdots, a_{n1}, \cdots, a_{nm}] \tag{8.52}$$

Also, for any integers $i \geq 1, k \geq i$, and row vector $\bar{P}_k^*$ of dimension n_x^k, there exists a matrix $\bar{P}_k^i \in \mathbf{R}^{n_x \times n_x^{k-1}}$ determined by $\bar{P}_k^*$ such that

$$\bar{P}_k^*(x^{(i-1)} \otimes I_{n_x} \otimes x^{(k-i)}) = (\bar{P}_k^i x^{(k-1)})^T \tag{8.53}$$

where $\bar{P}_k^*$ is partitioned to a 1 by n_x^i block matrix taking the form

$$\bar{P}_k^* = \left[P_{\underbrace{1\cdots 11}_{i\ tuple}} \cdots P_{\underbrace{1\cdots 1n_x}_{i\ tuple}}\ P_{\underbrace{1\cdots 21}_{i\ tuple}}\ P_{\underbrace{1\cdots 2n_x}_{i\ tuple}} \cdots P_{\underbrace{n_x\cdots n_x 1}_{i\ tuple}}\ P_{\underbrace{n_x\cdots n_x n_x}_{i\ tuple}} \right] \tag{8.54}$$

in which $P_{j_1,\cdots,j_i}$, $1 \leq j_1, \cdots, j_i \leq n_x$ is a row vector of dimension n_x^{k-i}. The resultant matrix $\bar{P}_k^i$ is given by

$$\bar{P}_k^i = \begin{bmatrix} P_{\underbrace{1\cdots 11}_{i\ tuple}} & P_{\underbrace{1\cdots 21}_{i\ tuple}} & \cdots & P_{\underbrace{n_x\cdots n_x 1}_{i\ tuple}} \\ P_{\underbrace{1\cdots 12}_{i\ tuple}} & P_{\underbrace{1\cdots 22}_{i\ tuple}} & \cdots & P_{\underbrace{n_x\cdots n_x 2}_{i\ tuple}} \\ \vdots & \vdots & \vdots & \vdots \\ P_{\underbrace{1\cdots 1n_x}_{i\ tuple}} & P_{\underbrace{1\cdots 2n_x}_{i\ tuple}} & \cdots & P_{\underbrace{n_x\cdots n_x n_x}_{i\ tuple}} \end{bmatrix}$$

The controller design process is as follows:

Let $S_2 = \bar{P}$, and the following intermediate matrices are computed

$$W_{ij}^2 = row(S_2 B_{ij}^1) = 0;\ i = 1, 2; j = 1, ..., 8 \tag{8.55}$$

$$Y_{11}^1 = B_{11}^T S_2^T = B_{11}^T \bar{P} \tag{8.56}$$

$$E_3 = row(\bar{P} A_2) \tag{8.57}$$

$$F_3 = \sum_{l=1}^{2} (C_l^T C_{3-l}) = 0 \tag{8.58}$$

$$I_3^1 = \sum_{l=2}^{2} \sum_{j=1}^{8} row((W_{1j}^l)^T Y_{1j}^{3-l}) = 0 \tag{8.59}$$

$$I_3^2 = \sum_{j=1}^{2} row((W_{2j}^2)^T Y_{2j}^1) = 0 \tag{8.60}$$

Then,

$$H_3 = -(E_3 + \frac{F_3 - 2I_3^2}{2} + \frac{I_3^1}{\gamma_h^2}) N_3 = -E_3 N_3 \tag{8.61}$$

$$N_3 = x^{(3)} (x^{[3]})^{-1} \in \mathbf{R}^{512 \times 120} \tag{8.62}$$

Also, the intermediate matrix U_3 is

$$U_3 = M_3 [\sum_{i=1}^{3} I_8^{(i-1)} \otimes \bar{T} \otimes I_8^{(3-i)}] N_3 \tag{8.63}$$

$$= M_3 [\bar{T} \otimes I_8^{(2)} + I_8^{(1)} \otimes \bar{T} \otimes I_8^{(1)} + I_8^{(2)} \otimes \bar{T}] N_3 \tag{8.64}$$

where

$$\bar{T} = H_{px} + H_{pp}\bar{P} \tag{8.65}$$

Then

$$\bar{P}_3 = H_3 U_3^{-1} \quad \bar{P}_3^* = \bar{P}_3 M_3 \quad S_3 = \sum_{i=1}^{3} (\bar{P}_3^i)^T \tag{8.66}$$

The next step is to compute $\bar{P}_4$, which is $\bar{P}_4 = H_4 U_4^{-1}$. The following intermediate matrices are calculated

$$E_4 = \sum_{l=2}^{3} row(S_l A_{5-l}) = row(\bar{P} A_3) + row(S_3 A_2) \tag{8.67}$$

$$F_4 = \sum_{l=1}^{3} row(C_l^T C_{4-l}) = 0 \tag{8.68}$$

$$Z_4 = row(S_3 H_{pp} S_3^T) \tag{8.69}$$

$$W_{ij}^3 = \sum_{l=2}^{3} row(S_l B_{ij}^{4-l}) = row(S_2 B_{ij}^2) + row(S_3 B_{ij}^2) = 0 \tag{8.70}$$

$$I_4^1 = \sum_{l=2}^{3} \sum_{j=1}^{8} row((W_{1j}^l)^T Y_{1j}^{4-l}) = 0 \tag{8.71}$$

$$G_4^1 = \sum_{l=2}^{2} \sum_{j=1}^{8} row((W_{1j}^l)^T W_{ij}^{4-l}) = 0 \tag{8.72}$$

$$I_4^2 = \sum_{l=2}^{3} \sum_{j=1}^{2} row((W_{2j}^l)^T Y_{2j}^{4-l}) = 0 \tag{8.73}$$

$$G_4^2 = \sum_{j=1}^{8} row((W_{2j}^2)^T W_{2j}^2) = 0 \tag{8.74}$$

$$M_4 = x^{[4]}(x^{(4)})^{-1} \in \mathbf{R}^{330\times 4096} \tag{8.75}$$

$$N_4 = x^{(4)}(x^{[4]})^{-1} \in \mathbf{R}^{4096\times 330} \tag{8.76}$$

Afterwards,

$$H_4 = -\frac{1}{2}(Z_4 + 2E_4)N_4 \tag{8.77}$$

The U_4 can be computed as

$$U_4 = M_4[\sum_{i=1}^{4} I_8^{(i-1)} \otimes \bar{T} \otimes I_8^{(4-i)}]N_4 \tag{8.78}$$

$$= M_4[\bar{T} \otimes I_8^{(3)} + I_8^{(1)} \otimes \bar{T} \otimes I_8^{(2)} + I_8^{(2)} \otimes \bar{T} \otimes I_8^{(1)} + I_8^{(3)}\bar{T}]N_4 \tag{8.79}$$

Afterward,

$$\bar{P}_4 = H_4 U_4^{-1} \quad \bar{P}_4^* = \bar{P}_4 M_4 \quad S_4 = \sum_{i=1}^{4} (\bar{P}_4^i)^T \tag{8.80}$$

The $\mathcal{H}_\infty$ controller takes the following form

$$U_c = (-R_h^{-1} B_2^T \bar{P})x + (-R_h^{-1} \begin{bmatrix} B_{21}^T S_3^T \\ B_{22}^T S_3^T \end{bmatrix} N_2)x^{[2]} + (-R_h^{-1} \begin{bmatrix} B_{21}^T S_4^T \\ B_{22}^T S_4^T \end{bmatrix} N_3)x^{[3]} \tag{8.81}$$

The suggested controller satisfies disturbance attenuation property in Eq. (8.31). For proof, interested readers can refer to [192].

8.4 Simulation Results

In this section, performance of the $\mathcal{H}_\infty$ controller is evaluated using parameters of the Vario helicopter shown in Appendix A. To make the results more applicable, servo dynamics are taken into account. Also, synchronization assessment is performed by adding pure lag components into the closed-loop simulation. This aims to test the ability of the $\mathcal{H}_\infty$ controller to tolerate the pure lags existing in the flight computer, and to provide insight into implementation of the proposed controller. Disturbance attenuation capability of the $\mathcal{H}_\infty$ controller is also examined in a gusty environment and compared with a PID controller.

The longitudinal and lateral flapping commands given in Eq. (8.81) need to be converted into longitudinal and lateral cyclic for implementation. As the flapping reacts instantaneously, the longitudinal and lateral cyclic can be calculated using a closed-form linear solution given the desired flapping angles a_1^{des} and b_1^{des} generated by the $\mathcal{H}_\infty$ controller, i.e.,

$$B_{lon} = q\tau_m - a_1^{des} - \frac{\partial a_1}{\partial u} u \tag{8.82}$$

$$A_{lat} = -p\tau_m - b_1^{des} + \frac{\partial b_1}{\partial v} v \tag{8.83}$$

It has been identified experimentally that servo dynamics can be approximated using the first-order transfer function with time constant τ_s [111, 194]. We tested the upper limit of τ_s that the $\mathcal{H}_\infty$ controller can tolerate. For the Vario platform, simulations show that the upper limit turns out to be 60 ms. In practice, performance of the controller is also affected by synchronization issues due to the fact that pure lags exist because sensor data arrive at different time. Pure lags are essentially caused by transmitting, decoding and waiting until the next control update cycle. Therefore, a group of signals are required to wait for certain time in order to generate control commands in conjunction with other signals of late arrival. Pure lags are unavoidable when a controller is to be applied in practice. The simulations reveal that the $\mathcal{H}_\infty$ controller can tolerate a pure lag up to 30 ms. Although servo dynamics and pure lag effect are not considered when designing the $\mathcal{H}_\infty$ controller, the upper bounds from the simulations provide a clue on the requirement of implementing our controller.

PID controllers have been widely applied due to their simplicity and effectiveness. In the considered application, height and yaw motion are stabilized using the feedforward and PD controllers. For the inner loop (roll and pitch) dynamics, two PD controllers are employed. Once control of inner loop is achieved, PID controllers are tuned for position and velocity (outer loop) control with the integral of the error signal eliminating undesired offsets.

The coupling effects between the inner loop and the outer loop of the helicopter dynamics make it challenging to tune PID control gains to achieve satisfactory responses. Simulations suggest that PID gains should be tuned separately [82]. The strategy is to firstly tune control gains for altitude and yaw motion. Then, control of roll and pitch in the inner loop can be accomplished by repeating the same procedure. Afterwards, control gains in the outer loop are tuned while control gains in the inner loop are freezed. In the simulation, six PID controllers with the form

$$U_{PID} = k_p + \frac{k_i}{s} + k_d s \tag{8.84}$$

are selected with five PD controllers for altitude, yaw, roll, pitch and longitudinal position. A PID controller is used to remove offsets in lateral position.

To obtain the proper PID control gains, we empirically choose a group of gains

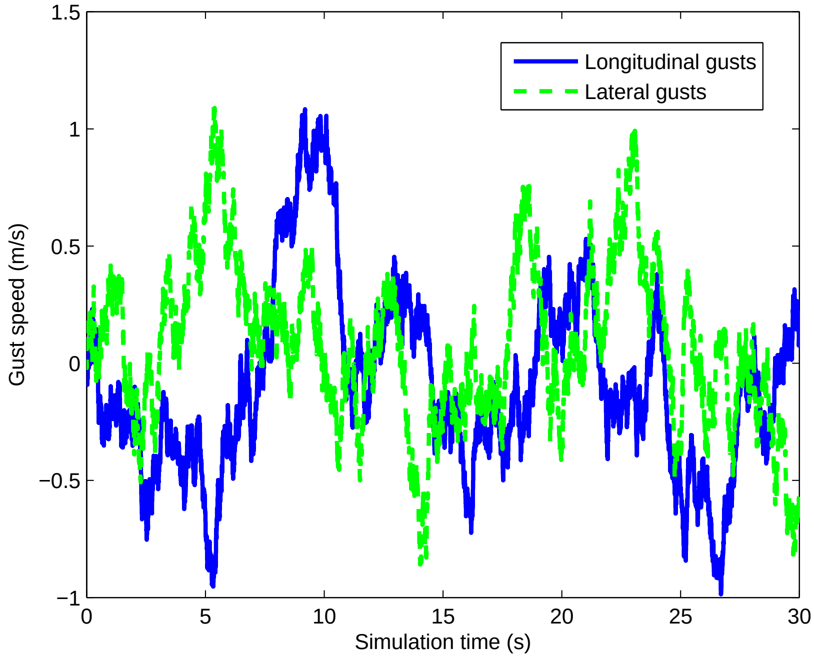

Figure 8.1. Horizontal gusts used to test the $\mathcal{H}_\infty$ controller

Table 8.1. Control gains for PID controllers

	k_p	k_i	k_d
Altitude–PD	0.4	0	0.05
Yaw–PD	0.8	0	1.05
Roll–PD	−0.9	0	−0.5
Pitch–PD	0.5	0	0.1
Longitudinal–PD	−0.1	0	−0.1
Lateral–PID	0.05	0.005	0.2

which satisfy performance specifications such as settling time ($< 40s$) and steady-state error ($<$ %5 of reference signal). The integral of squared errors

$$J_e = J_{in} + J_{out} = \int_0^T [e_z^2(t) + e_\psi^2(t) + e_\theta^2(t) + e_\phi^2(t)]dt + \int_0^T [e_x^2(t) + e_y^2(t)]dt \quad (8.85)$$

provides a principle to choose the proper control gains. Here, J_{in} and J_{out} are integral of square errors of inner and outer loops, separately. Symbols $e_z, e_\psi, e_\theta, e_\phi, e_x, e_y$ are attitude and position errors. The performance index J_e aims to investigate the

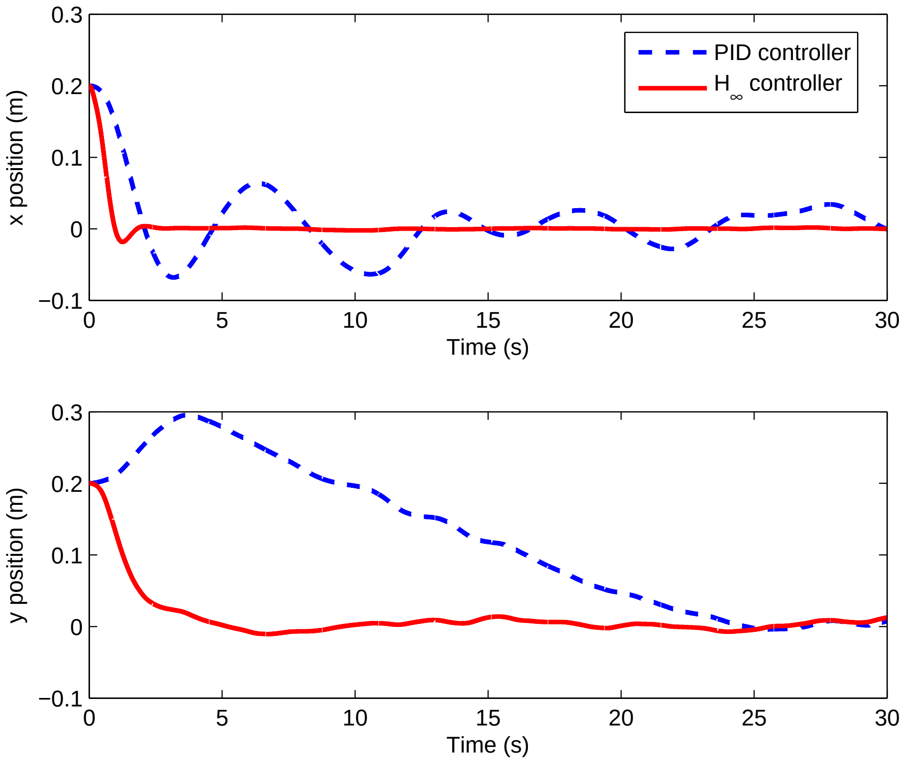

Figure 8.2. Helicopter position response using the PID controller and the $\mathcal{H}_\infty$ controller

overall squared errors when PID control gains are selected in different values. The proper PID control gains are chosen such that they can reduce J_e greatly while exhibiting satisfactory transient responses. These control gains are used for comparison purposes, as shown in Table 8.1.

The Dryden gust model typically captures characteristics of atmosphere turbulence at low altitudes and flight speeds [125]. Therefore, in our application where the RUAV is operated at a low height, it is used to produce representative gusts to test the performance of both $\mathcal{H}_\infty$ and PID controllers. In simulations, the same Dryden gust model is employed so that performance of different controllers can be compared under the same gusty environment. The gust model used for controller comparison is show in Fig. 8.1. To design the $\mathcal{H}_\infty$ controller, it is assumed that $\delta = 0.2$ and attenuation factor $\gamma_h = 6$. It takes 35.9 s to compute the weighting matrices in the controller. The horizontal position responses are shown in Fig. 8.2. It is noticed that positions x_b and y_b settle faster to the desired values $(x_b = 0, y_b = 0)$

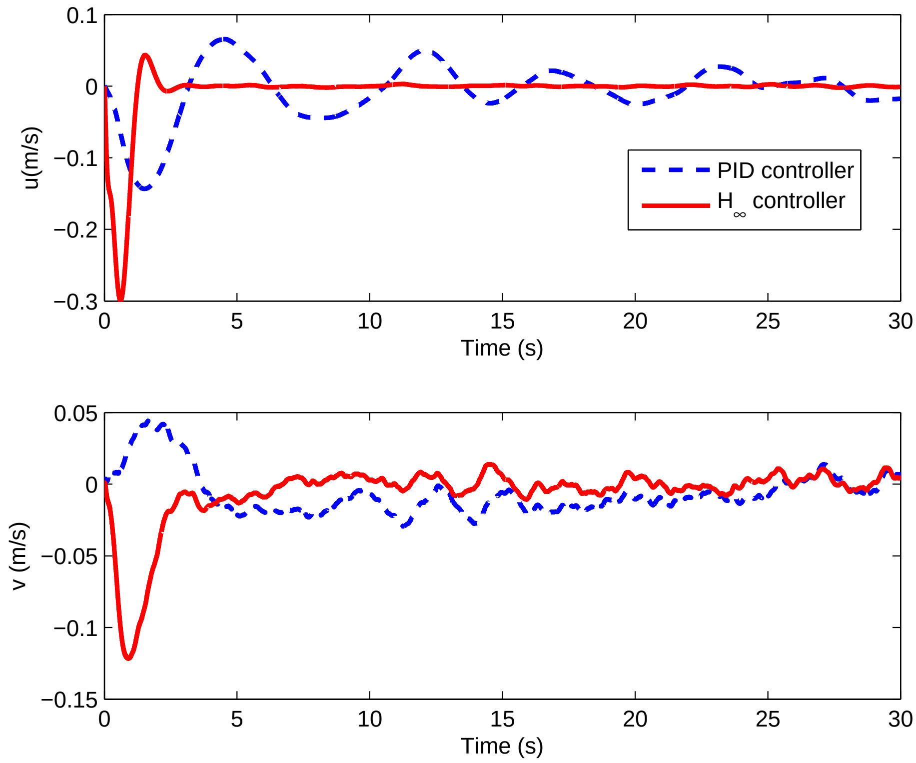

Figure 8.3. Helicopter velocity response using the PID controller and the $\mathcal{H}_\infty$ controller

from initial positions ($x_b = 0.2$ m, $y_b = 0.2$ m) when the $\mathcal{H}_\infty$ controller is applied. The faster responses are the outcome of the rapid velocity responses depicted in Fig. 8.3. It takes more than 25 s for the PID controller to attenuate gust effect to an acceptable level, and the oscillations in position cannot be damped completely. Control variables are shown in Fig. 8.4 and 8.5. The longitudinal cyclic using the $\mathcal{H}_\infty$ controller approaches that caused by the PID controller after 3 s. It is indicated in Fig. 8.5 that the $\mathcal{H}_\infty$ controller results in less oscillations in the lateral cyclic. Also, longitudinal and lateral cyclic are subject to larger transient response when the $\mathcal{H}_\infty$ controller is used. Thus for implementation of the $\mathcal{H}_\infty$ controller, more energy is required during the transient phase.

8.5 Summary

The horizontal position of the RUAV under disturbances is controlled using a nonlinear state feedback $\mathcal{H}_\infty$ controller in this chapter. Performance of the $\mathcal{H}_\infty$ controller

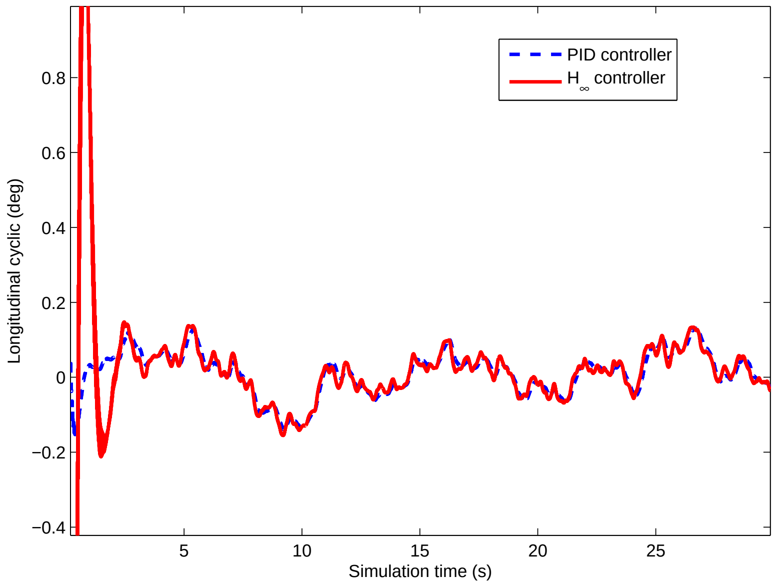

Figure 8.4. Longitudinal cyclic using the PID controller and the $\mathcal{H}_\infty$ controller

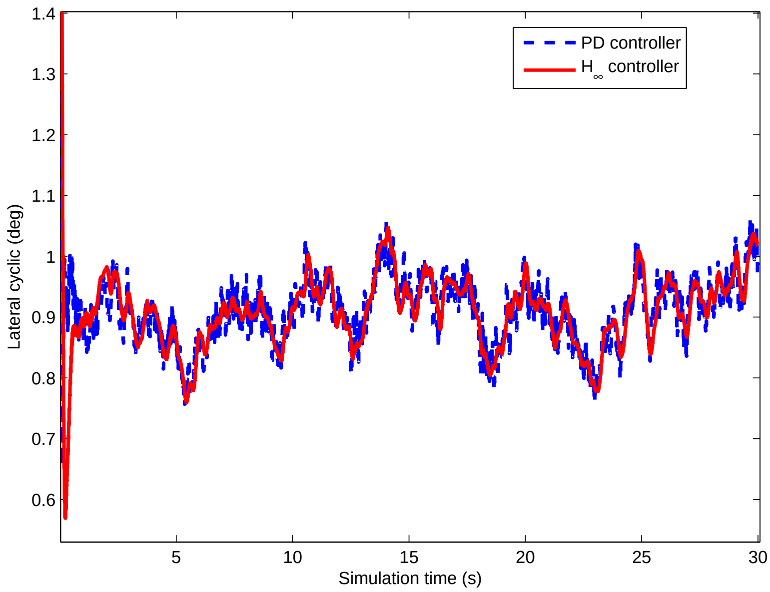

Figure 8.5. Lateral cyclic using the PID controller and the $\mathcal{H}_\infty$ controller

is evaluated through simulation in consideration of servo dynamics and pure lags. Comparison studies show that the $\mathcal{H}_\infty$ controller can settle the horizontal position of the RUAV more rapidly than a PID controller in a gusty environment.

Chapter 9

Automatic Landing of a RUAV in Rough Seas

9.1 Introduction

This chapter presents a generic and practical framework for automatic landing of a RUAV in rough seas. This framework is a synthesis of the work presented in previous chapters. Through extracting mean height of the landing deck using the recursive PA, the RUAV is able to track the dynamic mean deck height and avoid position oscillations. The feedback-feedforward controller is employed for height stabilization of the RUAV when gusts occur. To improve horizontal position tracking performance, the nonlinear $\mathcal{H}_\infty$ controller is applied. Moreover, a flight control system is designed to adjust positions and attitudes of the RUAV to achieve a smooth landing trajectory. The automatic landing strategy is tested for the Vario helicopter in simulations using real-time deck displacement data. A closed-loop high-fidelity simulation model using C-code S-function has been constructed to implement the proposed landing procedure and can be applied to other RUAV platforms.

9.2 Architecture of the RSLS

The proposed architecture of the RSLS is shown in Fig. 9.1. The primary objective of the RSLS is to specify the applicable landing trajectories in consideration of RUAV maximum operational limitations in a variety of sea conditions. A portion of the emphasis is also placed on maintaining adequate dynamic performance and in particular, on stability of the RUAV in the presence of variations in plant dynamics and atmospheric disturbances. Effect of wind gusts is taken into account to investigate characteristics of the flight dynamics when the RUAV approaches the ship deck. Flying qualities requirements of the RUAV under different sea conditions can also be studied to reduce the possibility of mission failures. The proposed RSLS also attempts to consider practical constraints to make the simulation results reliable and representative. Moreover, this RSLS can reflect the potential issues which possibly happen during the real-time landing operations, and contribute to finding solutions ahead of flight tests.

The top view of the RSLS depicted in Fig. 9.1 consists of the following subsystems: helicopter dynamics, sensor fusion, flight control system and servo dynamics. Detailed modeling of helicopter aerodynamics can be found in Chapter 3. Effect of turbulent gusts on helicopter flight dynamics is considered and simulated using the gust model described in Section 3.6. The sensor fusion algorithm which serves to estimate deck displacement and helicopter states is devised based on the EKF with detailed design procedure given in Chapter 5. Based on the helicopter positions and mean deck height, the desired approach trajectory is planned. Servo dynamics are modeled as the first-order transfer function with the time constant τ_s. Time lag and actuator saturation are also considered.

9.3 Automatic Landing Procedure

In this section, a feasible procedure for the purpose of automatic landing of the RUAV in rough seas is outlined, followed by a detailed description of the flight control system to implement the landing procedure.

9.3.1 Overall Landing Procedure

The proposed landing procedure consists of three phases:

- When the RUAV approaches the ship deck, The sensor fusion algorithm is employed to filter noisy measurements of positions and velocities of the RUAV. Ship deck positions are also estimated by integrating the relative position information provided by the TS;

- The recursive PA is employed to extract the mean deck height based on the estimated deck displacement;

- Based on the mean deck height, the RUAV follows a smooth descent trajectory to approach the landing deck without experiencing significant oscillations in height;

- When the RUAV is very close to the ship deck, it starts predicting the ship deck displacement. Once the moment when the ship deck reaches the maximum height (relative velocity is zero) is predicted, the RUAV arranges the landing

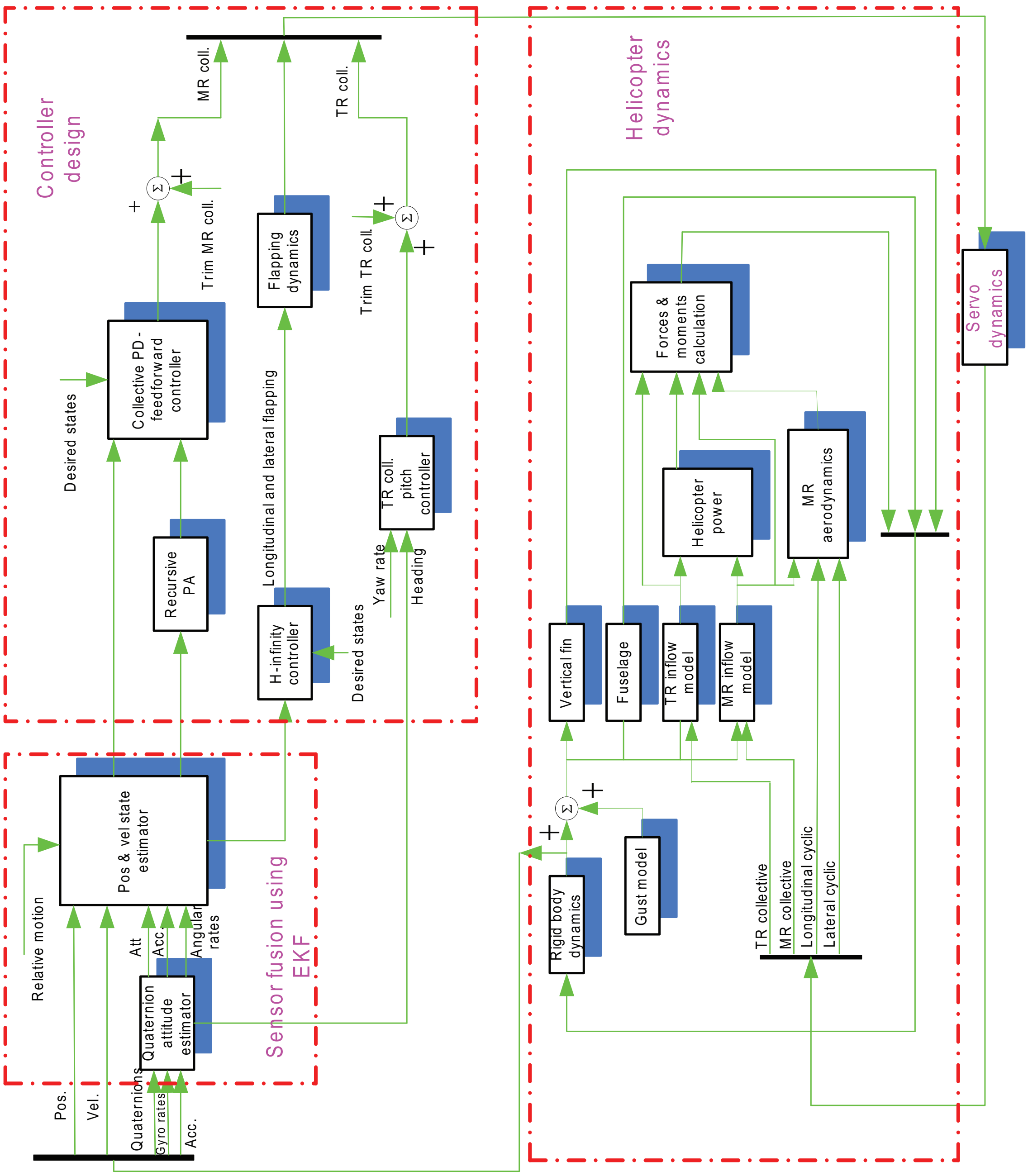

Figure 9.1. Top view of the integrated automatic landing system

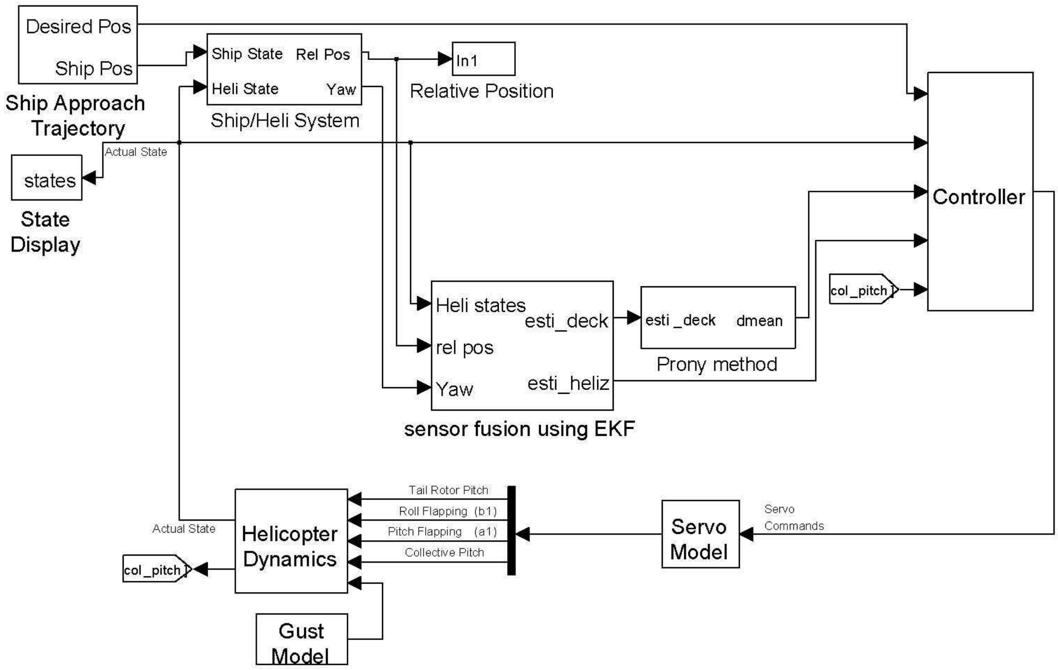

Figure 9.2. Top view simulation model of RSLS

trajectory to ensure the touchdown operation happens when the deck is around the maximum height.

It should be noted that the accurate estimation of deck displacement is crucial for the whole landing task. This requires the hover period to be long enough to obtain reliable estimation of the deck displacement. The desired landing trajectory is predefined before the landing operation is triggered. Normally, for different maritime environments, desired landing trajectories are designed beforehand in consideration of operational and flight envelope requirements. They are programmed and saved on the flight computer, and the most suitable one is chosen for the specific maritime environment.

9.3.2 Flight Control System

The flight control system aims to control positions and attitudes of the RUAV during the approach and landing process so that a smooth landing trajectory can be achieved. For an automatic landing in a gusty environment, height control is crucial as the RUAV is subject to significant oscillations when gusts occur. Loss of height control may cause the touchdown moment to happen when the impact force is maximum, and the RUAV could be destroyed. Therefore, stabilization of height in a gusty environment is a prerequisite for the automatic landing operation. To achieve gust attenuation in the vertical direction, the feedback-feedforward controller proposed in Chapter 7 is employed, which takes the form of

$$\theta_{col} = k_{mp} e_z + k_{md} w + \Delta\theta \tag{9.1}$$

where the proportional gain k_{mp} is expressed as

$$k_{mp} = \begin{cases} k_{mp1} & \text{if } t < T_1 \\ k_{mp1} + s_l(t - T_1) & \text{if } T_1 \leq t < T_2 \\ k_{mp1} + s_l(T_2 - T_1) & \text{if } t \geq T_2 \end{cases}$$

The altitude error $e_z = \hat{z}_b - z_d - \bar{z}_d$ indicates the RUAV is supposed to be driven to the mean deck height. Here, symbol $\hat{z}_b$ is the estimated altitude of the RUAV, z_d desired altitude of the RUAV, $\bar{z}_d$ the mean height of deck displacement, and w vertical velocity of the RUAV. It is seen that the k_{mp} increases from time moment T_1 to reduce the oscillations caused by the deck motion. Time moment T_1 should be chosen such that sufficient deck displacement data have been collected to make the Prony algorithm work. The initial gain k_{mp1} should be chosen to damp the oscillations to a small level. Also, time moment T_1 should be large enough to make sure that the mean deck height has been extracted, and T_2 should be chosen such that the RUAV approaches the landing deck by following a smooth trajectory within the operational availability. The slope s_l should be selected to guarantee the RUAV approaches the landing deck at a reasonable descending rate. The derivative gain is denoted by k_{md}. Offset $\Delta\theta$ is the amount of collective pitch required to dynamically compensate for gust effect, and it is calculated based on the estimated gusts which are given by the gust estimator. The detailed procedure to compute the $\Delta\theta$ is given in Chapter 7.

The horizontal positions and velocities of the RUAV are controlled using the nonlinear $\mathcal{H}_\infty$ controller. The controller aims to improve the position tracking capability of the RUAV in a gusty environment so that the desired landing trajectory can be achieved. Roll and pitch motion are also stabilized using this controller. The detailed procedure for design of the $\mathcal{H}_\infty$ controller is given in Chapter 8.

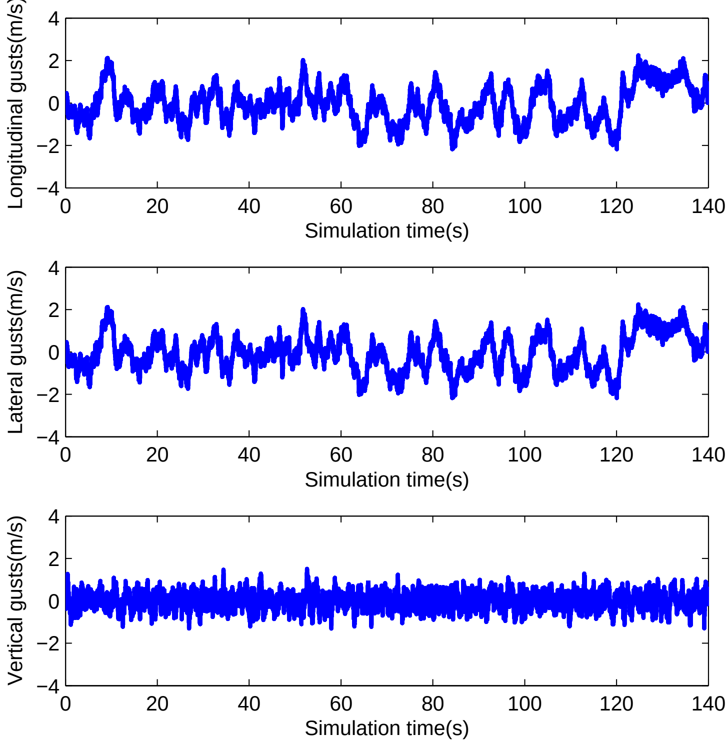

Figure 9.3. Gust model used in the simulation

The tail rotor collective pitch θ_{ped} is stabilized by a PD controller:

$$\theta_{ped} = k_{tp}e_{\psi} + k_{td}r \tag{9.2}$$

where the yaw error is $e_{\psi} = \psi_d - \psi$ and ψ_d is the desired yaw motion.

9.4 Simulation Results

In this section, performance of the proposed RSLS is examined using a 6-DOF dynamic model of the Vario helicopter based on simulation parameters consistent with those employed in real applications. To make the simulation results reliable, flapping dynamics and servo dynamics are considered. The Dryden gust model typically describing properties of atmospheric turbulence at low altitudes and flight speeds is employed to generate representative gusts to test performance of the proposed RSLS. Simulation seeds of turbulent gust models are set within an extensive range

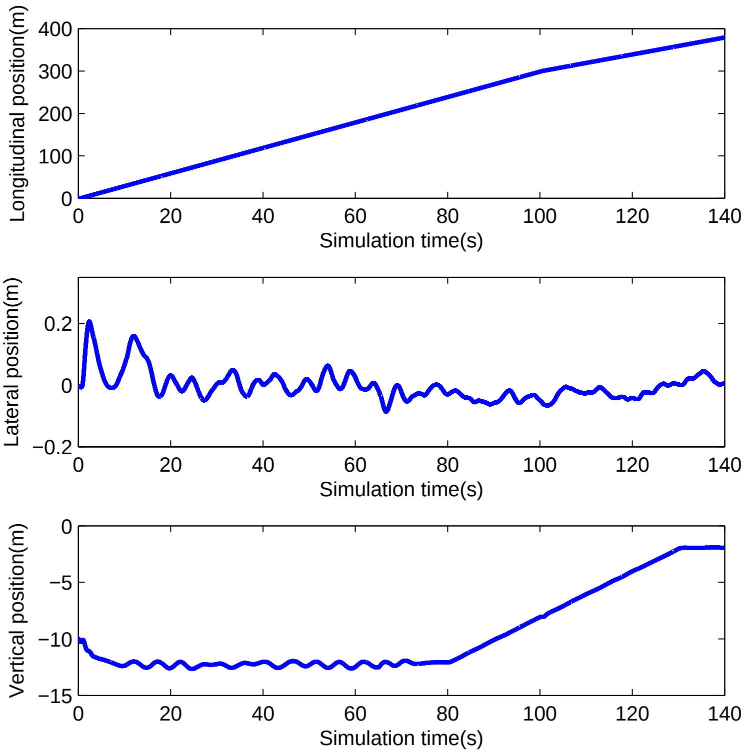

Figure 9.4. RUAV positions during the landing operation

to produce wind gusts with different statistical properties. The top view of the simulation model is shown in Fig. 9.2 with each subsystem depicted in Appendix C.

In the considered application, the desired trajectory is to hover the RUAV at a height of 10 m above the landing deck. Once the mean deck height is extracted, the RUAV follows a slope trajectory to approach and land on the ship deck. The expected slope during the landing phase is 0.2 m/s. Wind gusts are considered in the RSLS to model the gusty environment the RUAV experiences. Figure 9.3 shows the turbulent gusts used in the simulation with special emphasis placed on horizontal gusts. The estimated helicopter positions and velocities are shown in Fig. 9.4 and Fig. 9.5, which indicate the helicopter approaches the landing deck at a constant speed of 3 m/s in longitudinal direction. Also, it follows behind the middle line of the ship and there are slight oscillations in the lateral position. For the vertical velocity, it is noticed that oscillations the helicopter experiences last for around 70 s,

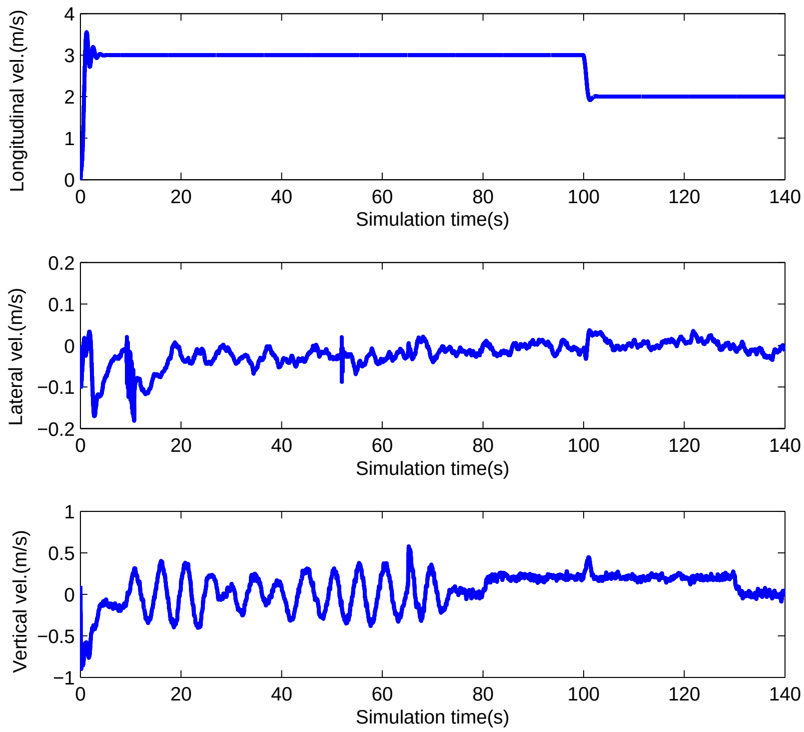

Figure 9.5. RUAV velocities during the landing operation

resulting from the fluctuating deck motion. The attitudes of the RUAV are shown in Fig. 9.6. It is noticed that roll angle is stabilized to around 4.6°, pitch and yaw are around zero. As is shown in Fig. 9.7, the ship proceeds with a constant speed and zero sideways motion is observed. The ship deck moves in an oscillating mode around -2 m (negative direction is above the sea level). It takes the EKF 10 s to track the real ship motion.

Table 9.1. Parameters used in the flight control system

Parameters	Value	Parameters	Value
k_{mp1}	0.03	k_{md}	0.2
k_{tp}	0.05	k_{td}	0.25
T_1	65	T_2	75
s_l	0.04		

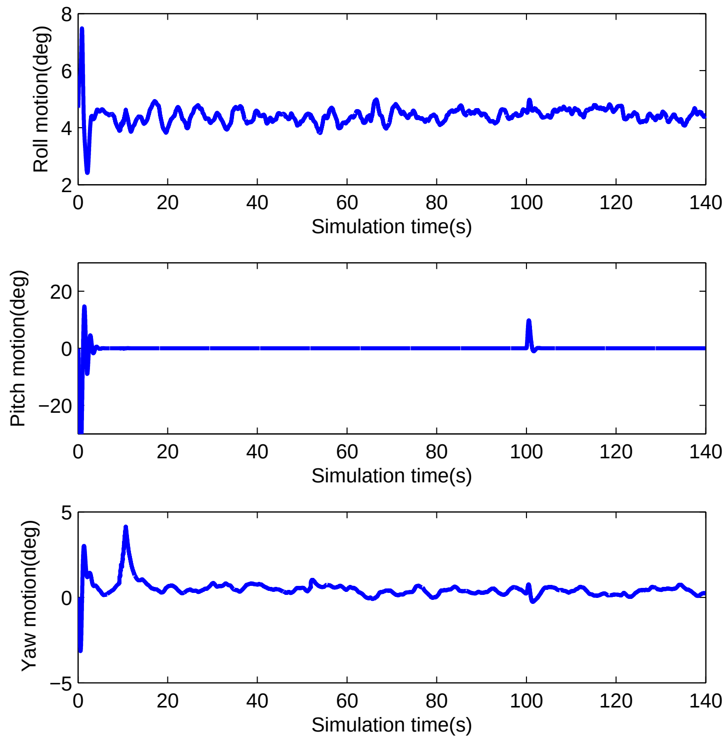

Figure 9.6. RUAV attitudes during the landing operation

The complete landing operation of the Vario is illustrated in Fig. 9.9 with control gains used in simulation shown in Table 9.1. The blue curve (solid) and the green curve (dashed) are the real and estimated deck displacement. The red curve (solid) corresponds to the estimated deck motion in the first 65 s, and the rest corresponds to the mean deck height. The cyan curve (dash dotted) is the vertical landing trajectory. Initially, the Vario helicopter starts hovering 10 m above the landing deck. Meanwhile, the EKF is activated to smooth out noise in vertical distance z_b, and estimate instantaneous deck displacement. It is seen that 10 s is needed before the EKF outputs an accurate estimation. The EKF continues to execute for 65 s before the modified PA is triggered to extract mean deck height $\bar{z}_d$. A slow-varying switch mode using the following weighting function is used to make the estimated deck displacement z_{esti_deck} change to the mean deck height $\bar{z}_d$ smoothly

$$\bar{z}_d = k_z z_{prony} + (1 - k_z) z_{esti\_deck} \tag{9.3}$$

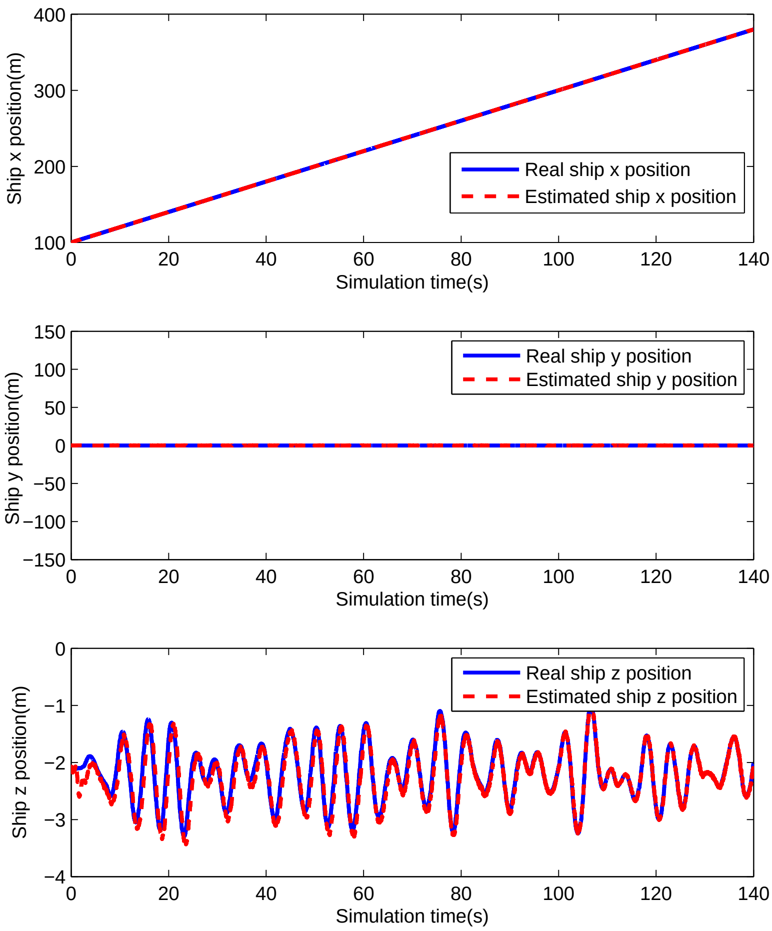

Figure 9.7. Estimation of ship positions during the landing operation

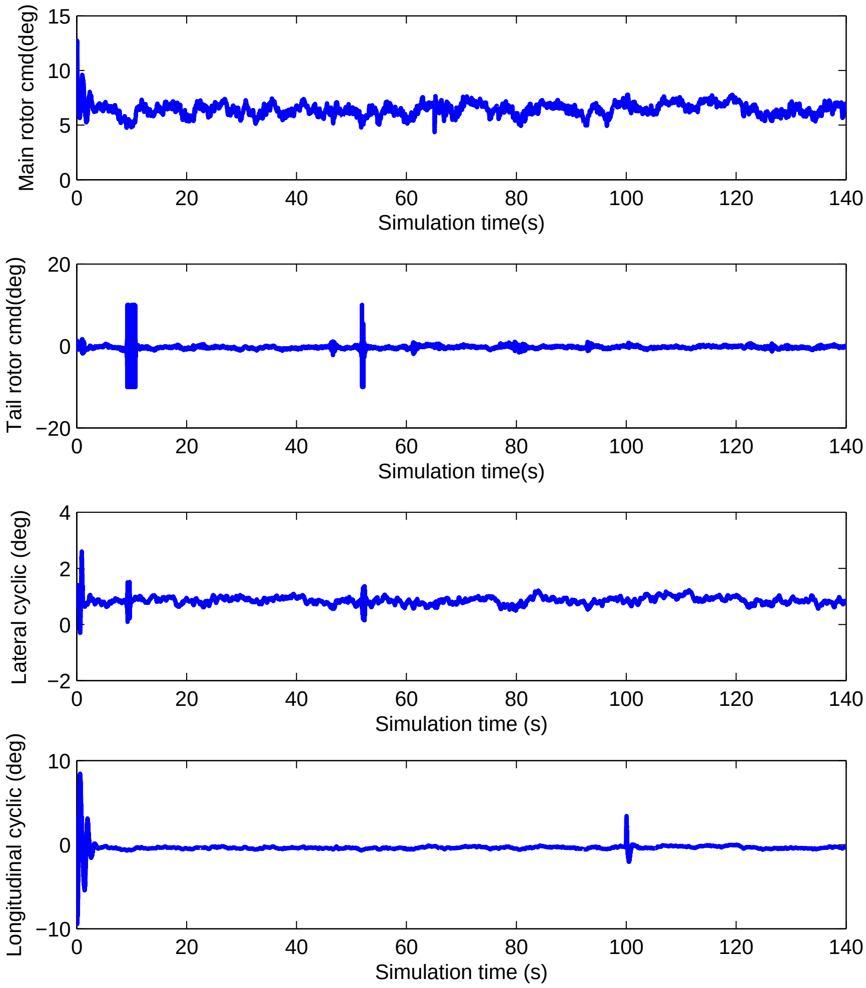

Figure 9.8. Control variables during the landing operation

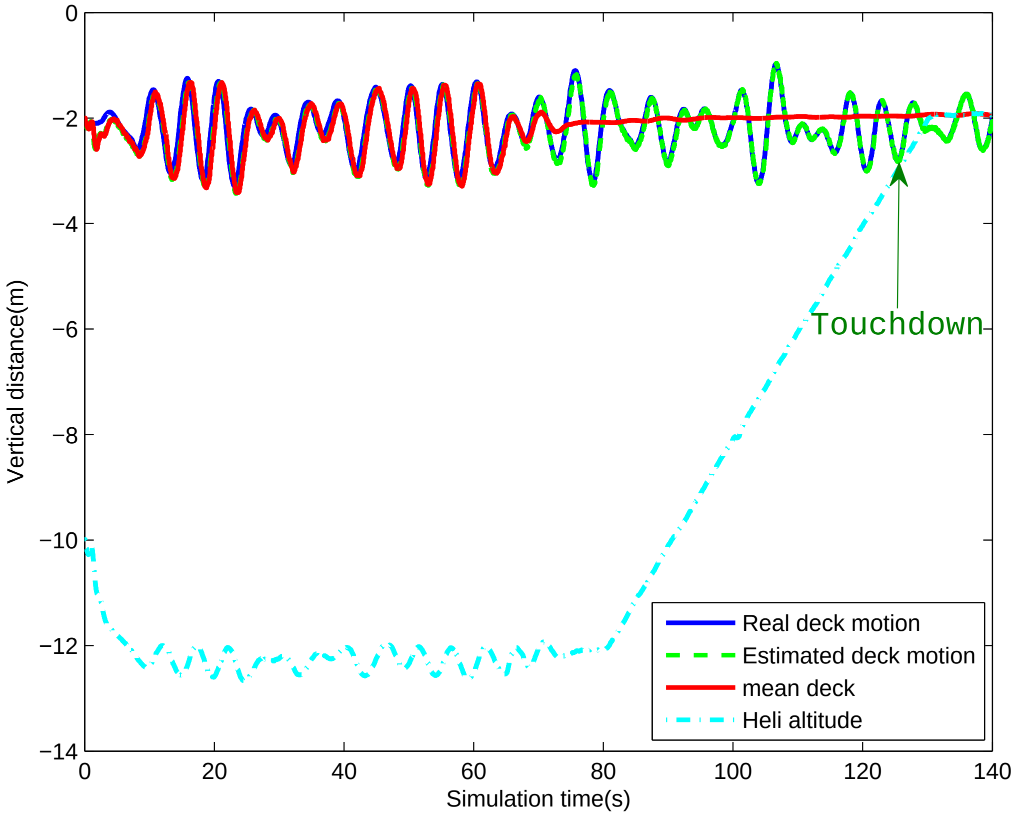

Figure 9.9. RUAV vertical landing trajectory using the proposed procedure

where

$$k_z = \begin{cases} 0 & \text{if } t < 65 \\ 0.1(t-65) & \text{if } 65 \leq t < 75 \\ 1 & \text{if } t \geq 75 \end{cases}$$

and z_{prony} is the mean height from the proposed PA. Afterwards, the RUAV starts descent operation by tracking the mean height of the deck. For the deck motion data shown here, it is seen that the deck height happens to reach the maximum when the RUAV tracks the mean deck height. Therefore, the RUAV completes the touchdown operation at that moment. Due to the time constraints, the ship motion predictor will be incorporated into the landing strategy as future work. Control variables during the landing phase are depicted in Fig. 9.8, which are kept within a reasonable range throughout the simulation. It is seen that a safe touchdown operation happens when time of flight is 126 s.

9.5 Summary

In this chapter, a recovery procedure is outlined for an automatic landing of the Vario helicopter in a gusty environment. A high-fidelity simulation model is developed. The closed-loop simulation shows that the proposed recovery system enables a successful automatic landing of RUAVs.

Chapter 10

Conclusion and Future Work

This dissertation has examined challenges in the design of RUAV control and navigation systems with the goal of developing a systematic scheme to increase stability of the RUAV and achieve reliable automatic landings in a gusty environment. Herein, the main contributions of the thesis are summarized and some possible future research directions are addressed.

10.1 Achievements

In this thesis, a generic landing framework has been designed with sufficient positioning accuracy and tracking capability to enable high levels of RUAV autonomy in rough sea states. The key to the automatic landing is to estimate ship positions and extract the mean deck height which can provide a reference for arranging the landing trajectory and designing the flight control system. A feedback-feedforward controller has been designed to stabilize helicopter height in a gusty environment, and its performance has been experimentally tested. In addition, horizontal position tracking ability has been improved using the nonlinear $\mathcal{H}_\infty$ controller. The automatic landing system has been verified using the parameters of the Vario helicopter, and can be adapted to accommodating other RUAV platforms. The complete landing system has been implemented using C-file S-function blocks in MATLAB/SIMULINK, and the code can be transferred directly to the helicopter autopilot for flight validations.

10.2 Recommendations

Some technical considerations which should be addressed are as follows:

1. The accuracy of sensors onboard affects that of the gust estimator. Thus, it is desirable that window widths for the MAFs should be chosen properly. For the chosen sensors, the window widths should be selected based on trial and error according to the flight test results;
2. When wind gusts are too small to be detected, it is very likely that the gust estimator will fail to work. Therefore, precautions should be taken in the code programming in case of gust estimator crash;

3. The number of measurements should be large enough so that the recursive PA is able to identify the dynamic trend of the deck height. In addition, carrying forward the error covariance matrix executed in the first step of the proposed PA is significant in conveying the trend information between adjacent data windows. Dimensions of this matrix determined by the PA model order affect the complexity of numerical computation. In simulations, it appears that the mean deck height is more likely to be extracted when model order is an odd integer. This indicates the Prony model is composed of a single exponential term together with a group of sinusoidal functions caused by complex conjugate poles. It is noted that the single exponential term is the primary source of the mean deck height;
4. Choice of the model order greatly affects the efficiency of the recursive PA in real-time applications. Simulations show that a large model order only slightly improves the model match accuracy. However, it slows down the processing speed. Therefore, a small model order is preferred when the prescribed match accuracy is satisfied for the sake of online implementation convenience.

10.3 Future Directions

The following are suggested as useful future directions in the development of automatic landing strategies for the RUAV.

10.3.1 Determination of Touchdown Moment

The proposed deck displacement predictor can be used to predict the moment when the landing deck reaches the peak positions, which can be incorporated into the landing system to enable the touchdown to happen during the period when the deck displacement moves at a small relative speed with respect to the RUAV. Also, the helicopter will be trivially flared using collective pitch just prior to touchdown to reduce the relative velocity between the ship deck and the helicopter.

10.3.2 Height Control using Stochastic Properties of Gusts

In the process of designing the feedback-feedforward controller, stochastic properties of wind gusts are not utilized. For the RUAV operating in a low altitude, since wind gusts can be modeled by passing white noise through shaping filters (Dryden model), it is possible that shaping filters can be integrated with heave motion dynamics to develop an augmented system. A state-space description of the augmented system could be established to design a controller based on modern control theory. By doing this, stochastic properties of wind gusts are explicitly considered and the resultant controller may further improve gust-attenuation capability;

10.3.3 Helicopter Control using Model Predictive Control Theory

Synchronization issues between sensors onboard and control algorithms may arouse implementation difficulties for state-feedback controllers which require signals from multiple channels. Owing to differences in signal transferring rate, the state-feedback controller needs to wait a certain amount of time before running the control algorithm and generating control commands. This would increase the possibility of the system becoming be unstable. For RUAVs, control commands usually update at a frequency of 50 Hz, resulting in a pure lag with the magnitude of up to 20 ms. In practice, it takes many milliseconds for sensor data to transmit, decode and wait before the next control update cycle. Typically, the pure lag is expected to be a minimum value of 40 ms subject to slow drifts in time. Since there is no applicable means of synchronizing the update cycles of various sensors and PWM signals. Pure lag should be considered in the controller design procedure, creating more requirements in the control performance. Model predictive control can be an option to solve this problem. Based on current system states, this control strategy computes a state trajectory to optimize behavior of the system for the next time interval. Once new sampled states become available, online calculations are repeated to compute the new controller by minimizing the cost function and to generate a new state trajectory. Design of a model predictive controller based on a system model of the RUAV which considers the time lag is a possible future direction.

Appendix A

Summary of Simulation Model and Parameters

The geometry and aerodynamic parameters of Eagle and Vario helicopters are given in the following tables.

Table A.1. Parameters of the Eagle helicopter in simulation

Parameters	Description	Value
a_{mr}	Main rotor blade 2D lift curve slope	5.7
a_{tr}	Tail rotor blade 2D lift curve slope	4.0
A_l	Lateral cyclic to main rotor pitch ratio	-0.17 rad/ms
B_l	Longitudinal cyclic to main rotor pitch ratio	-0.19 rad/ms
C_l	Longitudinal cyclic to flybar pitch ratio	-1.58 rad/ms
D_l	Lateral cyclic to flybar pitch ratio	-1.02 rad/ms
c_{mr}	Main rotor blade chord	0.058 m
c_{tr}	Tail rotor blade chord	0.026 m
C_{D_0}	Profile drag coefficient	0.012
I_{xx}	Moment of inertia about $x-$axis	0.30 kgm^2
I_{yy}	Moment of inertia about $y-$axis	0.82 kgm^2
I_{zz}	Moment of inertia about $z-$axis	0.40 kgm^2
I_{xz}	Product of inertia	-0.01 kgm^2
k_{ind}	Induced power correction factor	1.2
K_s	Flybar to main rotor pitch mixing ratio	0.8
k_β	center-spring rotor stiffness	270 N/m
M_a	All-up weight	8.2 kg
N_b	Number of main rotor blades	2
R_b	Main rotor radius	0.76 m
S^X_{fus}	Fuselage equivalent flat plate area in $x-$direction	0.025 m^2
S^Y_{fus}	Fuselage equivalent flat plate area in $y-$direction	0.084 m^2
S^Z_{fus}	Fuselage equivalent flat plate area in $z-$direction	0.027 m^2
κ_b	Profile drag power correction factor	4.7
Ω_{mr}	Main rotor angular velocity	167.5 rad/s
Ω_{tr}	Tail rotor angular velocity	884.3 rad/s

Table A.2. Parameters of the Vario helicopter in simulation

Parameters	Description	Value
a_{mr}	Main rotor blade 2D lift curve slope	5.7
a_{tr}	Tail rotor blade 2D lift curve slope	4.0
c_{mr}	Main rotor blade chord	0.076 m
c_{tr}	Tail rotor blade chord	0.043 m
C_{D_0}	Profile drag coefficient	0.012
I_{xx}	Moment of inertia about $x-$axis	12.3 kgm^2
I_{yy}	Moment of inertia about $y-$axis	18.7 kgm^2
I_{zz}	Moment of inertia about $z-$axis	6.6 kgm^2
I_{xz}	Product of inertia	0
k_{ind}	Induced power correction factor	1.2
k_{β}	center-spring rotor stiffness	1165.7 N/m
M_a	All-up weight	27.738 kg
N_b	Number of main rotor blades	3
R_b	Main rotor radius	1.25 m
S^X_{fus}	Fuselage equivalent flat plate area in $x-$direction	-0.036 m^2
S^Y_{fus}	Fuselage equivalent flat plate area in $y-$direction	0.0029 m^2
S^Z_{fus}	Fuselage equivalent flat plate area in $z-$direction	-0.6379 m^2
κ_b	Profile drag power correction factor	4.7
Ω_{mr}	Main rotor angular velocity	89.01 rad/s
Ω_{tr}	Tail rotor angular velocity	481.55 rad/s

Appendix B

Simulation Subsystems for the Feedback-feedforward controller

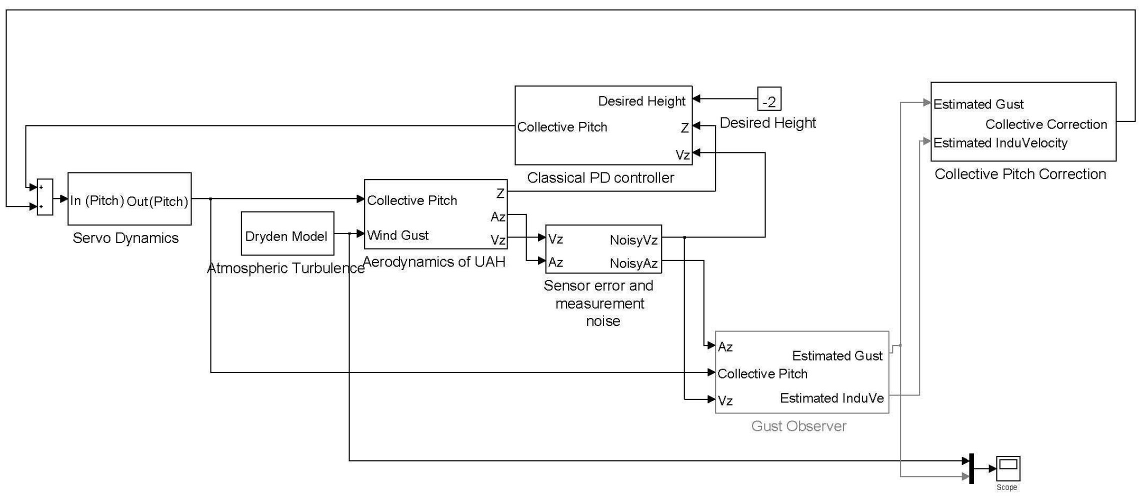

Figure B.1. Top view simulation model of the feedback-feedforward controller

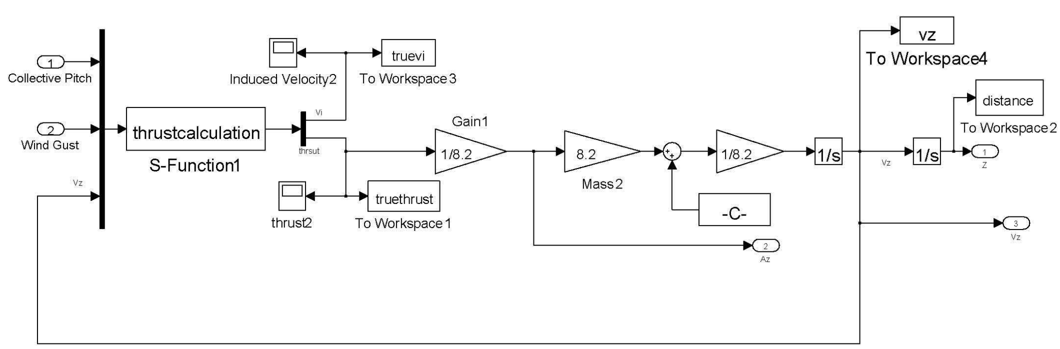

Figure B.2. Heave motion dynamics of the RUAV

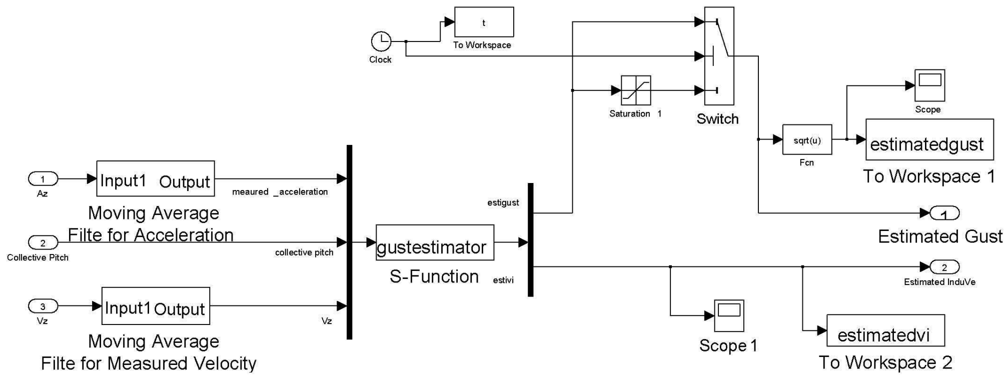

Figure B.3. Simulation model of the gust estimator

Appendix C

Simulation Subsystems for Automatic Landing of the Vario helicopter

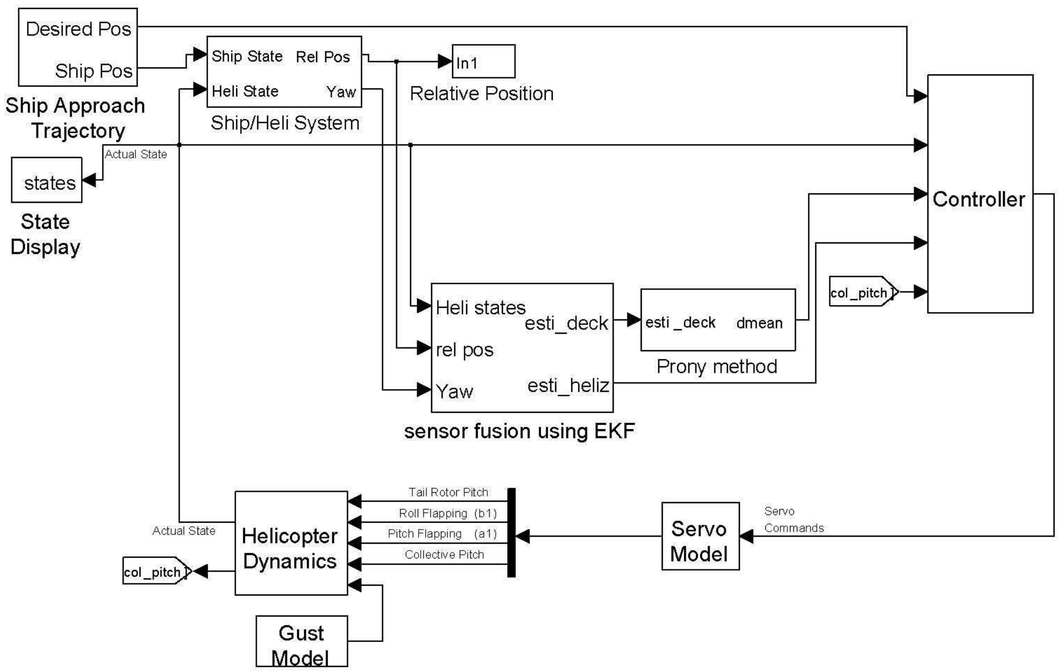

Figure C.1. Top view simulation of RSLS

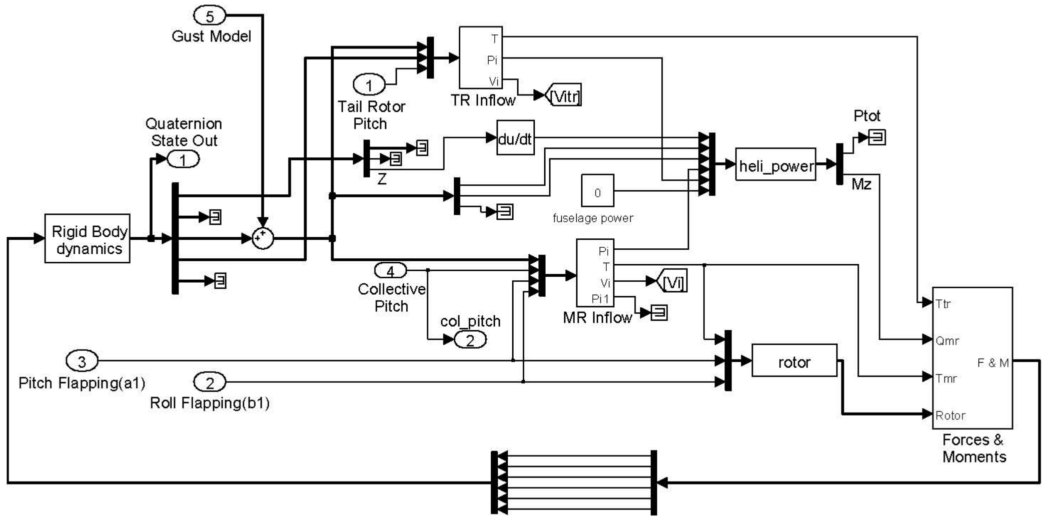

Figure C.2. Simulation model for the Vario helicopter

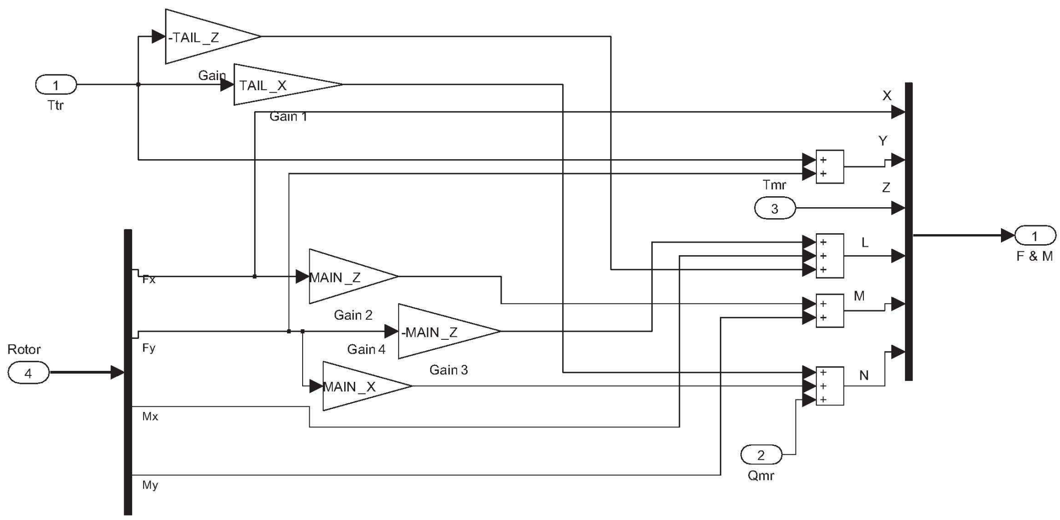

Figure C.3. Simulation of forces and moments

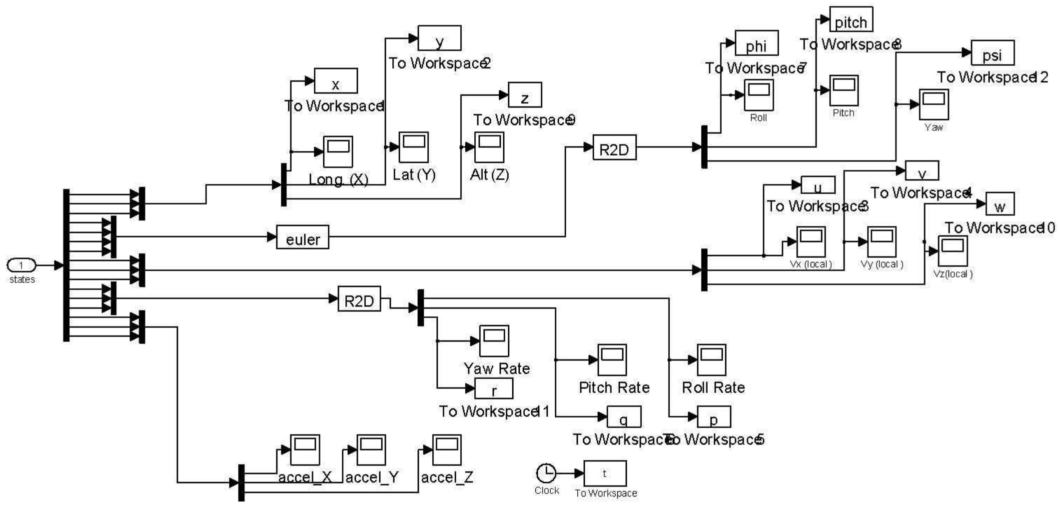

Figure C.4. Helicopter state display

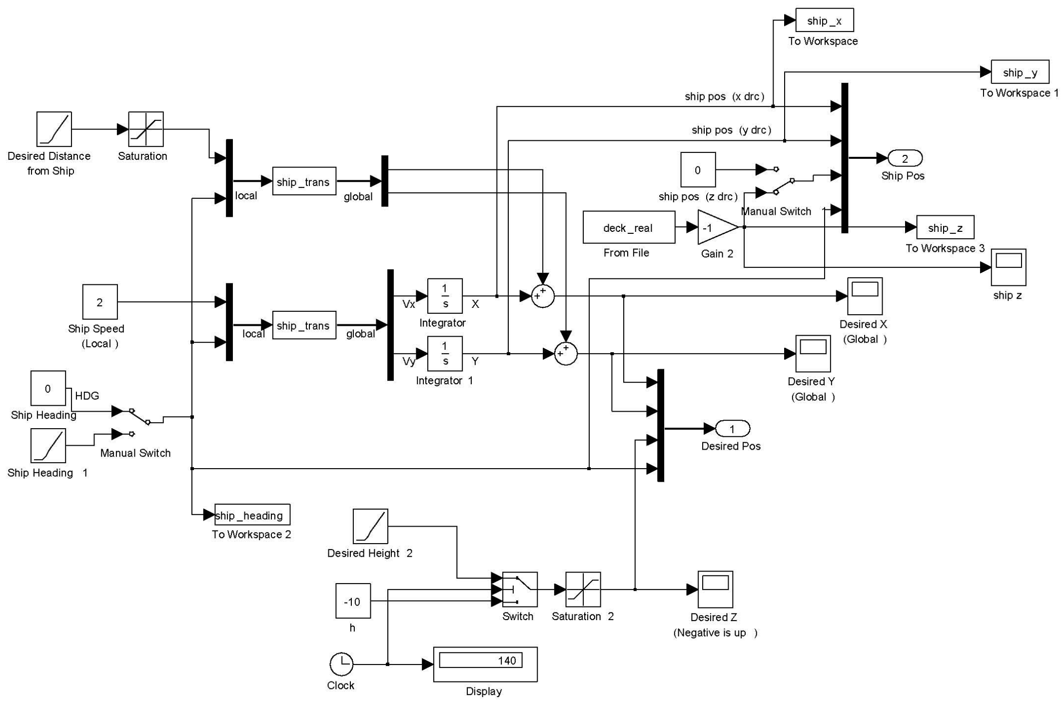

Figure C.5. Helicopter/ship relative motion

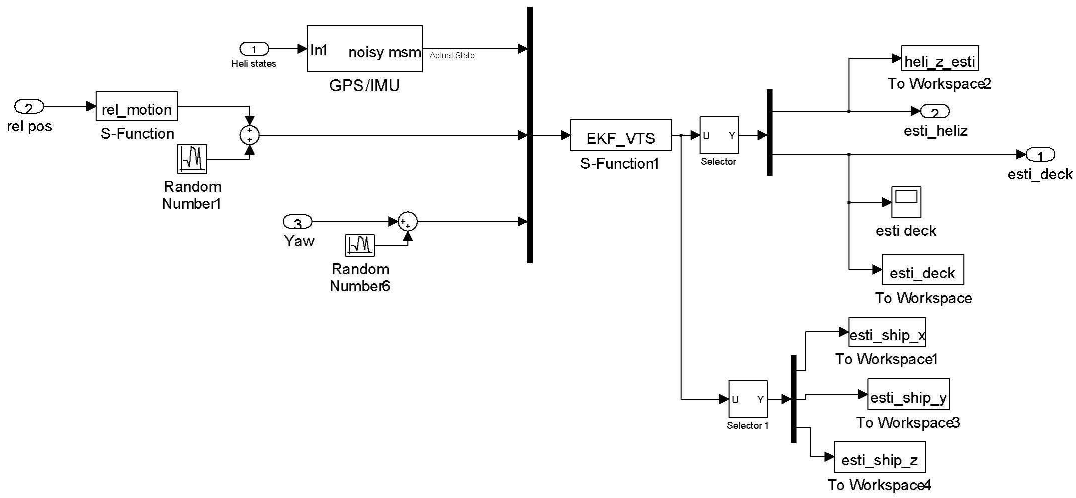

Figure C.6. Simulation model of the EKF

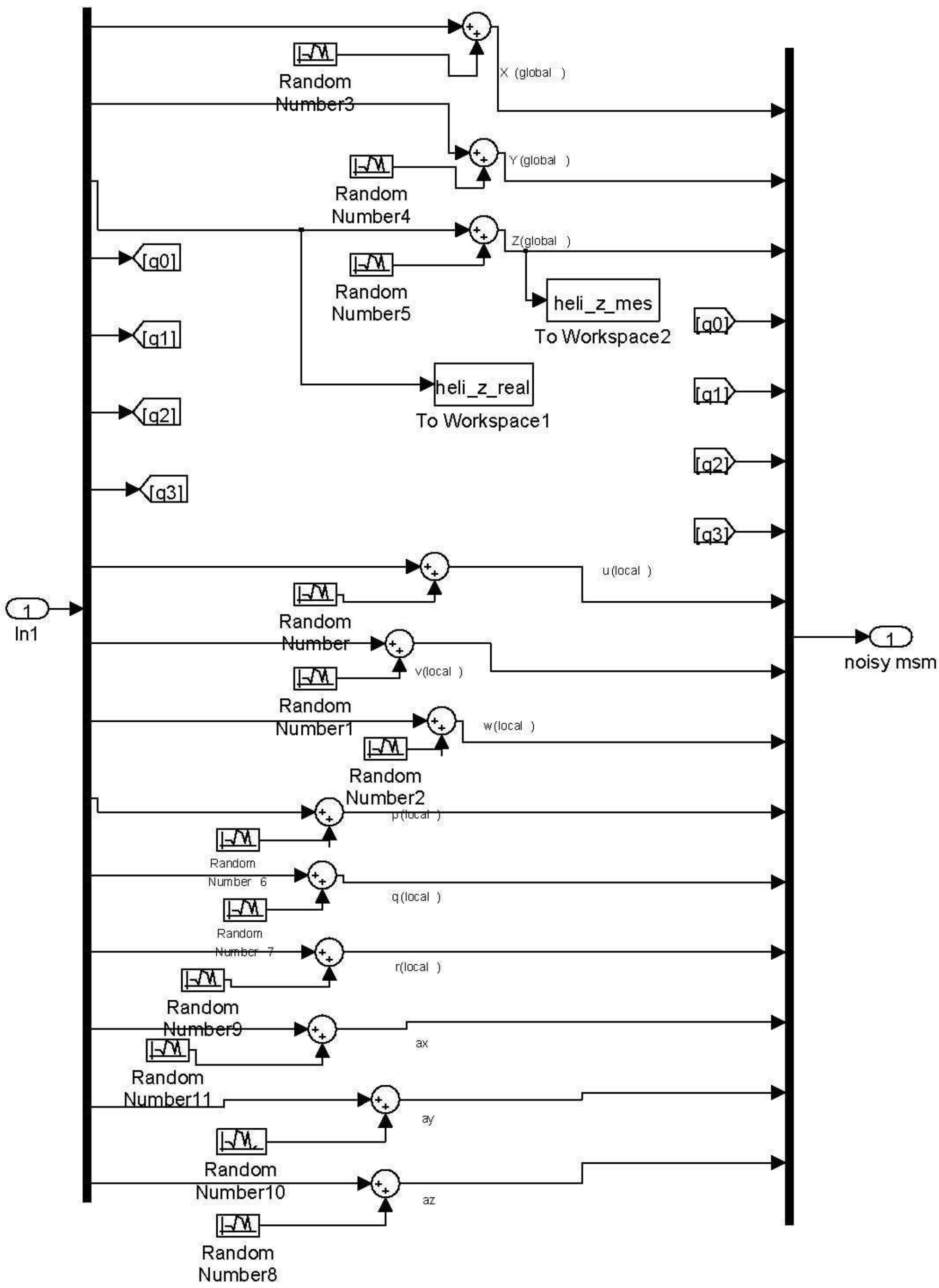

Figure C.7. Inputs to the EKF

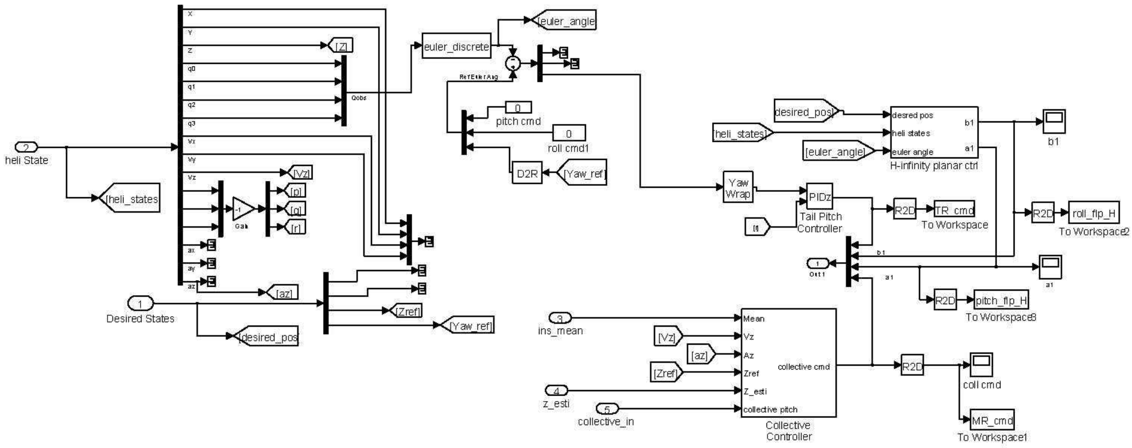

Figure C.8. Top view of the flight control system

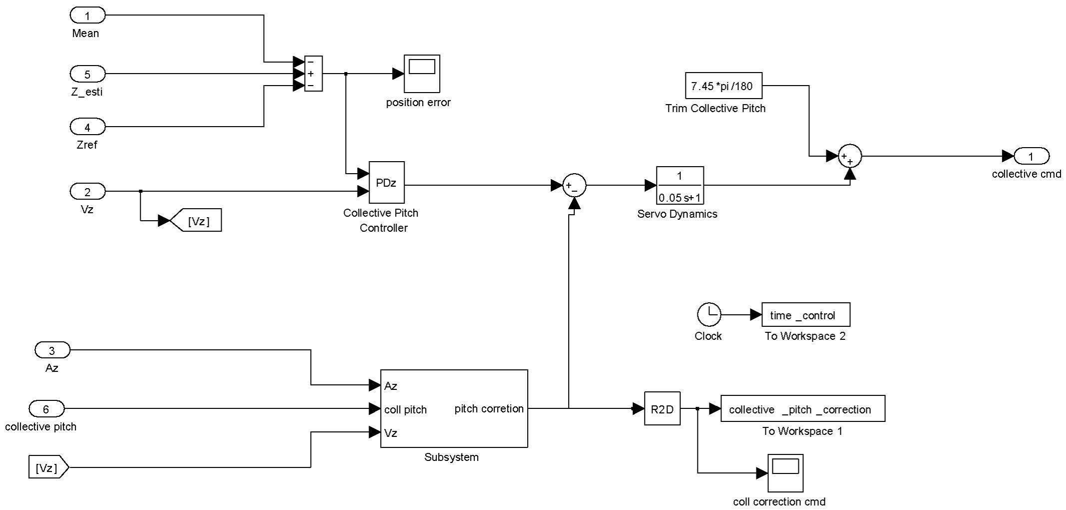

Figure C.9. Simulation subsystem for the feedback-feedforward controller

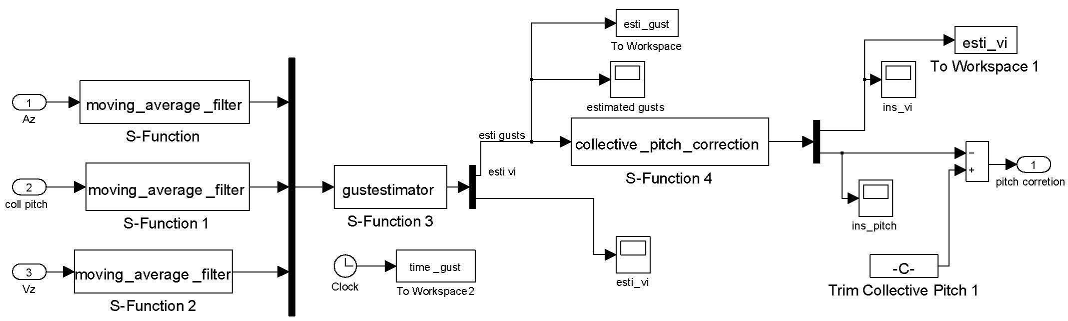

Figure C.10. Simulation model of the feedforward controller

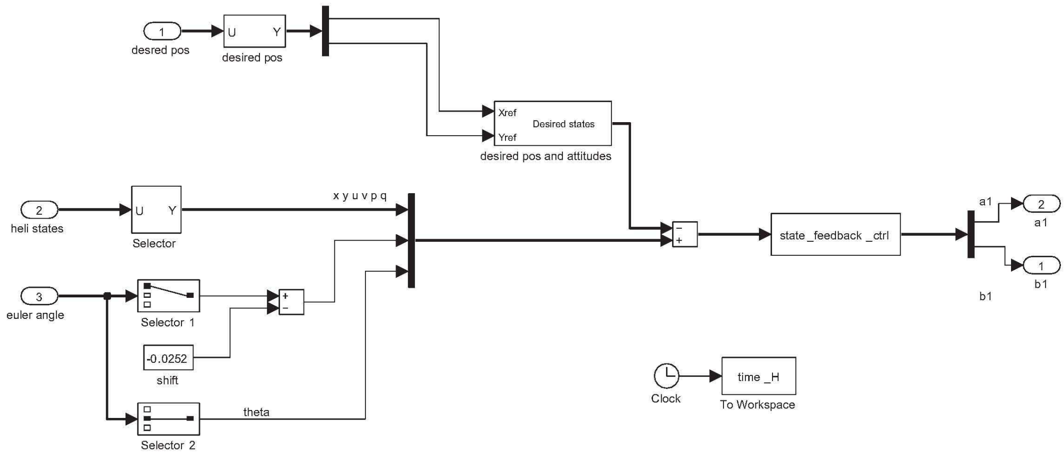

Figure C.11. Simulation subsystem for the H_∞ controller

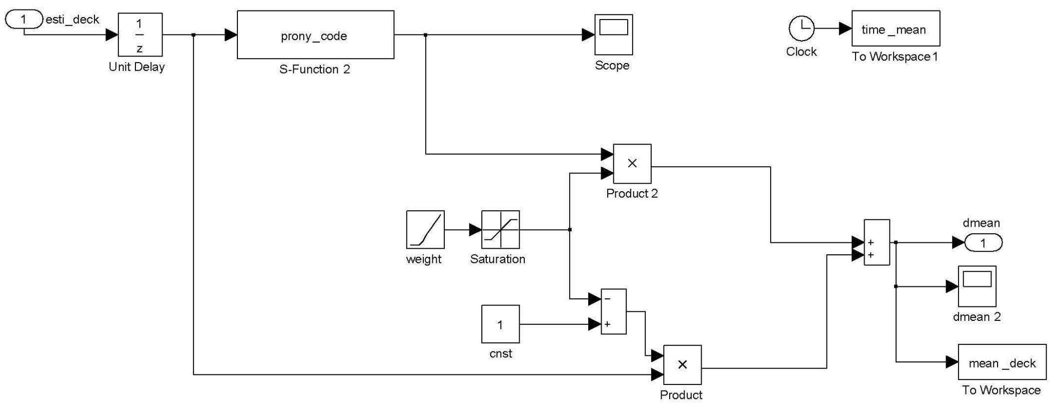

Figure C.12. Simulation subsystem for recursive Prony Analysis

References

[1] G. D. Padfield, *Helicopter Flight Dynamics: the Theory and Applications of Flying Qualities and Simulation Modelling, 2nd edition.* Blackwell Publishing, 2007.

[2] A. S. Hogg, "Development of a robust real-time colour tracking algorithm for helicopter UAV platforms," Bachelor Thesis, Oct. 2010.

[3] N. Stacy, D. Craig, J. Staromlynska, and R. Smith, "The global hawk UAV australian deployment: Imaging radar sensor modifications and employment for maritime surveillance," in *IEEE International Geoscience and Remote Sensing Symposium*, vol. 2, 2002, pp. 699 – 701.

[4] J. G. Drew, R. Shaver, K. F. Lynch, M. A. Amouzegar, and D. Snyder, *Unmanned aerial vehicle end-to-end support considerations.* RAND Corporation, 2005.

[5] J. Downs, R. Prentice, S. Dalzell, A. Besachio, C. M. Ivler, M. B. Tischler, and M. H. Mansur, "Control system development and flight test experience with the MQ-8B fire scout vertical take-off unmanned aerial vehicle (VTUAV)," in *American Helicopter Society 63rd Annual Forum.* Virginia Beach, VA: May, 2007.

[6] K. A. Gluck, J. T. Ball, G. Gunzelmann, M. A. Krusmark, D. R. Lyon, and N. J. Cooke, "A prospective look at a synthetic teammate for UAV applications," in *Proceedings of the American Institute of Aeronautics and Astronautics Infotech@Aerospace Conference*, Reston, USA, 2005.

[7] J. R. Reinhardt, J. E. James, and E. M. Flanagan, "Future employment of UAVs," *Joint Force Quarterly*, no. 22, 1999.

[8] Y. Jin, A. A. Minai, and M. M. Polycarpou, "Cooperative real-time search and task allocation in UAV teams," in *Proceedings of the 42nd IEEE conference on Decision and Control*, vol. 1, Dec. 2003, pp. 7–12.

[9] "Naval aviation force audit report," Canberra Commonwealth of Australia, Tech. Rep. 44, May 1999.

[10] R. Beard, T. McLain, M. Goodrich, and E. Anderson, "Coordinated target assignment and intercept for unmanned air vehicles," *IEEE Transactions on Robotics and Automation*, no. 18, pp. 911–922, 2002.

[11] J. S. Bellingham, M. Tillerson, A. G. Richards, and J. P. How, "Multi-task allocation and path planning for cooperating UAVs," in *Proceedings of Conference on Cooperative Control and Optimization*, 2001.

[12] M. Flint, M. M. Polycarpou, and E. F. Gaucherand, "Cooperative control of multiple autonomous UAV's seach for targets," in *Proceedings of the 41st IEEE Conference on Decision and Control*, 2823-2828 2002.

[13] L. Bo and L. Ping, "A stateflow based simulation of UAV multi-mode flight control," in *8th World Congress on Intelligent Control and Automation (WCICA),*, Jul. 2010.

[14] I. F. Mondragon, P. Campoy, J. F. Correa, and L. Mejias, "visual model feature tracking for UAV control," in *IEEE International Conference on Intelligent Signal Processing*, Oct. 2007, pp. 1–6.

[15] X. Wang and S. N. Balakrishnan, "Optimal and hierarchical formation control for UAV," in *Proceedings of American Control Conference*, Jun. 2005.

[16] R. R. Murphy, K. S. Pratt, and J. L. Burke, "Crew roles and operational protocols for rotary-wing micro-uavs in close urban environment," in *Proceedings of the 3rd ACM/IEEE International Conference on human robot interaction*, 2008.

[17] H. A. Kasdirin, M. H. Jamaluddin, A. Shukor, and A. Khamis, "Development of GUI panel for microprocessor-based controller of a mini-aerial helicopter application," in *2nd International Conference on Emerging Trends in Engineering and Technology*, Dec. 2009.

[18] C. Ozaki and H. H. Qiu, "A simple and convenient sensor for measuring gasoline engine speed and its application in flight control of a portable unmanned helicopter," in *International Conference on Mechatronics and Automation*, Aug. 2007.

[19] X. G. Zhao and J. D. Han, "Adaptive robust guaranteed cost control with application to yaw control of helicopter," in *International Conferenc on Machine Learning and Cybernetics*, vol. 2, Aug. 2007.

[20] S. K. Gavrilets, V. Dugail, D. Mettler, B. Feron, and E. Martinos, "Design and applications of an avionics system for a miniature acrobatic helicopter," in *20th Conference on Digital Avionics Systems*, vol. 1, Oct. 2001.

[21] X. G. Zhao, Z. Jiang, J. D. Han, and G. J. Liu, "Adaptive robust LQR control

with the application to the yaw control of small-scale helicopter," in *Proceedings of the IEEE International Conference on Mechatronics and Automation*, Jun. 2006.

[22] M. D. Sousa, "Unmanned aerial vehicles for rapid environmental assessment and mine countermeasure," Maritime Operations Division, Defense Science and Technology Organization, Tech. Rep., 2005.

[23] L. Young, "Small autonomous air/sea system concepts for coast guard missions," in *U.S. Coast Guard Maritime Domain Awareness Requirements, Capabilities, and Technology Forum, Santa Clara, CA*, Santa Clara, USA, 2005.

[24] R. Cobbold, "The maritime helicopter," *RUSI Journal*, vol. 139, no. 2, 1994.

[25] F. Mora and M. Craig, "AVSAR: a collaboration system for disaster search and rescue operations using autonomous vehicles," *INTERNATIONAL JOURNAL OF ARCHITECTURE ENGINEERING AND CONSTRUCTION*, vol. 2, no. 2, pp. 91–114, 2004.

[26] M. L. Civita, "Integrated modeling and robust control for full-envelope flight of robotic helicopters," Ph.D. dissertation, Department of Mechanical Engineering, Carnegie Mellon University, Pittsburgh, Pennsylvania, USA, Dec. 2002.

[27] E. N. Johnson and S. Fontaine, "Use of flight simulation to complement flight testing of low-cost UAVs," in *AIAA Modeling and Simulation Technologies Conference and Exhibit*, Aug. 2001.

[28] R. Mahony and T. Hamel, "Adaptive compensation of aerodynamic effects during takeoff and landing manoeuvres for a scale model autonomous helicopter," *EUROPEAN JOURNAL OF CONTROL*, vol. 7, pp. 43–57, 2001.

[29] P. J. Garcia-Pardo, G. S. Sukhatme, and J. F. Montgomery, "Towards vision-based safe landing for an autonomous helicopter," *Robotics and Autonomous Systems*, vol. 38, no. 1, pp. 19–29, 2002.

[30] E. Johnson and P. DeBitetto, "Modeling and simulation for small autonomous helicopter development," in *AIAA Modeling and Simulation Technologies Conference*, New Orleans, USA, Aug. 1997, pp. 41–51.

[31] R. Fang and P. J. A. Booij, "Helicopter-ship qualification testing," in *the American Helicopter Society 62nd Annual Forum*, vol. 2. Phoenix, Arizona: the American Helicopter Society International, Inc., May 2006, pp. 743–763.

[32] R. Toffoletto, R. Reddy, and J. Lewis, "Effect of ship frontal shape variation

on flow field in flight deck region," in *Proceedings of the 2nd International Conference on Computational Fluid Dynamics, ICCFD*, Sydney, Australia, 15-19th, Jul. 2002.

[33] G. D. Padfield, "Handling qualities criteria for maritime helicopter operations," in *Proceedings of American Helicopter Society 53rd Annual Forum of the*, vol. 2, 1997, pp. 1425–1440.

[34] M. Voskuijl, G. D. Padfield, D. J. Walker, B. J. Manimala, and A. W. Gubbels, "Simulation of automatic helicopter deck landings using nature inspired flight control," *Aeronautical Journal*, vol. 114, no. 1151, pp. 25–34, 2010.

[35] R. Austin, *Unmanned Aircraft Systems: UAV Design, Development and Deployment*. John Wiley and Sons, Inc., 2010.

[36] S. Khantsis, "Control system design using evolutionary algorithms for autonomous shipboard recovery of unmanned aerial vehicles," Ph.D. dissertation, Royal Melbourne Institute of Technology, August 2006.

[37] G. Gevaert and E. Schulze, "Shipboard launch and recovery of RPV helicopter in high sea states," in *AIAA Guidance, Navigation and Control Conference*, 1978.

[38] S. Oh, S. K. Agrawal, H. Pota, and M. Garratt, "Autonomous helicopter landing on a moving platform using a tether," in *IEEE International Conference on Robotics and Automation*, Apr. 2005, pp. 3960–3965.

[39] A. Y. Lee, J. A. E. Bryson, and W. S. Hindson, "Optimal landing of a helicopter in autorotation," *Journal of Guidance, Control, and Dynamics*, vol. 11, no. 1, pp. 7–12, 1988.

[40] S. M. Esmailifar and F. Saghafi, "Autonomous unmanned helicopter landing system design for safe touchdown on 6DOF moving platform," in *ICAS 5th International Conference on Automatic and Autononous Systems*, May 2009, pp. 245–250.

[41] F. Liao, J. L. Wang, E. K. Poh, and D. Li, "Fault-tolerant robust automatic landing control design," *Journal of Guidance, Control, and Dynamics*, vol. 28, no. 5, pp. 854–871, 2005.

[42] S. S. C. Theodore, D. Rowley, T. Mclain, M. Dai, and M. Takahashi, "Full mission simulation of a rotorcraft unmanned aerial vehicle for landing in a non-cooperative environment," in *the American Helicopter Society 61nd Annual Forum*. Grapevine, TX: the American Helicopter Society International, Inc.,

Jun. 2005.

[43] R. Frezza and C. Altafini, "Autonomous landing by computer vision: an application of path following in SE(3)," in *Proceedings of the 39th IEEE Conference on Decision and Control*, vol. 3, Dec. 2000, pp. 2527–2532.

[44] S. Saripalli, J. F. Montgomery, and G. S. Sukhatme, "Vision-based autonomous landing of an unmanned aerial vehicle," in *IEEE International Conference on Robotics and Automation*, Washington D. C. USA, May 2002, pp. 2799–2804.

[45] S. Saripalli, G. S. Sukhatme, and J. F. Montgomery, "An experimental study of the autonomous helicopter landing problem," *Experimental Robotics VIII*, vol. 5, pp. 466–475, 2003.

[46] O. Shakernia, Y. Ma, T. J. Koo, and S. S. Sastry, "Landing an unmanned air vehicle: Vision based motion estimation and nonlinear control," *Asia Journal of Control*, vol. 1, no. 3, pp. 128–145, 1999.

[47] T. Merz, S. Duranti, and G. Conte, "Autonomous landing of an unmanned helicopter based on vision and inertial sensing," *Experimental Robotics IX*, vol. 21, pp. 343–352, 2006.

[48] S. Bayrakar and E. Feron, "Experiments with small helicopter automated landings at unusual attitudes," *arXiv:0709.1744v1*, Feb. 2008.

[49] S. Saripalli and G. S. Sukhatme, "Landing on a moving target using an autonomous helicopter," in *Proceedings of the International Conference on Field and Service Robotics*, Mt Fuji, Japan, Jul. 2003.

[50] ——, "Landing a helicopter on a moving target," in *IEEE International Conference on Robotics and Automation*, Apr. 2007, pp. 2030–2035.

[51] J. M. Roberts, P. I. Corke, and G. Buskey, "Low-cost flight control system for a small autonomous helicopter," in *Proceedings of IEEE International Conference on Robotics and Automation*, vol. 1, Sep. 2003, pp. 546–551.

[52] H. Shim, D., H. J. Kim, and S. S., "Control system design for rotorcraft-based unmanned aerial vehicles using time-domain system identification," in *Proceedings of the IEEE International Conference on Control Applications*, 2000, pp. 808–813.

[53] D. Park, M. S. Park, and S. K. Hong, "A study on the 3-DOF attitude control of free-flying vehicle," in *IEEE International Symposium on Industrial Electronics*, vol. 2, Pusan, Korea, Jun. 2001, pp. 1260–1265.

[54] A. Dzul, R. Lozano, and P. Castillo, "Adaptive control for a radio-controlled helicopter in a vertical flying stand," *International Journal of adaptive control and signal processing*, vol. 18, no. 5, pp. 473–485, 2004.

[55] B. Mettler, T. Kanade, M. B. Tischler, and W. Messner, "Attitude control optimization for a small-scale unmanned helicopter," in *AIAA Guidance, Navigation, and Control Conference and Exhibit*, August 2000.

[56] P. Bendotti and J. C. Morris, "Robust hover control for a model helicopter," in *Proceedings of the American Control Conference*, vol. 1, Seattle, WA , USA, Jun. 1995, pp. 682–687.

[57] M. L. Civita, G. Papageorgiou, W. C. Messner, and T. Kanade, "Design and flight testing of a high-bandwidth $\mathcal{H}_\infty$ loop shaping controller for a robotic helicopter," *Journal of Guidance, Control, and Navigation*, vol. 29, no. 2, pp. 485–494, 2006.

[58] C. D. Yang, W. H. Liu, and C. C. Kung, "Nonlinear $\mathcal{H}_\infty$ decoupling control for hovering helicopter," in *Proceedings of the American Control Conference*, vol. 6, May 2002, pp. 4353–4358.

[59] C. D. Yang and W. H. Liu, "Nonlinear $\mathcal{H}_\infty$ decoupling hover control of helicopter with parameter uncertainties," in *Proceedings of the American Control Conference*, vol. 4, Denver, CO, USA, Jun. 2003, pp. 3454–3459.

[60] C. C. Kung, "Nonlinear $\mathcal{H}_\infty$ robust control for six DOF equations of motion of rigid body with mass uncertainty," in *Proceedings of the 17th World Congress, the International Federation of Automatic Control*, Seoul, Korea, Jul. 2008, pp. 11 346–11 351.

[61] R. Kureemun, D. J. Walker, B. Manimala, and M. Voskuijl, "Helicopter flight control law design using $\mathcal{H}_\infty$ techniques," in *Proceedings of the 44th IEEE Conference on Decision and Control*, 2005, pp. 1307–1312.

[62] S. Hashimoto, S. Adachi, Y. Segawa, G. Miyamori, and A. Tan, "Robust control design based on identified model for autonomous flight system of an unmanned helicopter," in *The 27th Annual Conference of the IEEE Industrial Electronics Society*, vol. 1, 2001, pp. 323–328.

[63] C. C. Luo, R. F. Liu, C. D. Yang, and Y. H. Chang, "Helicopter $\mathcal{H}_\infty$ control design with robust flying quality," *Aerospace Science and Technology*, vol. 7, no. 2, pp. 159–169, 2003.

[64] M. F. Weilenmann, U. Christen, and H. P. Geering, "Robust helicopter position control at hover," in *Proceedings of the American Control Conference*, vol. 3, Baltimore, USA, Jun. 1994, pp. 2491–2495.

[65] J. N. Rozak and A. Ray, "Robust multivariable control of rotorcraft in forward flight," *Journal of American Helicopter Society*, vol. 42, no. 2, pp. 149–160, 1997.

[66] H. Shim, T. J. Koo, F. Hoffmann, and S. Sastry, "A comprehensive study of control design for an autonomous helicopter," in *Proceedings of the 37th IEEE Conference on Decision and Control*, vol. 4, 1998, pp. 3653–3658.

[67] B. Kadmiry, P. Bergsten, and D. Driankov, "Autonomous helicopter control using fuzzy gain scheduling," in *Proceedings of the IEEE International Conference on Robotics and Automation*, vol. 3, 2001, pp. 2980–2985.

[68] R. Cunha and C. Silvestre, "Simmodelheli: A dynamic simulator for model-scale helicopter," in *11th IEEE Mediterranean Conference on Control and Automation*, 2003.

[69] R. Cunha, C. Silvestre, and A. Pascoal, "A path following controller for model-scale helicopters," Institute for Systems and Robotics, Tech. Rep., 2002.

[70] P. Abbeel, A. Coates, M. Quigley, and A. Y. Ng, "An application of reinforcement learning to aerobatic helicopter flight," in *In Advances in Neural Information Processing Systems 19*. MIT Press, 2007, pp. 1–8.

[71] Z. Jiang, J. Han, Y. Wang, and Q. Song, "Enhanced LQR control for unmanned helicopter in hover," in *1st International Symposium on Systems and Control in Aerospace and Astronautics*, 2006, pp. 1438–1443.

[72] J. C. Morris, M. V. Nieuwstadt, and P. Bendotti, "Identification and control of a model helicopter in hover," in *Proceedings of the American Control Conference*, vol. 2, Baltimore, Maryland, USA, 1994, pp. 1238–1242.

[73] N. Hovakimyan, N. Kim, A. J. Calise, and J. V. R. Prasad, "Adaptive output feedback for high-bandwidth control of an unmanned helicopter," in *AIAA Guidance, Navigation, and Control Conference*, August 2001.

[74] M. Béjar, A. Ollero, and F. Cuesta, "Modeling and control of autonomous helicopters," *Advances in control theory and applications, Lecture Notes in Control and Information Sciences*, vol. 353, pp. 1–30, 2007.

[75] E. N. Johnson and S. K. Kannan, "Adapative trajectory control for autonomous helicopters," *Journal of Guidance, Control, and Dynamics*, vol. 28,

no. 3, pp. 524–538, 2005.

[76] P. V. Kokotovic, "The joy of feedback: nonlinear and adaptive," *IEEE Control Systems Magazine*, vol. 12, no. 3, pp. 7–17, 1992.

[77] T. Cheviron, A. Chriette, and F. Plestan, "Robust control of an autonomous reduced scale helicopter in presence of wind gusts," in *AIAA Guidance, Navigation, and Control Conference and Exhibit*, Keystone, Colorado, USA, Aug. 2006.

[78] R. Mahony and T. Hamel, "Robust trajectory tracking for a scale model autonomous helicopter," *International Journal of Robust and Nonlinear Control*, vol. 14, no. 12, pp. 1035–1059, 2004.

[79] E. Frazzoli, M. A. Dahleh, and E. Feron, "Robust hybrid control for autonomous vehicle motion planning," in *Proceedings of the 39th IEEE Conference on Decision and Control*, vol. 1, Dec. 2000, pp. 821 – 826.

[80] ——, "Trajectory tracking control design for autonomous helicopters using a backstepping algorithm," in *Proceedings of the American Control Conference*, vol. 6, Chicago, Illinois, USA, Jun. 2000, pp. 4102–4107.

[81] C. L. Castillo, W. Alvis, M. C. Effen, W. Moreno, and K. Valavanis, "Small scale helicopter analysis and controller design for non-aggressive flights," in *IEEE International Conference on System, Man and Cybernetics*, vol. 4, 2005, pp. 3305–3312.

[82] E. N. Sanchez, H. M. Becerra, and C. M. Velez, "Combining fuzzy, PID and regulation control for an autonomous mini-helicopter," *Information Sciences*, vol. 177, no. 10, pp. 1999–2022, 2007.

[83] B. Kadmiry and D. Driankov, "A fuzzy gain-scheduler for the attitude control of an unmanned helicopter," *IEEE Transactions on Fuzzy Systems*, vol. 12, no. 4, pp. 502–515, 2004.

[84] K. Tanaka, H. Ohtake, and H. O. Wang, "A practical design approach to stabilization of a 3-DOF RC helicopter," *IEEE Transaction on Control Systems Technology*, vol. 12, no. 2, pp. 315–325, March 2004.

[85] A. T. G. B. and C. M. M., "Automatic helicopter motion control using fuzzy logic," in *The 10th IEEE International Conference on Fuzzy Systems*, vol. 3, Dec. 2001, pp. 860 – 863.

[86] M. Sugeno, I. Hirano, S. Nakamura, and S. Kotsu, "Development of an intelligent unmanned helicopter," *International Joint Conference of the 4th IEEE*

International Conference on Fuzzy Systems and the 2nd International Fuzzy Engineering Symposium, vol. 5, pp. 33–34, mar. 1995.

[87] S. Michio, W. Howard, H. Isao, and K. Satoru, "Intelligent control of an unmanned helicopter based on fuzzy logic," *American Helicopter Society Annual Forum*, pp. 791–803, 1995.

[88] T. Y. Jiang, J. V. R. Prasad, and A. J. Calise, "Adaptive fuzzy logic flight controller for rotorcraft," in *AIAA, Guidance, Navigation and Control Conference*, San Diego, CA, July 1996.

[89] M. Sasaki, H. Ishida, T. Katsuno, and A. Ogasawara, "Learning fuzzy logic controller for hovering a helicopter," in *Conference of the North American Fuzzy Information Processing Society*, Aug. 1998, pp. 25–28.

[90] C. Cavalcante, J. Cardoso, J. Ramos, and O. Neves, "Design and tuning of a helicopter fuzzy controller," in *Proceedings of IEEE International Conference on Fuzzy Systems*, vol. 3, Mar. 1995, pp. 1549 –1554.

[91] C. Phillips, C. L. Karr, and G. Walker, "Helicopter flight control with fuzzy logic and genetic algorithms," *Engineering Applications of Artificial Intelligence*, vol. 9, no. 2, pp. 175–184, 1996.

[92] F. Hoffmann, T. J. Koo, and O. Shakernia, "Evolutionary design of a helicopter autopilot," in *in 3rd On-line World Conf. on Soft Computing (WSC3*, 1998, pp. 201–214.

[93] E. A. Wan and A. A. Bogdanov, "Model predictive neural control with applications to a 6 DOF helicopter model," in *Proceedings of the American Control Conference*, vol. 1, Arlington, VA, USA, Jun. 2001, pp. 488–493.

[94] A. S. Dutka, A. W. Ordys, and M. J. Grimble, "Non-linear predictive control of 2 DOF helicopter model," in *Proceedings of the 42th IEEE Conference on Decision and Control*, vol. 4, Dec. 2003, pp. 3954–3959.

[95] L. Marconi, A. Isidori, and A. Serrani, "Autonomous vertical landing on an oscillating platform: an internal-model based approach," *Automatica*, vol. 38, no. 1, pp. 21–32, 2002.

[96] A. Isidori, L. Marconi, and A. Serrani, "Robust nonlinear motion control of a helicopter," *IEEE Transactions on Automatic Control*, vol. 48, no. 3, pp. 413–426, 2003.

[97] J. C. A. Vilchis, B. Brogliato, A. Dzul, and R. Lozano, "Nonlinear modeling and control of helicopters," *Automatica*, vol. 39, pp. 1583–1596, 2003.

[98] E. L. Castro, R. Bradley, and R. C. Linarest, "Helicopter control design using feedback linearization techniques," in *Proceedings of the 28th IEEE Conference on Decision and Control*, Dec. 1989, pp. 533–534.

[99] T. J. Koo and S. Sastry, "Output tracking control design of a helicopter model based on approximate linearization," in *Proceedings of the 37th IEEE Conference on Decision and Control*, vol. 4, Dec. 1998, pp. 3635–3640.

[100] D. M. Roper, I. Owen, and G. D. Padfield, "Integrating CFD and piloted simulation to quantify ship-helicopter operating limits," *the Aeronautical Journal*, vol. 110, no. 1109, pp. 419–428, 2006.

[101] R. G. Lee and S. J. Zan, "Unsteady aerodynamic loads on a helicopter fuselage in a ship airwake," in *the American Helicopter Society 58th Annual Forum*, vol. 1. Montreal, Canada: the American Helicopter Society, Jun. 2002, pp. 10–21.

[102] J. H. Steven, J. Z. Steven, R. M. David, P. D. Gareth, and O. Ieuan, "Time-accurate ship airwake and unsteady aerodynamic loads modeling for maritime helicopter simulation," *Journal of American Helicopter Society*, vol. 54, no. 2, pp. 1–16, 2009.

[103] D. Lee, N. S. Uzol, J. F. Horn, and L. N. Long, "Simulation of helicopter shipboard launch and recovery with time-accurate airwakes," in *the American Helicopter Society 59th Annual Forum*, vol. 1. Phoenix, Arizona, USA: the American Helicopter Society, May 2003, pp. 1113–1131.

[104] Z. Min, C. Chang, S. C. Siang, L. N. Yong, S. Z. Q. Jacqueline, and W. T. B. Adrian, "Analytical approach to helicopter-ship certification," in *American Helicopter Society 60th Annual Forum*, vol. 1. Baltimore, MD, USA: American Helicopter Society, Jun. 2004, pp. 257–268.

[105] G. Turner, W. Clark, I. Cox, B. Finlay, and J. Duncan, "Project SAIF-assessment of ship helicopter operating limits using the merlin helicopter simulator," in *American Helicopter Society 62nd Annual Forum*, vol. 1. Phoenix, Arizona, USA: American Helicopter Society, May 2006, pp. 226–235.

[106] H. Kang, C. He, and H. Saberi, "Dynamic interface simulation of rotorcraft shipboard on-deck operation," in *the American Helicopter Society 59th Annual Forum*, vol. 1. Phoenix, AZ, USA: the American Helicopter Society International, Inc., May 2003, pp. 1089–1100.

[107] D. H. Titterton and J. L. Weston, *Strapdown Inertial Navigation Technology*,

2nd ed., P. Zarchan, Ed. American Institute of Aeronautics and Astronautics, 2004, vol. 207.

[108] P. D. Groves, *Principles of GNSS, Inertial, and Multisensor Integrated Navigation Systems.* Artech House, 2008.

[109] M. W. Spong, S. Hutchinson, and M. Vidyasagar, *Robot Modeling and Control.* John Wiley and Sons, Inc., 2006.

[110] J. Seddon, *Basic Helicopter Aerodynamics.* Blackwell Science Ltd., 1990.

[111] M. A. Garratt, "Biologically inspired vision and control for an autonomous flying vehicle," Ph.D. dissertation, Australian National University, Australia, Oct. 2007.

[112] A. R. S. Bramwell, *Helicopter Dynamics.* Halsted Press, 1976.

[113] W. Stewart, "Higher harmonics of flapping on the helicopter rotor," *Aeronautical Research Council*, p. C.P. No. 121, 1952.

[114] A. R. S. Bramwell, G. Done, and D. Balmford, *Helicopter Dynamics 2nd edition.* Butterworth-Heinemann, 2001.

[115] M. B. Tischler and R. K. Remple, *Aircraft and Rotorcraft System Identification: Engineering Methods with Flight Test Examples.* American Institute of Aeronautics and Astronautics, 2006.

[116] R. K. Heffley and M. A. Mnich, "Minimum-complexity helicopter simulation math model program," U. S. Army Aeroflight Dynamics Directorate, Ames Research Center, Tech. Rep., October 1986.

[117] A. K. Cooke and E. W. H. Fitzpatrick, *Helicopter Test and Evaluation*, ser. AIAA Education Series. AIAA, 2002.

[118] J. G. Leishman, *Principles of Helicopter Aerodynamics.* Cambridge University Press, 2000.

[119] W. Johnson, *Helicopter Theory.* Dover Publications, Inc, 1994.

[120] R. Cunha and C. Silvestre, "Dynamic modeling and stability analysis of model-scale helicopters with Bell-Hiller stabilizing bar," in *AIAA Guidance, Navigation, and Control Conference and Exhibit*, Aug. 2003.

[121] M. Garratt, H. Pota, A. Lambert, S. E. Maslin, and C. Farabet, "Visual tracking and LIDAR relative positioning for automated launch and recovery of an unmanned rotorcraft from ships at sea," *Naval Engineers Journal*, vol. 121, no. 2, pp. 99–110, 2009.

[122] M. Garratt and J. S. Chahl, "Visual control of a rotary wing UAV," in *UAV*

Asia-Pacific Conference, Feb. 2003.

[123] N. Aouf, B. Boulet, and R. Botez, "Robust gust load alleviation for a flexible aircraft," *Canadian Aeronautics and Space Journal*, vol. 46, no. 3, pp. 131–139, 2000.

[124] N. C. Nigam and S. Narayanan, *Application of Random Vibration*. Springer-Verlag, 1994.

[125] D. Lee and J. F. Horn, "Optimization of a helicopter stability augmentation system for operation in a ship airwake," *American Helicopter Society 61st Annual Forum*, vol. 2, pp. 1149–1159, 2005.

[126] "Flying qualities of piloted aircraft MIL-F-8785C," United States Department of Defence, Tech. Rep., 1980.

[127] D. Lee, "Simulation and control of a helicopter operating in a ship airwake," Ph.D. dissertation, The Pennsylvania State University, Aug. 2005.

[128] O. M. Faltinsen, *Sea loads on ships and offshore structures*. Cambridge University Press, 1990.

[129] T. Perez, *Ship Motion control: course keeping and roll stabilization using rudder and fins*. Springer, 2005.

[130] M. S. Triantafyllou, M. Bodson, and M. Athans, "Real time estimation of ship motions using kalman filtering techniques," *IEEE Journal of Oceanic Engineering*, vol. OE-8, no. 1, pp. 9–20, 1983.

[131] D. G. Lainiotis, C. Charalampous, P. Giannakopoulos, and S. Katsikas, "Real time ship motion estimation," in *Proceedings of OCEANS '92.'Mastering the Oceans Through Technology'*, Oct. 1992, pp. 283–287.

[132] W. S. Ra and I. H. Whang, "Real-time long-term prediction of ship motion for fire control applications," *Electronics Letters*, vol. 42, no. 18, pp. 1020–1021, 2006.

[133] X. Zhao, R. Xu, and C. Kwan, "Ship-motion prediction: algorithms and simulation results," in *Proceedings of IEEE International Conference on Acoustics, Speech, and Signal Processing*, vol. 5, Montreal, Canada, 2004, pp. 125–128.

[134] M. Jie, T. Li, and G. Li, "Comparison of representative methods for time series prediction," in *Proceedings of the 2006 IEEE International Conference on Mechatronics and Automation*, China, Jun. 2006, pp. 2448–2459.

[135] R. L. Kashyap, "Inconsistency of the AIC rule for estimating the order of autoregressive model," *IEEE Transactions on Automatic Control*, vol. 25, no. 5,

pp. 996–998, 1980.

[136] W. Dong, J. Ye, X. Wu, and L. Liang, "Time series prediction for generalized heave displacement of a shipborne helicopter platform," in *ISECS International Colloquium on Computing, Communication, Control, and Management*, Guangzhou, China, Aug. 2008, pp. 80–84.

[137] L. Ljung, *System Identification: Theory for the User.* Prentice-Hall, 1987.

[138] A. Vahidi, A. Stefanopoulou, and H. Peng, "Recursive least squares with forgetting for online estimation of vehicle mass and road grade: Theory and experiments," *Vehicle System Dynamics*, vol. 43, no. 1, pp. 31–55, 2005.

[139] T. Soderstrom and P. Stoica, *System Identification.* Prentice-Hall, 1989.

[140] H. Akaike, "A new look at the statistical model identification," *IEEE Transactions on Automatic Control*, vol. AC-19, no. 6, pp. 716–723, 1974.

[141] G. Schwarz, "Estimating the dimension of a model," *Annals of Statistics*, vol. 6, no. 2, pp. 461–464, 1978.

[142] E. M. Hemerly and M. H. A. Davis, "Strong consistency of the PLS criterion for order determination of autoregressive processes," *Annals of Statistics*, vol. 17, no. 2, pp. 1941–1946, 1989.

[143] H. Chen and J. Zhang, "Identification and adaptive control for systems with unknown orders, delay, and coefficients," *IEEE Transactions on Automatic Control*, vol. 35, no. 8, pp. 866–877, 1990.

[144] J. Kuha, "AIC and BIC: Comparisons of assumptions and performance," *Sociological Methods and Research*, vol. 33, no. 2, pp. 188–229, 2004.

[145] R. Shibata, "Selection of the order of an autoregressive model by Akaike's information criterion," *Biometrika*, vol. 63, no. 1, pp. 117–126, 1976.

[146] M. A. Garratt, H. R. Pota, A. Lambert, and S. E. Maslin, "Systems for automated launch and recovery of an unmanned aerial vehicle from ships at sea," *Proceedings of the 22nd International UAV Systems Conference*, pp. 1401–1415, 2007.

[147] J. S. Dittrich and E. N. Johnson, "Multi-sensor navigation system for an autonomous helicopter," in *Proceedings of the 21st Digital Avionics Systems Conference*, vol. 2, Oct. 2002, pp. 8C1–1—8C1–9.

[148] F. A. Faruqi and K. J. Turner, "Extended kalman filter synthesis for intergrated global positioning/inertial navigation systems," *Applied Mathematics and Computation*, vol. 115, no. 2-3, pp. 213–227, 2000.

[149] J. Wendel, O. Meister, C. Schlaile, and G. F. Trommer, “An integrated GPS/MEMS-IMU navigation system for an autonomous helicopter,” *Aerospace Science and Technology*, vol. 10, no. 6, pp. 527–533, 2006.

[150] R. V. D. Merwe and E. A. Wan, “Sigma-point kalman filters for integrated navigation,” in *Proceedings of the 60th Annual Meeting of the Institute of Navigation*, Dayton, OH, USA, 2004, pp. 641–654.

[151] S. J. Julier, “The scaled unscented transformation,” in *Proceedings of the American Control Conference*, no. 6, 2002, pp. 4555–4559.

[152] B. D. O. Anderson and J. B. Moore, *Optimal Filtering.* Englewood Cliffs, N.J : Prentice-Hall, 1979.

[153] D. J. Trudnowski, “Characteristics of identifying linear dynamic models from impulse response data using Prony analysis,” Pacific Northwest Laboratory, Tech. Rep., Dec. 1992.

[154] J. F. Hauer, “Application of Prony analysis to the determination of modal content and equivalent models for measured system response,” *IEEE Transactions on Power Systems*, vol. 6, no. 3, pp. 1062–1068, 1991.

[155] J. F. Hauer, C. J. Demeure, and L. L. Scharf, “Initial results in Prony analysis of power system response signals,” *IEEE Transactions on Power Systems*, vol. 5, no. 1, pp. 80–89, 1990.

[156] J. Hauer, “The use of Prony analysis to determine modal content and equivalent models for measured power system response,” in *IEEE Symposium on Eigenanalysis and Frequency Domain Methods for System Dynamic Performance.* IEEE Publication 90 TH0292-3-PWR, 1989, pp. 105–115.

[157] R. Lorsaiswami and W. Liu, “Real-time estimation of the parameters of power system small signal oscillations,” *IEEE Transactions on Power Systems*, vol. 8, no. 1, pp. 74–83, 1993.

[158] J. R. Smith, J. F. Hauer, and D. J. Trudnowski, “Transfer function identification in power system applications,” *IEEE Transactions on Power Systems*, vol. 8, no. 3, pp. 1282–1290, 1993.

[159] D. J. Trudnowski, M. K. Donnelly, and J. F. Hauer, “Estimating damping effectiveness of BPA’s thyristor controlled series capacitor by applying time and frequency domain methods to measured response,” *IEEE Transactions on Power Systems*, vol. 11, no. 2, pp. 761–766, 1996.

[160] D. J. Trudnowski, J. M. Johnson, and J. F. Hauer, “Making Prony analysis

more accurate using multiple signals," *IEEE Transactions on Power Systems*, vol. 14, no. 1, pp. 226–231, 1999.

[161] L. Qi, L. Qian, S. Woodruff, and D. Cartes, "Prony analysis for power system transient harmonics," *EURASIP Journal of Advances in Signal Processing*, vol. 2007, p. Article ID:48406, 2007.

[162] P. Davies, "A recursive approach to Prony parameter estimation," *Journal of Sound and Vibration*, vol. 89, no. 4, pp. 571–583, 1983.

[163] R. Carriere and R. L. Moses, "High resolution radar target modeling using a modified Prony estimator," *IEEE Transactions on Antennas and Propagation*, vol. 40, no. 1, pp. 13–18, 1992.

[164] J. J. Sacchini, W. M. Steedly, and R. L. Moses, "Full polarization two-dimensional Prony modeling with application to radar target identification," in *Automatic Object Recognition III*, vol. 1960. SPIE, Oct. 1993, pp. 125–139.

[165] V. Viti, C. Petrucci, and P. Barone, "Prony methods in NMR spectroscopy," *International Journal of Imaging Systems and Technology*, vol. 8, no. 6, pp. 565–571, 1997.

[166] C. W. Therrien and C. H. Velasco, "An iterative Prony method for ARMA signal modeling," *IEEE Transactions on Signal Processing*, vol. 43, no. 1, pp. 358–361, 1995.

[167] P. C. Young, "Time-variable parameter and trend estimation in non-stationary economic time series," *Journal of Forecasting*, vol. 13, no. 2, pp. 179–210, 1994.

[168] P. B. Kenny and J. Durbin, "Local trend estimation and seasonal adjustment of economic and social time series," *Journal of the Royal Statistical Society. Series A*, vol. 145, no. 1, pp. 1–41, 1982.

[169] S. GreenLand and M. P. Longnecker, "Methods for trend estimation from summarized dose-response data with applications to meta-analysis," *American Journal of Epidemiology*, vol. 135, no. 11, pp. 1301–1309, 1992.

[170] N. Zhou, D. Trudnowski, J. W. Pierre, S. Sarawgi, and N. Bhatt, "An algorithm for removing trends from power-system oscillation data," in *Proceedings of the IEEE Power and Engineering Society General Meeting*, Pittsburgh, PA, USA, Jul. 2008, pp. 1–7.

[171] T. Kohonen, *Self-organization and associative memory: 3rd edition.* New York, NY, USA: Springer-Verlag New York, Inc., 1989.

[172] T. Tambouratzis and M. Antonopoulos-Domis, "On-line signal trend identification," *Annals of Nuclear Energy*, vol. 31, no. 14, pp. 1541–1553, 2004.

[173] X. Wang, L. H. Tsoukalas, T. I. C. Wei, and J. Reifman, "An innovative fuzzy-logic-based methodology for trend identification," *Nuclear Technology*, vol. 135, no. 1, pp. 67–84, 2001.

[174] E. Zio and I. C. Popescu, "Recognizing signal trends on-line by a fuzzy-logic-based methodology optimized via genetic algorithms," *Engineering Applications of Artificial Intelligence*, vol. 20, no. 6, pp. 831–849, 2007.

[175] M. A. A. Moussa and M. Y. Cheema, "Non-parametric regression in curve fitting," *Journal of the Royal Statistical Society. Series D (The Statistician)*, vol. 41, no. 2, pp. 209–225, 1992.

[176] A. A. Goshtasby, "Fitting parametric curves to dense and noisy points," in *4th International Conference on Curves and Surfaces*, St. Malo, France, 2000.

[177] M. M. Tawfik and M. M. Morcos, "Prony application for locating faults on loop systems," *IEEE Power Engineering Review*, vol. 21, no. 8, pp. 41–43, 2001.

[178] A. Bracale, P. Caramia, and G. Carpinelli, "Adaptive Prony method for waveform distortion detection in power systems," *International Journal of Electrical Power and Energy Systems*, vol. 29, no. 5, pp. 371–379, 2007.

[179] G. R. B. Prony, "Essai experimental et analytique des vibrations libres amorties," *J. de l'Ecole Polytech*, vol. 1, pp. 24–76, 1795.

[180] M. A. Johnson, I. P. Zarafonitis, and M. Calligaris, "Prony analysis and power system stability-some recent theoretical and applications research," in *IEEE Power Engineering Society Summer Meeting*, vol. 3, 2000, pp. 1918–1923.

[181] W. Zhuang, "RLS algorithm with variable forgetting factor for decision feedback equalizer over time-variant fading channels," *Wireless Personal Communications*, vol. 8, no. 1, pp. 15–29, 1998.

[182] K. Ramdas, D. W. Tufts, and L. L. Scharf, "A Prony method for noisy data: Choosing the signal components and selecting the order in exponential signal models," in *Proceedings of the IEEE*, vol. 72, no. 2, 1984, pp. 230–233.

[183] K. Ogata, *Modern Control Engineering*, 3rd ed. Prentice Hall, 1997.

[184] H. Kang, C. He, and D. Carico, "Modeling and simulation of rotor engagement and disengagement during shipboard operations," in *the AHS International 60th Annual Forum and Technology Display*, vol. 1, Baltimore, MD, USA,

Jun. 2004, pp. 315–324.

[185] H. Xin, C. He, and J. Lee, "Combined finite state rotor wake and panel ship deck models for simulation of helicopter shipboard operations," in *American Helicopter Society 57th Annual Forum*, vol. 2. Washington, DC, USA: American Helicopter Society, May 2001, pp. 1187–1200.

[186] J. M. Buffington, H.-H. Yeh, and S. S. Banda, "Robust control design for an aircraft gust attenuation problem," *Proceedings of the 31st IEEE Conference on Decision and Control*, vol. 1, pp. 560–561, 1992.

[187] S. Jackson, J. Tisdale, M. Kamgarpour, B. Basso, and J. K. Hedrick, "Tracking controllers for small UAVs with wind disturbances: Theory and flight results," *Proceedings of the 47th IEEE Conference on Decision and Control*, pp. 564–569, 2008.

[188] T. Cheviron, F. Plestan, and A. Chriette, "A robust guidance and control scheme of an autonomous scale helicopter in presence of wind gusts," *International Journal of Control*, vol. 82, no. 12, pp. 2206–2220, 2009.

[189] A. Martini, F. Léonard, and G. Abba, "Dynamic modelling and stability analysis of model-scale helicopters under wind gust," *Journal of Intelligent and Robotic Systems*, vol. 54, no. 4, pp. 647–686, 2008.

[190] Australian Bureau of Meteorology, "Australian capital territory weather and warnings," http://www.bom.gov.au/act/, May 2010.

[191] A. Isidori and A. Astolfi, "Disturbance attenuation and $\mathcal{H}_\infty-$control via measurement feedback in nonlinear systems," *IEEE transactions on automatic control*, vol. 37, no. 9, pp. 1283–1293, 1992.

[192] M. A. Khalaf, J. Huang, and F. L. Lewis, *Nonlinear $\mathcal{H}_2/\mathcal{H}_\infty$ Constrained Feedback Control: A Practical Design Approach Using Neural Networks (Advances in Industrial Control).* Springer, 2006.

[193] K. M. Zhou, J. C. Doyle, and K. Glover, *Robust and Optimal Control.* Upper Saddle River: Prentice Hall, 1995.

[194] B. Ahmed, H. Pota, and M. Garratt, "Flight control of a rotary wing UAV using backstepping," *International Journal of Robust and Nonlinear Control*, vol. 20, no. 6, pp. 639–658, 2010.